Dynamically Tunable Photonic Bandgap Materials

Dominic Etienne Schaub

A Ph.D. Thesis

Presented to the Faculty of Graduate Studies of

The University of Manitoba

In Partial Fulfillment of the Requirements for the Degree of

Doctor of Philosophy

Department of Electrical & Computer Engineering

University of Manitoba

Winnipeg, Canada

September 2010

Abstract

Photonic bandgap materials are periodic structures that exclude electromagnetic field propagation over frequency intervals known as bandgaps. These materials exhibit remarkable wave dispersion and have found use in many applications that require control over dynamic electromagnetic fields, as their properties can be tailored by design. The two principal objectives of this thesis are the development of a liquid crystal-based microwave photonic bandgap device whose bandgap could be tuned during operation and the design and implementation of a spectral transmission-line modeling method for band structure calculations.

The description of computational methods comprises an overview of the implemented numerical routines, a derivation of the spectral properties of the transmission-line modeling method in periodic domains, and the development of an efficient sparse matrix eigenvalue algorithm that formed the basis of the spectral transmission-line modeling method. The discussion of experimental methods considers the use of liquid crystals in microwave applications and details the design and fabrication of several devices. These include a series of modified twisted nematic cells that were used to evaluate liquid crystal alignment and switching, a patch resonator that was used to measure liquid crystal permittivity, and the liquid crystal photonic bandgap device itself.

Numerical experiments showed that the spectral transmission-line modeling method is accurate and substantially faster and less memory intensive than the reference plane wave method for problems of high dielectric contrast or rapidly varying spatial detail. Physical experiments successfully realized a microwave photonic bandgap structure whose bandgap could be continuously tuned with a bias voltage. The very good agreement between simulated and measured results validate the computational and experimental methods used, particularly the resonance-based technique for permittivity measurement. This work's results may be applied to many applications, including microwave filters, negative group velocity/negative refraction materials, and microwave permittivity measurement of liquid crystals.

Acknowledgements

I wish to thank my advisor Dr. Derek Oliver for his support, direction, and sagacious advice. I am deeply grateful for the opportunity to have carried out this research under his guidance. I sincerely thank the members of my advisory committee, Dr. Greg Bridges, Dr. Peter Loly, and Dr. Torsten Hegmann for supervising my work and providing invaluable feedback. I am very grateful to Dr. Julien Arino for reviewing the more difficult mathematics of this thesis and providing constructive comments. I thank Dr. Joe LoVetri and Dr. Lotfollah Shafai for recommending improvements to a paper that was later published.

I am grateful to the nanosystems fabrication laboratory manager Dwayne Chrusch and director Dr. Cyrus Shafai for lending considerable guidance and assistance during the fabrication process. I wish to thank CMC Microsystems and James Dietrich of the collaboratory's Advanced RF Systems Lab for carrying out radio-frequency measurements. I appreciated the assistance of the machine shop and technical shop staff, particularly Guy Jonatschick, whose knack of complex computer systems facilitated demanding simulations. I am very grateful to Cory Smit, whose skill and attention to detail contributed materially to the positive outcomes of this thesis.

During the course of my studies I have had the privilege of working with many wonderful fellow students and postdoctoral fellows. I have benefited from the expertise and assistance of Steve Woodrow, Alireza Motieifar, Nusraat Masood, Dr. Jun Hui Zhao, and Dr. Auxence Minko. I am particularly grateful to Pommy Patel, who gave generously of her time during my initial foray into cleanroom work.

I wish to acknowledge the funding I have received from the Natural Sciences and Engineering Research Council of Canada, the University of Manitoba, the University of Manitoba Graduate Fellowship, the University of Manitoba Students Union, and the Faculty of Engineering.

Finally, but not least, I wish to express my profound gratitude to my parents, whose personal interest in my learning and unwavering support over the years have made this thesis possible.

To my parents

Contents

List of Tables

List of Figures

List of Copyrighted Material for which Permission was Obtained

List of Notation

Symbols & Constants

α ..... x-component of the wave vector
α_c ..... Constant of attenuation due to conductor loss
β ..... y-component of the wave vector
Γ ..... Reflection coefficient or torque
γ ..... Viscosity
$\delta(\cdot)$ ..... Dirac delta functional
δ_{ij} ..... Kronecker delta function
$\tan\delta$ ..... Dielectric loss tangent
$\Delta\epsilon$ ..... Difference between parallel and perpendicular permittivities
Δn ..... Index of refraction
Δt ..... Timestep or duration of time
Δx ..... Node width
Δz ..... Thickness
ϵ ..... Scalar permittivity ($\epsilon_0\epsilon_r$)
$\underline{\epsilon}$ ..... Tensor permittivity
ϵ_0 ..... Permittivity of free space (8.854×10^{-12} farads/meter)
ϵ_{eff} ..... Effective permittivity
ϵ_r ..... Scalar or tensor relative permittivity
$\epsilon_\perp$ ..... Perpendicular component of permittivity tensor of a uniaxial medium
$\epsilon_{//}$ ..... Parallel component of permittivity tensor of a uniaxial medium
η ..... Dielectric impedance
θ ..... Polar angle
θ_p ..... Pretilt angle
λ ..... Eigenvalue or wavelength
μ ..... Scalar or tensor permeability ($\mu_0\mu_r$) or Gaussian mean
μ_0 ..... Permeability of free space ($4\pi \times 10^{-7}$ henries/meter)
μ_r ..... Scalar or tensor relative permeability ($\mu_0\mu_r$)
ρ ..... Volumetric electric charge density or radial component of position
ρ_S ..... Surface electric charge density
σ ..... Conductivity, Gaussian standard deviation, or operator spectrum

τ ..... Time constant
ϕ ..... Phase shift or azimuthal angle
Ω ..... A subset of $\mathbb{R}^n$ where $n = 1, 2, 3$ or a frequency shift
ω ..... Angular frequency ($2\pi f$)

a ..... Lattice constant or radius
$\mathbf{A}$ ..... General matrix
$\mathbf{B}$ ..... Magnetic flux density
c ..... Speed of light in vacuum (2.998×10^8 m/s) or complex scalar
C ..... Capacitance
C' ..... Per unit length shunt capacitance
$\mathbf{d}$ ..... Spacing between cylinders
$\mathbf{D}$ ..... Electric flux density or diagonal matrix
$\hat{\mathbf{e}}_{x/y/z}$ ..... Unit basis vector of $\mathbb{R}^3$
$\mathbf{E}$ ..... Electric field intensity
E ..... Electric field magnitude
$\mathbf{F}$ ..... Field recovery operator
F ..... Total free energy or a distribution
f ..... Frequency
F_B ..... Bulk free energy
f_c ..... Cutoff frequency
F_S ..... Surface free energy
F_V ..... Volume free energy
$\mathbf{G}$ ..... Reciprocal lattice vector
G ..... Set of all reciprocal lattice vectors
G' ..... Per unit length shunt conductance
$\mathbf{H}$ ..... Magnetic field intensity or upper Hessenberg matrix
h ..... Height or thickness
$i(\cdot)$ ..... Time-varying current
I ..... Identity matrix
i ..... Positive imaginary number of unit modulus or integer index
j ..... Positive imaginary number of unit modulus or integer index
$\mathbf{J}$ ..... Volumetric electric current density
$\mathbf{J}_S$ ..... Surface electric current density
K ..... Elastic modulus
$\mathbf{k}$ ..... Wave vector in the irreducible Brillouin zone
k ..... Wavenumber or integer timestep
$\mathcal{K}_n$ ..... Krylov subspace of dimensions n
L ..... Inductance
L' ..... Per unit length series inductance
$\hat{\mathbf{n}}$ ..... Unit normal vector or nematic liquid crystal director
$\mathcal{O}(\cdot)$ ..... Computational complexity

Q ..... Quality factor
$\mathbf{Q}$ ..... Orthogonal matrix
$\mathbf{R}$ ..... Rotation matrix or reflection matrix
r ..... Radius
$\mathbf{r}$ ..... Position (x, y, z)
R' ..... Per unit length series resistance
R_S ..... Surface resistivity
$\mathbf{S}$ ..... Scattering matrix or microscopic order parameter
$\mathbf{T}$ ..... Transmission matrix
T ..... Transmission coefficient, time reversal operator, or temperature
T_c ..... Clearing point (temperature of nematic-isotropic transition)
t ..... Time or thickness
v ..... Time-varying voltage or velocity
V ..... Constant voltage
v_p ..... Phase velocity
w ..... Width
Z ..... Impedance
Z_0 ..... Characteristic impedance

Operators & Operations

D^α ..... Partial derivative of order α
∇^2 ..... Laplacian
∇ ..... Gradient
$\nabla\cdot$ ..... Divergence
$\nabla\times$ ..... Curl
$\nabla_{\mathbf{k}}$ ..... Modified del operator defined as $\nabla + i\mathbf{k}$
$\text{supp}(\cdot)$ ..... Support
$< \cdot, \cdot >$ ..... Linear functional
$< \cdot >$ ..... Ensemble average
$(\cdot, \cdot)$ ..... Inner product
$|\cdot|$ ..... Magnitude
$\|\cdot\|$ ..... Norm
$\dagger$ ..... Hermitian adjoint
$^{\mathrm{T}}$ ..... Matrix transpose
$\Im(\cdot)$ ..... Imaginary component
$\Re(\cdot)$ ..... Real component
$\times$ ..... Cross product
$\cdot$ ..... Dot product
$\oplus$ ..... Direct sum

$//$ ..... In parallel with (i.e. $a//b = ab/(a+b)$) or parallel orientation
$\perp$ ..... Perpendicular orientation

Sets

$\mathbb{C}$	Set of complex numbers
$\mathbb{N}_0$	Set of natural numbers including zero
$\mathbb{N}_1$	Set of natural numbers not including zero
$\mathbb{R}$	Set of real numbers
$\mathbb{Z}$	Set of integers

Vector Spaces

$\mathcal{D}(\Omega)$	Space of infinitely differentiable functions having compact support ($C_0^\infty(\Omega)$)
$\mathcal{S}(\Omega)$	Schwartz space
$L_w^2(\Omega)$	Space of weighted scalar square integrable functions
$[L_w^2(\Omega)]^3$	Space of weighted vector square integrable functions
$H^1(\Omega)$	Space of scalar square integrable functions whose divergence lies in $[L^2(\Omega)]^3$
$H(\mathrm{curl}, \Omega)$ ..	Space of vector square integrable functions whose curl lies in $[L^2(\Omega)]^3$
$\nabla_{\mathbf{k}} S$	Subspace of $H(\mathrm{curl}, \Omega)$ whose members may be written as $\nabla_{\mathbf{k}}\phi, \phi \in H^1(\Omega)$
$H_2(\mathrm{curl}, \Omega)$ ..	$\nabla_{\mathbf{k}} S^\perp$ satisfying $H(\mathrm{curl}, \Omega) = H_2(\mathrm{curl}, \Omega) \oplus \nabla_{\mathbf{k}} S$

Abbreviations

3M2CPOOB	(2S, 3S)-3-methyl-2-chloropentanoic acid 4',4"-octyloxybiphenyl ester
5CB	4-n-pentyl-4-cyanobiphenyl
DC	Direct Current
DUT	Device Under Test
EBG	Electromagnetic Bandgap
FCPM	Fluorescence confocal polarizing microscopy
FDTD	Finite-Difference Time-Domain
ITO	Indium Tin Oxide
LC	Liquid Crystal
MW	Molecular Weight

NSFL ..... Nano Systems Fabrication Laboratory (University of Manitoba)
PBG ..... Photonic Bandgap
PC ..... Photonic Crystal
PEC ..... Perfect Electric Conductor
PMC ..... Perfect Magnetic Conductor
PVA ..... Polyvinyl Alcohol
RF ..... Radio Frequency
RMM ..... Rayleigh Multipole Method
RMS ..... Root mean square
RPM ..... Revolutions Per Minute
S-matrix .... Scattering Matrix
SMA ..... Subminiature A
SOLT ..... Short-Open-Load-Thru
TE ..... Transverse Electric
TEM ..... Transverse Electromagnetic
TLM ..... Transmission-Line Modeling
TM ..... Transverse Magnetic
TRL ..... Thru-Reflect-Line

Units

A ..... ampere
B ..... byte
°C ..... degrees Celsius
dB ..... decibel
F ..... farad
H ..... henry
Hz ..... hertz
kg ..... kilogram
m ..... meter
Ω ..... ohm
Ω/sq ..... ohm per square
Pa ..... pascal
s ..... second
S ..... siemens
sccm ..... standard cubic centimeters per minute
T ..... torr
V ..... volt
Vpp ..... volts peak to peak
W ..... watt

Chapter 1

Introduction

1.1 Periodic Structures in Electromagnetics

Periodic materials are an important subject in wave mechanics that occurs in many branches of physics [1]. The interaction of waves with periodic materials gives rise to varied and rich phenomena that have been exploited in many applications. The most notable example comes from solid-state physics, where the interaction of electron waves with a crystalline semiconductor material gives rise to discrete electron energies. The operation of a transistor is based on the fact that the energy associated with electrical conduction can be shifted with an electric field, inducing changes in conductivity. While the significance of the transistor is difficult to overstate, periodic structures are also of substantial importance in the fields of optics, electromagnetics, and acoustics. For example, periodic structures are used in optics as highly efficient mirrors in lasing cavities [2], while in electromagnetics they form the basis of phased array antennas [3].

The study of spatially periodic systems was initiated in 1887 by Strutt [4], who investigated the electromagnetic properties of laminated media and identified Hill's

differential equation [5], which was originally developed for the study lunar orbits, as the mathematical basis for studying one-dimensional periodic systems. The work of Hill was developed independently by Floquet in 1883 [6] and was subsequently generalized to three dimensions by Felix Bloch during the course of developing a quantum description of solids in the 1920s [7].

While the history of this analytical framework lies with electromagnetics and quantum mechanics, the theory is applicable to all systems characterized by the Helmholtz equation, which describes waves in a steady state. This equation arises frequently when steady-state conditions are imposed on a differential equation associated with a time-dependent physical process. In particular, the mathematics describing wave propagation in periodic media applies to the Schrödinger equation of quantum mechanics, the wave equation of linear acoustics, and Maxwell's equations of electromagnetics, and provides a quantitative explanation for common properties found among periodic systems governed by entirely different physical laws.

Periodicity influences many aspects of wave propagation, from velocity, refraction, and dispersion to the very existence of waves at all. In the latter case, where waves within range of frequencies (or energies) cannot exist, the material is said to possess a bandgap (or stopband). This is a consequence of constructive and destructive interference, the most elementary example of which is thin film interference. In electromagnetics, periodicity arises from the periodic variation of material properties such as electrical permittivity, magnetic permeability and domain boundaries. As in the general case, periodic electromagnetic media may possess bandgaps, or regions of the electromagnetic spectrum where the material does not support propagating modes. Bandgaps are sensitive to direction, frequency, and also polarization, as electromagnetic waves are transverse. The periodicity of a material also strongly

influences the phase and group velocities in a manner that is highly dependent upon these parameters.

Periodicity in electromagnetics has enjoyed substantial investigation following the work of Lord Rayleigh, remaining a fruitful and active area of research to the present day. An early application to exploit the reduction in wave velocity is the traveling wave tube, which is used for broadband amplification of microwave frequencies [8–10]. The principle of amplification derives from the modulation an electron beam by an input electromagnetic wave, whose speed is matched to that of the beam by virtue of traveling along a helical transmission line.

A second application to exploit the reduced wave velocity is the slow wave antenna [11–15]. This antenna consists of periodic radiating elements such as periodically-spaced holes in a waveguide and can produce a very narrow beam in the direction of periodicity due to the reduction in phase velocity. Subsequent antenna design has also exploited frequency selective surfaces, which allow waves of certain frequencies to pass while reflecting those in the stopband [16–18]. Such surfaces can allow a reflector antenna to operate at multiple frequencies simultaneously using several focal points.

More recently, periodicity has been adopted in planar circuits for the suppression of parallel plate noise, which arises from switching in high-frequency circuits [19,20]. Periodicity is realized as etchings in the parallel plate waveguide conductors, which induce a bandgap that inhibits switching noise. Research of planar periodic structures has also included several types of microstrip filters, which derive bandstop characteristics from periodicity in the signal line [21–23], the dielectric [24, 25], or the ground plane [26–29].

As research of periodic structures in electromagnetics has taken place alongside that in optics, quantum mechanics, and acoustics, there has been considerable mu-

tual influence in mathematical analysis and design methodologies. In particular, it has become common in electromagnetics to conduct analysis using the formalism developed in solid state physics, whereby periodic systems are considered in terms of their band structure and density of states. This practice has been widely adopted following a seminal paper by Eli Yablonovitch, which explored the use of periodic structures to inhibit spontaneous emission from excited atoms [30]. Research that followed has given rise to several overlapping classifications. Materials whose bandgap features prominently are known as photonic bandgap (PBG) or electromagnetic bandgap (EBG) materials. Photonic bandgap materials consisting exclusively of dielectrics are also known as photonic crystals (PCs), while such one-dimensional materials at optical frequencies are also known as Bragg mirrors. Owing to the lossy nature of metal at higher frequencies, optical structures are usually photonic crystals made of such materials as silicon, sapphire and air. At microwave frequencies PBG materials are commonly fabricated from dielectric as well as metallic materials. As both PCs and EBG materials are described by Maxwell's equations, the distinction between PCs and EBG materials arises primarily from the practical differences between microwave and optical engineering [2, 31–33].

A related class of materials called metamaterials are also periodic [34]. However, whereas photonic bandgap materials are typically used at frequencies on the order of the bandgap, metamaterials are usually employed at frequencies that are so much lower than first bandgap that they may be viewed as an approximation to a homogeneous medium [2]. Metamaterials also share some electromagnetic characteristics with photonic bandgap devices. For example, negative refraction can also be found in photonic bandgap materials, owing to the negative group velocity of certain frequency bands [2, 32].

The electromagnetic properties of conventional photonic bandgap devices com-

prising discrete materials are derived from the underlying geometry and material properties, which remain fixed upon fabrication. Recently, substantial research has been devoted to developing "tunable" devices, whose electromagnetic properties, such as stopbands, can be modified after fabrication or even during operation. In particular, liquid crystal (LC)-based devices have received considerable attention after tunable three-dimensional photonic crystal using nematic liquid crystals were experimentally realized [35–37]. Such devices derive bandgap tuning from the special properties of nematic liquid crystals, whose remarkable orientational order on a molecular scale can be manipulated with macroscopic fields and careful preparation of material surfaces [38–41]. Development of optical photonic bandgap devices based on liquid crystals has intensified over the last few years, and it is expected that this area of research will remain a fruitful source of new devices and avenues of investigation.

1.2 Contributions

This thesis presents contributions to the research of photonic crystals in the areas of numerical modeling and dynamically tunable materials. The first contribution concerns the development of a spectral transmission-line modeling (TLM) method for computing dispersion diagrams and Bloch modes of photonic crystals. This work rests upon expressing steady-state conditions as an eigenvalue equation derived from the matrices arising from the TLM discretization. Its derivation required the original TLM method to be adapted to allow complex-valued voltages and the periodic boundary conditions. As the resultant eigenvalue problem is large and sparse, it was necessary to carefully develop an eigenvalue algorithm using a combination of sparse matrix techniques in order to fully exploit the latent structure present

in the scattering matrices. The method has been found to possess a speed that is comparable to that of its time-marching counterpart but holds several advantages over conventional TLM, including the automatic calculation of Bloch modes and the removal of time stepping and Fourier transforms.

The second topic concerns the design and fabrication of two microwave devices incorporating liquid crystals. These structures are a patch resonator for the measurement of permittivity and a photonic bandgap device designed to exhibit a tunable bandgap. The principal aim of this work was to produce a quasi two-dimensional photonic bandgap device for microwave frequencies whose stopband can be shifted and stretched in frequency using a static electric field, thereby allowing the material to be "tuned" after fabrication and even during operation. The fabricated device exhibited significant bandgap shifting in the range of 6–9 GHz in response to a quasi-static electric field. Tunable structures of this kind are anticipated to have considerable relevance to the design of filters, waveguides, noise suppression, and many others areas of microwave engineering.

The remainder of this thesis is divided into five chapters with content arranged as follows. The second chapter provides a literature review of the areas of research spanned by this thesis. It begins with a mathematical framework of photonic bandgap materials derived from Maxwell's Equations, continues with a review of conventional modeling methods and an overview of nematic liquid crystal physics that is relevant to the work of this thesis, and concludes with a review of existing tunable bandgap and microwave liquid crystal devices.

The third chapter details the computational and experimental methods employed in carrying out this research. Discussion of computational methods includes the development of the spectral transmission-line modeling method and the implementation of numerical codes used in subsequent design. The discussion of exper-

imental methods covers the design, simulation, fabrication, and testing of several optical and microwave structures. These include several modified twisted nematic cells used for the identification of suitable rubbing parameters and evaluation of switching, a circular patch resonator for the measurement of liquid crystal permittivity, a precursory linear microstrip photonic bandgap device used to validate the experimental approach, and a second photonic bandgap device incorporating a liquid crystal material. In addition, network analyzer calibration and the development of a precision buffing machine used in the preparation of liquid crystal-based samples are discussed.

The fourth chapter presents the results of the numerical and experimental work. A comparison of runtimes, computed band diagrams, and eigenmodes are given for several unit cells simulated with the spectral transmission-line modeling method and the algorithms reviewed in the second chapter. The results of experiments involving microwave structures (resonator and bandgap devices) are given as scattering parameters that were measured using two-port network analyzers. These results are compared with simulated values.

The fifth chapter contains a discussion of the results. The spectral transmission-line modeling method is found to be not only accurate but also faster than the plane wave method for problems characterized by high contrast in permittivity or rapidly varying spatial detail. The simulated resonant frequencies and quality factors of the unfilled circular patch resonator are found to be in excellent agreement with measurements. Simulations of the liquid crystal photonic bandgap structure based on the extracted permittivities are similarly found to be in excellent accord.

The sixth and final chapter concludes the thesis. A summary of the work is given and potential future directions are explored. Three appendices follow. Appendix A contains a derivation of the spectral properties of the inhomogeneous curl-curl op-

erator subject to Bloch's theorem, showing that the spectrum of a general photonic bandgap material is discrete for given location in reciprocal space. This analysis rigorously justifies the numerical routines encountered in this thesis. Appendix B outlines the Rayleigh multipole method (RMM), a semi-analytical technique used for the simulation of periodic structures based on circular geometries, and Appendix C provides a detailed tabulation of nanofabrication process parameters employed in the construction of physically-realized devices and mechanical drawings that include the photolithographic masks used. Readers are advised that references to equations, figures, and cited works are hyperlinked in document viewers that are equipped with this facility.

1.3 Publications Arising From This Work

1 D. E. Schaub and D. R. Oliver, "Rapid Simulation of Linear PBG Microstrip Structures Using the Rayleigh Multipole Method," *IEEE Transactions on Microwave Theory and Techniques*, vol. 56, no. 1, pp. 49–55, January 2008.

2 D. E. Schaub and D. R. Oliver, "A Spectral Transmission-Line Method for Computing Band Diagrams and Eigenmodes of Photonic-Bandgap Structures," *IEEE Transactions on Micro-wave Theory and Techniques*, vol. 57, no. 3, pp. 627–636, March 2009.

3 D. E. Schaub and D. R. Oliver, "A Circular Patch Resonator for the Measurement of Microwave Permittivity of Nematic Liquid Crystals," *Submitted to Review of Scientific Instruments in September, 2010.*

4 D. E. Schaub and D. R. Oliver, "A Liquid Crystal-Based Dynamically Tunable Photonic Bandgap Structure," *In Preparation.*

Chapter 2

Literature Review

2.1 Mathematical Overview of Periodic Systems

2.1.1 Photonic Crystals in General Electromagnetics

The electromagnetic analysis of photonic bandgap materials begins with Maxwell's equations, stated here in differential form [42]

$$\begin{aligned} \nabla \times \mathbf{E}(\mathbf{r},t) &= -\frac{\partial \mathbf{B}(\mathbf{r},t)}{\partial t} \\ \nabla \times \mathbf{H}(\mathbf{r},t) &= \frac{\partial \mathbf{D}(\mathbf{r},t)}{\partial t} + \mathbf{J}(\mathbf{r},t) \\ \nabla \cdot \mathbf{D}(\mathbf{r},\mathbf{t}) &= \rho(\mathbf{r},t) \\ \nabla \cdot \mathbf{B}(\mathbf{r},t) &= 0 \end{aligned} \tag{2.1}$$

where $\mathbf{E}$, $\mathbf{H}$, $\mathbf{D}$, $\mathbf{B}$, $\mathbf{J}$, and ρ are the electric field, magnetic field, electric flux density, magnetic flux density, electric current density, and electric charge density, respectively. Each of these is a function of position $\mathbf{r} \in \mathbb{R}^3$ and time $t \in \mathbb{R}$ and, with

the exception of ρ, a vector quantity. Additionally, the field and flux quantities are assumed to satisfy the constitutive equations

$$\begin{aligned} \mathbf{D}(\mathbf{r},\mathbf{t}) &= \epsilon_r(\mathbf{r})\,\epsilon_0\mathbf{E}(\mathbf{r},t) \\ \mathbf{B}(\mathbf{r},t) &= \mu_r(\mathbf{r})\,\mu_0\mathbf{H}(\mathbf{r},t) \end{aligned} \tag{2.2}$$

where ϵ_0 is the permittivity of free space and μ_0 is the permeability of free space. The relative permittivity $\epsilon_r(\mathbf{r})$ and the relative permeability $\mu_r(\mathbf{r})$ are scalar functions of $\mathbf{r}$ and may be discontinuous. These equations describe materials that are isotropic, dispersionless, and whose magnetic and electric polarizations are linear functions of their respective field intensities. It is noted that while these restrictions serve to simplify the present discussion of modeling, they must be relaxed in a general discussion of liquid crystals.

A material's periodicity is manifested in (2.2). For periodic structures of infinite extent the permeability and permittivity satisfy

$$\begin{aligned} \epsilon_r(\mathbf{r}) &= \epsilon_r(\mathbf{r}+n_1\mathbf{a}_1+n_2\mathbf{a}_2+n_3\mathbf{a}_3) \\ \mu_r(\mathbf{r}) &= \mu_r(\mathbf{r}+n_1\mathbf{a}_1+n_2\mathbf{a}_2+n_3\mathbf{a}_3) \end{aligned} \tag{2.3}$$

for $n_1, n_2, n_3 \in \mathbb{Z}$ and where $\mathbf{a}_1$, $\mathbf{a}_2$, and $\mathbf{a}_3$ are the elementary lattice translations, as depicted in Fig. 2.1. In the case where $\mathbf{a}_i \cdot \mathbf{a}_j = 0$ and $|\mathbf{a}_i| = |\mathbf{a}_j|$ for $i \neq j$, the lattice is square and described by the scalar lattice constant $a = |\mathbf{a}_1|$.

As the study of photonic bandgap materials concerns waves, only the two curl equations appearing in (2.1) are relevant. Furthermore, these equations fix ρ up to

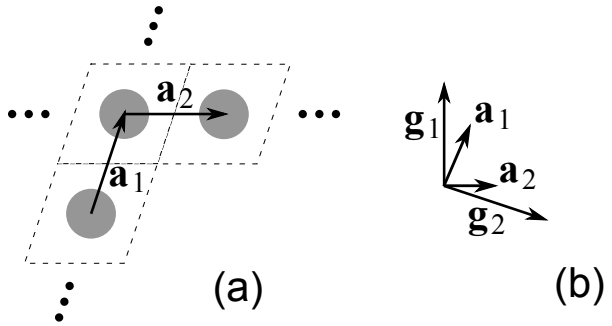

Figure 2.1: Unit cell of an arbitrary two-dimensional photonic crystal (a) and the corresponding elementary direct and reciprocal lattice vectors (b).

a constant, a result of the current continuity equation [42]

$$\frac{\partial \rho\left(\mathbf{r},t\right)}{\partial t} = -\nabla \cdot \mathbf{J}\left(\mathbf{r},t\right) \tag{2.4}$$

For convenience, this constant can be set to zero, which corresponds to the absence of a static electric field.

The spatial derivatives appearing in (2.1) may be stated in a strong or weak sense. In the former, the field quantities are members of the space of continuous functions, and the equations are only valid in regions where $\epsilon_r(\mathbf{r})$ and $\mu_r(\mathbf{r})$ are themselves continuous. Should material properties be discontinuous, supplementary normal and tangential boundary conditions must be enforced along the discontinuities such that [42]

$$\begin{aligned} \hat{\mathbf{n}} \cdot \left(\mathbf{D}_1\left(\mathbf{r},t\right) - \mathbf{D}_2\left(\mathbf{r},t\right)\right) &= \rho_S\left(\mathbf{r},t\right) \\ \hat{\mathbf{n}} \cdot \left(\mathbf{B}_1\left(\mathbf{r},t\right) - \mathbf{B}_2\left(\mathbf{r},t\right)\right) &= 0 \end{aligned} \tag{2.5}$$

and

$$\begin{aligned} \hat{\mathbf{n}} \times \left(\mathbf{E}_1 \left(\mathbf{r}, t\right) - \mathbf{E}_2 \left(\mathbf{r}, t\right)\right) &= 0 \\ \hat{\mathbf{n}} \times \left(\mathbf{H}_1 \left(\mathbf{r}, t\right) - \mathbf{H}_2 \left(\mathbf{r}, t\right)\right) &= \mathbf{J}_S \left(\mathbf{r}, t\right) \end{aligned} \tag{2.6}$$

where ρ_S and $\mathbf{J}_S$ are the surface charge and current densities, respectively, and $\hat{\mathbf{n}}$ is the unit vector normal to the interface between the two materials, which are distinguished by the subscripts 1 and 2. Equations 2.1–2.6, in conjunction with the appropriate boundary conditions, serve as the point of departure for the transmission-line modeling method discussed in §2.2.2.

Further analysis and additional modeling methods can be developed by restating the problem in the frequency domain. By applying the Fourier transform with respect to time, Maxwell's equations can be re-written as a function of frequency

$$\begin{aligned} \nabla \times \mathbf{E} \left(\mathbf{r}, \omega\right) &= -j\omega \mathbf{B} \left(\mathbf{r}, \omega\right) \\ \nabla \times \mathbf{H} \left(\mathbf{r}, \omega\right) &= j\omega \mathbf{D} \left(\mathbf{r}, \omega\right) + \mathbf{J} \left(\mathbf{r}, \omega\right) \\ \nabla \cdot \mathbf{D} \left(\mathbf{r}, \omega\right) &= \rho \left(\mathbf{r}, \omega\right) \\ \nabla \cdot \mathbf{B} \left(\mathbf{r}, \omega\right) &= 0 \end{aligned} \tag{2.7}$$

where the angular frequency ω is related to the frequency f by

$$\omega = 2\pi f \tag{2.8}$$

The frequency-domain counterparts to (2.5) and (2.6) are

$$\begin{aligned} \hat{\mathbf{n}} \cdot (\mathbf{D}_1(\mathbf{r},\omega) - \mathbf{D}_2(\mathbf{r},\omega)) &= \rho_S(\mathbf{r},\omega) \\ \hat{\mathbf{n}} \cdot (\mathbf{B}_1(\mathbf{r},\omega) - \mathbf{B}_2(\mathbf{r},\omega)) &= 0 \end{aligned} \tag{2.9}$$

and

$$\begin{aligned} \hat{\mathbf{n}} \times (\mathbf{E}_1(\mathbf{r},\omega) - \mathbf{E}_2(\mathbf{r},\omega)) &= 0 \\ \hat{\mathbf{n}} \times (\mathbf{H}_1(\mathbf{r},\omega) - \mathbf{H}_2(\mathbf{r},\omega)) &= \mathbf{J}_S(\mathbf{r},\omega) \end{aligned} \tag{2.10}$$

Henceforth, the $\mathbf{r}$ and ω dependencies are suppressed for the frequency dependent quantities. Equations 2.7–2.10 are the starting point of the Rayleigh multipole method (§2.2.3 and Appendix B). The use of continuous functions to represent field quantities represents a significant obstacle to analytical characterization of structures comprising different materials. However, by appealing to the functional analytical framework of weak derivatives, the need to explicitly satisfy these boundary conditions can be removed, thereby simplifying analysis.

A distribution may be defined as a continuous linear functional on $\mathcal{D}(\Omega) \equiv C_0^\infty(\Omega)$, the space of infinitely differentiable functions having compact support in the open set $\Omega \subset \mathbb{R}^3$ [43]. Regular distributions are linear functionals satisfying [43]

$$F : \mathcal{D}(\Omega) \to \mathbb{C}, \qquad \langle F, \phi \rangle = \int_\Omega f(\mathbf{r})\,\phi(\mathbf{r})\,d\mathbf{r}, \qquad \phi \in \mathcal{D}(\Omega) \tag{2.11}$$

which is stated in terms of Lebesgue measure theory and associates the distribution F with the locally integrable function f. Singular distributions, such as the Dirac delta function, are also linear functionals. However, such distributions are not associated with locally integrable functions.

The derivative D^α of a distribution F may be defined as [43]

$$\langle D^\alpha F, \phi \rangle = (-1)^{|\alpha|} \langle F, D^\alpha \phi \rangle \qquad \forall \phi \in \mathcal{D}(\Omega) \tag{2.12}$$

where the multi-index $\alpha = (\alpha_x, \alpha_y, \alpha_z)$ is the order of the derivative with respect to each spatial direction and $|\alpha| = \alpha_x + \alpha_y + \alpha_z$. For regular distributions, this becomes [43]

$$\langle D^\alpha F, \phi \rangle = (-1)^{|\alpha|} \int_\Omega f(\mathbf{r}) \frac{\partial^{|\alpha|} \phi(\mathbf{r})}{\partial x^{\alpha_x} \partial y^{\alpha_y} \partial z^{\alpha_z}} d\mathbf{r} \tag{2.13}$$

which defines the derivative of any regular distribution. For example, this equation may be used to show that the derivative of the Heaviside step function is the Dirac delta function. If $D^\alpha F$ is itself regular, (2.13) may be written as [43]

$$\int_\Omega \left(\frac{\partial^{|\alpha|} f(\mathbf{r})}{\partial x^{\alpha_x} \partial y^{\alpha_y} \partial z^{\alpha_z}} \right) \phi(\mathbf{r}) \, d\mathbf{r} = (-1)^{|\alpha|} \int_\Omega f(\mathbf{r}) \frac{\partial^{|\alpha|} \phi(\mathbf{r})}{\partial x^{\alpha_x} \partial y^{\alpha_y} \partial z^{\alpha_z}} d\mathbf{r} \tag{2.14}$$

This equation defines the weak derivative for the function $f(\mathbf{r})$, which, when sufficiently smooth, becomes the classical Green's theorem [43]. Note that the boundary term is absent due to the fact that functions in $\mathcal{D}$ must vanish on the boundary, a consequence arising from

$$\text{supp}(\phi) \subseteq X \subset \Omega, \qquad \forall \phi \in \mathcal{D}(\Omega) \tag{2.15}$$

where $\text{supp}(\phi)$ is the support of ϕ and X is a closed and bounded subset of Ω (recall that Ω is open).

In cases where a classical derivative exists, the weak derivative will be identical up to a measure of zero. The advantage of using weak derivatives lies in the fact that Maxwell's equations can be recast into a system of distributional differential

equations [44], which may be written as

$$\begin{aligned}
\nabla \times \mathbf{E}(\mathbf{r},\omega) &= -j\omega \mathbf{B}(\mathbf{r},\omega) \\
\nabla \times \mathbf{H}(\mathbf{r},\omega) &= j\omega \mathbf{D}(\mathbf{r},\omega) + \mathbf{J}_V(\mathbf{r},\omega) + \mathbf{J}_S(\mathbf{r},\omega)\,\delta_S \\
\nabla \cdot \mathbf{D}(\mathbf{r},\omega) &= \rho_V(\mathbf{r},\omega) + \rho_S(\mathbf{r},\omega)\,\delta_S \\
\nabla \cdot \mathbf{B}(\mathbf{r},\omega) &= 0
\end{aligned} \tag{2.16}$$

where the subscripts V and S are associated with volume and surface quantities respectively, and δ_S is the Dirac delta distribution, whose argument vanishes on the boundaries that carry a surface current or charge. These equations automatically satisfy the normal and tangential boundary conditions along material discontinuities, which may be seen by equating the singular distributions of each equation.

Applying a second curl to each of the curl equations in (2.7) produces two equations describing waves at steady state

$$\nabla \times \mu(\mathbf{r})^{-1} \nabla \times \mathbf{E} + \epsilon(\mathbf{r})\,\omega^2 \mathbf{E} = -\mathbf{J}_V(\mathbf{r},\omega) - \mathbf{J}_S(\mathbf{r},\omega)\,\delta_S \tag{2.17a}$$

$$\nabla \times \epsilon(\mathbf{r})^{-1} \nabla \times \mathbf{H} + \mu(\mathbf{r})\,\omega^2 \mathbf{H} = \nabla \times (\mathbf{J}_V(\mathbf{r},\omega) + \mathbf{J}_S(\mathbf{r},\omega)\,\delta_S) \tag{2.17b}$$

which may also be written as

$$\epsilon(\mathbf{r})^{-1} \nabla \times \mu(\mathbf{r})^{-1} \nabla \times \mathbf{E} + \omega^2 \mathbf{E} = -\epsilon(\mathbf{r})^{-1} (\mathbf{J}_V(\mathbf{r},\omega) + \mathbf{J}_S(\mathbf{r},\omega)\,\delta_S) \tag{2.18a}$$

$$\mu(\mathbf{r})^{-1} \nabla \times \epsilon(\mathbf{r})^{-1} \nabla \times \mathbf{H} + \omega^2 \mathbf{H} = \mu(\mathbf{r})^{-1} \nabla \times (\mathbf{J}_V(\mathbf{r},\omega) + \mathbf{J}_S(\mathbf{r},\omega)\,\delta_S) \tag{2.18b}$$

Either equation alone is sufficient to describe wave propagation in a photonic

crystal, as each field quantity can be recovered from the other by means of applying the curl operator. Note that (2.18a) and (2.18b) are self-adjoint under the standard $[L^2(\Omega)]^3$ inner product when $\epsilon_r(\mathbf{r}) = 1$ and $\mu_r(\mathbf{r}) = 1$, respectively.

Both analytical and numerical analysis of periodic structures falls into two categories, depending on whether an electromagnetic source is present in calculations. The source may be a current (appearing in the right-hand side of equation 2.17) or a term arising from an inhomogeneous impedance boundary condition [45]. In the absence of a source, the problem consists of solving for the propagating (or evanescent) modes supported by the structure. This arises when calculating the eigenmodes supported by an infinite lattice, and it is expressed mathematically as the general operator equation [42]

$$Ax = \lambda x \tag{2.19}$$

where A is a given differential operator, λ is a scalar, and x is a (possibly vector) solution to the eigenvalue equation.

Development of the analytical problem is continued in Appendix A, which provides a detailed derivation of the spectral properties of periodic structures. This analysis shows that the spectrum of a photonic crystal, when restricted to a particular location in the irreducible Brillouin zone (introduced in §2.1.2), comprises only discrete, real, and positive eigenvalues, thereby justifying the numerical algorithms discussed in the latter part of this section. These algorithms have been used to find approximate solutions to (2.17), having allowed for the evaluation of design alternatives and verification electromagnetic properties prior to fabrication.

2.1.2 Dispersion Diagrams and Symmetry

Wave dispersion is a nonlinear dependence of the wavenumber $\mathbf{k}$ on frequency. While a nonlinear relationship necessarily exists when $\epsilon(\mathbf{r}, \omega)$ or $\mu(\mathbf{r}, \omega)$ exhibit a frequency dependence, such a relationship can also arise in guided wave problems where constituent materials show no such dependence. This is the case with periodic structures, where dispersion is a fundamental property regardless of whether constituent materials are themselves inherently dispersive. Investigation of a periodic structure's dispersion relations commences with the Bloch theorem, which states that the steady-state eigenmodes of an infinitely periodic structure (also known as Bloch modes) may be expressed as [31]

$$\mathbf{E}_{\mathbf{k}}(\mathbf{r}) = \mathbf{u}_{\mathbf{k}}(\mathbf{r})\, e^{j\mathbf{k}\cdot\mathbf{r}} \tag{2.20}$$

where $\mathbf{k} \in \mathbb{R}^3$, and $\mathbf{u}_{\mathbf{k}}(\mathbf{r} + \mathbf{a}_i) = \mathbf{u}_{\mathbf{k}}(\mathbf{r})$ for $i = 1, 2, 3$, such that $\mathbf{u}_{\mathbf{k}}(\mathbf{r})$ is a strictly periodic function in $\mathbb{R}^3$ of the form

$$\mathbf{u}_{\mathbf{k}} = \sum_{\mathbf{G}\in G} \mathbf{u}_{\mathbf{k},\mathbf{G}} e^{j\mathbf{G}\cdot\mathbf{r}} \tag{2.21}$$

The term $\mathbf{u}_{\mathbf{k},\mathbf{G}}$ is a vector coefficient, and $\mathbf{G}$ is a given reciprocal lattice vector from G, the set of reciprocal lattice vectors defined as [33]

$$G \equiv \{\mathbf{G} \in \mathbb{R}^3 : (\exists l, n, m \in \mathbb{Z})\,(\mathbf{G} = l\mathbf{g}_1 + m\mathbf{g}_2 + n\mathbf{g}_3)\} \tag{2.22}$$

where $\mathbf{g}_1$, $\mathbf{g}_2$, and $\mathbf{g}_3$ are the elementary reciprocal lattice vectors (Fig. 2.1). These vectors satisfy the relation

$$\mathbf{g}_p \cdot \mathbf{a}_q = 2\pi\delta_{p,q} \tag{2.23}$$

where $\delta_{p,q}$ is the Kronecker delta function for $p, q = 1, 2, 3$ and $\mathbf{a}_p$ are the elementary direct lattice vectors that define the translational invariance of the structure. The set of reciprocal lattice vectors define the reciprocal space, which assumes a prominent role in the study of a structure's eigenmodes.

Of significant importance is the fact that a given solution of (2.20) does not uniquely define $\mathbf{k}$ and its corresponding function $\mathbf{u}_\mathbf{k}$. In particular, if $(\mathbf{k}, \mathbf{u}_\mathbf{k})$ form a pair that satisfies (2.20), the shifted pair $(\mathbf{k} + \mathbf{G}, e^{-j\mathbf{G}\cdot\mathbf{r}}\mathbf{u}_\mathbf{k})$ also does so for any $\mathbf{G} \in G$. This implies that any dispersion relation between f and $\mathbf{k}$ is periodic in $\mathbf{k}$ with respect to the reciprocal lattice vectors. This result applies to any system that admits Bloch's theorem and fundamentally shapes the mathematical properties of periodic structures.

For the purposes of analysis, the values of $\mathbf{k}$ are restricted to a single repeating parallelepiped defined by the reciprocal lattice vectors and centered at $\mathbf{k} = \mathbf{0}$. This region of reciprocal space is known as the irreducible Brillouin zone. Any function of $\mathbf{k}$ may be extended to the entirety of reciprocal space by replicating and translating the portion that lies within the irreducible Brillouin zone in a manner that may be likened to laying tiles in three dimensions. Thus, while a periodic structure is completely defined by its unit cell and lattice vectors, its electromagnetic characteristics are likewise entirely described by the irreducible Brillouin zone and its associated reciprocal lattice vectors. The foregoing arguments, with slight modification, also apply to one-dimensional and two-dimensional periodic structures.

The dispersion diagram (also known as a band diagram) graphically represents the dispersion of a system's Bloch modes. Figure 2.2 shows a typical band diagram of a two-dimensional photonic crystal comprising regularly spaced sapphire cylinders. In this case, a complete plot would require two degrees of freedom to represent the wavenumber and a third to provide variation of frequency. However,

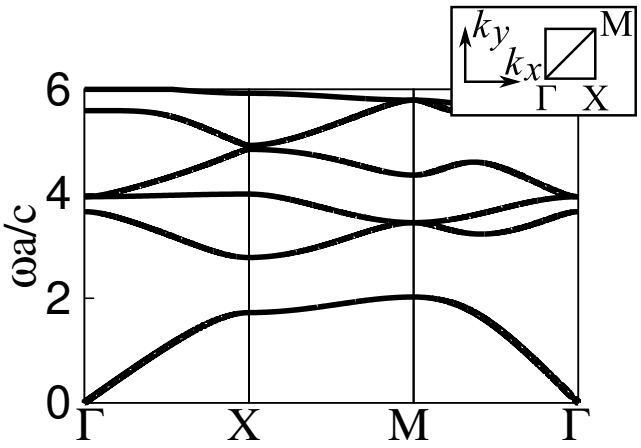

Figure 2.2: Dispersion diagram of a two-dimensional photonic crystal possessing a square lattice of cylindrical rods made of sapphire ($\epsilon_r = 8.9$ [32]), where the cylinder radius is equal to 20% of the lattice constant a. The Rayleigh multipole method (§2.2.3 and Appendix B) was used to produce this plot.

it is customary to plot frequency values parametrically along a closed path in the irreducible Brillouin zone using only two degrees of freedom. Such a plot is significantly less onerous computationally but is adequate for determining dispersion characteristics and the presence and directional dependence of bandgaps.

The choice of path emerges from symmetry considerations such that points of high symmetry are included in the resultant contour. For example, the location Γ in a square lattice of cylinders possesses quadruple reflection symmetry (once about each axis and each diagonal) and triple rotational symmetry (for the angles of $\pi/2$, π, and $3\pi/2$). Rigorous analysis of symmetry requires the use of a group theoretical framework and may be used to analytically prove many characteristics of a crystal's eigenmodes [33]

While many symmetries arise from geometrical characteristics of the unit cell and lattice vectors, time-reversal symmetry is common to all lossless and linear periodic structures regardless of dimension or composition [46]. The time-reversed

state $\mathbf{E}^{\mathrm{tr}}$ may be found with the time reversal operator T defined as [46]

$$\mathbf{E}^{\mathrm{tr}} = T\mathbf{E} \tag{2.24}$$

This operator effects time reversal by complex conjugation and is consequently non-linear. A given state and its time-reversed counterpart both travel forward through time. However, each evolves as the other would if time were to run backwards. For example, outgoing waves become incoming waves and vice versa. Time-reversal symmetry is a consequence of the fact that the complex conjugate of any solution of (2.17) is itself a solution. The origins of this outcome ultimately lie with the nature of the wave equation, which is second order in time and must permit two solutions.

In scattering problems, a state may be distinguished from its time-reversed counterpart by appealing to power flow considerations, as the scattered field must be outgoing at a distance far removed from the scatterer. The distinction is less clear in the study of photonic crystals. Moreover, a time-reversed Bloch mode may be written as

$$\mathbf{E}^{\mathrm{tr}}_{\mathbf{k}}(\mathbf{r}) = \overline{\mathbf{u}_{\mathbf{k}}(\mathbf{r})} e^{-j\mathbf{k}\cdot\mathbf{r}} = \mathbf{E}_{-\mathbf{k}} \tag{2.25}$$

which shows that the time-reversed state for a given $\mathbf{k}$ is simply the non-time-reversed state for $-\mathbf{k}$. The resultant property

$$\mathbf{E}_{\mathbf{k}} \implies \mathbf{E}_{-\mathbf{k}} \tag{2.26}$$

is known as inversion symmetry and is a characteristic of all periodic structures comprising linear materials [33]. The existence of time-reversed modes in the analytical problem is preserved by the spectral TLM discretization, as shown in §3.2.2

2.2 Methods of Modeling Periodic Structures

Several methods for modeling photonic bandgap devices are described in the following sections. While by no means exhaustive, the techniques presented have gained currency as standard modeling methods and have been used in this thesis to model structures.

2.2.1 Plane Wave Method

The plane wave method is the earliest method used to study periodic structures and has remained, to the present, the reference standard for modeling photonic crystals. Its history dates back to the very first works on periodicity in electromagnetics undertaken by Lord Rayleigh, Floquet, and Hill [4–6]. Its present use for modeling crystals possessing discontinuous dielectric functions, however, is very much a consequence of the computational resources that have become available over the last several decades, which have allowed the spectral decomposition of very large matrices. In work prior to this time [1], only low-contrast materials were considered. The following paragraphs and equations are a summary of the discussion found in [2] (see also [31–33]).

The plane wave method begins by expressing both the field and material properties as Fourier series expansions, which may be viewed as a sum of plane waves (after which the method is named). Note that these plane waves are solutions to Maxwell's equation in homogeneous materials. In the presence of material inhomogeneities, these waves are coupled and therefore not solutions to Maxwell's equations when considered individually. The curl-curl equation for the electric field

subject to these expansions may be written as

$$\nabla \times \nabla \times \left[\sum_{\mathbf{G}' \in G} \sum_{\mathbf{G} \in G} \epsilon^{-1} (\mathbf{G}) \mathbf{D} (\mathbf{G}') \right] e^{i(\mathbf{k}+\mathbf{G}+\mathbf{G}')\cdot\mathbf{r}} = -\frac{\omega^2}{c^2} \left[\sum_{\mathbf{G} \in G} \mathbf{D} (\mathbf{G}) e^{i(\mathbf{k}+\mathbf{G})\cdot\mathbf{r}} \right] \tag{2.27}$$

where $\epsilon^{-1}(\cdot)$ and $\mathbf{D}(\cdot)$ are the coefficients of the Fourier series expansion of the inverse of permittivity and electric flux density, respectively, and G is the set of reciprocal lattice vectors. Shifting $\mathbf{G}'$ about $\mathbf{G}$ gives [2]

$$\nabla \times \nabla \times \left[\sum_{\mathbf{G}' \in G} \sum_{\mathbf{G} \in G} \epsilon^{-1} (\mathbf{G} - \mathbf{G}') \mathbf{D} (\mathbf{G}') \right] e^{i(\mathbf{k}+\mathbf{G})\cdot\mathbf{r}} = -\frac{\omega^2}{c^2} \left[\sum_{\mathbf{G} \in G} \mathbf{D} (\mathbf{G}) e^{i(\mathbf{k}+\mathbf{G})\cdot\mathbf{r}} \right] \tag{2.28}$$

Two applications of the relation $\nabla \times (\mathbf{V} e^{i\mathbf{u}\cdot\mathbf{r}}) = i\mathbf{u} \times \mathbf{V} e^{i\mathbf{u}\cdot\mathbf{r}}$ for arbitrary vectors $\mathbf{u}$ and $\mathbf{V}$ eliminates the differential operators, giving [2]

$$\begin{aligned} \sum_{\mathbf{G}' \in G} \sum_{\mathbf{G} \in G} \epsilon^{-1} (\mathbf{G} - \mathbf{G}') (\mathbf{k} + \mathbf{G}) [(\mathbf{k} + \mathbf{G}) \times \mathbf{D} (\mathbf{G}')] e^{i(\mathbf{k}+\mathbf{G})\cdot\mathbf{r}} \\ = -\frac{\omega^2}{c^2} \left[\sum_{\mathbf{G} \in G} \mathbf{D} (\mathbf{G}) e^{i(\mathbf{k}+\mathbf{G})\cdot\mathbf{r}} \right] \end{aligned} \tag{2.29}$$

Projecting onto $e^{i(\mathbf{k}+\mathbf{G})\cdot\mathbf{r}}$ yields [2]

$$\sum_{\mathbf{G}' \in G} \epsilon^{-1} (\mathbf{G} - \mathbf{G}') (\mathbf{k} + \mathbf{G}) [(\mathbf{k} + \mathbf{G}) \times \mathbf{D} (\mathbf{G}')] = -\frac{\omega^2}{c^2} \mathbf{D} (\mathbf{G}) \tag{2.30}$$

This equation is incomplete, as the longitudinal component of $\mathbf{D}$ is not fixed. This may be remedied by enforcing the transversality condition, $\nabla \cdot \mathbf{D} = 0$, which may also be written as $\mathbf{D}(\mathbf{G}) \cdot (\mathbf{k} + \mathbf{G}) = 0 \ \forall \mathbf{G} \in G$. The electric flux density may be

projected onto the two unit vectors orthogonal to $(\mathbf{k}+\mathbf{G})$ [2]

$$\mathbf{D}(\mathbf{G}) = d_{1,\mathbf{G}}\mathbf{e}_{1,\mathbf{G}} + d_{2,\mathbf{G}}\mathbf{e}_{2,\mathbf{G}} \tag{2.31}$$

Substituting (2.31) into (2.30) yields the infinite-dimensional eigenvalue equation [2]

$$\sum_{\mathbf{G}'\in G} \epsilon^{-1}(\mathbf{G}-\mathbf{G}')\left|\mathbf{k}+\mathbf{G}\right|^2 \begin{bmatrix} \mathbf{e}_{1,\mathbf{G}}\cdot\mathbf{e}_{1,\mathbf{G}'} & \mathbf{e}_{1,\mathbf{G}}\cdot\mathbf{e}_{2,\mathbf{G}'} \\ \mathbf{e}_{2,\mathbf{G}}\cdot\mathbf{e}_{1,\mathbf{G}'} & \mathbf{e}_{2,\mathbf{G}}\cdot\mathbf{e}_{2,\mathbf{G}'} \end{bmatrix} \begin{bmatrix} d_{1,\mathbf{G}'} \\ d_{2,\mathbf{G}'} \end{bmatrix} = \frac{\omega^2}{c^2} \begin{bmatrix} d_{1,\mathbf{G}} \\ d_{2,\mathbf{G}} \end{bmatrix} \tag{2.32}$$

Two-dimensional problems can be readily decomposed into two separate equations. When $\epsilon(\mathbf{r})$ is completely invariant to translation in the z-direction, $k_z = 0$, and the reciprocal lattice vectors will contain no z component (which would give rise to variation of the field in the z-direction). This implies that $G_z = G'_z = 0\ \forall \mathbf{G}, \mathbf{G}' \in G$. Hence the transversality condition can always be satisfied by choosing $\mathbf{e}_{1,\mathbf{G}}$ and $\mathbf{e}_{1,\mathbf{G}'}$ to be $(0,0,1)^{\mathrm{T}}$. By orthogonality, the off-diagonal components of the matrix in (2.32) vanish, yielding two individual eigenvalue equations, which correspond to the transverse magnetic (TM) and transverse electric (TE) polarizations.

Equation 2.32 may be approximated by truncating the terms to a finite number around $\mathbf{G} = \mathbf{0}$ and solving the resultant finite-dimensional eigenvalue problem. The accuracy depends heavily upon the geometries and materials of the unit cell and the number of terms retained. Moreover, many plane waves are required to accurately approximate materials possessing high contrast or rapid spatial variation of permittivity. Unfortunately, the matrix arising from the truncation is dense, resulting in eigenvalue analysis whose computational cost is proportional to the cube of the number of terms retained [33].

2.2.2 Time Marching Transmission-Line Modeling Method

The transmission-line modeling (TLM) method is a computational technique that models the time evolution associated with wave propagation in materials of arbitrary composition. The technique was originally developed for electromagnetics by Johns [47], who expanded upon earlier contributions by Kron [48]. The method discretizes both space and time and is derived from Huygens's principle of wave propagation. Space is discretized as a Cartesian network of interconnected transmission lines, while time is treated as discrete intervals. A brief overview of transmission line theory is presented here in order to provide the relevant context for subsequent analysis.

Transmission lines are physical systems that support the propagation of waves and energy in one dimension and occur in acoustics [49], electrical power transmission [50], and electromagnetics [51]. Such structures are characterized by a uniform cross section of finite or infinite extent that is extruded in the third dimension. In electromagnetics, transmission lines comprise a combination of conducting and dielectric materials. Transmission lines consisting of two conductors and a single dielectric such as the coaxial line (Fig. 2.3) support the quasi-transverse electromagnetic (TEM) mode. Analysis of this mode with Maxwell's equations yields the

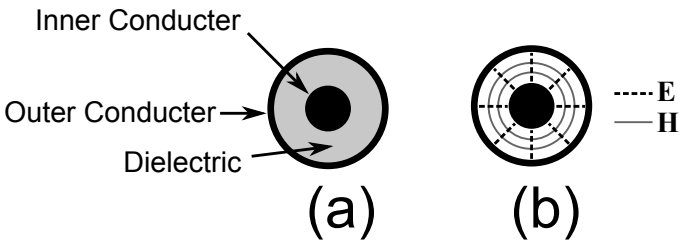

Figure 2.3: Cross section of a coaxial transmission line (a) and the electric and magnetic fields of the transverse electromagnetic mode (b).

telegrapher equations for the voltage $v(z,t)$ and current $i(z,t)$ [51]

$$\begin{aligned}\frac{\partial v\left(z,t\right)}{\partial z} &= -R'i\left(z,t\right) - L'\frac{\partial i\left(z,t\right)}{\partial t} \\ \frac{\partial i\left(z,t\right)}{\partial z} &= -G'v\left(z,t\right) - C'\frac{\partial v\left(z,t\right)}{\partial t}\end{aligned} \tag{2.33}$$

where propagation is assumed to take place along the z-direction, and R', L', G', and C' are the per unit length series resistance, series inductance, shunt conductance, and shunt capacitance, respectively, of the transmission line (Fig. 2.4). The lossless case is considered here such that $R' = G' = 0$. With these conditions, only the fundamental TEM mode propagates for frequencies beneath the cutoff of the first higher order mode(s). Applying a second partial derivative with respect to z and performing a substitution for either v of i yields two one-dimensional wave equations

$$\begin{aligned}\frac{\partial^2 v\left(z,t\right)}{\partial z^2} - L'C'\frac{\partial^2 v\left(z,t\right)}{\partial t^2} &= 0 \\ \frac{\partial^2 i\left(z,t\right)}{\partial z^2} - L'C'\frac{\partial^2 i\left(z,t\right)}{\partial t^2} &= 0\end{aligned} \tag{2.34}$$

The values C' and L' are assumed to bear no dependence on frequency, and thus the TEM mode is dispersionless. In the present discussion, voltages and currents that are solutions to (2.34) are assumed to be real and therefore correspond directly

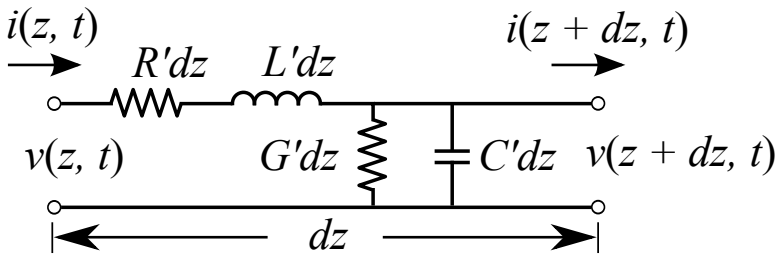

Figure 2.4: Infinitesimal segment dz of an arbitrary transmission line showing the associated voltages and currents, and definitions of R', L', G', and C' [51].

to physically permissible quantities.

Assuming that $i(z,t), v(z,t) \in \mathcal{S}'(z,t)$ (the continuous dual of the Schwartz space $\mathcal{S}(z,t)$), a Fourier transform may be taken of the lossless form of (2.33), giving

$$\begin{aligned} jk_z v\left(k_z,\omega\right) &= -jL'\omega i\left(k_z,\omega\right) \\ jk_z i\left(k_z,\omega\right) &= -jC'\omega v\left(k_z,\omega\right) \end{aligned} \tag{2.35}$$

from which the phase velocity v_p may be defined as

$$v_p = \frac{1}{\sqrt{L'C'}} \tag{2.36}$$

Equation 2.35 also gives

$$v\left(k_z,\omega\right) = \sqrt{\frac{L'}{C'}} i\left(k_z,\omega\right) \tag{2.37}$$

and

$$v\left(z,t\right) = \sqrt{\frac{L'}{C'}} i\left(z,t\right) \tag{2.38}$$

These equations define the ratio of voltage to current for arbitrary solutions to (2.34). This ratio is fixed for all frequencies (the material is dispersionless) and is defined by the characteristic impedance

$$Z_0 = \sqrt{\frac{L'}{C'}} \tag{2.39}$$

which is used extensively in transmission line analysis.

As the systems under consideration are linear and dispersionless, a voltage (or current) characteristic solution of (2.34) may be rewritten as a function of a single

parameter

$$v\left(z - v_p t\right) = v\left(z, t\right) \tag{2.40}$$

for waves traveling in the $+z$-direction, and

$$v\left(z + v_p t\right) = v\left(z, t\right) \tag{2.41}$$

for waves traveling in the $-z$-direction. Waves are scattered upon encountering a discontinuity of impedance, which may arise at a junction between two lines of different impedance or at the connection to a terminal load (Fig. 2.5). Each case produces a reflected wave, whose magnitude depends on the mismatch between the impedances. Where the discontinuity arises from the connection of a second line, a transmitted wave is also produced. The dispersionless character of the transmission lines considered here permits the transmitted and reflected waves to be found by multiplying the incoming wave by frequency-independent transmission

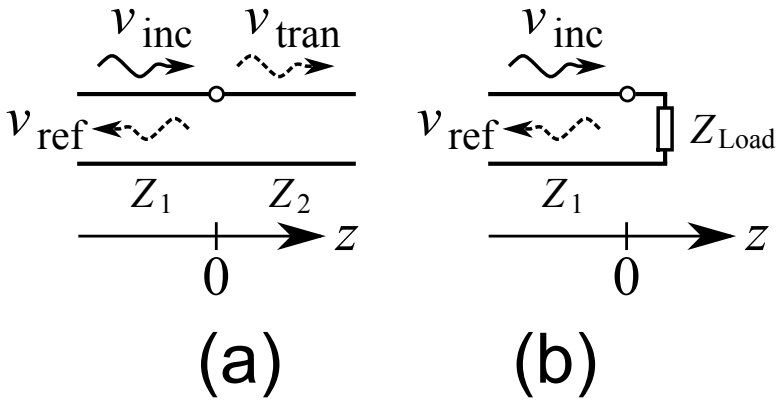

Figure 2.5: Impedance discontinuities arising from a junction of two lines of different impedance (a) and a line termination (b).

and reflection coefficients T_{21} and Γ_{11}, respectively

$$\begin{aligned} v_{\text{tran}}\left(z - v_{2p}t\right) &= T_{21} v_{\text{inc}}\left(z - v_{1p}t\right) \\ v_{\text{ref}}\left(z + v_{1p}t\right) &= \Gamma_{11} v_{\text{inc}}\left(z - v_{1p}t\right) \qquad\qquad \text{when } z = 0 \end{aligned} \tag{2.42}$$

where v_{inc} and v_{ref} are defined for $z < 0$, and v_{tran} is defined for $z > 0$. The subscripts of the coefficients specify the direction of the incoming wave for which they are valid (Fig. 2.5). These coefficients may be found by enforcing continuity of voltage and conservation of current at the junction such that

$$\begin{aligned} \left(1 + \Gamma\right) v_{\text{inc}} &= v_{\text{tran}} \\ \left(1 - \Gamma\right) i_{\text{inc}} &= i_{\text{tran}} \end{aligned} \tag{2.43}$$

giving

$$\begin{aligned} \Gamma_{11} &= \frac{Z_2 - Z_1}{Z_2 + Z_1} \\ T_{21} &= \frac{2Z_2}{Z_2 + Z_1} \end{aligned} \tag{2.44}$$

where (2.38) has been used twice. Note that the definitions in (2.44) are idealizations. The transmission and reflection coefficients of physically realized systems will also depend on the geometry of the junction, particularly its size with respect to wavelength.

The scattering matrix (S-matrix) for the junction depicted in Fig. 2.5a may be defined as

$$\mathbf{S} = \begin{bmatrix} \Gamma_{11} & T_{12} \\ T_{21} & \Gamma_{22} \end{bmatrix} \tag{2.45}$$

This matrix provides a mapping between incoming and outgoing voltage solutions

of (2.34) by means of a matrix multiplication

$$\begin{bmatrix} v_1^{\text{out}}(t) \\ v_2^{\text{out}}(t) \end{bmatrix} = \mathbf{S} \begin{bmatrix} v_1^{\text{in}}(t) \\ v_2^{\text{in}}(t) \end{bmatrix} \tag{2.46}$$

The scattering matrix may be generalized to cases where the junction comprises connections to any number of individual transmission lines. It may readily be shown that the matrix will always be square, possess a dimension equal to the number of transmission lines connected to the junction, and be unitary in the case where the connected transmission lines possess the same impedance.

Wave propagation on a network of interconnected transmission lines is completely described by applying (2.46) and (2.45) to each junction after revising $\mathbf{S}$ to reflect the number of transmission lines and their impedances. However, this approach may lead to very complicated expressions for the voltage and current. For certain networks, analysis may be simplified by approximating the continuous voltages as pulses whose amplitudes are constant for discrete intervals of time, the duration of which corresponds to the length of time required for a wavefront to travel between two neighboring junctions. Consequently, scattering remains constant for the duration of the time interval and may be computed with a single scattering calculation. For a given set of initial voltage pulses, the system may be advanced to the next time interval by

$$\mathbf{v}(1) = \mathbf{MSv}(0) \tag{2.47}$$

where $\mathbf{S}$ is a block-diagonal matrix whose submatrices are the individual scattering matrices of each junction, $\mathbf{M}$ is the matrix that maps each junction's outgoing voltage pulses to incoming pulses at neighboring junctions, and $\mathbf{v}(0)$ and $\mathbf{v}(1)$ are

sets of voltages on the network of transmission lines for two successive intervals. The time evolution of a system may be investigated by repeatedly evaluating (2.47).

The approach outlined above is only valid when the time required for a wavefront to travel from one junction to the next is identical for each pair of neighboring junctions. Such a case arises, for example, when identical transmission lines are arranged as a Cartesian mesh (Fig. 2.6a).

TLM exploits the fact that wave propagation in an arbitrary material can be approximated by wave propagation occurring in discrete time steps on a mesh of interconnected transmission lines [52, 53]. The TLM formulation provides an explicit correspondence between the transmission-line quantities of voltage and current, and the electric and magnetic fields of the system being modeled (2.1). The mesh may assume one of several forms, depending on the dimensionality of the problem. The Cartesian mesh of Fig. 2.6a may be used to model a two-dimensional problem formulated in the TM polarization. The mesh comprises individual nodes (Fig. 2.6b and 2.6c), each of which contains a junction of five transmission lines, four of which are connected to neighboring nodes. The fifth transmission line is a shunt stub whose length equals half that of the connecting lines and is terminated by an open circuit. The impedances of the transmission lines and the termination of the mesh are related to the material properties and boundary conditions of the system being

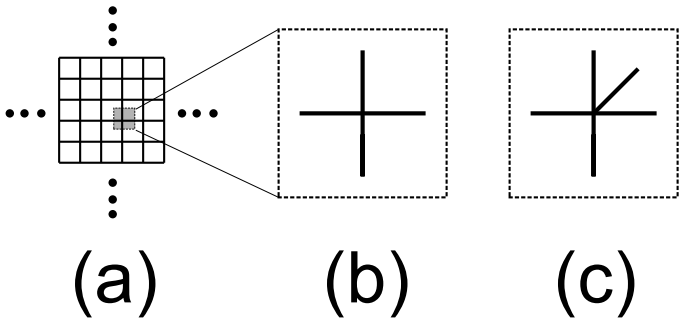

Figure 2.6: A 2D TLM mesh comprising shunt nodes for the TM polarization.

modeled and are discussed in further detail in §3.2.

Typical use of the transmission-line modeling method parallels that of other time-domain simulation techniques such as Finite-Difference Time-Domain (FDTD). The primary difference between the methods derives from the dynamical variables used, which are voltages in the case of TLM and the electric and magnetic fields in the case of FDTD, and the method of calculating the evolution of these variables. The transmission-line modeling method simulations commence by assigning a series of initial voltages to a subset of the nodes of the mesh, which is then repeatedly incremented in time using (2.47). The initial voltages on the mesh are produced by injecting a set of voltage pulses in the first few timesteps, which may be accomplished with the discrete, truncated Gaussian

$$\begin{aligned} v_n(k) = &\quad e^{-\frac{(\Delta tk-\mu)^2}{\sigma^2}} && |\Delta tk-\mu| \leq p \\ = &\quad 0 && |\Delta tk-\mu| > p, \quad p \in \mathbb{R}^+ \end{aligned} \tag{2.48}$$

or alternatively the Kronecker delta

$$v_n(k) = \delta_{k,0} \tag{2.49}$$

where k is the time increment and n is the index of the node(s) subject to the injection of the initial voltages. Equation 2.49 contains all frequencies that are supported by the mesh in equal proportion for a given point on the mesh, while the parameters of (2.48) are chosen such that the resultant pulse contains only the frequencies of interest.

During the course of the mesh's time evolution, voltages are recorded for selected nodes such that the entire history of voltages on these nodes is known upon com-

pletion of the time-stepping. A Fourier transform is performed on each of the time series of voltages when the frequency dependence of the excitation is desired, such as when computing the frequency dependence of scattering parameters, calculating the frequency-dependent radiation pattern of an antenna, or when determining the resonant modes of a structure (such as the unit cell of a photonic crystal).

Implementing steady-state boundary conditions may be difficult when using time-domain methods for problems whose boundary conditions are stated as phase delays. Such boundary conditions arise in the modeling the unit cell of a photonic crystal, where waves passing through a boundary and leaving the unit cell are made to reappear on the opposing side as an identical wave shifted in phase. As the phase shift is fixed, such a boundary must necessarily be dispersive. This may be illustrated by considering the associated time delay

$$\Delta t = \frac{\phi}{kv} \tag{2.50}$$

where Δt is the time delay, ϕ is the phase delay, k is the wavenumber, and v is the phase velocity. While shifts in time may be readily incorporated in time-domain methods, implementing frequency dependence requires complicated expressions involving dynamical quantities that span many timesteps [54]. An alternative approach exploits the fact that an arbitrary phase shift can be effected by combining two signals of a single frequency that are $\pi/4$ radians out of phase with each other

$$\cos(\omega t + \phi) = A\cos(\omega t) + B\sin(\omega t) \tag{2.51}$$

where A and B are real constants that satisfy the equation for a given value of ϕ. A successful approach employed by [55, 56] employs a dual mesh, where the

eigenmodes evolve in time on both meshes but are $\pi/4$ radians out of phase. The mathematics of this assertion receive additional treatment during the analysis of the spectral problem in §3.2. The coupling at the boundary for a dual mesh system is

$$\begin{aligned} v_1^{\text{in}} &= v_1^{\text{out}} \cos(\mathbf{k}\cdot\mathbf{a}) - v_2^{\text{out}} \sin(\mathbf{k}\cdot\mathbf{a}) \\ v_2^{\text{in}} &= v_1^{\text{out}} \sin(\mathbf{k}\cdot\mathbf{a}) + v_2^{\text{out}} \cos(\mathbf{k}\cdot\mathbf{a}) \end{aligned} \tag{2.52}$$

where $\mathbf{k}$ is the location in the irreducible Brillouin zone that defines the boundary conditions, $\mathbf{a}$ is the spatial translation of the pulse across the unit cell, and where the subscripts indicate the mesh for the given voltage.

2.2.3 Rayleigh Multipole Method

The Rayleigh multipole method is a two-dimensional semi-analytical algorithm for computing the electromagnetic characteristics of diffraction gratings comprising dielectric or metallic cylinders [57, 58]. The technique calculates the diffracted and reflected fields (propagating and evanescent) in response to an incident plane wave. This method may be applied to studying two-dimensional photonic crystals composed of periodically arranged circular dielectric elements by decomposing the structure into individual diffraction grating layers (Fig. 2.7), and stating the relation between the diffracted and reflected orders as an eigenvalue problem.

While limited to circular geometries, RMM is exceptionally fast owing to explicit use of geometry. As the prototype microstrip test structure employed circular scattering elements (disks), RMM was a natural choice for performing band diagram and finite structure simulations, particularly for parameter optimization where many thousand variations were calculated in order to determine the disk radius that maximized the width of the stopband.

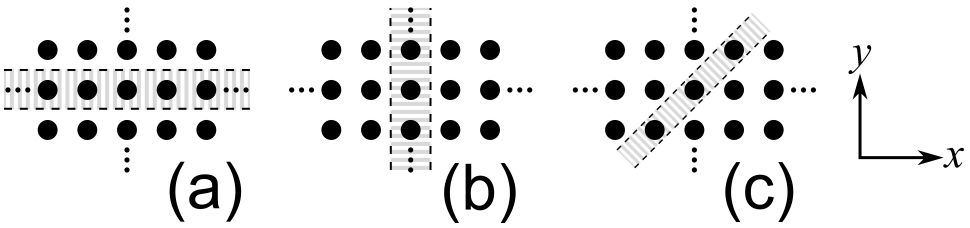

Figure 2.7: Photonic crystal possessing a square lattice showing the three elementary decompositions into individual diffraction gratings.

The essence of RMM lies with finding the relation between incoming and scattered fields. This is done by expanding the field in the vicinity of one cylinder as a sum of cylindrical harmonic functions and equating outgoing harmonics with incoming ones using the boundary conditions at the surface of the cylinder and periodicity of the field. This relation is expressed as a matrix that, when inverted, gives the scattered field in terms of the diffracted modes. A detailed derivation of the method is presented in Appendix B.

In addition to the restriction on geometry, a second disadvantage of the Rayleigh multipole method lies with nature of the eigenvalue calculation. Whereas the plane wave method finds eigenvalues ω^2 for a given (k_x, k_y), the Rayleigh multipole method finds values of k_y for a given ω. As bands are generally more "flat" than "vertical", the plane wave method requires fewer simulated values to produce an acceptable band diagram. When using the Rayleigh multipole method to compute bands that are nearly flat, ω must be incremented in very small steps, an approach that produces very large data sets that complicate post-processing. Notwithstanding, this program has been used in this thesis wherever it was necessary to simulate structures comprising disks as its speed compares very favorably to other methods.

2.3 Physics of Nematic Liquid Crystals

Liquid crystals are remarkable materials that exist in one or more mesophases over certain temperature range(s). This state of matter is a fluid that lies between the solid crystalline and isotropic liquid phases. It is characterized by long-range molecular order, the presence of which corresponds to a Hamiltonian of reduced symmetry when compared to that of an isotropic material. Liquid crystals may be classified according to their molecular arrangement in their respective mesophases, the least ordered being the nematic mesophase, which is characterized by long-range orientational order and the absence of positional order (Fig. 2.8). Cholesteric (also known as chiral nematic) liquid crystals comprise molecules arranged in continuous helical distortions. Finally, the smectic mesophase possess orientational order as well as some positional order in the form of layers. Variation in these properties gives rise to several additional subclassifications, particularly in the case of smectic liquid crystals where there many different modifications [38].

Of the different varieties of liquid crystals, nematics are perhaps the most widely used in applications such as displays. An example of a nematic liquid crystal is 5CB [59] (Fig. 2.9). This molecule (like many nematics) possesses a strong permanent dipole due to the cyano group [38]. Analysis may be simplified by modeling such nematics as rod-like structures whose average local orientation is described by the unit vector known as the director $\hat{\mathbf{n}}$. The liquid crystals considered

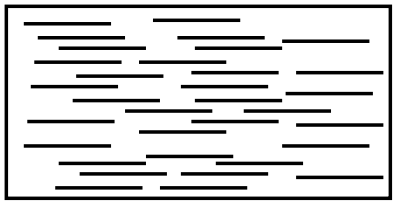

Figure 2.8: Molecular arrangement of a liquid crystal in the nematic phase.

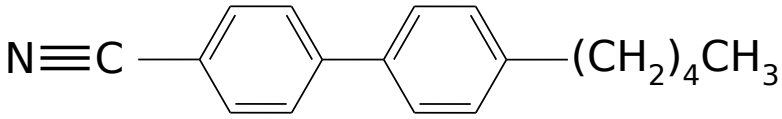

Figure 2.9: Chemical structure of 5CB (4-n-pentyl-4-cyanobiphenyl) [59]. Note the cyano group, which endows the molecule with a very strong dipole moment [38].

in the present discussion are not ferroelectric, and as a result the bulk material (in contrast to individual molecules) lacks a spontaneous polarization. Consequently, the director is only unique up to a sign [38]. As the subject of liquid crystals is quite expansive, the remainder of this section concerns only nematic liquid crystals, which are used in experiment.

In thermotropic nematic liquid crystals, phase transitions occur with change in temperature. The mesophase exists between the melting point (the temperature at which the solid material melts and yields the liquid crystal mesophase) and the clearing point T_C. The latter is the temperature at which the mesophase loses its reduced symmetry and becomes an isotropic liquid. In many cases, the melting point can be reduced by forming a eutectic mixture of two or more liquid crystals such that the resultant mixture will exist in a mesophase for a greater range of temperature than either material alone [38].

2.3.1 Orientational Order

The orientational order in a uniaxial nematic liquid crystal is described quantitatively by the microscopic scalar order parameter [38, 41]

$$S = \frac{1}{2}\left\langle \cos^2(\theta) - 1 \right\rangle \tag{2.53}$$

where $< \cdot >$ is an ensemble average over a small volume and θ is the angle between a given molecule and the director. The distribution of molecular orientations with respect to the director is shown for a typical case in Fig. 2.10. The order parameter may range in value from $-1/2$ to 1 and is strongly dependent upon temperature. A value of zero corresponds to an isotropic liquid, while positive and negative values correspond to orientations that are planar and perpendicular to the director, respectively, where the magnitude indicates the degree of alignment. The order parameter is positive for the rod-like nematic liquid crystals considered in the present discussion [38, 41].

Orientational order is also manifested in macroscopic properties such as dielectric, optical, and magnetic anisotropy in the form of second-rank tensor susceptibilities [60]. In particular, the diamagnetic susceptibility bears a direct correspondence to the microscopic order parameter as a consequence of the fact that molecular magnetic properties, ultimately dipolar in nature, are largely free of intermolecular interactions. While dielectric susceptibility is also related to the microscopic order parameter, strong electrical interaction between molecules (such as induced dipoles) precludes drawing a simple and reliable connection between molecular and

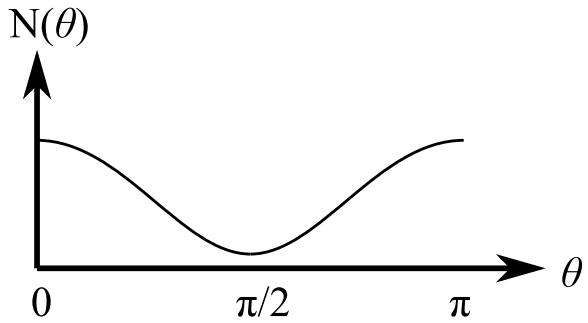

Figure 2.10: Distribution of molecular orientations in a nematic liquid crystal, where θ is the angle with respect to the director [38]. The function shown corresponds approximately to that of a nematic liquid crystal. Note that $\mathrm{N}(\theta)$ must be symmetric about $\pi/2$ due to the equivalence between $\hat{\mathbf{n}}$ and $-\hat{\mathbf{n}}$.

bulk electrical properties [61,62]. Nonetheless, the axial symmetry of the bulk liquid crystal allows the permittivity of the medium to be expressed as the tensor [38]

$$\underline{\epsilon} = \begin{bmatrix} \epsilon_{\perp} & 0 & 0 \\ 0 & \epsilon_{\perp} & 0 \\ 0 & 0 & \epsilon_{//} \end{bmatrix} \tag{2.54}$$

where the basis vectors are formed from the director and two (degenerate) vectors that span the plane that is normal to the director. The permittivity tensor depends strongly on frequency and temperature [41] (Fig. 2.11). The latter dependence may be exploited in a crude fashion to dynamically switch the permittivity of the material.

2.3.2 Elastic Properties

In general, the orientation of the director is a function of position, time, temperature, externally applied electric and magnetic fields, bounding surfaces, and

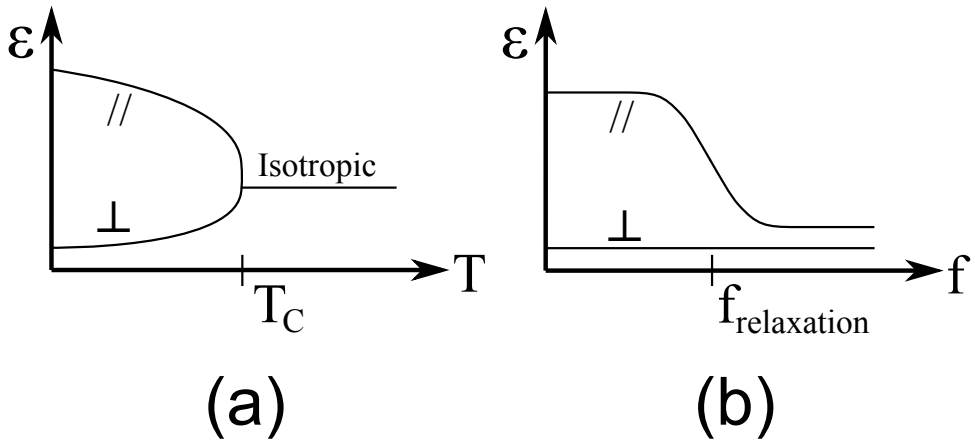

Figure 2.11: Temperature dependence (a) and frequency dependence for $T < T_C$ (b) of the parallel and perpendicular components of the permittivity for a nematic liquid crystal possessing a positive dielectric anisotropy [41]. Note that the lack of orientation at temperatures above T_C results in an isotropic permittivity.

the intrinsic elastic, viscous, and electrostatic properties of the material [38]. The picture is simplified considerably by first considering the static case, where none of the quantities exhibit dependence on time and where the temperature is held constant at some T below T_C. Under these conditions, motion is limited to small thermal fluctuations, and the forces acting on the director will be at equilibrium and correspond to the solution that minimizes the free energy [41]

$$F = F_S + F_B \tag{2.55}$$

where F_S is the free energy resulting from interaction between the liquid crystal and the bounding surface, and F_B is the free energy of the bulk material. Note that minimization of (2.55) may not yield a unique solution, an issue that may arise in the design of a twisted nematic cell [38].

The free energy in the bulk material may be written as [41]

$$F_B = \int_V (g_f + g_k + g_\epsilon + g_H)\, dV \tag{2.56}$$

where the terms labeled with the subscripts, f, k, ϵ, and H are the volumetric free energy densities due to the flexoelectric, elastic, electric, and magnetic forces, respectively. The contribution due to a magnetic field is assumed to be zero in the present discussion. The volumetric density of elastic free energy in a nematic liquid crystal is given as [41]

$$g_k = \frac{1}{2}\left[K_{11}\left(\nabla \cdot \hat{\mathbf{n}}\right) + K_{22}\left(\hat{\mathbf{n}} \cdot \nabla \times \hat{\mathbf{n}}\right) + K_{33}\left(\hat{\mathbf{n}} \times \nabla \times \hat{\mathbf{n}}\right)\right] \tag{2.57}$$

where the first, second and third terms correspond to the splay, twist, and bend deformations, respectively, and the various K are the associated elastic moduli.

The volumetric density of electric free energy is given as [41]

$$g_\epsilon = -\frac{1}{8\pi}\mathbf{D}\cdot\mathbf{E} = -\frac{1}{8\pi}\left(\epsilon_\perp E^2 + \Delta\epsilon\left(\mathbf{E}\cdot\hat{\mathbf{n}}\right)^2\right) \tag{2.58}$$

where $\Delta\epsilon = \epsilon_{//} - \epsilon_\perp$, $\mathbf{D}$ is the electric flux density, and $\mathbf{E}$ is the electric field. The volumetric free energy density due to the flexoelectric polarization may be written as [41]

$$g_f = -\left(\mathbf{P}_f\cdot\mathbf{E}\right) \tag{2.59}$$

where $\mathbf{P}_f$ is the flexoelectric polarization,

$$\mathbf{P}_f = e_{11}\hat{\mathbf{n}}\nabla\cdot\hat{\mathbf{n}} - e_{33}\left(\hat{\mathbf{n}}\times\nabla\times\hat{\mathbf{n}}\right) \tag{2.60}$$

and e_{11} and e_{33} are the flexoelectric moduli.

While the minimization of free energy generally favors a smoothly varying director field, in certain instances the director may exhibit discontinuous points or surfaces known as disclinations. Several types of disclinations are possible, depending on a given sample's boundary conditions and history. In nematic liquid crystals, defects often appear as threads when viewed through a polarizing microscope that either terminate at the boundaries or form closed loops. In the case of the twisted nematic cell, twist disclinations may arise at the boundaries between regions of right and left-handed twists, as both twists are equally favored energetically. Defects may be a permanent feature of a given sample or may vanish with time (as happens with twist disclinations) [38].

2.3.3 Alignment

The surface term F_S of (2.55) may be similarly defined in terms of several constituent elements and will assume a minimum value when molecules on the surface are aligned along the direction favored by the surface (note that a minimum value of F_S does not necessarily coincide with that of F). In the case where strong surface anchoring is assumed, its inclusion in the minimization of (2.55) may be replaced with boundary conditions that fix the director orientation along the preferred direction of the bounding surface [41]. The reduced minimization problem then becomes [41]

$$\begin{aligned} F_V &= \int_V (g_k + g_\epsilon + g_f)\, dV \\ \hat{\mathbf{n}}|_S &= \hat{\mathbf{n}}_0 \end{aligned} \tag{2.61}$$

where $\hat{\mathbf{n}}_0$ is the director on the surface S.

Many surface alignments are possible. Some induce unique alignments (monostable orientation) while others permit several different alignments (multistable orientation) [41]. The present work is concerned only with the homogeneous (or planar) alignment (Fig. 2.12), which is characterized by a specific azimuthal angle that is constant across the surface and a polar angle that is $\pi/2 + \theta_\mathrm{p}$, where the vector normal to the surface is oriented in the z-direction, and θ_p is a small or zero value known as the pretilt angle [63].

This orientation can be induced by mechanical rubbing of a polymer-coated surface. The rubbing process causes a permanent reorientation in the direction of rubbing of the randomly directed polymer molecules near the surface (Fig. 2.13). The resultant dispersion interactions between the liquid crystal material and the uniformly directed polymer molecules result in planar alignment for many combinations of liquid crystals and polymers (including those considered here) [63, 64].

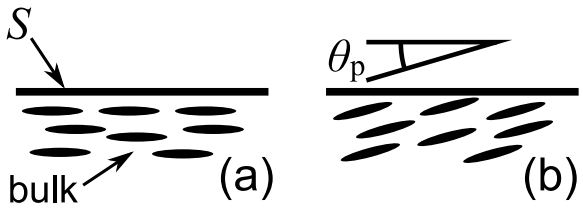

Figure 2.12: Planar alignment of a nematic liquid crystal without pretilt (a) and with a pretilt angle of θ_p (b).

While solving (2.61) for arbitrary geometries and surface alignments may be nontrivial, the solutions of two elementary problems that are relevant to the present work are found easily. The problems consist of a nematic liquid crystal that is "sandwiched" between two parallel plates, which have been prepared to induce a planar surface alignment (Fig. 2.14). The problem is first considered in the absence of electric and magnetic fields and is assumed to have an infinite planar extent such that only the boundaries due to the upper and lower plates are relevant to the calculation. When both the upper and lower plates induce surface alignment in a single direction, the director alignment simply extends homogeneously (without deformation) into the bulk material. This is confirmed by inspection of (2.61), which reveals that a uniform director orientation gives way to vanishing spatial

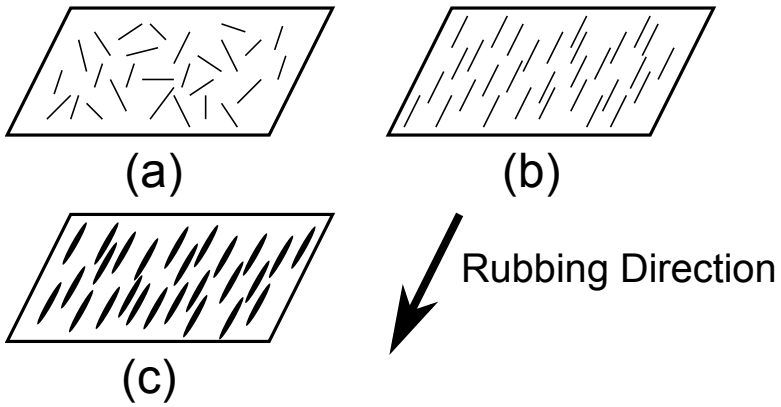

Figure 2.13: Unrubbed (a) and rubbed (b) polymer layer, and the resultant liquid crystal alignment (c). The polymer and liquid crystal molecules are represented by the thin lines and ovals, respectively.

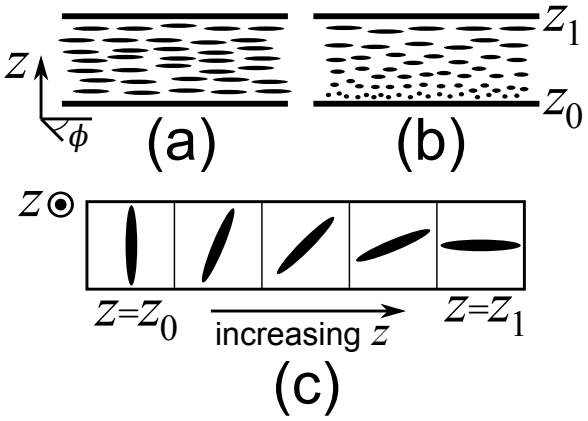

Figure 2.14: Basic nematic liquid crystal cell for $\phi_1 - \phi_0 = 0$ (a) and $\phi_1 - \phi_0 = \pi/2$ (b). Molecules that are oriented out of the plane are shown as shorter ellipsoids. The cross sections of a twisted nematic cell are shown in (c).

derivatives and consequently an elastic free energy of zero.

Where an angle exists between the alignment directions (denoted by $\Delta\phi$), (2.61) may be minimized by making the (intuitive) assumption that only the twist deformation contributes to the elastic energy of the bulk and that the director may be written as [41]

$$\hat{\mathbf{n}} = (\cos[\phi(z)], \sin[\phi(z)], 0) \tag{2.62}$$

The extrema of (2.61) are found by differentiating with respect to z (the only remaining parameter), and equating the result to 0. The resultant global minimum that satisfies the boundary conditions is given by [38]

$$\phi(z) = \phi_0 + (\phi_1 - \phi_0)\left(\frac{z - z_0}{z_1 - z_0}\right) \tag{2.63}$$

which corresponds to a director rotation as a function of z. Note that in the presence of perfect planar alignment, the twist direction is degenerate for $\phi_1 - \phi_0 = \pi/2$, as both left-handed and right-handed twists yield a minimum energy solution. A particular twist may be ensured by using alignment surfaces that exhibit a nonzero

pretilt angle [41].

2.3.4 Response to an Electric Field

While the foregoing analysis may be broadened in a straightforward fashion to incorporate static electric fields, a simple qualitative description is sufficient when considering the effect of a strong static electric field. In this case, (2.58), which attains a minimum value when the director is aligned with the electric field, dominates the minimization of the total free energy. In the presence of strong anchoring, a transition region exists where the director is elastically distorted due to the competing forces arising from the surface alignment and electric field (Fig. 2.15) [41].

Unfortunately, the interaction of a liquid crystal with time-varying field is considerably more complex, a sufficient description of which requires an extensive nematodynamic framework that properly describes time-dependent viscous processes. In the case where the field variations are slow with respect to the viscous relaxation time frames, the system retains its essentially static characteristics. In this regime, the electric field brings about a reorientation of molecular dipoles [38].

At higher frequencies, the material's viscous properties impede dipole reorienta-

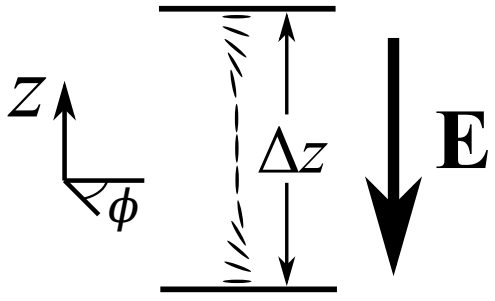

Figure 2.15: Nematic liquid crystal cell in the presence of a strong electric field. Shown is the S-effect [41]. For clarity, only a column of molecules is shown, and the proportions of the transition region have been exaggerated.

tion but not director realignment, a phenomenon which may be studied superficially by considering the competing torques, whose sum [38] must vanish

$$\Gamma^E + \Gamma^K + \Gamma^V = 0 \tag{2.64}$$

where Γ^E, Γ^K, and Γ^V are the electric, elastic, and viscous torques, respectively, the last of which is given by [38]

$$\Gamma^V = \gamma_1 \left(\hat{\mathbf{n}} \times \frac{\partial \hat{\mathbf{n}}}{\partial t} \right) \tag{2.65}$$

where γ_1 is the rotational viscosity. The electric torque is given by [38]

$$\Gamma^E = \Delta\epsilon \left(\hat{\mathbf{n}} \cdot \mathbf{E} \right) \hat{\mathbf{n}} \times \mathbf{E} \tag{2.66}$$

Clearly, the viscous torque is proportional to the time rate of change of the director. Of considerable importance is the fact that the electric torque is invariant to change in sign of the electric field. This implies that the torque will remain constant over timescales greatly exceeding those of a cycle of a moderately high-frequency time-harmonic field. Moreover, upon application of an electric field, the terminal position of the director will correspond to the balancing of the elastic and electric torques, which is simply another manifestation of the minimization of free energy in the static case [38].

A considerable density of ions is inevitably present in practically attainable liquid crystal samples. At very low frequencies, ionic movement may significantly alter the character of the liquid crystal material, and thus field-induced director alignment is usually effected with a low-frequency time-harmonic field whose frequency exceeds the characteristic frequencies of the ionic processes. The frequency

can also be chosen to exceed the viscous relaxation frequency of the liquid crystal such that resultant effect is comparable to that of a direct current (DC) field [38].

Two characteristic relaxation times are relevant to the S-effect (Fig. 2.15) in the parallel plate setting [41]

$$\begin{aligned} \tau_r &= \frac{\gamma_1^*}{\Delta\epsilon E^2/4\pi - K_{11}\pi^2/\Delta z^2} \\ \tau_d &= \frac{\gamma_1^* \Delta z^2}{K_{11}\pi^2} \end{aligned} \tag{2.67}$$

where γ_1^* is the effective rotational viscosity, and τ_r and τ_d are the time constants corresponding to the rise time and decay time, respectively. These constants appear in arguments of exponential functions that describe director orientation in the center of the sample as a function of time. The rise time is the approximate time scale on which the director completes its reorientation in response to an external electric field, while the decay time is that of the reversed process when the field is switched off. These time constants are the solution to the dynamical problem when the director is assumed to be only slightly deformed by the electric field. At higher field strengths, which are of interest, these equations may at best serve as approximations. However, the quadratic dependence upon Δz is important, particularly for the decay time, which clearly illustrates that thicker cells take considerably longer to return to a relaxed state [41].

2.4 Prior Work on Tunable Photonic Bandgap Structures

Recently, substantial research has been devoted to developing "tunable" devices, whose electromagnetic properties, such as bandgaps and dispersion characteristics, can be modified after fabrication or even during operation. Two avenues based on distinct mechanisms of tuning have emerged. The first relies upon the mechanical deformation of geometry, while the second is based on tuning the electromagnetic properties of the medium's constituent materials, such as electric permittivity or magnetic permeability. The following sections elaborate on these approaches in a review of the theoretical and experimental research that has been conducted to date.

2.4.1 Mechanically Tunable Devices

The tuning of the band structure as a result of mechanical tension and shear for a silicon-air photonic crystal was considered numerically by Jun and Cho [65], who calculated significant tuning for tension deformations resulting from a 3% strain. Similarly, Kim and Gopalan [66] determined numerically that a triangular lattice of air holes in silicon subject to 3% shear strain would exhibit a 73% reduction in the width of the first bandgap.

It remains doubtful, however, that such a degree of tuning can be experimentally realized with silicon (or other crystal)-based devices, given that Young's modulus of crystalline silicon is on the order of 10^{11} Pa [67]. Tellingly, the resonant frequency of a fabricated silicon-based tunable one-dimensional photonic crystal microcavity embedded in a one-dimensional lattice could be tuned by only 0.1% in response to

a 0.04% strain [68]. Similarly, the angles of the diffracted orders of a realized one-dimensional micro-diffraction grating could be tuned by at most 486 microradians with a strain of 0.21% [69]. However, it is worth noting that while strain-induced tuning may be of marginal practical utility, even a small shift in the measured bandgap may be used to infer strain. In particular, one-dimensional fiber Bragg grating sensors have found use in measuring strain in civil engineering applications [70].

2.4.2 Liquid Crystal Devices

Liquid crystal-based devices have been intensely researched after three papers published in 1999 that describe the experimental realization of tunable optical three-dimensional photonic crystals using liquid crystals [35–37]. Busch and Sajeev [35] found that the bandgap of an inverted silicon opal structure partially infiltrated with a nematic liquid crystal could be opened and closed by varying the direction of an applied electric field, while Yoshino et al. [36,37] investigated silica opal structures infiltrated with nematic and ferroelectric smectic liquid crystals, finding the resultant structures to be sensitive to temperature and the frequency of an applied electric field. In research that followed, many aspects of liquid crystal-based photonic crystals have been theoretically and experimentally explored and utilized in several applications. The following review concerns primarily optical structures, as comparatively little research has been conducted on microwave liquid-crystal devices, with only Ghattean et al. [71] having experimentally demonstrated a liquid-crystal based tunable structure for microwave frequencies. Despite the considerable differences in experimental aspects, the successful numerical and experimental outcomes of such optical devices suggest analogous microwave structures bearing similar (but

frequency-scaled) traits.

One-dimensional structures have been investigated theoretically in [72–74]. In particular, Tolmachev et al. [72] studied the effect of varying the filling factor of silicon in one-dimensional silicon/liquid crystal photonic crystals and identified the silicon/liquid crystal volume ratio that maximizes bandgap tuning. Tuning of one-dimensional structures infiltrated with liquid crystals has been experimentally demonstrated by Astrova et al. [75], who fabricated an interdigital silicon structure whose optical properties could be varied with the application of a static electric field. Similarly, Tolmachev et al. [76, 77] developed a one-dimensional grooved silicon structure containing E7 (a nematic liquid crystal mixture) whose reflection spectra was tunable with the application of an electric field. Additionally, several structures possessing tunable defects have also been demonstrated experimentally [78–83].

Numerical investigation of bandgap tuning for two-dimensional PCs has also been carried out. In particular, Liu et al. [84–86] found that significant tuning of the absolute bandgap was possible in various lattices infiltrated with 5CB (a nematic liquid crystal) and showed that this tuning could be used in applications requiring negative refraction or tunable polarizers. Similar results were obtained by Halevi et al. [87], who considered two-dimensional crystals infiltrated with E7. Other characteristics of two-dimensional liquid crystal-based PCs have also been investigated numerically, including the low-frequency properties of two-dimensional square lattices of void cylinders in silica filled with 5CB [88], material and geometry combinations that lack omnidirectional TE bandgaps [89], and the characterization of FDTD as a method for modeling the transmittance of finite periodic structures [90,91]. Takeda et al. [92] showed that in the general case, the anisotropic character of liquid crystal materials necessarily implies coupling between the TE and TM modes in both square and triangular lattices, a result that is relevant to the present

work. Several applications of tunable two-dimensional structures have also been considered numerically, including tunable cavities [93, 94], switchable waveguide T-junctions [95, 96], couplers [97], and polarization splitters [98].

Experimentally realized two-dimensional structures have been demonstrated by Leonard et al. [99], who used temperature to tune the bandgap of an infrared photonic crystal based on a triangular lattice of E7 cylinders embedded in silicon, and Martz et al. [100], who developed a technique for infiltrating two-dimensional indium phosphide-based PCs with K15 (a nematic liquid crystal). In particular, Ghattean et al. [71] developed a microwave two-dimensional photonic crystal based on a lattice of 5CB cylinders embedded in high-density polyethylene. Measurements showed that the structure could serve as on/off switch at 91 GHz with an extinction ratio of 13.3 dB. Additionally, many tunable defect cavities have been fabricated [101–105].

Three-dimensional LC-based PCs have been studied numerically by Liu et al. [106, 107], who found that the band structure of several devices comprising silicon and 5CB could be tuned with the application of an electric field, and D'Orazio [108], who also established numerically the possibility of tuning the transmission spectra of networks of intersecting square rods of silica immersed in 3M2CPOOB (a smectic liquid crystal shown in Fig. 2.16). In addition to the early work of [35–37], tunable three-dimensional photonic crystals have also been experimentally realized by Meng et al. [111] and Kang et al. [112], who constructed optical photonic crystals

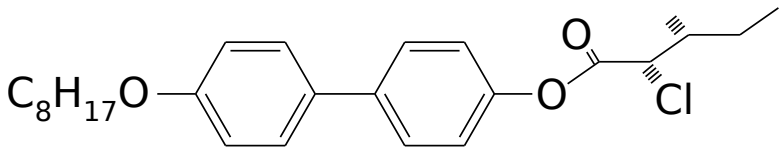

Figure 2.16: Chemical structure [109] of 3M2CPOOB ((2S, 3S)-3-methyl-2-chloropentanoic acid 4',4"-octyloxybiphenyl ester) [110].

comprising periodically arranged silica spheres immersed in nematic liquid crystals and found that the measured bandgap and Bragg reflection peak, respectively, could be tuned with an electric field. Similarly, Mertens et al. [113] and Kubo et al. [114] developed three-dimensional bandgap structures infiltrated with nematic liquid crystals and found the resultant reflectivities of the structures to be tunable by varying temperature.

Photonic crystals must consist of at least two different materials in order to realize a contrast in permittivity sufficient to induce a bandgap. Hence, liquid crystal materials will necessarily contact another material when used in a photonic crystal. As the optical (and electromagnetic) properties of liquid crystals are strongly influenced by such contact, several works have sought to clarify the role of bounding surfaces in liquid crystal-based photonic crystals. In particular, Remenyuk et al. [116, 117] found weakly planar alignment of E7 on the liquid crystal/silicon surfaces in one-dimensional grooved silicon structures. Matthias et al. [115] studied liquid crystal alignment in a hexagonal lattice hourglass-shaped cavities in silicon. The cavities were treated with a surfactant to induce homeotropic anchoring and subsequently filled with a glass-forming nematic liquid crystal polymer. The resultant director field was measured with fluorescence confocal polarizing microscopy (FCPM) and was found to possess pronounced disclination rings (Fig. 2.17). Further work of Matthias et al. [118] involved the numerical simulation of a cholesteric liquid crystal confined to similar pores, which was found to suppress the exhibition of the material's otherwise chiral structure. Finally, Halevi et al. [119] numerically evaluated the director field of a two-dimensional photonic crystal comprising a periodic array of 5CB cylinders, where alignment was taken to be homeotropic with respect to cylindrical bounding surfaces. The director field was found to be non-uniform in the absence of an electric field, resulting, once again, in coupling

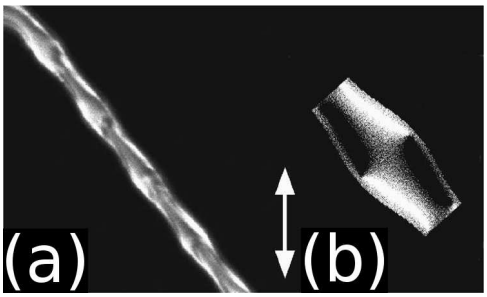

Figure 2.17: Fluorescence confocal polarizing microscopy (FCPM) picture [115] of a liquid crystalline rod (a). The angle between the plane of polarization and the pore axis is 42°. Simulated pattern (b). Reprinted with permission from "Spatially periodic liquid crystal director field appearing in a photonic crystal template," *Applied Physics Letters*, vol. 87, no. 24, p. 241105, December 2005. Copyright 2005, American Institute of Physics.

between the TE and TM modes.

Finally, it is worth noting that in addition to basic tunable lattices, several optical tunable devices based on photonic crystals structures have been experimentally realized, including tunable photonic crystal fibers [120–122], tunable Mach–Zehnder interferometers [123, 124], photonic crystal lasers [125–128], a tunable Fabry–Pérot interferometer [129], and an optically-activated switch [130].

2.5 Existing Microwave Structures using Liquid Crystals

The earliest work that considers liquid crystals as a tunable microwave dielectric may be attributed to Lee [131] and Carr and Spence [132], who in 1954 studied the effect of magnetic fields on the microwave dielectric constant of liquid crystals. Further work carried out by Carr involved microwave dielectric permittivity measurements [133] and an investigation of the effect of electric fields on liquid crystal samples [134].

More recently, interest has developed in using liquid crystal materials in applications that exploit their switchable nature. In particular, considerable work has been reported on tunable phase shifters. Several designs have been explored based on liquid crystal layers that are "sandwiched" between a ground plane and an inverted microstrip line [135–140] and a coplanar waveguide [141–145]. Other designs have been based on a stripline geometry [146] and a microstrip trace that floats over a liquid crystal layer due to surface tension [147]. Improvement in switching speed has been realized with polymer-stabilized devices [148,149], wherein a liquid crystal material is hosted in a network of polymer fibers. The intimate contact with closely spaced fibers imparts a strong restorative force on the liquid crystal, which thereby returns more quickly to a relaxed state after the alignment field is turned off. Other microwave applications of liquid crystals, including tunable capacitors [150], wavelength selectors [151,152], a variable phase grating [153] and resonators [154,155], have also been experimentally demonstrated. In particular, nematic liquid crystals have shown to be especially promising as substrate materials in tunable phased array [156] and reflectarray antennas [157–161].

While the optical properties of most widely available nematic liquid crystals are well known, a comparable body of knowledge on the microwave dielectric properties is still in an early stage of development. Characterization of liquid crystal materials poses difficulty beyond that which is encountered with most materials, as dielectric properties are anisotropic, extremely sensitive to bounding surfaces, and must be measured in the liquid phase. Several approaches have been explored. Methods based on liquid crystal-filled capacitors have been successfully used for frequencies of 500 MHz [162], 10 MHz–6 GHz [163], and 1 Hz–1 GHz [164]. However, such methods are likely of limited value at higher frequencies where discrete components are more difficult to realize.

Methods of permittivity measurement-based resonant planar geometries were developed by Utsumi et al. [165, 166], who fabricated ring resonators using an inverted microstrip configuration, and Yang and Sambles [167,168], who constructed Fabry–Pérot-type devices. Other resonant geometries were considered by Parka et al. [169], who developed a cylindrical dielectric resonator, and Mueller et al. [170–172], who used a rectangular cavity perturbed with a polytetrafluoroethylene tube containing various nematic liquid crystals.

Approaches derived from the broadband measurement of scattering parameters have also been developed, including planar devices based on balanced stripline [173, 174] and microstrip [175] geometries, where rubbed polymer layers and low-frequency electric fields were used to produce distinct alignments in nematic samples. Coaxial-based transmission lines have been similarly employed. However, while such structures support a DC field, challenges to preparing interior surfaces have precluded the use of rubbing to induce alignment. In published works, secondary alignment was realized by a magnetic field [176], or abandoned in favor of measuring the isotropic permittivity by heating samples to temperatures past the clearing point [177].

Finally, the design of experiments in the present work has been guided by the observation of modest discrepancies between permittivities evaluated through different techniques [165]. A planar structure was thus selected for carrying out permittivity measurements in order to allow a common method of surface preparation, temperature, dielectric thickness, and switching field to be used for the devices fabricated in this thesis.

Chapter 3

Computational & Experimental Methods

This chapter details the implementation of numerical codes, the development of the spectral transmission-line modeling method, and the design, construction, and experimental procedures used in the evaluation of several fabricated devices.

3.1 Implementation of Simulation Algorithms

The plane wave method was implemented as a computer program in the C programming language [178] using the magnetic field formulation. The program can simulate two-dimensional photonic crystals described by arbitrary lattice vectors and has been equipped with auxiliary functions for computing the Fourier series of basic shapes, including a dielectric cylinder and a square dielectric rod. Other shapes can be modeled by providing the program with a file that contains the first few Fourier series terms of the inverse permittivity function. Interaction with the program takes place using command-line arguments, which must consist at mini-

mum of the lattice vectors, the location in the irreducible Brillouin zone, the number of plane waves used in the expansion, the number of eigenvalues to be found, the names of the output files, and, optionally, the names of the Fourier series files. The program's output consists of the calculated eigenmode frequencies expressed as $\omega a/c$. The code has been compiled and successfully run on Linux and has been employed as a reference standard for validating other modeling methods used in this thesis.

The time-domain transmission-line modeling method was implemented as a computer program in the C programming language [178] for the TM polarization. The program is capable of simulating two-dimensional photonic crystals possessing square lattices comprising arbitrary dielectrics. Either a Gaussian or a Kronecker delta may be used as an excitation, and a time series is collected at 128 randomly chosen points in the mesh. The fast Fourier transforms are computed using the FFTW software library [179], and the resultant magnitude spectra are added together. The peaks are detected manually or by means of a peak detection function. The boundary conditions (range and increment of $\mathbf{k}$), number of timesteps, mesh files, and output files are specified by command-line arguments. The output frequency is given in terms of $\omega a/c$. The program has been compiled and successfully run on Linux.

The Rayleigh multipole method was implemented as a computer program in the C programming language [178]. The program is capable of dispersion diagram and finite-structure calculations involving two-dimensional periodic structures comprising dielectric or perfect electric conductor (PEC) circular discontinuities arranged in a square or hexagonal lattice. The implementation uses the LAPACK software package [180] to compute matrix inverses and eigenvalues and has been successfully compiled and run on Microsoft Windows, Linux, and UNIX systems. Arguments

are passed to the program via the command line and results are written to text files. At several steps the program must decide when to truncate a series. This is handled adaptively in a manner specific to the task. The B_n coefficients (Appendix B) are calculated for increasing n until the magnitude of the last computed coefficient has fallen beneath a user-defined threshold. The program retains all propagating plane wave orders and a user-defined number of the most slowly decaying evanescent orders. The infinite series arising from the lattice sum calculations are truncated once the last term has fallen below a user-specified threshold. Finally, eigenvalues are deemed to correspond to propagating modes if their modulus is no less than 0.999 and no greater than 1.001. In each case, the user can readily change the default values with arguments passed from the command line.

3.2 Spectral Transmission-Line Modeling Method

3.2.1 Introduction

The spectral transmission-line modeling method was conceived by approaching TLM in a somewhat unconventional manner. The transmission-line modeling method discussed in §2.2.2 calculates eigenmodes indirectly by computing the time evolution for a given initial field and subsequently calculating its discrete Fourier transform. In contrast, frequency-domain methods such as the finite element method approach the eigenvalue problem more directly. These methods discretize only space, as they are developed from the time-harmonic form of Maxwell's equations, whose dependence on time has been eliminated by the inclusion steady-state conditions. However, eigenvalue analysis is not limited to frequency-domain problems

and may be extended to time-domain methods by imposing steady-state conditions with respect to a discrete increment in time as follows

$$\begin{aligned} \mathbf{v}\left(k+1\right) &= \mathbf{A}\mathbf{v}\left(k\right) \\ \mathbf{v}\left(k+1\right) &= e^{j\omega\Delta t}\mathbf{v}\left(k\right) \end{aligned} \tag{3.1}$$

which implies

$$e^{j\omega\Delta t}\mathbf{v}\left(k\right) = \mathbf{A}\mathbf{v}\left(k\right) \quad \forall k \in \mathbb{N}_0 \tag{3.2}$$

where $\mathbf{A}$ is the matrix that increments the timestep, and $\mathbf{v}(k)$ is the state of the system at the k^{th} time step. Such an approach has been explored for TLM by Lukashevich et al. [181–183], who considered a spectral technique that reduces the time required to analyze high-Q structures.

Note that (3.1) implies calculations involving complex values, which represents the most significant departure from conventional time-domain methods where computed field values are assumed to have a direct correspondence to the physical system. For a time step matrix comprising only real coefficients, the $e^{j\omega\Delta t}$ eigenvalues must always be paired with their complex conjugates $e^{-j\omega\Delta t}$, which is a manifestation of time-reversal symmetry in electromagnetics. As discussed in §2.1.2, photonic crystals possess this symmetry and, as a consequence, inversion symmetry in reciprocal space. In the case of dispersion diagram calculations, the matrix is no longer perfectly real due to the complex nature of quasi-periodic boundary conditions. However, it will be shown that the eigenvalues of this problem are indeed also paired with their complex conjugates. Moreover, when combined with their respective time dependencies, the associated eigenstates comprise the set of forward and backward traveling solutions.

The spectral transmission-line modeling method developed in this section replaces dual meshes, time stepping, the selection of random field samples, and the discrete Fourier transform of the time-domain method with an eigenvalue algorithm that, in the process of calculating the band diagram, automatically computes the spatial configuration of the Bloch modes. The discussion begins with the TLM discretization of the unit cell and is followed by the formulation of the eigenvalue problem, whose properties are studied in order to construct an efficient eigenvalue algorithm. Several numerical examples, which are based on comparing simulation results with those produced by Ansoft HFSS, the Rayleigh multipole method, the plane wave method, and the time-marching transmission-line modeling method, are presented in §4.1. The first set of examples establish the numerical accuracy of the method and demonstrate a significant runtime advantage over the plane wave method when applied to problems characterized by high contrasts in permittivity and high aspect ratios. The second set of examples show that the method's runtime requirements are comparable to those of time-marching TLM. However, unlike elementary time-domain methods (such as time-marching TLM), the method developed here does not require subsequent frequency-domain computation to calculate the eigenmodes. While work has been carried out for the TM polarization in two dimensions, the analysis and algorithm may readily be extended to the TE polarization and three dimensions by appropriately revising the treatment of spurious modes.

3.2.2 The Eigenvalue Problem

The TLM problem may be discretized on one of several meshes, depending on the characteristics of the problem. The two-dimensional mesh comprising shunt nodes

(Fig. 3.1) is used here, as it corresponds to a two-dimensional problem restricted to the TM polarization. This mesh comprises nodes that are connected to each other by link transmission lines and contains shunt lines whose impedances are selected to reflect the properties of the materials. The impedance of the link line is given by [52]

$$Z_L = \sqrt{2} Z_{\max} \tag{3.3}$$

where $Z_{\max}$ is the impedance of the dielectric material with the smallest relative permittivity ($\epsilon_{r,\min}$). The impedances of the shunt stubs are related to the material properties by [52]

$$Z_S = \frac{Z_L}{4\left(\epsilon_r/\epsilon_{r,\min} - 1\right)} \tag{3.4}$$

where ϵ_r is the relative permittivity of the material in the volume represented by the given shunt node. Note that the material is assumed to be lossless and non-magnetic.

TLM simulates time evolution by carrying out consecutive scattering operations at junctions where transmission lines meet. These are located at the center of nodes,

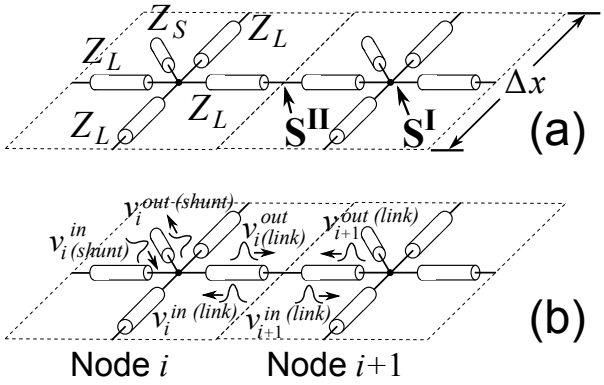

Figure 3.1: Two neighboring shunt nodes of width and length Δx (a). Each node comprises four link lines and one shunt stub possessing impedances of Z_L and Z_S, respectively. Scattering occurs at junctions and is described by the scattering matrices $\mathbf{S^I}$ and $\mathbf{S^{II}}$. The traveling wave voltages involved in the scattering processes are shown in (b).

where the link lines are joined to the shunt stub, and at the periphery, where link lines of adjacent nodes are connected. Scattering is performed in two steps by converting incoming traveling-wave voltages to outgoing traveling-wave voltages at every central junction in the mesh and subsequently repeating this process at every peripheral junction. These operations may be carried out as sparse matrix-vector multiplications effected by the matrices $\mathbf{S^I}$ and $\mathbf{S^{II}}$ for the central junctions and peripheral junctions, respectively.

One application of $\mathbf{S^I}$ followed by $\mathbf{S^{II}}$ (or vice versa) advances the system by one timestep

$$\mathbf{v}\,(k+1) = \mathbf{S^I S^{II}} \mathbf{v}\,(k) \tag{3.5}$$

The product of $\mathbf{S^I}$ and $\mathbf{S^{II}}$ forms the timestep matrix. This discrete operation corresponds to a duration of time Δt in the analytical problem and is related to the permittivity of the background medium and node width Δx by

$$\Delta t = \frac{\Delta x}{v_{\text{link}}} = \sqrt{\frac{\epsilon_{r,\min}}{2}} \frac{\Delta x}{c} \tag{3.6}$$

where v_{link} is the velocity of wave propagation along the link lines, and c is the velocity of light in free space. The time-harmonic problem associates a timestep with a change in phase

$$\mathbf{v} e^{j\omega\Delta t} = \mathbf{S^I S^{II}} \mathbf{v} \tag{3.7}$$

where $\mathbf{v}$ is an eigenmode. The spectral transmission-line modeling method is concerned with finding solutions to (3.7) that correspond to physically acceptable fields. Numerical analysis can be facilitated by working with the modified system

$$\sqrt{\mathbf{Z}}^{-1} \mathbf{S^I S^{II}} \sqrt{\mathbf{Z}} \mathbf{v}' = e^{j\omega\Delta t} \mathbf{v}' \tag{3.8}$$

where $\mathbf{v}' = \sqrt{\mathbf{Z}}^{-1}\mathbf{v}$ and $\mathbf{Z}$ is the invertible matrix defined as

$$\mathbf{Z}_{i,j} = \delta_{i,j} Z_L \tag{3.9}$$

for elements corresponding to link lines, or

$$\mathbf{Z}_{i,j} = \delta_{i,j} Z_S \tag{3.10}$$

for those elements corresponding to the shunt stubs. Scaling by $\sqrt{\mathbf{Z}}$ affects only the eigenvectors, leaving the eigenvalues unchanged. The scattering matrices may be defined as follows

$$\mathbf{S^I} = \text{diag}\left(\mathbf{S}_i{}^{\mathbf{I}}\right) \tag{3.11}$$

where

$$\mathbf{S^I}_i = \begin{bmatrix} a_i & b_i & b_i & b_i & d_i \\ b_i & a_i & b_i & b_i & d_i \\ b_i & b_i & a_i & b_i & d_i \\ b_i & b_i & b_i & a_i & d_i \\ b_i & b_i & b_i & b_i & c_i \end{bmatrix} \tag{3.12}$$

and

$$\begin{aligned} a_i &= \Gamma_L^i = \frac{\frac{1}{3}Z_L//Z_S^i - Z_L}{\frac{1}{3}Z_L//Z_S^i + Z_L} = \frac{1 - 2\epsilon_r^i/\epsilon_{r,\min}}{2\epsilon_r^i/\epsilon_{r,\min}} \\ b_i &= T_L^i = \frac{2\left(\frac{1}{3}Z_L//Z_S^i\right)}{\frac{1}{3}Z_L//Z_S^i + Z_L} = \frac{1}{2\epsilon_r^i/\epsilon_{r,\min}} \\ c_i &= \Gamma_S^i = \frac{\frac{1}{4}Z_L - Z_S^i}{\frac{1}{4}Z_L + Z_S^i} = \frac{2\epsilon_r^i/\epsilon_{r,\min} - 4}{2\epsilon_r^i/\epsilon_{r,\min}} \\ d_i &= T_S^i = \frac{\frac{1}{2}Z_L}{\frac{1}{4}Z_L + Z_S^i} = \frac{4\epsilon_r^i/\epsilon_{r,\min} - 4}{2\epsilon_r^i/\epsilon_{r,\min}} \end{aligned} \tag{3.13}$$

where i is an index that uniquely identifies each node. The values Z_L^i and Z_S^i appearing in (3.13) may be found by evaluating (3.3) and (3.4) using the material properties of the i^{th} node. The entries of the first four rows and columns are associated with the link lines, while those of the fifth row and column are related to the shunt stub. The matrix may also be viewed as a collection of reflection coefficients, which appear on the diagonal, and transmission coefficients, which occur as off-diagonal entries. The second scattering matrix $\mathbf{S^{II}}$ effects scattering between nodes and has the following effect on the traveling wave voltages (Fig. 3.1)

$$\begin{bmatrix} & \vdots & \\ v_i^{\text{in(link)}} & = & e^{j\phi}\beta \\ v_{i+1}^{\text{in(link)}} & = & e^{-j\phi}\alpha \\ v_{i+1}^{\text{in(shunt)}} & = & \gamma \\ & \vdots & \end{bmatrix} = \mathbf{S^{II}} \begin{bmatrix} & \vdots & \\ v_i^{\text{out(link)}} & = & \alpha \\ v_{i+1}^{\text{out(link)}} & = & \beta \\ v_{i+1}^{\text{out(shunt)}} & = & \gamma \\ & \vdots & \end{bmatrix} \tag{3.14}$$

$$-\pi \leq \phi \leq \pi$$

When the connection in (3.14) involves neighboring nodes, ϕ assumes a value of zero such that pulses travel from one node to the other unaffected. For connections involves a boundary, pulses leaving the mesh on the periphery undergo a phase shift prior to reappearing on the opposite side. This phase shift can be made to satisfy the periodic boundary conditions by setting ϕ to $\mathbf{k} \cdot \mathbf{d}$, where $\mathbf{k}$ is found in the irreducible Brillouin Zone and $\mathbf{d}$ is the spatial translation of the pulse ($\pm a\hat{\mathbf{x}}$ or $\pm a\hat{\mathbf{y}}$ in the case of a square lattice). The repeated structure found in $\mathbf{S^{II}}$ that

induces this action may be expressed as the group of matrix elements

$$\mathbf{S^{II}}_{\text{repeated}} = \begin{bmatrix} 0 & e^{j\phi} & 0 \\ e^{-j\phi} & 0 & 0 \\ 0 & 0 & 1 \end{bmatrix} \tag{3.15}$$

Whereas the matrix elements appearing in $\mathbf{S^I}$ are dependent solely upon the permittivities and geometries of the materials present in the unit cell, the elements of $\mathbf{S^{II}}$ depend only on the boundary conditions. Consequently, band diagram simulations for a photonic crystal require that $\mathbf{S^I}$ be filled only once, at the outset of computations. Conversely, $\mathbf{S^{II}}$ must be updated for each location in the irreducible Brillouin Zone. Once both matrices have been constructed, the eigenvalue equation can be solved for $e^{j\omega\Delta t}$ and the related Bloch modes.

Assuming that $\epsilon_{r,\min} = 1$, the electric field can be recovered from the state vector by using the relation

$$\mathbf{E} = E_z\hat{\mathbf{e}}_z = \frac{2\left(V_1^i + V_2^i + V_3^i + V_4^i\right) + 2V_{\text{shunt}}^i\left(4\epsilon_r^i - 4\right)}{4\Delta z\epsilon_r^i}\hat{\mathbf{e}}_z \tag{3.16}$$

which has been derived from [52]. The voltages appearing in (3.16) may be drawn from the set of incoming or the set of outgoing voltages, provided that only one set is employed for a given evaluation of (3.16). The field may thus be recovered using a matrix defined as

$$\mathbf{F}_{i,j} = \frac{1}{2\Delta z\epsilon_r^i}\left(\delta_{5i,j} + \delta_{5i,j-1} + \delta_{5i,j-2} + \delta_{5i,j-3} + 4\delta_{5i,j-4}\left(\epsilon_r^i - 1\right)\right) \tag{3.17}$$

where the indices i and j commence at 0. Note that this matrix is not square, representing a surjective mapping that is not injective. By symbolic computation,

it may be readily shown that

$$\mathbf{F}\mathbf{S}^{\mathbf{I}} = \mathbf{F} \tag{3.18}$$

justifying the assertion that either the incoming or outgoing voltages may be used to calculate the electric field.

The scaled timestep matrix in (3.8) is expected to possess eigenvalues of unit modulus, as the unit cell contains only lossless materials and the periodic boundary conditions ensure that the system's energy remains constant over the course of successive time increments. This may be confirmed by showing that the scaled timestep matrix is unitary, which may be performed in two steps. From (3.15) it may be seen that for arbitrary values of ϕ

$$\left(\mathbf{S}^{\mathbf{II}}\right)^{\dagger}\left(\mathbf{S}^{\mathbf{II}}\right) = \left(\mathbf{S}^{\mathbf{II}}\right)\left(\mathbf{S}^{\mathbf{II}}\right)^{\dagger} = \mathbf{I} \tag{3.19}$$

where $\mathbf{I}$ is the identity matrix and $\dagger$ denotes the adjoint. Equation 3.19 satisfies the definition of a unitary matrix [184], and hence, $\mathbf{S}^{\mathbf{II}}$ is unitary. Similarly, by symbolic computation for each block in $\mathbf{S}^{\mathbf{I}}$, the following can be shown to hold

$$\left(\sqrt{\mathbf{Z}}^{-1}\mathbf{S}^{\mathbf{I}}\sqrt{\mathbf{Z}}\right)^{\dagger}\left(\sqrt{\mathbf{Z}}^{-1}\mathbf{S}^{\mathbf{I}}\sqrt{\mathbf{Z}}\right) = \left(\sqrt{\mathbf{Z}}^{-1}\mathbf{S}^{\mathbf{I}}\sqrt{\mathbf{Z}}\right)\left(\sqrt{\mathbf{Z}}^{-1}\mathbf{S}^{\mathbf{I}}\sqrt{\mathbf{Z}}\right)^{\dagger} = \mathbf{I} \tag{3.20}$$

illustrating that $(\sqrt{\mathbf{Z}}^{-1}\mathbf{S}^{\mathbf{I}}\sqrt{\mathbf{Z}})$ is also unitary. Moreover, as the product of two unitary matrices yields a unitary matrix, the composition

$$\left(\sqrt{\mathbf{Z}}^{-1}\mathbf{S}^{\mathbf{I}}\sqrt{\mathbf{Z}}\right)\mathbf{S}^{\mathbf{II}} \tag{3.21}$$

is also unitary. Noting that $\sqrt{\mathbf{Z}}$ commutes with $\mathbf{S^{II}}$, the following holds

$$\left(\sqrt{\mathbf{Z}}^{-1}\mathbf{S^{I}}\sqrt{\mathbf{Z}}\right)\mathbf{S^{II}} = \sqrt{\mathbf{Z}}^{-1}\mathbf{S^{I}}\mathbf{S^{II}}\sqrt{\mathbf{Z}} \tag{3.22}$$

where the term appearing on the right-hand side is recognized as the scaled timestep matrix, thus shown to be unitary. Furthermore, under the weighted inner product

$$(\mathbf{u},\mathbf{v})_{\mathbf{Z}^{-1}} \equiv \mathbf{u}^{\dagger}\mathbf{Z}^{-1}\mathbf{v} \tag{3.23}$$

the timestep matrix is itself unitary, suggesting that the selection of an eigenvalue algorithm should made with the view of finding eigenvalues that lie on the unit circle in the complex plane.

The analytical description of the problem provided by (2.17) permits the time dependence of steady-state solutions to be resolved as either $e^{j\omega t}$ or $e^{-j\omega t}$. As steady-state conditions are absent from the formulation of the time-marching TLM discretization, a steady-state eigenmode is expected to be associated with a pair of eigenvalues, $e^{j\omega\Delta t}$ and $e^{-j\omega\Delta t}$. This may be confirmed by considering the similarity transform effected by $\mathbf{S^{I}}$

$$\mathbf{S^{I}}\left(\mathbf{S^{I}}\mathbf{S^{II}}\right)\left(\mathbf{S^{I}}\right)^{-1} = \mathbf{S^{II}}\left(\mathbf{S^{I}}\right)^{-1} = \mathbf{S^{II}}\mathbf{S^{I}} \tag{3.24}$$

where the final equality follows from the fact that $\mathbf{S^{I}}$ (whose spectrum lies on the unit circle of the complex plane) possesses only real eigenvalues and is therefore its own inverse. It may also be shown that $\mathbf{S^{II}}$ is also its own inverse and thus

$$\left(\mathbf{S^{I}}\mathbf{S^{II}}\right)^{-1} = \mathbf{S^{II}}\mathbf{S^{I}} \tag{3.25}$$

Combining (3.24) and (3.25) gives

$$\mathbf{S^I}\left(\mathbf{S^I S^{II}}\right)\left(\mathbf{S^I}\right)^{-1} = \left(\mathbf{S^I S^{II}}\right)^{-1} \tag{3.26}$$

which shows that the timestep matrix is unitarily similar to its inverse. Consequently, every eigenvalue must be paired with its complex conjugate (recall that $\mathbf{S^I S^{II}}$ is unitary under (3.23)). The associated eigenstates are related to each other by $\mathbf{S^I}$ and are mutually orthogonal under the inner product of (3.23). While the individual states for each pair of eigenvalues are distinct, they yield the same electric field configuration when subject to the field recovery operator defined in (3.17). This result follows as a consequence of (3.18) and illustrates that that the field recovery operator is non-injective. The foregoing analysis showed that TLM discretization retains much of the character present in the analytical problem.

3.2.3 Eigenvalue Algorithm

For coarse discretizations of the computational domain, (3.8) may be approximated to a high precision using an arbitrary dense matrix solver for general matrices, such as one from the LAPACK software package [180]. However, the length of the calculation rapidly increases with increasing node density owing to the fact that eigenvalue algorithms for dense matrices usually bear a computational complexity of at least $\mathcal{O}(n^3)$, where n is the dimension of the matrix [33]. As the timestep matrix is sparse, numerical efficiency can be improved by using sparse matrix techniques. Moreover, by carefully developing a tailored algorithm, the latent structure found in the eigenvalue problem can be exploited to shorten runtime and lessen memory requirements. The algorithm developed in this section is based on a hybrid of the power and Arnoldi methods [185], which are two sparse matrix techniques that

make use of a computationally inexpensive matrix-vector product

$$\mathbf{x}_2 = \mathbf{A}\mathbf{x}_1 \tag{3.27}$$

which has a computational complexity of $\mathcal{O}(n)$ when the number of nonzero entries in the matrix $\mathbf{A}$ is a linear function of its dimension n [186].

The power method iteratively approximates the largest eigenvalue of a general matrix, which in the present work is assumed to be sparse. The method commences by selecting an initial (usually random) vector. Each iteration involves multiplying the previously computed vector by the matrix, where the first iteration utilizes the initial vector. The action of the method may be considered by expanding both the matrix and vector with the eigenvectors of the matrix

$$\mathbf{A}\mathbf{x} = \left(\sum_i \lambda_i \mathbf{v}_i \mathbf{v}_i^\dagger\right)\left(\sum_i x_i \mathbf{v}_i\right) = \sum_i \lambda_i x_i \mathbf{v}_i \tag{3.28}$$

where λ_i is the i^{th} eigenvalue of $\mathbf{A}$. Note that $\mathbf{A}$ is assumed to be normal (and hence diagonalizable), and the left and right eigenvectors are related by the Hermitian adjoint, denoted by the $\dagger$ symbol. Repeated applications of (3.27) give

$$\mathbf{A}^n\mathbf{x} = \sum_i \lambda_i^n x_i \mathbf{v}_i \tag{3.29}$$

For a sufficiently large number of iterations n, only the eigenvector that corresponds to the eigenvalue of largest magnitude contributes appreciably to the final vector of (3.29). However, a considerable number of iterations are required when the contrast in magnitude between eigenvalues is small. After the j^{th} iteration, the

largest eigenvalue can be approximated with the Rayleigh Quotient [186] as

$$\lambda_{|\mathbf{A}|} \approx \frac{(\mathbf{x}^j)^\dagger \mathbf{A}\mathbf{x}^j}{(\mathbf{x}^j)^\dagger \mathbf{x}^j} \tag{3.30}$$

where $\lambda_{|\mathbf{A}|}$ is the eigenvalue of largest magnitude. The eigenvalues of (3.8) are of equal magnitude owing to the unitary nature of the scaled timestep matrix. To apply the power method, the system must be shifted in order to induce a contrast in magnitude between different eigenvalues. The shifted system

$$\sqrt{\mathbf{Z}}^{-1}\mathbf{S}^{\mathbf{I}}\mathbf{S}^{\mathbf{II}}\sqrt{\mathbf{Z}} + c\mathbf{I} = \sqrt{\mathbf{Z}}^{-1}\mathbf{S}^{\mathbf{I}}\mathbf{S}^{\mathbf{II}}\sqrt{\mathbf{Z}} + e^{j\Omega\Delta t}\mathbf{I} \tag{3.31}$$

possesses eigenvectors that are identical to those of the original unshifted system but a spectrum that has been shifted such that $\lambda_i \longrightarrow \lambda_i + c$, where c is a phase given by Ω and Δt. In this revised equation, the magnitude of each eigenvalue is determined by the proximity in phase of its unshifted value to that of c. Setting Ω in (3.31) allows the eigenmode closest in frequency to be selected by the power method. For example, when Ω is set to 0, the power method converges to the lowest frequency mode, which corresponds to the first band. This process is illustrated in Fig. 3.2.

Applying the power method to the shifted system rapidly eliminates modes that

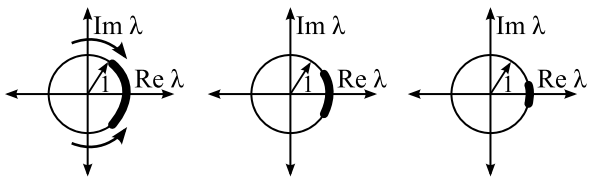

Figure 3.2: Unit circle in the complex plane illustrating the action of the power method. In this example, the timestep matrix is shifted about $\Omega = 0$. The thickened line shows where eigenvalues of appreciable magnitude remain after successive iterations.

are substantially out of phase with c. However, modes that exhibit a smaller difference in phase persist in appreciable magnitude for a greater number of iterations. The nature of this persistence may be investigated by expressing the modulus of the shifted system's eigenvalues as the first two terms of a Taylor series expansion

$$\left|e^{j\omega\Delta t} + e^{j\Omega\Delta t}\right| \approx 2 - \frac{1}{4}\left(\omega - \Omega\right)^2 \Delta t^2 \tag{3.32}$$

which shows that as ω approaches Ω, the discrimination between modes diminishes quadratically. Also note that the contrast in magnitude for closely spaced modes depends quadratically on the timestep Δt. This is particularly problematic at higher frequencies, where modes are spaced more closely together. As $\Delta t \ll 1$, finer meshes also leads to slower convergence. In numerical calculations performed in the preliminary investigation of this method, convergence to a single mode was never observed using the power method alone.

While it may appear that the power method is a fruitless approach to solving (3.8), its ability to quickly remove all but a few modes can be used to condition the starting vector of a subsequent Krylov subspace routine by significantly reducing the effective dimension of the problem. In particular, the Arnoldi method may be used to efficiently establish the eigenspace of the remaining modes. In its most general form, this method approximates the largest eigenvalues of a general matrix. The Krylov subspace is defined as [185]

$$\mathcal{K}_n = span\{\mathbf{b}, \mathbf{Ab}, \mathbf{A^2b}, \mathbf{A^3b}, \ldots\} \tag{3.33}$$

where $\mathbf{b}$ is an initial guess (in this case the last vector from the power method iteration), and n is the dimension of the Krylov subspace. Note that the vectors

that span this space are formed by additional iterations of the power method. However, in Krylov subspace routines, the vectors from previous iterations are retained as they carry significant information that may be exploited to increase the rate of convergence. The vectors of (3.33) may be orthogonalized using the Gram–Schmidt process [184, 187], where the i^{th} vector of the series may be found from

$$\mathbf{u}_i = \frac{\mathbf{v}_i - \sum_{j=0}^{i-1} \mathbf{u}_j \mathbf{u}_j^\dagger \mathbf{v}_i}{\left| \mathbf{v}_i - \sum_{j=0}^{i-1} \mathbf{u}_j \mathbf{u}_j^\dagger \mathbf{v}_i \right|} \tag{3.34}$$

where $\mathbf{v}_i = \mathbf{A}^i \mathbf{b}$. Numerical accuracy may be improved by using the modified Gram–Schmidt process [184, 187] by setting $\mathbf{v}_i = \mathbf{A}\mathbf{u}_{i-1}$ for $i > 0$. The resulting vectors from either the stabilized or non-stabilized processes form the columns of the orthogonal matrix $\mathbf{Q}$, which satisfies

$$\mathbf{H} = \mathbf{Q}^\dagger \mathbf{A} \mathbf{Q} \tag{3.35}$$

where $\mathbf{H}$ is an $n \times n$ upper Hessenberg matrix [186]. For sufficiently large n, the largest eigenvalues of this matrix, known as the Ritz values [185], may serve as good estimates of those of $\mathbf{A}$, allowing the approximation

$$\mathbf{A} \approx \mathbf{Q} \mathbf{H} \mathbf{Q}^\dagger \tag{3.36}$$

The Ritz values may be found with a dense matrix solver when the dimension of $\mathbf{H}$ is sufficiently small (usually much smaller than that of $\mathbf{A}$). Equation 3.36 becomes an equality when $\mathbf{b}$ contains components of each eigenvector of $\mathbf{A}$, n coincides with the dimension of $\mathbf{A}$, and calculations are performed without rounding. In practice, only the first condition is likely to be met as generating a Krylov subspace of such large dimension is computationally prohibitive for all but the smallest prob-

lems and because calculations must be performed with finite precision. However, the numerical examples of §4.1.1 illustrate that this approximation can be highly accurate.

When $\mathbf{A}$ is Hermitian, the recurrence relation of (3.34) can be truncated such that successive vectors are only orthogonalized with respect to the last three computed vectors. The scaled and shifted timestep matrix of (3.31) is normal but not Hermitian. An equivalent Hermitian system may be constructed as $\mathbf{A}^\dagger\mathbf{A}$, which possesses eigenvectors identical to those of $\mathbf{A}$, due to the normality of latter. While the full recurrence Gram–Schmidt procedure has a computational complexity of $\mathcal{O}(n^2)$, the three-term process for Hermitian matrices has a complexity of only $\mathcal{O}(n)$ and consequently possesses the potential to drastically reduce the computational burden of orthogonalization [186]. However, the primary drawback to this approach may be loss of orthogonality due to round-off error. As the numerical issues surrounding the use of the three-term relation are complex and subtle with the possibility of compromised accuracy, the full-term recurrence approach was implemented in the numerical code. The pseudocode of the hybrid algorithm is presented below. Note that `GeomFile` refers to the file that contains the geometries and materials of the unit cell, `BZpath` is the set of points in the irreducible Brillouin zone, `NumPMiter` is an integer containing the number of power method iterations, `DimKry` is the dimension of the Krylov space, and `ShiftVals` is the set of values for Ω.

algorithm SpectralTLM(`GeomFile`, `BZpath`, `NumPMiter`, `DimKry`, `ShiftVals`)

1: **setup** $\mathbf{S^I}$ **from** `GeomFile`
2: **setup** $\sqrt{\mathbf{Z}}$ **from** `GeomFile`
3: **for each** $\mathbf{k} \in$ `BZpath` **do**

```
    setup S^II from k
    for each Ω ∈ ShiftVals do
      c ← e^{jΩΔt}
      u_0 ← rand()
      A ← √Z^{-1} S^I S^II √Z + cI
      //PowerMethodIterations
      for i = 1,  i ≤ NumPMiter do
        u_0 ← A u_0
        if i mod 100 = 0 then
          u_0 ← u_0/|u_0|
        end if
      end for
      u_0 ← u_0/|u_0|
      //ArnoldiMethod
      Q ← H ← 0
      for i = 1,  i < DimKry do
        u_i ← A u_{i-1}
        for j = 0,  j < i do
          y ← u_j^† u_i
          H_{j,i-1} ← y
          u_i ← u_i − y u_j
        end for
        u_i ← u_i/|u_i|
        addColumnToMatrix(Q, u_i)
      end for
      σ ← eigenvalues(H)
      V ← eigenvectors(H)
      for each λ_i ∈ σ do
        λ_i ← λ_i − c
        ω ← angle(λ_i)/Δt
        if |Ω − ω| < ΔΩ/2 then
          //ComputeElectricField
          f ← FQV_i
          writeToFile(k, ω, f)
        end if
      end for
    end for
end for
```

The algorithm was implemented in the C programming language [178] using the

ZGEEV function from the LAPACK library [180] to solve for the eigenvalues of $\mathbf{H}$. Extensive runtime evaluations are presented in §4.1.2.

3.2.4 Computational Complexity & Implementation Issues

The computational complexity of the spectral transmission-line modeling method is a function of the mesh size and the separation of bands in frequency. While the latter is difficult to quantify, it is possible to establish upper and lower bounds on the computational complexity as a function of mesh size when the frequency range of interest is kept constant.

A simple lower bound derives from the fact that the algorithm requires a certain amount of time to process each node, regardless of subsequent computation. This lower bound is $\mathcal{O}(m)$, where m is the number of nodes. An upper bound may be found by considering the effect of increasing the density of nodes. In a mesh comprising square nodes, the relation between the timestep, number of nodes, and node width is given by

$$\Delta t \propto \Delta x \propto \sqrt{m} \tag{3.37}$$

where Δt is the timestep and Δx is the node width. Decreasing the timestep does not appreciably change the value of ω in (3.32), provided that the mesh possesses a sufficiently fine discretization. In this case, halving the timestep (increasing the number of nodes fourfold) permits (3.32) to be rewritten as

$$\left| e^{j\omega\Delta t} + e^{j\Omega\Delta t} \right| \approx 2 - \frac{1}{4}\left(\omega - \Omega\right)^2 \left(\frac{\Delta t}{2}\right)^2 \tag{3.38}$$

where Δt is the timestep corresponding to the original mesh. Raising this expression

to the fourth power and neglecting contributions from higher orders of Δt gives

$$\left|e^{j\omega\Delta t} + e^{j\Omega\Delta t}\right|^4 \approx 8\left[2 - \frac{1}{4}\left(\omega - \Omega\right)^2 \Delta t^2\right] \tag{3.39}$$

Equations 3.38 and 3.39 show that the reduction of nearby modes is constant when the number of power method iterations is proportional to the number of nodes. The complexity of m power method iterations is $\mathcal{O}(m^2)$, which follows from the fact that the complexity of a single iteration is $\mathcal{O}(m)$. The Arnoldi method possesses a complexity of $\mathcal{O}(m)$ when the dimension is fixed. Thus, the the upper bound is found to be $\mathcal{O}(m + m^2) = \mathcal{O}(m^2)$. The actual computational complexity lies between the bounds of $\mathcal{O}(m)$ and $\mathcal{O}(m^2)$, which may be sharpened by considering the numerical consequence of reducing the number of power method iterations while simultaneously increasing the dimension of the Krylov subspace.

Numerical dispersion (as opposed to the analytical dispersion of waves considered earlier) is an undesired spurious dependence of the wavenumber on direction that arises from the analytical problem being discretized on a mesh. The severity of numerical dispersion is directly proportional to frequency and node width. To obtain reasonable accuracy, the node width should not exceed approximately $\lambda/10$, where λ is the wavelength in the material of highest permittivity. A detailed analysis of numerical dispersion in TLM may be found in [188] and [189].

Photonic crystals, like many electromagnetic structures, may support modes that are degenerate with respect to frequency [32]. While the presence of such modes does not affect the calculation of dispersion diagrams, the computed modes may belong to a degenerate subspace. A mode satisfying particular criteria such as symmetry may be found by performing several simulations using different values of $\mathbf{b}$ and orthogonalizing the resultant eigenvectors accordingly.

3.3 Design of Microwave Liquid Crystal Devices

Use of liquid crystals in microwave engineering brings forth several challenges beyond those encountered with ordinary dielectrics, placing demands on geometry, surface preparation, and electrical characteristics. The ensuing discussion contains an examination these issues, which serves as a rationale for the selection of a planar geometry as the basis of the microwave devices presented in the latter sections of this chapter.

3.3.1 Alignment Methods & Geometry

Microwave devices containing liquid crystals have employed a combination of heating [176], rubbed surfaces [155,166], and multiple low-frequency electric fields [139] to produce the director alignments (§2.3), or absence thereof, required for switching. Each of these methods raises specific design considerations. Temperature-controlled switching (Fig. 2.11), which falls short of fully utilizing available dielectric contrast, is likely impractical in many applications and may be incompatible with the use of alignment layers whose glass transition (or decomposition) temperature is exceeded by the clearing point of the liquid crystal. The use of rubbed surfaces is constrained by the fact that, as discussed in §2.3.4, the switching time increases quadratically with dielectric thickness, which is thus limited to perhaps a few hundred microns. Due to the nature of the rubbing process, results may be inconsistent and involve trial and error during the course of establishing a successful process. As curved and irregular surfaces pose still greater difficulty, rubbed surfaces are usually planar.

Electrical switching requires that the structure support a (quasi) static electric field in the region containing the liquid crystal. This precludes electrical switching of liquid crystal materials embedded in rectangular and circular waveguides, which

possess a low-frequency cutoff. For structures supporting a (quasi) TEM mode, electrical switching may be achieved by applying a sufficiently high DC voltage across the conductors that guide the high-frequency field. However, if the energy of the radio frequency (RF) field is distributed amongst regions of significantly disparate field strengths or the conductors are widely separated, high voltages may be required to effect complete switching. The former is illustrated in Fig. 3.3, which shows the fringing field around a narrow microstrip line. A large DC voltage may be required to align the dipoles of a material along the field lines in the voluminous regions occupied by the weak (but energetically significant) fringing field. This issue, in the context of microstrip transmission lines, is explored extensively in [166]. Even moderately high voltages may be incompatible with RF measurement equipment, where size constraints place limits the breakdown voltage of DC blocks. These constraints originate from the requirement that the physical size of RF components must (generally) scale proportionally with wavelength. Hence, this issue restricts the combinations of geometry, auxiliary equipment, and RF operating frequency that may be realized.

Design of a structure to exhibit particular dynamical electromagnetic characteristics requires careful design of the physical implementations that produce director orientation. In three dimensions, this may amount to a formidable task when

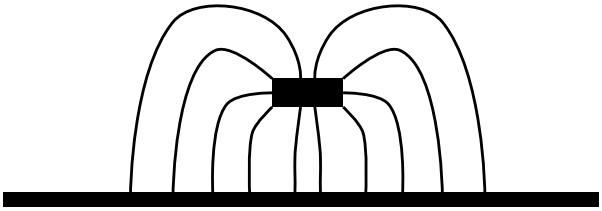

Figure 3.3: Narrow microstrip line in air ($\epsilon_r = 1$) showing the fringing field of the fundamental TEM mode. Much of the energy is located in regions where the field strength is weak (corresponding to lengthier field lines). In these regions the alignment strength of the field is commensurately less.

complicated material and field geometries are involved. In two dimensions, the decomposition of waves in a uniaxial liquid crystal (2.54) in terms of conventionally-defined TE and TM modes is only possible when $\nabla \cdot \mathbf{D} = 0 \implies \nabla \cdot \mathbf{E} = 0$, which is satisfied by a director orientation that is normal to the plane of propagation. However, in the presence of two closely spaced planar conductors, transverse components of the electric field are strongly suppressed, and the resultant interaction of the TM mode with a liquid crystal material enjoys a particularly simple description wherein an effective permittivity may be defined as the scalar quantity

$$\epsilon_{\text{eff}} = \hat{\mathbf{a}}_z \cdot \mathbf{R}\underline{\epsilon} \tag{3.40}$$

where $\mathbf{R}$ is a rotation matrix corresponding to a rotation in $\mathbb{R}^3$ that rotates the permittivity tensor $\underline{\epsilon}$, from its reference frame to that of the director. Under these conditions, switching is manifested as a change in effective permittivity. The contrast in permittivities associated with the two states may be maximized by an appropriate combination of surface and field alignment mechanisms.

Further practical difficulties arise from the fact that the functional characteristics of liquid crystal materials occur in the liquid phase. Thus, in practical applications, liquid crystal materials lack structural integrity, providing no mechanical support to the aggregate construction, and require a method of containment. Consequently, a liquid crystal cannot serve as the substrate material in structures such as conventional microstrip lines or coplanar waveguides. Addition of a superstrate to support the conductors may provide a solution.

The final consideration concerns loss, which originates from both the material itself and guiding conductors. Dielectric loss is partly due to ionic currents, but for many nematics it is mainly due to the residual loss arising from dielectric relaxation

at somewhat lower frequencies [177]. Significant ohmic losses result from the close spacing of guiding conductors that is necessary when using rubbed surfaces. This is most clearly illustrated by considering the attenuation constant due to conductor loss for the TEM mode of a parallel plate waveguide [51],

$$\alpha_c = \frac{R_s}{\eta \Delta z} \tag{3.41}$$

where R_s is the surface resistivity of the conductors, and η is the dielectric impedance. Loss is inversely proportional to the conductor spacing Δz. These losses are significant in resonator devices and are discussed in further detail in §3.6.1.

3.3.2 Common Design Features

The design of each structure incorporates a common planar geometry that supports only TM wave propagation over the frequencies of interest, thereby admitting the simplified electromagnetic description of (3.40) and allowing director alignment to be produced with rubbed surfaces and low-frequency electric fields. This arrangement comprises a planar conductor suspended over a ground plane, where the intervening space of approximately 200 μm is filled with a nematic liquid crystal. In each device, feed-line structures are used to bring the signal lines to the liquid-crystal regions. These were fabricated from the commercially available Rogers RO4003c substrate, which comprises a 203 μm-thick dielectric ($\epsilon_r = 3.55$) sandwiched between two layers of 17 μm-thick copper. Surfaces in contact with the liquid crystal were coated with a layer of polymer that was rubbed with the method developed in §3.5, thereby inducing uniform planar alignment. The director may be rotated 90° with a uniform low-frequency field, which may be effected by applying a 1-kHz voltage across the conductors. While a spacing of 200 μm is associated with modest

conductor loss, this is of limited consequence in the present work and was explicitly incorporated into simulations. The reproducibility and adequacy of the rubbing process is of greater importance and has been addressed with the design and construction of a precision buffing machine (§3.4) and the determination of suitable rubbing parameters through a series of rubbing experiments involving modified twisted nematic cells (§3.5).

The liquid crystal used in constructed devices was selected following a review of published microwave dielectric properties of several commercially available nematic liquid crystals [177]. BL006 (produced by Merck KGaA and obtained from EMD Chemicals, Hawthorne, New York) was chosen for its considerable dielectric contrast at both DC and microwave frequencies, where the former property endows the material with a strong response to low-frequency switching fields. Polyvinyl alcohol (98% hydrolyzed, molecular weight (MW) $\sim$16,000, obtained from Scientific Polymer Products, Inc., Ontario, New York) was selected as the alignment layer as it produces excellent planar alignment [63], does not require refrigerated storage, and was readily available commercially. Alignment layers were formed by spin coating an aqueous solution of 1.5% w.t. polyvinyl alcohol (PVA), which was prepared by dissolving anhydrous polyvinyl alcohol in distilled water heated to 85 °C. Spin coating was performed for a duration of 30 seconds at a rotational speed of 2000 RPM.

Surfaces that were to make contact with the liquid crystal were carefully selected and handled. Only materials that possessed specularly reflective surfaces and whose measured roughness was on the order of nanometers were used. Samples were discarded in cases where the deposition of copper incurred a visible or measured increase of roughness. Prior to processing with the wafer saw, samples were coated in a protective layer of photoresist that was later removed by rinsing in acetone,

then isopropyl alcohol, and finally distilled water. The samples were then dried with nitrogen. The water of the final rinse was found to make a very small contact angle with each of the surfaces (which were difficult to dry). This confirmed that samples retained their hydrophilic character, a requirement for spin coating aqueous solutions of PVA.

Care was taken to ensure that the deposition of copper and polyvinyl alcohol, and rubbing of the latter were performed consistently for all constructed devices. The thicknesses of these layers were found by removing a portion of the deposited material on a sample and measuring the resultant step profile. In the case of polyvinyl alcohol, this was carried out by partially covering a sample with a mask, removing the exposed material by plasma etching (Appendix C), and measuring the height of the resultant step with a surface profiler (Tencor Alpha Step 500). The thickness of the deposited PVA was found to be approximately 25 nm, a value that has allowed its omission from computer simulations. In the case of copper, the surface profiles of several copper edges in fabricated devices were scanned, yielding an average thickness of approximately 1.175 μm. The sheet resistivity was measured in six locations of a large sample using a four-point probe (Miller Design & Equipment Model FPP-5000) and was found to be approximately 4.75×10^{-2} Ω/sq, corresponding to a bulk conductivity of 1.79×10^{7} S/m. This value is considerably less than that of pure copper (5.81×10^{7} S/m [51]) and its inclusion in simulations led to a significant improvement in agreement between simulated and experimental results, particularly those of the resonator Q-values.

3.4 Apparatus for the Preparation of Rubbed Surfaces

The rubbing process is characterized by several parameters, including the material of the cloth, its speed and direction, and the length of fiber in contact with the sample (known as the pile impression). While rubbing may be performed by hand, this approach affords only approximate control over these parameters. In view of the sensitivity of liquid crystal alignment to surface preparation, it was deemed necessary to construct a machine that would allow these parameters to be precisely controlled.

The fabricated machine is based on a conventional design consisting of a stage that passes under a rotating drum that is covered in a clean cloth and whose height above the stage is adjustable (Fig. 3.4). Mechanical drawings depicting the dimensions and the placement of components are given in Fig. C.5 in Appendix C while the constructed machine is shown in Fig. 3.5. Components are mounted on an aluminum platform (43.18 cm×20.32 cm×0.635 cm), which is seated on four leveling pads. The stage comprises an aluminum plate (25.4 cm × 10.16 cm × 0.635 cm) that is connected to the platform by a linear bearing (DT-118, obtained from Reid

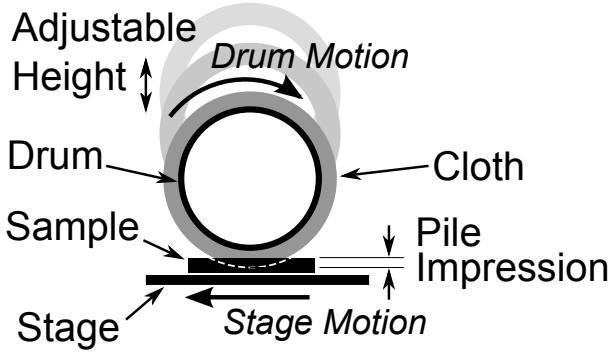

Figure 3.4: Conventional method of buffing a liquid crystal alignment layer. The pile impression and speeds of the drum and stage can be defined by the user.

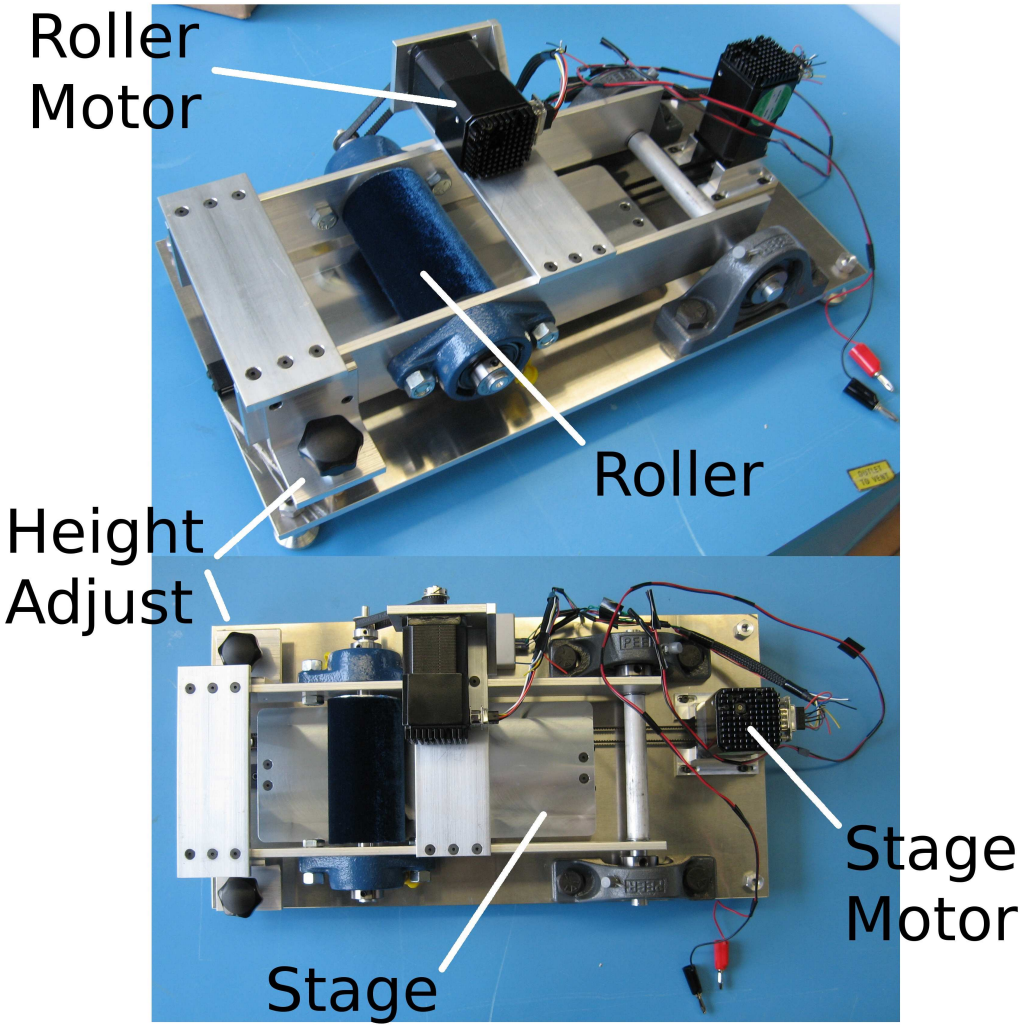

Figure 3.5: Constructed buffing machine.

Supply Company, Muskegon, Michigan). The drum assembly consists of a precisely machined 5.08 cm-diameter aluminum rod that is connected to a rigid frame by two ball bearings. The frame is joined to the platform at one extremity by two pillow block bearings that support some of the assembly's weight, the remainder of which is born by two bolts on the opposing side, which protrude from tapped holes in the frame and rest on the platform. The angle between the assembly and the platform (and therefore the distance of the drum above the stage) may be

set precisely by adjusting the protrusion of the bolts, which is accomplished by manually rotating the knobs (Fig. 3.5), where each 1/6 revolution corresponds to a vertical displacement of the drum of 145 μm. The drum assembly may also be lifted by hand in order to free access to the stage and sample.

Motion of the drum and stage is effected by two stepper motors (IMC17, obtained from RMS Motion, Carson City, Nevada), whose control circuitries ensure that a constant speed is maintained in the presence of a variable of load. The motors are controlled by a personal computer-based software program, which allows rubbing programs to be created, saved, recalled, and executed (Fig. 3.6). The program abstracts the underlying communication with the motors, requiring that the user specify only the distance of stage traversal and the velocities of the stage and roller surface in either metric or imperial units. Testing of the machine established the maximum speed of the drum surface to be approximately 2 m/s when buffing a typical sample. Failure of a motor to sustain its prescribed speed is abrupt and invariably results in complete discontinuance of rotation, the absence of which verifies that a given course of rubbing has conformed to the programmed settings.

A precisely sized velour cloth was cleaned using an aqueous detergent (Sparkleen, obtained from Fisher Scientific, Ottawa, Ontario), thoroughly rinsed in distilled water, and attached to the drum using an adhesive (LePage BondFast) that readily dissolves in acetone, facilitating future replacement of the cloth. This step was carefully performed in the Nano Systems Fabrication Laboratory (NSFL) using clean latex gloves to ensure that the outer surface of the washed cloth remained perfectly free of contaminants (including adhesive). Samples were affixed to the stage using doubled-sided tape. Immediately prior to, and after rubbing, the stage, roller, and surrounding areas were cleared of dust and debris with an ionizing nitrogen gun. Upon removal of the sample, residual tape was abraded and the stage

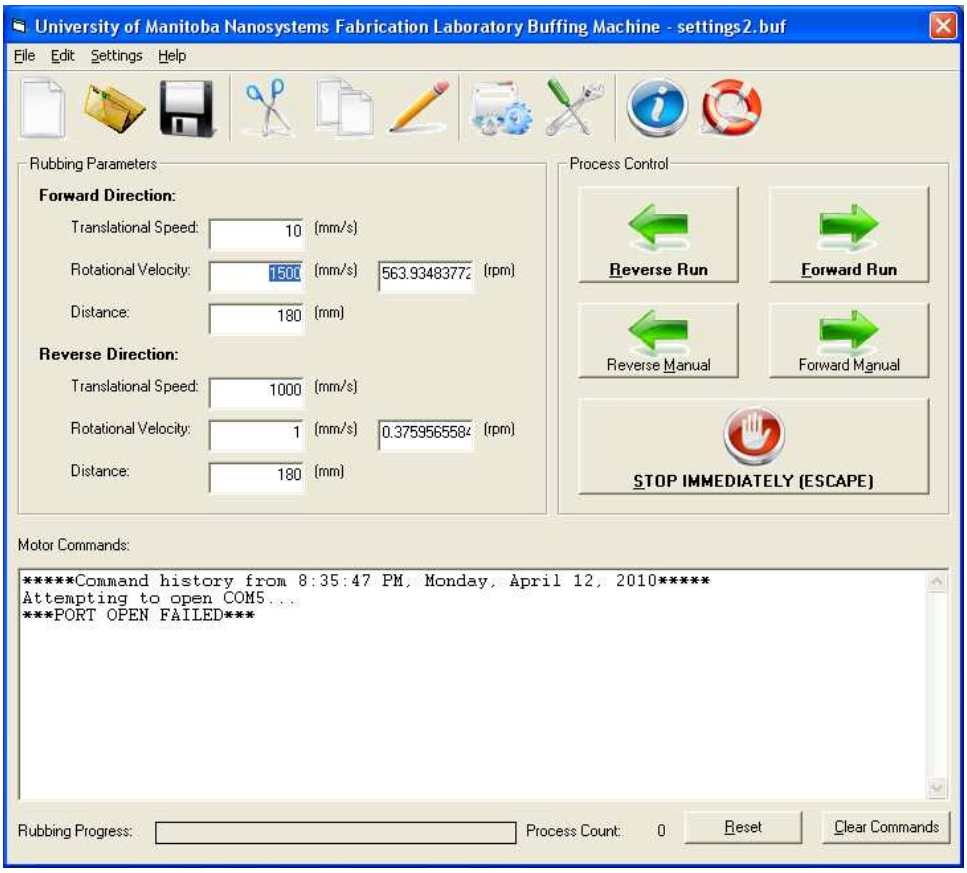

Figure 3.6: Buffing machine control software (for Microsoft Windows). The direction of the drum's rotation is determined by the sign of the specified rotational velocity. A program consists of forward and reverse routines. Upon executing the forward routine, the displayed program will move the stage at 10 mm/s over a total of 180 mm, during which time the sample will be rubbed by the drum at 1490 mm/s. The reverse routine quickly returns the stage to its initial position without appreciable movement of the drum (requiring the user to lift the drum assembly to prevent the roller from contacting the sample a second time). This general format allows programs to alternate between the forward and reverse rubbings if so desired. Note that the pile impression is not controlled by the software.

was cleaned with isopropyl alcohol. The machine is operated and stored under a cover in the NSFL in order to minimize exposure to dust.

3.5 Twisted Nematic Cells For the Evaluation of Rubbing Parameters

The search for a set of rubbing parameters (pile impression, speed, and duration) that produced acceptable alignment for the given combination of cloth, alignment layer, and liquid crystal was carried out with series of modified twisted nematic cells (Fig. 3.7), each prepared with a unique set of rubbing parameters. This approach exploited the simple construction and evaluation of such cells, whose optical properties readily reveal imperfections in alignment.

In accordance with the discussion in §2.3.3, the director in a twisted nematic cell possesses a helical shape. The electro-optical properties are readily described in terms of the ordinary and extraordinary rays normally incident upon the cell when [41]

$$\frac{\Delta n h}{\lambda} \gg 1 \tag{3.42}$$

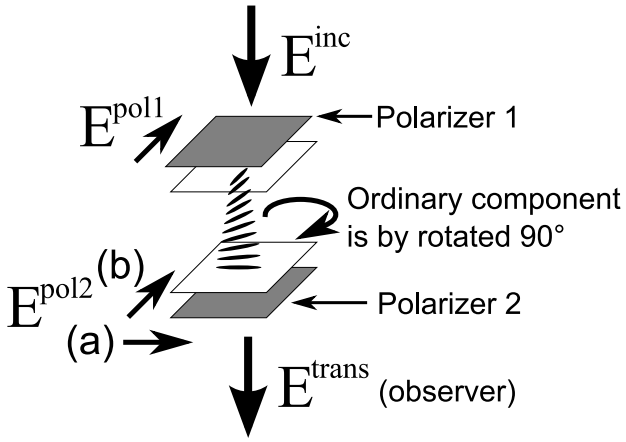

Figure 3.7: Normal/modified twisted nematic cell [38]. Crossed (a) and parallel (b) polarizers give a normal and modified twisted nematic cell, respectively. In the absence and presence of an applied electric field, the cell with the normal polarizer configuration is transparent and opaque, respectively. This behavior behavior is reversed for the modified configuration. The ellipsoids represent liquid crystal molecules.

where λ is a given wavelength of light and $\Delta n = \sqrt{\epsilon_{//}} - \sqrt{\epsilon_{\perp}}$. In this regime, which applies to all of the fabricated devices, the ordinary ray follows the director such that its polarization has been rotated by 90° upon leaving the structure. In the presence of two crossed polarizers (Fig. 3.7), the incident light passed by the first polarizer is similarly passed by the second. In this "off" state the cell's transmissivity is at a maximum. Applying a static electric field across the structure causes the director to become vertically oriented and lose its birefringence with respect to normally incident light. Thus, for the "on" state, a twisted nematic cell's transmissivity is at a minimum, as light undergoes no change in polarization and is therefore rejected by the second polarizer. A structure whose second polarizer by is rotated by 90° (corresponding to a modified twisted nematic cell) exhibits the reversed behavior. The quality of the alignment layers may be judged by viewing the cells through polarizers, where defects appear as dark and bright spots for the crossed and non-crossed configurations respectively.

As the space of variables attendant to the rubbing process is quite large, trials were conducted around an approximate average of eight parameter sets that were used in the rubbing of polyimide layers, as reported in [190–197]. This average corresponds to a pile impression, stage translation speed, and drum-surface speed of approximately 0.6 mm, 13 mm/s, and 1.5 m/s, respectively. Eight cells were prepared using the parameters given in Table 3.1. Each cell comprises two 25.4 mm × 25.4 mm flat and smooth glass squares, which were immersed in a piranha solution (heated sulphuric acid and hydrogen peroxide) to remove any organic residue (Appendix C). A thin layer of a few nanometers of indium tin oxide (ITO) was sputtered onto a single side of each of the cleaned samples, forming a transparent conductive coating. Polyvinyl alcohol was spin coated on each of the ITO surfaces, and the resultant films were rubbed in accordance with the parameters of

Variation No.	Drum Speed (m/s)	Stage Speed (mm/s)	Pile Impression (mm)
1	0.75	10	0.25
2	0.75	5	0.25
3	1.5	10	0.25
4	1.5	5	0.25
5	0.75	10	0.55
6	0.75	5	0.55
7	1.5	10	0.55
8	1.5	5	0.55

Table 3.1: Rubbing parameters used in the preparation of eight twisted nematic cells.

Table 3.1. A felt pen was used to place a mark on a peripheral area of each sample in order to preserve information on the rubbing direction. Two samples that were subject to identical rubbings were then brought together to form a completed cell. Immediately prior to this step, a small drop of BL006 was placed onto the inner surfaces of one of the samples to which two spacers of had been previously affixed. These spacers were constructed from three layers of double-sided tape, whose combined thickness was approximately 250 μm. A constructed device is shown in Fig. 3.8.

Disclination lines (§2.3.2) were clearly visible when the samples were viewed through polarizers under an optical microscope. These lines, which were not observed on the following day, tended to form closed curves that shrank with time and eventually vanished. Cells whose alignment layers were rubbed with a pile impression of 0.55 mm appeared scratched when viewed through polarizers. Conversely, those rubbed with a pile impression of 0.25 mm showed regions where signs of alignment were visibly absent. The other rubbing parameters appeared to have comparatively smaller effects on the quality of alignment.

In view of these observations, another cell was prepared using a pile impression of 0.35 mm, a stage speed of 10 mm/s, and roller speed of 1.5 m/s. The cloth was

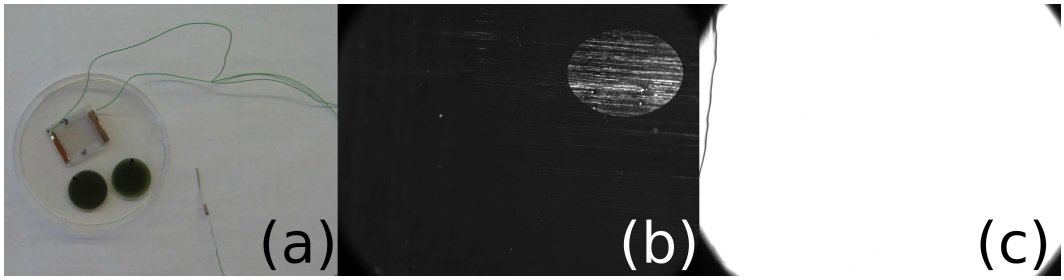

Figure 3.8: Transmission of light through a modified twisted nematic cell (a) as viewed through an optical microscope set to 10× magnification. The polarizers are mounted parallel to each other. This cell was prepared in accordance with the 7$^{\text{th}}$ entry of Table 3.1. The "off" state (b) corresponds to an absence of alignment field, while the "on" state (c) was produced by applying 7.07 V RMS (1 kHz) across the cell. Note that (c) is completely white due to the fact that the transmissivity of the cell is at a maximum in this state. The camera exposure settings used to capture (b) and (c) were identical, and the contrast and brightness were enhanced in an oval region in of (b) to illustrate the scratch marks left by the rubbing process. Scratch marks on later samples were diminished by reducing the pile impression.

changed to remove the possibility of contaminants affecting rubbing quality. This appeared perfectly transparent through crossed polarizers, and images conveyed through the sample appeared undistorted. By rotating the polarizer by 90°, the cell was made opaque. In both cases, the cell's transmissivity was identical when viewed from the other side (corresponding to an exchange of the observer and electric field source in Fig. 3.7). Upon observation of the sample under 10× magnification, small defects were observed. However, their scale was orders of magnitude smaller than the wavelengths of interest, and their collective area constituted a very small portion of the overall cell. This set of parameters was therefore used to rub all subsequently prepared samples.

The fabricated cells were also used to investigate electrical switching. During their construction, the two glass slides were laterally offset from one another, exposing the inner surface of each slide. These were scratched with a fingernail to remove the layer of polyvinyl alcohol (exposure of the underlying ITO layers was

confirmed by measuring the conductivity of the surfaces), and a segment of copper tape possessing a conductive adhesive was affixed to each ITO surface. Wire wrap was soldered to each of the copper pieces and connected in series with a 91-kΩ resistor to a function generator (Stanford Research Systems Model DS340). It was found that the modified twisted nematic cells could be switched with both DC and 1-kHz signals. Increasing the frequency past 1 kHz resulted in progressively longer switching times until switching no longer occurred. In each case, the threshold voltage that produced a noticeable change in the cell's transmissivity was found to be about 2 V RMS (measured across the cell). Switching time ranged from on the order of a minute with 2 V RMS to a few seconds with 7.07 V RMS. Upon discontinuance of the voltage, the cells returned to their prior state within a few seconds.

3.6 Circular Patch Resonator

3.6.1 Design

The microwave characteristics of BL006 were studied with a circular microstrip patch resonator, the design, simulation, and construction of which is presented in this section. The most basic form of such a resonator consists of a ground plane, substrate, microstrip patch, and coupling lines. As a resonance-based method of permittivity measurement, the current approach rests on the fact that the resonant frequency f as given by

$$f \propto \frac{1}{\sqrt{\epsilon_r}} \tag{3.43}$$

is exactly or approximately valid. Note that while a microstrip ring resonator is often the method of choice for performing permittivity measurements in the case

of solid isotropic substrates, a patch resonator was found to be better suited in view of the issues discussed in §3.3.1. The patch was chosen to be circular, as this geometry possesses a maximal surface area to peripheral length ratio.

The semi-analytically derived resonant frequencies of a circular patch resonator possessing a superstrate may be expressed as [198]

$$f_{r,n,m} = \frac{\alpha_{n,m} c}{2\pi a_{\text{eff}} \sqrt{\epsilon_{r,\text{eff}}}} \qquad n \in \mathbb{N}_0,\ m \in \mathbb{N}_1 \tag{3.44}$$

where $\alpha_{n,m}$ is m^{th} zero of the first derivative of the regular Bessel function of order n, c is the speed of light in vacuum, a_{eff} is the effective radius, and $\epsilon_{r,\text{eff}}$ is the effective dielectric constant, which is a function of frequency, substrate and superstrate permittivities, and geometry. For a measured frequency, (3.44) may be evaluated iteratively to find the substrate permittivity that satisfies this equation. By expanding (3.44) as a Taylor series and retaining only the linear term, successive values of $\epsilon_{r,\text{eff}}$ may be computed as

$$\epsilon_{r,\text{eff}}^{n+1} = \epsilon_{r,\text{eff}}^{n} - 2\epsilon_{r,\text{eff}}^{n} \left(\frac{f_{\text{meas}} - f_{\text{sim},n}}{f_{\text{meas},n}} \right) \tag{3.45}$$

where $\epsilon_{r,\text{eff}}^{0}$ is taken as a guess and f_{meas} and $f_{\text{sim},n}$ are the measured and n^{th} simulated resonant frequencies, respectively. For greater accuracy, this procedure was modified by replacing evaluations of (3.44) with full-wave simulations that explicitly incorporated the effects of conductor and radiation loss, coupling lines, and geometrical imperfections introduced during construction. These simulations were carried out with Ansoft HFSS, a commercial finite element software program that solves the curl-curl equation for the electric field using a mesh of tetrahedra on which edge elements are defined. Resonances may be modeled as those of a par-

allel inductor-capacitor circuit, for which resonant frequencies ω_0 are given by the geometric mean [199]

$$\omega_0 = \sqrt{\omega_1 \omega_2} \tag{3.46}$$

where ω_1 and ω_2 are the half-power frequencies. The quality factor Q is defined as [199]

$$Q = \frac{\omega_0}{\omega_1 - \omega_2} \tag{3.47}$$

During the iterative searches for the dielectric constants and loss tangents of BL006, the measured and simulated resonances were compared using (3.46) and (3.47). This approach was deemed more accurate than using the frequencies associated with the absolute transmission peaks, which are liable to shift in the presence of noise.

The diameter of the patch was chosen to be 2 cm, as such a value admits a reasonable number of modes in the frequency span of interest (0–15 GHz) and yields a diameter-to-substrate thickness ratio that keeps the fringing field proportionally small (as discussed in §3.3.1). Unfortunately, the quality factor of such a resonator is low due primarily to the lossy nature of BL006 [177] but also radiation loss and the spacing and geometrical configuration of the conductors [3]. Loose coupling was thus precluded, and the resonator was designed to be directly coupled to its feed lines.

The designed resonator comprised four principal components: two feed-line structures based on the Rogers RO4003c substrate, a 500 μm-thick crystalline quartz superstrate patterned with a copper patch and connecting microstrip lines, and a ground-plane structure consisting of a slab of soda-lime glass coated in copper (Fig. 3.9 and Appendix C). Upon assembly of these components (Fig. 3.10), each port is connected to the circular patch by a microstrip trace whose width

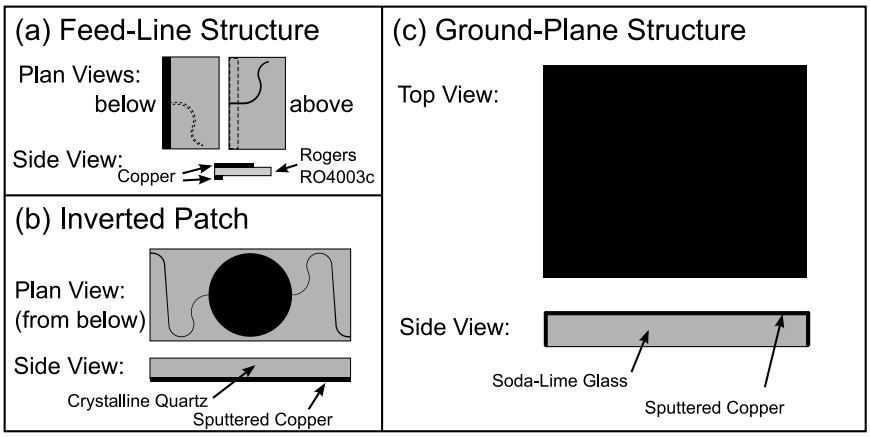

Figure 3.9: Individual components of the circular patch resonator consisting of two feed-line structures (a), one inverted patch structure (b), and one ground-plane structure (c). Copper is shown in black. Note the presence of copper sidewalls on the ground-plane structure, whose deposition is deliberate and which serve to facilitate electrical connection to ground conductors of the feed-line structures.

tapers exponentially from 450 μm to 50 μm (the minimum dimension consistently attainable with the available photolithographic process), thereby minimizing loading of the resonator and the further degradation of the resonator's Q. Between each port and the patch, the microstrip line traverses the Rogers substrate to air/BL006 transition. Reflections arising from this transition may give rise to standing waves that result in a shift of the resonant frequencies. The microstrip line was thus made to cross this boundary at an oblique angle of 86° from normal, resulting in a less abrupt change of impedance and a reduction of associated reflection. Satisfactory performance of the coupling lines and associated transitions was confirmed in a separate simulation, which showed a return loss no greater than approximately -20 dB over the frequency range of interest.

The entire unfilled resonant structure, including the coupling lines, was simulated with Ansoft HFSS (Fig. 3.11). The layers of polyvinyl alcohol were omitted from the simulation because they contribute negligibly to the structure's electromagnetic properties, while the copper layers were fully discretized as 1.175 μm-thick

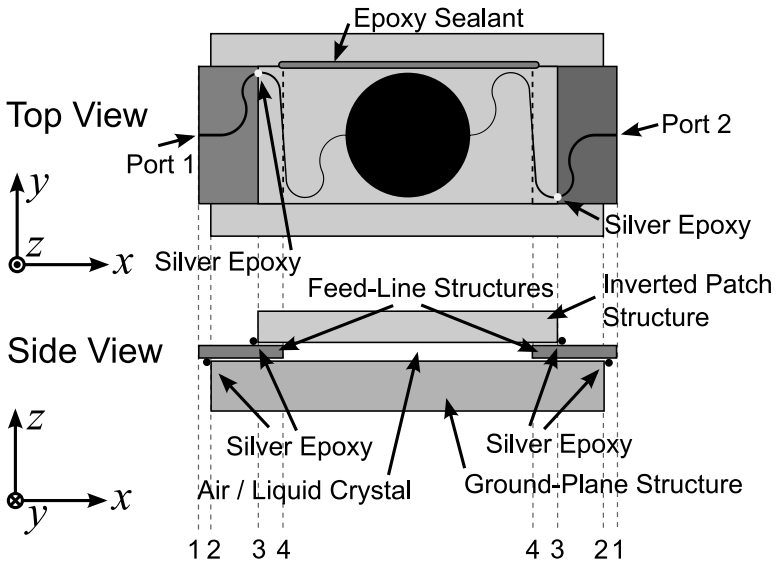

Figure 3.10: Drawing of the circular patch resonator. The structure is symmetric with in-plane rotations of π. The impedance of each microstrip line is 50 Ω at each port. The width of each line is exponentially tapered from 450 μm to 50 μm where it meets the the circular patch. The 203 μm-thick Rogers RO4003c substrates extend from (1) to (4), while the air/BL006 dielectric is contained within (4)–(4). A portion of the microstrip line is printed on the upper metalization of the Rogers RO4003c substrates (1)–(3), while the remainder, including the patch, is printed on the underside of the 500 μm-thick quartz superstrate, which extends from (3) to (3). Note that the separate ground planes and microstrip lines are joined electrically at (2) and (3), respectively.

metal layers possessing a conductivity of 1.79×10^7 S/m (in accordance with measurements given in §3.3.2). Owing to the extreme computational cost associated with solving the vector wave equation in metal, only the portion of the ground plane beneath the signal metalizations was discretized, with the addition of 2 mm margins to capture the fringing field. The error in placement of the superstrate during construction (which resulted in a tilt of 0.1° about the y-axis and a height above the ground plane of 0.26 mm) was included in this simulation. The small relative magnitude of the third peak in transmission may be explained by appealing to the field distributions of the resonant modes (Fig. 3.12). Whereas the first, second, and fourth modes possess maximal anti-nodes at each of the two feed lines,

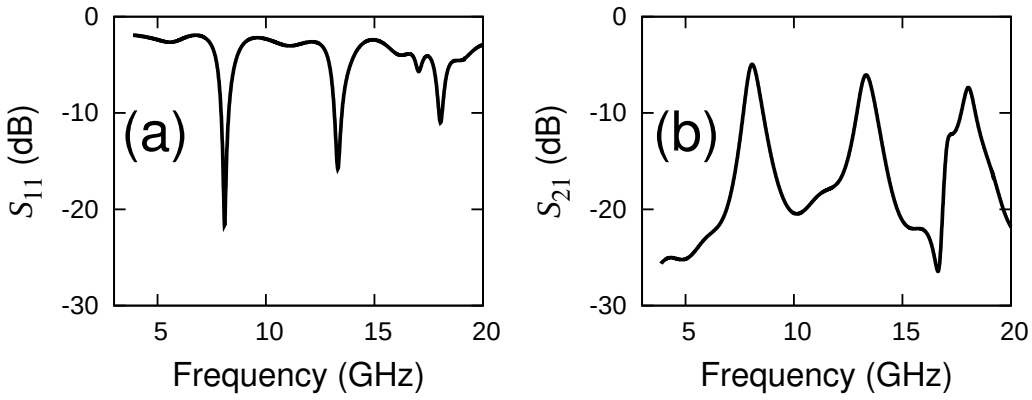

Figure 3.11: Simulated S_{11} (a) and S_{21} (b) magnitudes of the unfilled circular patch resonator depicted in Fig. 3.10. The frequency resolution is 10 MHz. This simulation incorporates the non-idealities arising from construction, including the error in superstrate placement and the diminished conductivity of sputtered copper.

the third mode, which is even with respect to the exchange of ports, possesses a significantly smaller peripheral field that yields reduced coupling to the microstrip lines. Moreover, it undergoes destructive interference with the fourth mode (in terms of S_{21}), which is odd with respect to the exchange of ports. The consequent lack of definition of the third and fourth modes required to determine the half-power frequencies excluded their use in permittivity calculations. The first two resonant modes of the simulated structure (Fig. 3.11) are well-defined and correspond in frequency to within approximately two percent of those computed with the semi-analytical method of [198].

3.6.2 Fabrication

The construction of the resonator spanned several steps that commenced with the preparation of the photolithographic masks, which were designed using the Inkscape vector graphics package [200]. The tapers were approximated as 1000 linear segments, which were generated by a purpose-written software program. The designs

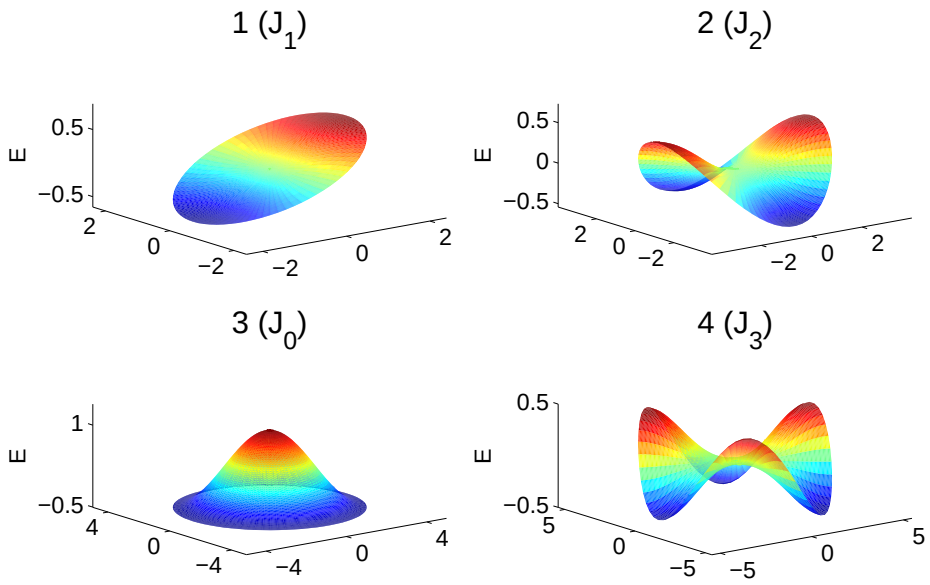

Figure 3.12: Normal electric field distributions of the first four eigenmodes of an ideal circular patch resonator. These modes are solutions to the homogeneous Helmholtz equation on a disk subject to Neumann boundary conditions. The second and third modes are even with respect to the exchange of ports one and two, while the first and fourth modes are odd. Note that the anti-nodes of the first, second, and fourth modes are located solely on the periphery of the disk and, moreover, are always present at the junctions to the feed lines (owing to symmetry associated with their diametrical placement), resulting in strong coupling to the connected microstrip lines. In contrast, the third mode possesses anti-nodes at both the center and periphery of the disk, where the latter is comparatively weak, resulting in significantly less coupling. This outcome originates from the fact that only the zeroth order Bessel function of the first kind possesses a maximum at zero.

were rendered on transparency film by Embassy Graphics, Winnipeg, Manitoba. Examination of the masks under a microscope uncovered no defects in the microstrip feed lines. However, a small number of pinholes were observed in the patch and ground regions and corrected with a black felt pen.

Construction of the feed-line structures began with cutting a rectangle measuring approximately 40 mm × 50 mm from a larger sheet of Rogers RO4003c substrate (obtained from Rogers Corporation, Rogers, Connecticut). Margins of approximately 1 cm were included in anticipation of edge-beading during the spin

coating of the photoresist. Burrs were removed with a fine emery cloth in order to ensure flush contact between the sample and mask during photolithography. The sample was cleaned with isopropyl alcohol, and photoresist was spin coated on one side and hard baked to form a protective layer on the ground conductor. Photoresist was then spin coated on the second side, exposed to ultraviolet light under the mask of Fig. C.3b (Appendix C), developed, and immersed in a bath of ferric chloride and hydrochloric acid, which etched the exposed copper (Fig. 3.13a).

The excess material was precisely trimmed from the substrate with a wafer saw (Diamond Touch Technology) using the patterned cross hairs to align the blade (Fig. 3.13b). The photolithographic process was then repeated for the ground conductor (Fig. 3.13c) using the mask of Fig. C.3c, after which the two individual structures were separated with the wafer saw.

Fabrication of the inverted patch structure started with cleaning a single side-polished 500 μm-thick crystalline quartz wafer (obtained from University Wafer,

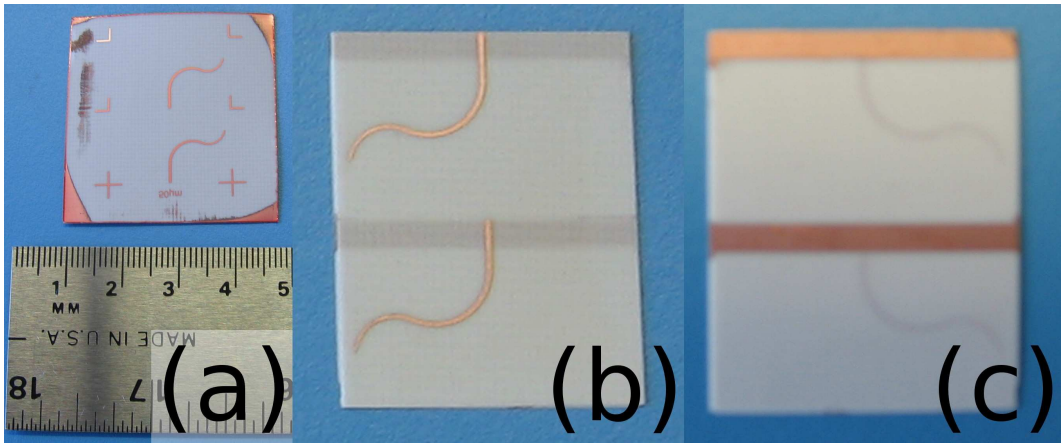

Figure 3.13: Rogers RO4003c substrates of the circular patch resonator during various stages of construction. After etching the signal layer (a), excess material is precisely removed with a wafer saw (b), allowing the exterior dimensions to be aligned to the mask during the photolithographic process used to pattern the ground layer (c). The substrates were separated with a wafer saw upon completion of patterning.

Boston, Massachusetts) in a piranha solution. Approximately 1.2 μm of copper was sputtered onto the polished side of the wafer that had been covered in a few nanometers of sputtered titanium to aid adhesion. Adequate smoothness of the sputtered copper was confirmed visually and with the Alpha Step surface profiler. Photoresist was spin coated onto the copper and patterned with the mask of Fig. C.3a. The unprotected copper was etched with ammonium persulfate, exposing the underlying adhesion layer, which was subsequently removed with a buffered solution of hydrofluoric acid (Fig. 3.14a). The individual structures were were separated from the wafer using the wafer saw, where the cross hairs were once again used for alignment. Prior to this step, a thick layer of protective photoresist ($\sim$2 μm) was spin coated onto the wafer and hard baked. Upon removal of the photoresist, a 25 nm-thick layer of polyvinyl alcohol was spin coated on each sample, where the

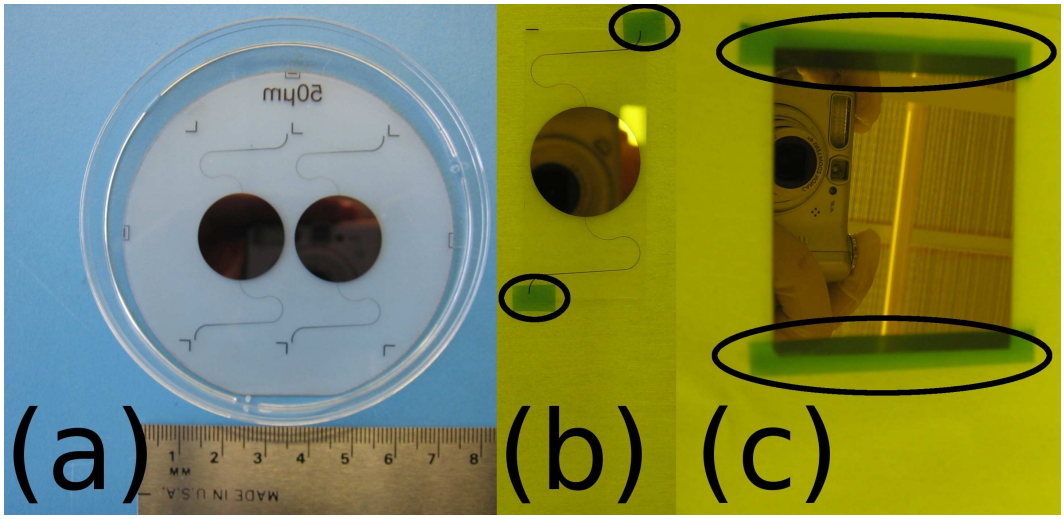

Figure 3.14: Signal and ground structures of the circular patch resonator. The signal structures were fabricated by sputtering copper onto a quartz wafer, which was then patterned with photoresist and etched (a). Individual samples were cut from the wafer using a wafer saw (b), and a ground plane was prepared by sputtering copper onto a flat glass plate (c). A 25 nm-thick layer of polyvinyl alcohol was then spin coated onto each sample, where regions requiring subsequent electrical connection were temporarily covered with self-adhesive tape (shown in circles) to prevent coverage.

terminal region of each microstrip line was protected with tape to prevent coverage that would inhibit the formation of an electrical connection. The samples were then rubbed with the buffing machine using the parameters developed §3.5, after which a felt pen was used to place a mark in a peripheral region indicating the direction of rubbing.

The ground structure was prepared in a similar manner. A rectangular slab (63 mm × 50.8 mm × 1.5 mm) was cut from a larger slab of soda-lime glass and, with the exception of photolithography, subject to the same processing used in the fabrication of the inverted patch structure.

The components were assembled in several steps. The two feed-line structures were placed downside-up on a flat aluminum plate and pressed flush against a steel bar and a silicon spacer that was cut to a precise size using the wafer saw (Fig. 3.15). The copper sections of the feed-line structures were then fixed to the aluminum plate with tape, which was carefully placed only on the structures' copper strips, ensuring that remaining surfaces were free of obstruction. The steel bar was then

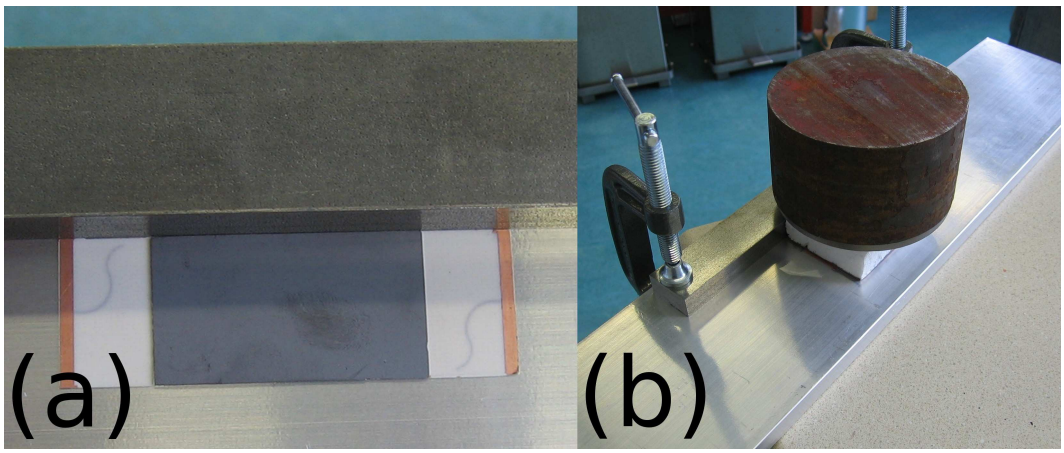

Figure 3.15: Construction of the circular patch resonator. The two Rogers RO4003c substrates were were placed on a flat aluminum plate and positioned to be flush with a steel bar and precisely cut silicon spacer (a). The ground-plane structure was then connected to the Rogers substrates using an epoxy (b).

set back 14 cm and clamped to the aluminum plate. A minimal amount of epoxy (LePage #11 Regular Epoxy Glue) was evenly distributed over the exposed surfaces of the feed-line structures. The ground structure, oriented downside-up, was then carefully placed on the feed-line structures and pressed flush against the steel bar. Small adjustments were made to the position of the ground-plane structure to eliminate gaps between adjacent ground conductors. The epoxy was allowed to set under the pressure of a 3.4 kg steel block, whose weight was evenly transfered to the structure by small Styrofoam pads placed directly over the epoxied surfaces. After the epoxy had hardened, the structure was placed right-side-up. A very small amount of epoxy was placed on the exposed surfaces of the Rogers substrates, upon which the superstrate was then carefully placed. Small adjustments to the position of the superstrate were made in order to ensure that the microstrip traces were aligned. An attempt at applying a compressive force was abandoned after it was found to result in lateral movement of the superstrate. The same epoxy was used to seal one side of the open resonator. As capillary action draws liquids into the cell, the epoxy was allowed to thicken for approximately one hour prior to its application. Electrical connections of the ground planes and microstrip traces were formed using a two-component silver epoxy (Epo-Tek H20E), which required the structure to be baked at 80 °C for 3 hours. The position of the quartz superstrate above the ground structure was then measured with a depth gauge. Measurements were taken in five locations (in the center and at each of the four corners) with a resolution of approximately 2 μm. The final step involved the connection of an aluminum heat sink to the underside of the ground structure. Thermal grease was spread on each of the mated surfaces, which were bonded with a small amount of fast-setting epoxy (LePage 5 Minute Epoxy Glue) that was applied near the edges.

The completed structure (Fig. 3.16) was mounted in a test fixture (Anritsu

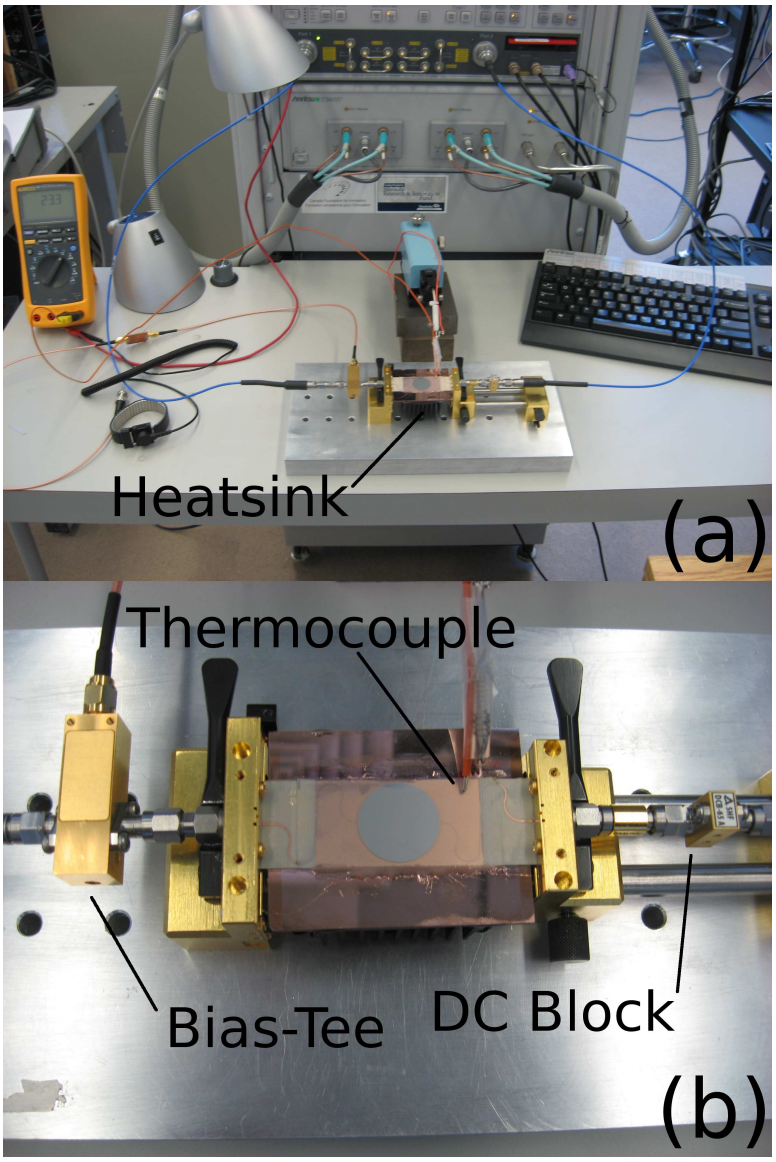

Figure 3.16: Experimental setup of the circular patch resonator (a) and a closeup of the resonator (b).

Model 3680) and its scattering parameters were measured using a calibrated network analyzer (Anritsu Lightning Model 37397D). Measurements were conducted prior to filling the resonator with BL006 and afterwards, where those involving the unfilled structure were used to confirm the validity of the HFSS simulation. The response of the scattering parameters to a range of applied voltages was measured

for a temperature of 23 °C. The structure was also heated to the clearing point of BL006 in an attempt to measure its isotropic permittivity. Measurements were taken for various bias voltages between 0 Vpp and 20 Vpp. In each case, a period of five minutes elapsed between the application of a given voltage and the onset of measurement, allowing the liquid crystal to assume a steady-state molecular configuration. This was approximately one or two orders of magnitude greater than the time required for the real-time scattering parameters (displayed by the network analyzer) to visibly stabilize.

3.7 Microstrip Photonic Bandgap Device Prototype

This section details the design and fabrication of a tunable quasi two-dimensional microstrip test structure. The aim of the design was to produce a test device that both possesses some inherent utility, and also avails the experimental characterization of the electromagnetic properties of a tunable two-dimensional microwave photonic crystal. While designed to physically accommodate a liquid crystal material, the first device was fabricated for the sole purpose of evaluating its adequacy as a test structure. It was therefore constructed and tested without a liquid crystal material in order to limit the number of experimental variables, which would otherwise confound the interpretation of measurements.

3.7.1 Design

The device was designed in accordance with the requirement for two closely spaced conductors, which is readily shown to be compatible with a two-dimensional elec-

tromagnetics wave problem that supports photonic crystal phenomena. In a homogeneous and source-free medium between the plates, the steady-state Maxwell equations yield the Helmholtz equation

$$\left(\nabla^2 + k^2\right)\mathbf{E} = \mathbf{0}. \tag{3.48}$$

where $k = \omega\sqrt{\mu_0\epsilon_0}$ and the z-axis is normal to the plates. The local properties of this set of three equations in a parallel plate environment may be investigated by neglecting the boundaries in the x- and y-directions. Using the ∇^2 operator from [42] and expressing the E_x (or E_y) component through separation of variables in cylindrical coordinates results in

$$\begin{aligned} &\left(\nabla^2 + k^2\right) E_x\left(x, y, z\right) = 0 \\ &\left(\frac{1}{\rho}\frac{\partial}{\partial\rho}\left(\rho\frac{\partial}{\partial\rho}\right) + \frac{1}{\rho^2}\frac{\partial^2}{\partial\phi^2} + \frac{\partial^2}{\partial z^2} + k^2\right) E_x\left(\phi, \rho, z\right) = 0 \end{aligned} \tag{3.49}$$

where

$$E_x\left(\rho, \phi, z\right) = E_{xr}(\rho)E_{x\phi}(\phi)E_{xz}(z) \tag{3.50}$$

Note that in general these solutions must be combined with those of E_y and E_z in order for $\nabla \cdot \mathbf{E} = 0$ to hold. The PEC boundaries constrain E_{xz} to the form

$$\begin{aligned} E_{xz}\left(z\right) &= \sin\left(k_{xz}z\right) \\ &= 0|_{z=0,h} \end{aligned} \tag{3.51}$$

where h is the spacing between the plates and $k_{xz} = \pi/h$ is the smallest nontrivial value satisfying this relation. The solution to the radial component of (3.49) is

given by

$$E_{xr}(\rho) = A_n J_n(k'\rho) + B_n Y_n(k'\rho) \tag{3.52}$$

where J_n and Y_n are the Bessel functions of the first and second kind, respectively, and

$$k'^2 = k^2 - k_{xz}^2 \tag{3.53}$$

When h is very small, balancing (3.53) for a real value of k requires that k' be imaginary. Consequently, the solutions of (3.52) become evanescently decaying and growing (where the coefficient of the latter term is set to zero to discard solutions of infinite energy), such that the E_x and E_y components of the field decay exponentially from a given disturbance that produces these fields. Under such conditions, only E_z is relevant and the two-dimensional scalar problem corresponding to the TM case

$$\left(\nabla_{2\mathrm{D}}^2 + k^2\right) E_z(x,y) = 0 \tag{3.54}$$

may be recovered by setting $E_{zz} = 1$, which is required to satisfy the zero divergence condition.

While (3.54) applies to problems characterized by a homogeneous medium, rewriting k as a function of position (assuming that μ_r remains constant),

$$\left(\nabla_{2\mathrm{D}}^2 + k(x,y)^2\right) E_z(x,y) = 0 \tag{3.55}$$

enlarges its scope to include those of inhomogeneous media and in particular those of a photonic crystal nature. For example, $k(\mathbf{r})$ may be written as $k(\mathbf{r}) = \omega\sqrt{\mu_0\epsilon_0\epsilon_r(\mathbf{r})}$, where $\epsilon_r(\mathbf{r})$ is given by (2.3) of §2.1.1. Analysis involving parallel plate structures of finite extent (Fig. 3.17) may be facilitated considerably by approximating the boundaries as perfect magnetic conductor (PMC), the accuracy of which is improved

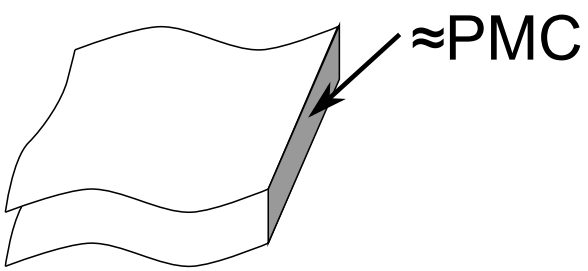

Figure 3.17: Approximate perfect magnetic conductor (PMC) boundary at the periphery of a parallel plate structure.

for thinner structures (small h). The origins of this approximation rest with the assumption that charge is limited to the inner surfaces of the structure and that the normal current vanishes at the boundaries due to the dominance of attractive forces between opposite charge on the opposing plates [3]. As a result of this simplification, (3.55) becomes a straightforward modal problem endowed with Neumann boundary conditions.

The experimental evaluation of realized photonic crystals cannot probe Bloch modes directly, as in the strictest sense, these modes are only defined for structures of infinite extent. The coupling between the eigenmodes of a finite crystal and an incident field may also be nontrivial and require careful consideration. Nonetheless, experimentally obtained scattering data from a photonic crystal of finite size may still provide considerable information on the band structure and the presence of bandgaps [2, 31–33].

Perhaps the most elementary investigation of scattering involves measuring the transmitted and reflected fields produced by a plane wave that is normally incident on a finite slab of material whose edges fall upon the crystal planes. For a two-dimensional crystal possessing a square lattice, this corresponds (approximately) to probing the Γ–X portion of a standard dispersion diagram. When the slab is sufficient in width and the incident field is spatially localized (such as a Gaussian

beam), it may be modeled as a stack of diffraction gratings (Fig. 3.18), whose electromagnetic characteristics are strongly influenced by the lateral translational invariance of the material. This modeling approach is discussed in considerable detail in Appendix B.

The experiment described in the foregoing discussion is readily performed in a parallel plate setting, where reflections arising from PMC boundaries may be exploited to simulate a diffraction grating environment. A simple structure whose electromagnetic characteristics are similar to those of a stack of diffraction gratings may be constructed with a single scattering element per row (Fig. 3.19). In the absence of scatterers, this arrangement of planar conductors is known as a parallel plate waveguide (a transmission-line in the y-direction), supporting the TM modes

$$E_z^n = A_n \cos\left(\alpha_n x\right) e^{i\pm\beta_n y} + B_n \sin\left(\alpha_{n+1/2} x\right) e^{i\pm\beta_{n+1/2} y} \tag{3.56}$$

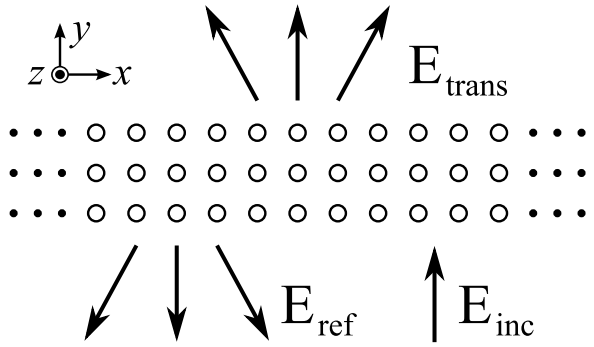

Figure 3.18: Three-layer photonic crystal slab subject to illumination by an incident plane wave ($\mathbf{E}_{\text{inc}}$), which is in plane and normal to the structure. While the structure depicted comprises only three rows of scatterers, its extent in the x-direction is assumed to be sufficient for translational invariance to shape its electromagnetic properties.

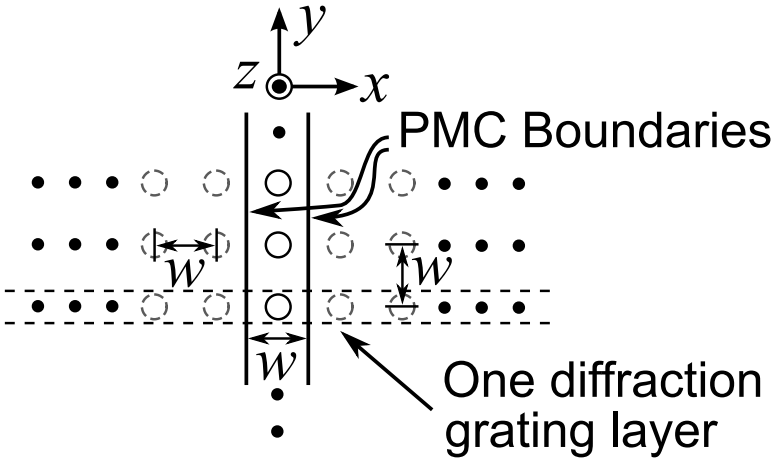

Figure 3.19: Top view of a structure containing only a single scattering element per row. The dashed circles are the reflections/images of the disks looking into the PMC boundaries. The 2D lattice of these disks may be treated as a periodic array of diffraction gratings.

where

$$\alpha_n = \frac{2\pi n}{w}$$
$$\beta_n = \sqrt{k^2 - \alpha_n^2} \tag{3.57}$$

for $n \in \mathbb{N}_0$. Note that these modes are distinct from the conventionally-defined TM modes of a parallel plate structure [51] and are easily verified to be solutions of (3.54) that satisfy the PMC boundary conditions. Note that all but a few modes near n are evanescent, i.e. non-propagating. To ensure that electromagnetic activity does not extend to higher order modes, the combination of maximum operating frequency $f_{\max}$ and waveguide thickness h must satisfy

$$f_{\max} < f_c = \frac{c}{2h\sqrt{\epsilon_r}}. \tag{3.58}$$

where c is the speed of light in vacuum and f_c is the cutoff frequency of the first higher order mode(s). Terms of (3.56) may be combined to form an expansion of an arbitrary field in any homogeneous region between the disks. Similarly, the field

in homogeneous regions between diffraction gratings may be expressed as a sum of the terms [57]

$$E_z = \frac{C_n e^{i(\alpha'_n x \pm \beta'_n y)}}{2} \tag{3.59}$$

where

$$\begin{aligned} \alpha'_n &= \frac{2\pi n}{w} + \alpha_0 \\ \beta'_n &= \sqrt{k^2 - \alpha_n^2} \end{aligned} \tag{3.60}$$

and α_0 is the x component of the wavenumber of an incident plane wave that produces these fields. The modal expansion of the parallel plate structure is clearly subsumed by that of the diffraction grating, and its terms may be recovered by the relations

$$\begin{aligned} A_n &= C_n + C_{-n} \\ B_{n+1/2} &= -i\left(C_{n+1/2} - C_{-n-1/2}\right) \end{aligned} \tag{3.61}$$

which corresponds to a symmetrically/antisymmetrically illuminated diffraction grating whose incident fields are restricted such that $-\alpha'_{-n} = \alpha'_n = \alpha_n$, which may be attained by setting $\alpha'_0 = 0$. As both the material and the incident field exhibit mirror symmetry about $x = \pm w/2$, this restricted diffraction grating problem also satisfies the PMC boundary conditions, both between and within layers.

A particularly convenient regime of operation is given by

$$f < f_c^1 = \frac{c}{w} \tag{3.62}$$

where f_c^1 is the cutoff frequency of the first even harmonic ($n = 1$). Where the connected apparatus also possesses symmetry about $x = 0$, the entire problem is symmetric, and the B_n coefficients of (3.56) are zero. In this case, f_c^1 gives the frequency beneath which propagating modes are limited to the fundamental

TM mode, and the incident, reflected, and transmitted fields may be represented by scalar quantities, affording a particularly simple interaction with a two-port network analyzer.

Connection to measurement equipment brings forth two additional design issues. The first arises from the fact that, unlike a parallel plate waveguide, the coaxial lines used in the connection of test equipment are not balanced transmission lines. This is most easily remedied by replacing the parallel plate waveguide with a microstrip line (Fig. 3.20). This substitution leaves the modal characteristics unchanged due to the mirror symmetry induced by the ground plane for the modes under consideration. The second issue concerns the coaxial to microstrip transition and the impedance matching therein. The latter is readily implemented in the form of microstrip tapers, while the former depends on the frequencies involved and is discussed in further detail for specific devices.

The structure depicted in Fig. 3.20 forms the basis of a physically realized device. The first bandgap was chosen to lie within the frequency span of 0–7.5 GHz, as the resultant dimensions facilitated manual fabrication. This choice does not disqualify experimentally-derived characterizations from applying to structures of smaller size, as the frequency-length scaling property of photonic crystals ensures that a scaled replica will possess nearly identical electromagnetic characteristics

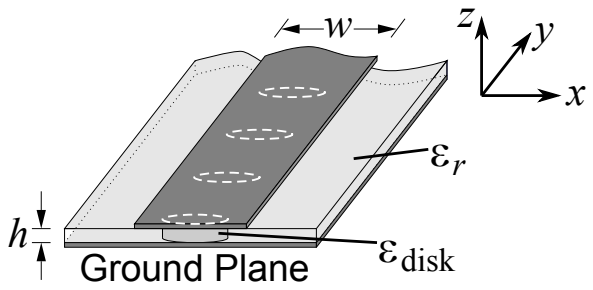

Figure 3.20: Microstrip line with dielectric disk placement overlaid. The y boundaries are $z = 0$ and $z = w$. Note that $\epsilon_r = 1$ for the prototype structure.

(scaled in frequency) [33]. Sapphire was chosen as the disk material because it exhibits very low loss and was commercially available in the required dimensions from Silian Tech Company Ltd., Vancouver, British Columbia. A parametric simulation of the band structure was performed using the Rayleigh multipole method (Appendix B) in order to approximately identify the ratio of disk radius to lattice constant associated with a maximally wide bandgap (Fig. 3.21). As a result of these simulations, the lattice constant and microstrip width were chosen to be 19.625 mm, while the disk radius was chosen to be 3.925 mm (20% of the period).

The band structure of a square lattice characterized by these dimensions is shown in Fig. 3.22. Note that because α is limited to multiples of π, only the paths Γ–X and Y–M apply. As a square lattice of circular disks is described by the C_{4v} point group, reflections about $y = x$ and $y = -x$ leave the lattice unchanged, thereby allowing Y–M to be substituted with X–M [31]. Consequently, such a quasi two-dimensional structure shares the first two sections a of standard band diagram with its fully two-dimensional counterpart. A thickness of 0.5 mm was selected as a

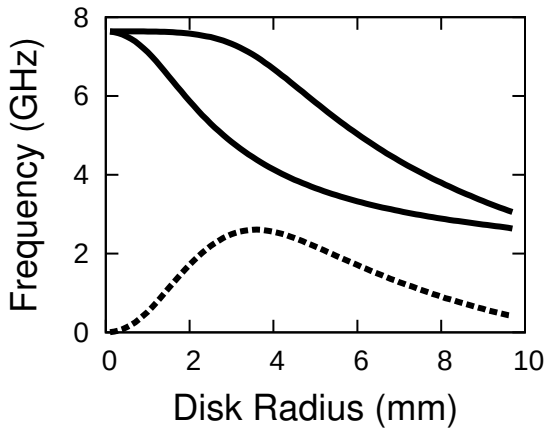

Figure 3.21: Bandgap at X in the irreducible Brillouin zone versus disk radius for a lattice constant of 19.625 mm. The solid curves delineate the bandgap edges, and the dashed curve represents the width of the bandgap (i.e. the difference between the bandgap edges). Note the maximum near a disk radius of 4 mm.

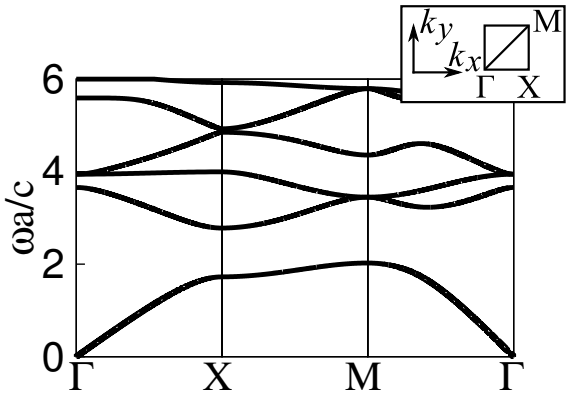

Figure 3.22: Simulated band diagram of the photonic bandgap structure described by Fig. 3.19. The present work is concerned with symmetric incidence (Γ–X). The X–M portion corresponds to antisymmetric incidence and is not considered here.

compromise between minimizing the effect of the fringing field and minimizing the length of the impedance matching tapers. Note that for $\epsilon_r = 1$, this value satisfies (3.58) for frequencies up to 300 GHz, which is well above the bandgap shown in Fig. 3.22.

The transmission coefficient (S_{21}) was found by using the Rayleigh multipole method to simulate the finite structure as a stack of 10 individual diffraction gratings (Fig. 3.23). These results were confirmed with Lumerical FDTD, a finite-difference time-domain full-wave solver. The latter was carried out on a uniform Cartesian grid of 51×1005 nodes, where the boundaries at $z = 0, h$ were PEC and those at $x = -w/2, w/2$ were PMC. The mesh was terminated in the y-direction with absorbing boundaries. Note the good agreement save for some discrepancy at low frequencies (possibly due to the absorbing boundaries).

3.7.2 Construction

The structure described in the preceding sections was fabricated in three stages. The first step involved preparing a ground plane from a 5.1 cm × 34.2 cm steel

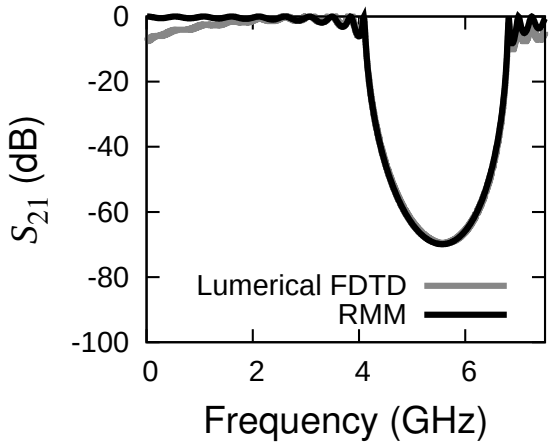

Figure 3.23: Simulated S_{21} magnitude of the structure shown in Fig. 3.20. The 10-disk structure possesses a lattice constant of 19.625 mm and a disk radius of 3.925 mm.

plate. The plate was visually inspected for planarity and was chosen to be ∼2 mm in thickness (and thus rigid). Three holes were drilled in each end for the coaxial end launchers and two supporting bolts. In order to minimize the effect of the transitions, the diameters of the center holes were chosen to match the outer conductor diameter of the coaxial end launchers, which were subsequently fastened to the steel plate.

The second step involved preparation the microstrip line, sapphire disks, and polyethylene backside. Adhesive copper tape (Venture Tape, 1697AT) was cut to the dimensions shown in Fig. 3.24 and affixed to a 0.5 mm-thick polypropylene sheet possessing planar dimensions identical to those of the steel plate. In order to allow connections to the subminiature A (SMA) pins, two small holes were cut out of the tape at each end, underneath which two larger holes were previously drilled in the polypropylene sheet to allow access with a soldering iron. Two polypropylene spacers were then affixed to the backside on either side of the copper tape using a cyanoacrylate adhesive. Finally, the sapphire disks were bonded to the exposed

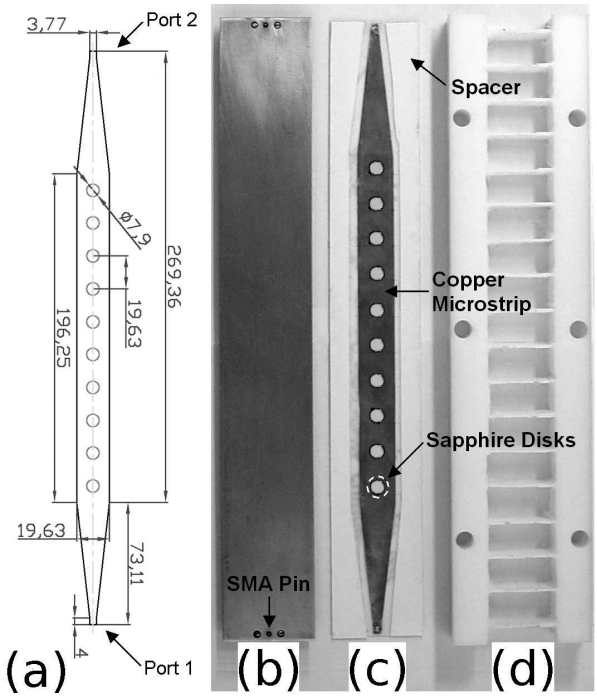

Figure 3.24: Plan view of the fabricated microstrip PBG structure (a) and photograph of device including: ground plane with SMA connectors fastened underneath (b), microstrip, sapphire disks, and spacers resting on polypropylene sheet (c), and polyethylene board used to minimize leaky modes (d). All dimensions are in millimeters. The microstrip width equals the disk spacing.

side of the copper tape using the same glue. In both cases, a firm compressive force was applied to the parts that were bonded, and the adhesive was applied as sparingly as possible.

The third and final step consisted of constructing the rigid portion of the backside using a flat polyethylene slab. This material was chosen for its low relative permittivity ($\epsilon_r = 2.26$ [201]), which was further reduced by removing regularly spaced cuboids, leaving thin ridges for support. The complete structure was assembled by attaching the microstrip/backside and steel plate assemblies, which involved soldering the copper tape to the SMA pins. The resultant structure was clamped between two flat and rigid boards using the polyethylene slab as a spacer to ensure an air gap directly over the backside.

The completed structure was tested using a vector network analyzer (Anritsu Model 360B), which was calibrated using a short-open-load-thru (SOLT) calibration kit.

3.8 Liquid Crystal Photonic Bandgap Device

3.8.1 Design Considerations

While the microstrip structure has demonstrated its suitability for the purpose of evaluating a quasi two-dimensional photonic bandgap structure (§4.3), several improvements may be identified. The first of these involves the uniformity of thickness of the waveguide structure. Using the construction methods discussed, there is likely some variation in local thickness, which may give rise to a non-uniform waveguide impedance. This hypothesis was formed after observing some variation in the measured S-parameters in response to adjusting the tension of the bolts. This may be remedied by using a more rigid supporting structure. In the previous experiment, the supporting structure was chosen to reduce energy on the backside of the waveguide. Reduction in the unwanted field may also be effected by using a wider structure, permitting the backside to be chosen from a greater selection of materials.

The second improvement concerns the transition from the coaxial lines to the device. The transition employed in the structure may be modeled using lumped elements (Fig. 3.25). For a given set of materials and geometries, this transition performs progressively worse at higher frequencies and is likely partially responsible for the attenuation observed above the bandgap. This may be remedied by using a microstrip test fixture, which carefully controls the impedance of the transition,

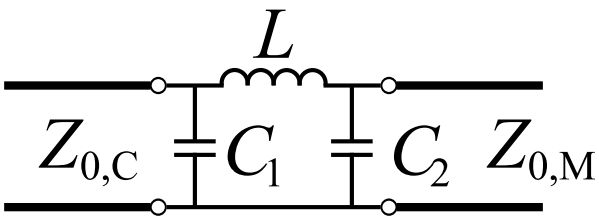

Figure 3.25: Lumped element circuit equivalent of a transmission line connection consisting of a coaxial line ($Z_{0,\mathrm{C}}$) joined to a microstrip line ($Z_{0,\mathrm{M}}$) at a 90° angle [51]. The lumped element parameters, C_1, C_2, and L depend on particular geometries and materials present in the junction.

primarily by minimizing the size of the critical dimensions. Moreover, as such fixtures permit the free connection and removal of samples, a calibration kit may be used to significantly lessen the remaining effects of the transition.

The last improvement concerns a minimization of the effect of the fringing field (the non-ideality of the PMC boundaries), which is reduced for smaller values of h and larger values of w. The extent to which the structure may be made thinner depends on a few issues. From (3.41) it may be seen that conductor losses increase inversely with thickness. While this may pose a problem in practical applications, in the present work this effect may be accounted for with full-wave simulations. The issues of impedance matching and fabrication cause significantly more difficulty. Maintaining a port impedance of 50 Ω while decreasing the substrate thickness requires that the width of the microstrip line be commensurately reduced in accordance with [51]

$$\begin{aligned} Z_0 &= \frac{60}{\sqrt{\epsilon_{\mathrm{eff}}}} \ln\left(\frac{8h}{w} + \frac{w}{4h}\right), && w/h \leq 1 \\ &= \frac{120\pi}{\sqrt{\epsilon_{\mathrm{eff}}}\left[w/h + 1.393 + 0.667 \ln\left(w/h + 1.444\right)\right]}, && w/h \geq 1 \end{aligned} \tag{3.63}$$

Beneath a certain width, the electromagnetic characteristics of the coaxial to microstrip transition may become compromised. For example, if the width of the

probe exceeds that of the microstrip line, its position over the substrate will result in a large shunt capacitance. Hence, the smallest practical width that may be used is on the order of 400 μm. Fabrication challenges result from the fact that the acceptable tolerance in h is proportional to thickness. For very thin structures, the manual placement of the backside and presence of the adhesive become significant sources of thickness variation. Collectively, these issues illustrate the design trade-offs between substrate thickness and fringing field, and they have been thoroughly considered in the design of the liquid crystal structure presented in the subsequent section.

3.8.2 Design

The design of the earlier prototype photonic bandgap structure was used as the basis for the liquid crystal-based device. In accordance with the discussion of the previous section, a thinner dielectric thickness was employed. As the use of the universal test fixture requires a solid substrate, the device was designed as three primary components: a parallel plate structure containing the liquid crystal and silicon scattering elements (squares), and two microstrip taper structures based on a conventional microwave substrate. These sections are connected mechanically and electrically.

In conjunction with the design of the resonator, the high-frequency 203 μm-thick Rogers RO4003c board ($\epsilon_r = 3.55 \pm 0.05$) was selected as the substrate for the microstrip taper structures. As a result of its thickness and dielectric constant, a 50-Ω microstrip line fabricated from this substrate possesses a trace width of 450 μm, a value close to the minimum that is practically attainable. Moreover, its dielectric constant is very near that of BL006 ($\epsilon_r =$ 2.6–3.1), resulting in minimal

reflections of waves at the interface between the liquid crystal and microstrip taper dielectric.

The backside was chosen to be crystalline quartz ($\epsilon_r = 4.6$ [202]) due to its low dielectric constant, rigidity, and earlier results showing that quartz surfaces yield high quality sputtered films that are specularly-reflective, a quality required of surfaces on which alignment layers are deposited. Undoped silicon ($\epsilon_r = 11.6$ [202]) was selected in favor of sapphire as the material of the dielectric scattering elements to partly compensate for a reduction in dielectric contrast arising from the use of BL006. The individual components of the device are shown schematically in Fig. 3.26.

The final dimensions were chosen in the course of balancing several competing requirements. The lattice dimensions (and resultant frequency of the bandgap) were constrained by the accuracy of the manual assembly process. Numerical sen-

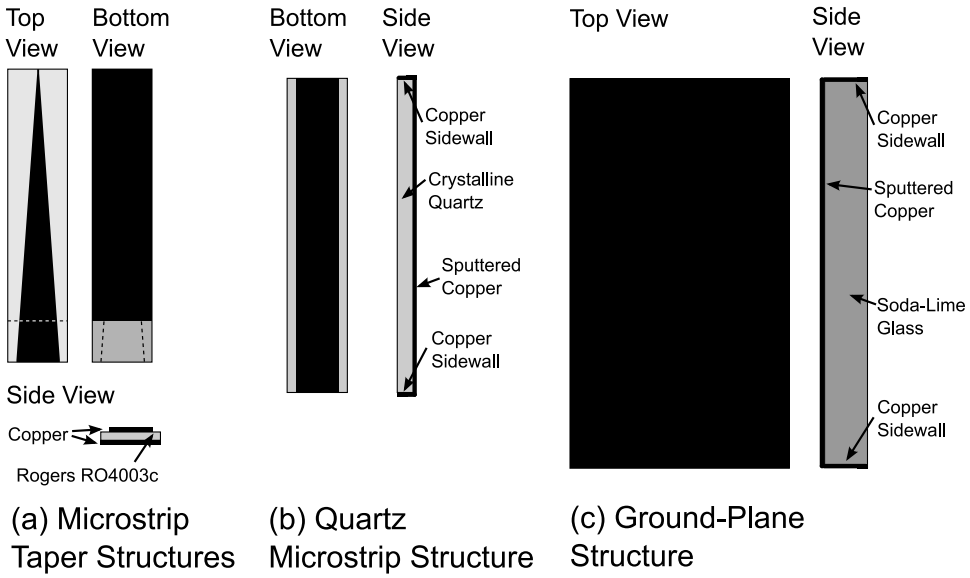

Figure 3.26: Individual components of the liquid crystal-based microstrip photonic bandgap device, where planar dimensions are to scale and copper is shown as black. The copper sidewalls at each end of the structures in (b) and (c) facilitate the formation of an electrical connection with silver epoxy.

sitivity analyses were conducted in order to identify a lattice geometry and size whose attendant electromagnetic response is robust in the presence of the assumed dimensional tolerances. As a result of these simulations, the lattice of the prototype structure was retained and the lattice constant was chosen to be one centimeter. The silicon scattering elements were chosen to be square, as this geometry is most easily realized with the wafer saw. The final trade-off concerned the size of the scattering elements, the number of unit cells, and the length of the impedance matching tapers. As the dimensions of the test fixture placed an absolute limit on the structure's total length, the sum of the lengths of the tapers and series of unit cells was fixed. Longer tapers yield less ripple and more uniform incident and reflected fields, while a greater number of scattering elements produce stronger attenuation in the stopband, which is also influenced by the size of the square with respect to the lattice constant. These requirements were balanced by selecting 5 mm, 67.5 mm, and 71.5 mm for the lengths of the squares, liquid crystal region, and tapers, respectively. The quartz backside was extended by 2 mm on each side of the conductor to facilitate modeling by ensuring that the fringing field interacted with the liquid crystal in a well-defined state. The aggregate construction is shown to scale in Fig. 3.27.

The quartz superstrate rests on each of the microstrip taper structures, which have a total thickness of 220 μm when the contribution of the copper signal layers is included. As the thickness of the realized squares was 190 μm, a gap of 30 μm resulted between the silicon squares and the upper conductor. The gap is significantly less than the planar dimensions, and an effective dielectric may be defined as

$$\epsilon_{\text{eff}} = \frac{\epsilon_1 \epsilon_2 \left(h_1 + h_2\right)}{h_1 \epsilon_2 + h_2 \epsilon_1} \tag{3.64}$$

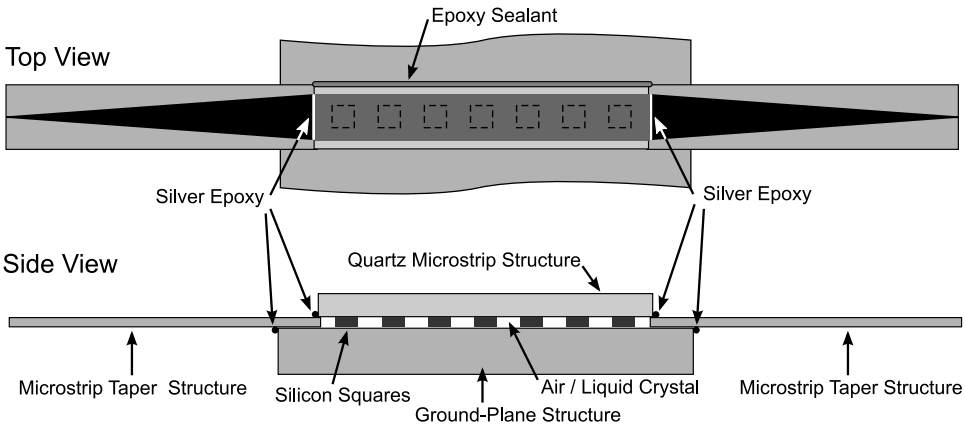

Figure 3.27: Drawing of the liquid crystal-based microstrip photonic bandgap device with square silicon scattering elements overlaid. Planar dimensions are to scale. Note that copper is shown as black.

where $h_1 = 190\ \mu$m, $h_2 = 30\ \mu$m, $\epsilon_1 = 11.6$, $\epsilon_2 = 2.62$ are the thicknesses of the silicon square and the gap (assumed to be filled with BL006), and dielectric constants of silicon and BL006, respectively. The liquid crystal in the gap was assumed to possess a planar orientation, as this alignment is favored by both the the silicon surface [116, 117] and the polyvinyl alcohol layer.

The band diagram associated with the structure's unit cell was computed for both the "on" and "off" states with the plane wave method (Fig. 3.28), using an effective dielectric constant of 7.91 for the squares. Finite-structure simulations were carried out with Ansoft HFSS 12 for the unfilled structure (Fig. 3.29) and each of the liquid crystal alignment states (Fig. 3.30 and 3.31). These simulations incorporated explicit representations of known loss mechanisms, including radiation, dielectric, and conductor losses, and utilized experimentally-derived complex permittivity values for BL006 (§4.2.3). The transmission coefficients associated with each alignment are plotted juxtaposed in Fig. 3.32, which shows considerable tuning of the bandgap.

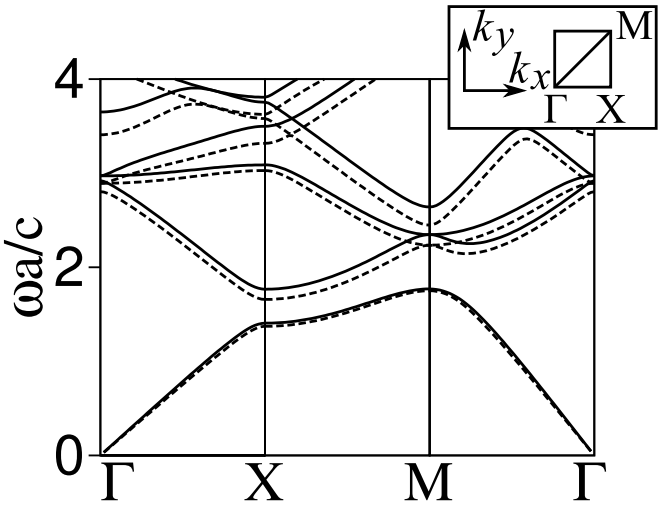

Figure 3.28: Band structure of silicon/BL006 photonic crystal as computed with the plane wave method. The solid and dashed lines correspond to the low and high permittivities of BL006, respectively. The photonic crystal comprises silicon squares (5 mm × 5 mm) in a square lattice (10 mm × 10 mm). The squares were assigned an effective permittivity of 7.91 to account for a difference of 15% between the thickness of the silicon squares and the spacing of the conductors (the void is assumed to be filled with BL006).

3.8.3 Construction

The construction of the liquid crystal photonic bandgap device followed the same general procedure as that of the circular patch resonator. The Rogers substrates, in various stages of preparation, are shown in Fig. 3.33.

Fabrication of the quartz superstrate was modified slightly in order facilitate electrical contact between the signal conductors. The additional step involved cutting the quartz wafer to the correct length prior to sputtering, resulting in the deposition of copper sidewalls at each end of the structure (Fig. 3.34). A 0.5 mm-thick undoped silicon wafer (obtained from University Wafer, Boston, Massachusetts) was thinned to approximately 0.2 mm in a heated solution of potassium hydroxide. Roughly 100 squares measuring 5 mm×5 mm were cut from the thinned wafer using the wafer saw. The thickness of each square was measured with a depth gauge to

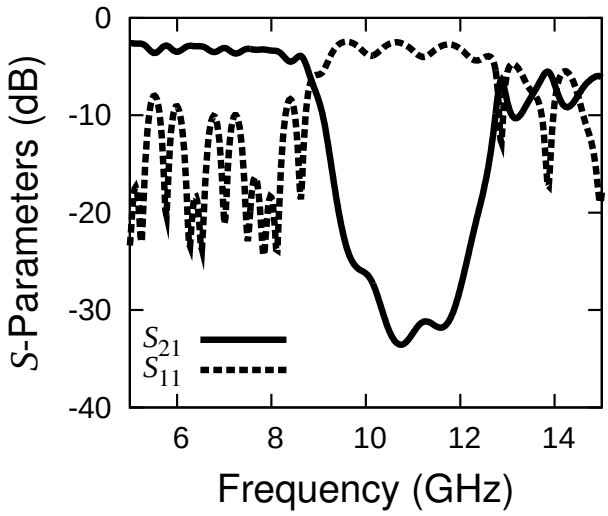

Figure 3.29: Simulated scattering parameter magnitudes of the entire unfilled photonic bandgap device depicted in Fig. 3.27. This simulation, conducted with Ansoft HFSS 12, includes losses due to radiation, the dielectric, and the conductors, where the model incorporates both ohmic losses and those due to surface roughness. The silicon squares were assigned the measured thickness of 190 μm and a dielectric constant of 11.6 [202], while the Rogers RO4003c substrates were assigned microwave properties that were specified by the manufacturer ($\epsilon_r = 3.55$, $\tan\delta = 0.0027$).

within approximately 2 μm. A variance of about 5 μm was found, indicating that the thinning process was somewhat non-uniform. The squares were then divided in accordance with their measured thickness; those whose thickness were closest to the mean (190 μm) were set aside for later use.

After gluing the microstrip taper and ground-plane structures, the selected silicon squares were adhered to the aggregate structure. This step was performed with an absolutely minimal amount of epoxy using a purpose-constructed square placement tool (Fig. 3.35), which allowed precise placement of the squares and protected the alignment layer from inadvertent scratches. The quartz superstrate was then placed on the squares and Rogers substrates using a pen whose tip had been wrapped in double-sided tape (in lieu of a vacuum pick and place tool). One corner of the superstrate was then epoxied to one of the Rogers substrates using the

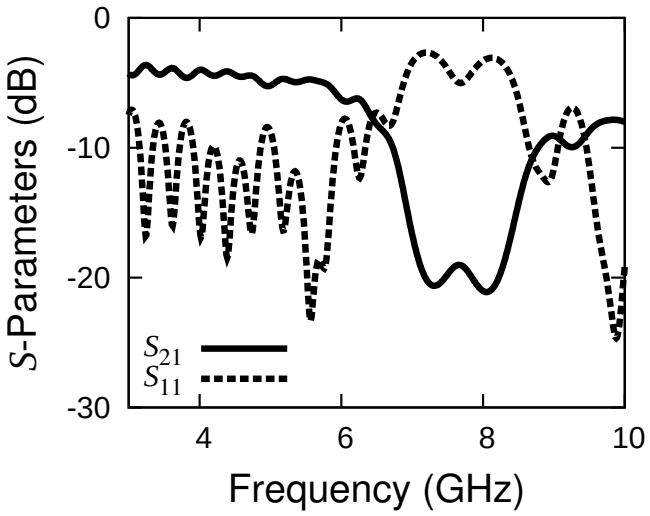

Figure 3.30: Simulated scattering parameter magnitudes of the entire photonic bandgap device depicted in Fig. 3.27 in the absence of an alignment field. This simulation was based on that of Fig. 3.29, where an experimentally-derived dielectric constant of 2.62 and loss tangent of 0.035 (Table 4.3) were used to describe the BL006 material in the simulation.

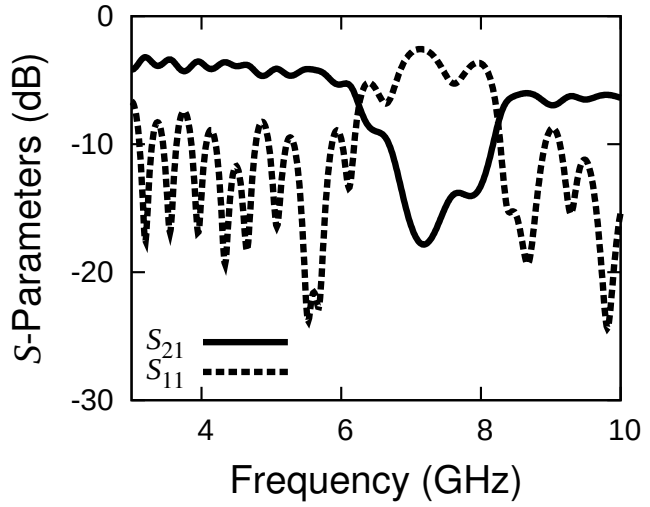

Figure 3.31: Simulated scattering parameter magnitudes of the entire photonic bandgap device depicted in Fig. 3.27 in the presence of an alignment field. Once again, an experimentally-derived dielectric constant of 3.11 and loss tangent of 0.007 (Table 4.3) were used to describe the BL006 material in the simulation.

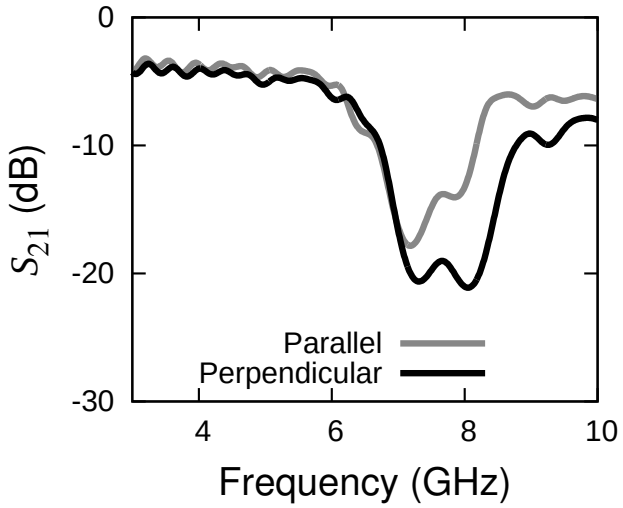

Figure 3.32: Simulated bandgap tuning of the linear silicon/BL006 photonic bandgap device manifested in the transmission coefficient (S_{21}) magnitude.

fast-setting epoxy, which, after about five minutes, allowed pressure to be applied to superstrate without risk of lateral movement. Epoxy was then similarly applied to the other corners of the superstrate, and a weight that rested on a segment of Styrofoam was placed on the structure. This approach, which employed a compressive force and restricted the application of epoxy to the sidewalls of the superstrate, prevented the excess superstrate height that was incurred in the construction of the resonator.

The final step involved the attachment of a supporting structure, which provided the rigidity necessary for installation in the universal test fixture (the Rogers substrate is very flexible). This was performed in two steps, the first of which involved gluing two rectangular segments of 1.5 mm-thick soda-lime glass to the underside of each microstrip taper structure using LePage 5 Minute Epoxy Glue. These spacers ensured that the Rogers substrate remained horizontal when the structure was placed on a flat surface. The second step consisted of gluing (using the same adhesive) a long strip of balsa wood of rectangular cross section to undersides of the

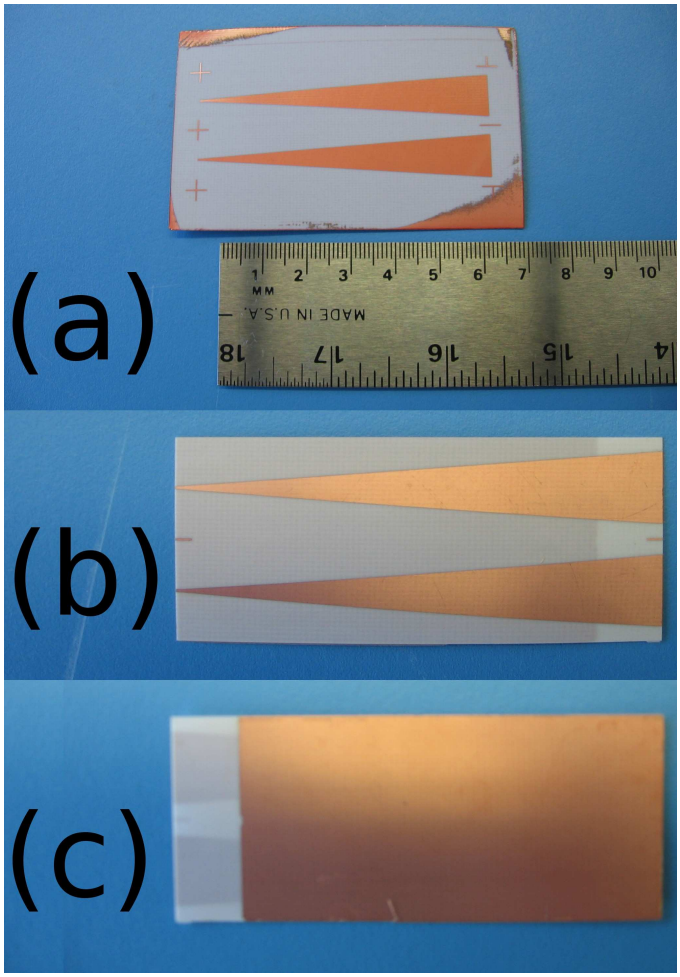

Figure 3.33: Rogers RO4003c substrates of the linear silicon/BL006 photonic bandgap device during various stages of construction. After etching the signal layer (a), the excess is precisely removed with a wafer saw (b), allowing the exterior dimensions to aid alignment in the photolithographic process used to pattern the ground layer (c). The substrates were detached with a wafer saw upon completion of the patterning.

spacers and ground-plane structure. The sizing and placement of the glass spacers and balsa wood were such that about 1 mm of the ground plane protruded from each port, allowing unobstructed access to the lower jaws of the test fixture that establish the ground contacts.

The completed structure (Fig. 3.36) was mounted in the test fixture, and its scattering parameters were measured using a calibrated network analyzer (Anritsu

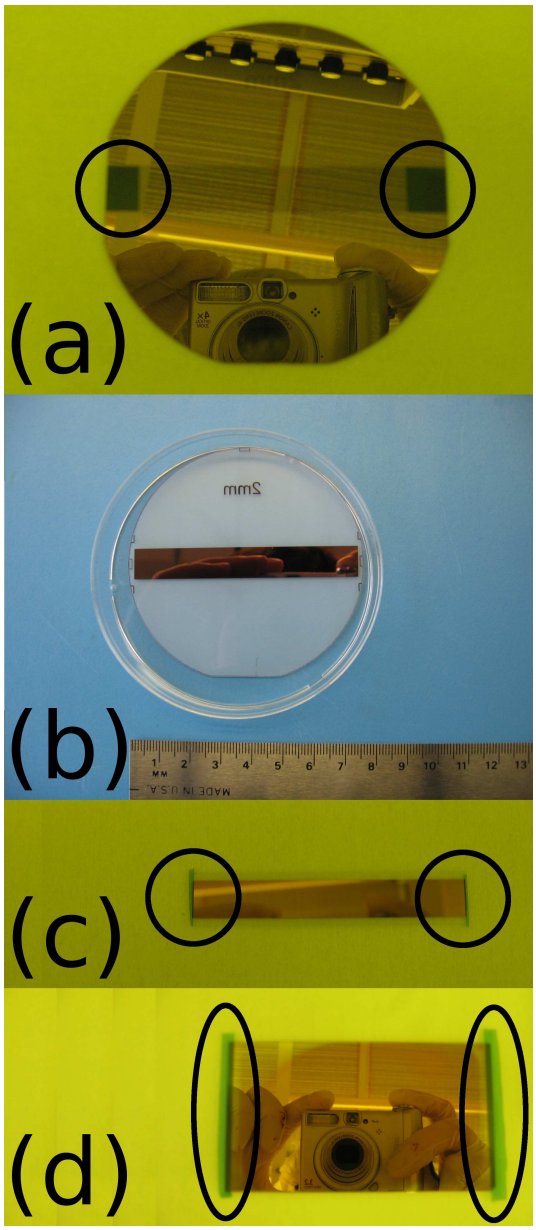

Figure 3.34: Signal and ground structures of the linear silicon/BL006 photonic bandgap device. The signal structures were fabricated by patterning the copper layer that was sputtered on a quartz wafer (a, b), which had previously been cut to the correct length, thereby resulting in the deposition of copper sidewalls. Samples were cut from the wafer using a wafer saw (c), and a ground plane was prepared by sputtering copper onto a flat glass plate (d). A 25 nm-thick layer of polyvinyl alcohol was then spin coated onto each sample, where regions requiring subsequent electrical connection were temporarily covered with blue tape (shown circled) to prevent coverage (c, d).

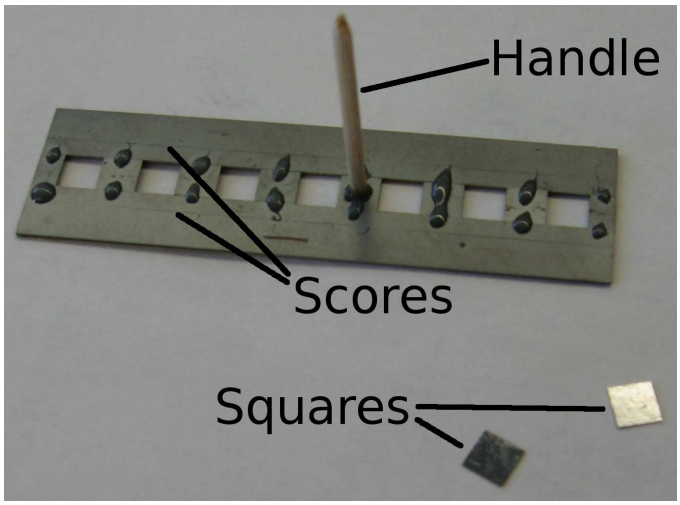

Figure 3.35: Placement tool for the accurate positioning of silicon squares. This tool was constructed from individual rectangles of varying size that had been cut from a 0.5 mm-thick silicon wafer using a wafer saw. Two narrow strips of tape were adhered to its underside and run lengthwise along each edge. These strips serve as spacers that prevent contact between the tool and the active region of the alignment layer. The scores that run lengthwise along the structure allow precise alignment of the tool with the signal conductors of the microstrip taper structures, thereby ensuring accurate lateral placement of the silicon squares.

Lightning Model 37397D). Measurements were conducted prior to filling the structure with BL006 and afterwards. The response of the scattering parameters to a range of applied voltages was measured for a temperature of 23 °C. Once again, a period of five minutes was allowed to pass between the application of a given voltage and the onset of measurement.

3.9 Network Analyzer Calibration

The microwave structures presented in the foregoing sections were experimentally evaluated using two-port network analyzers. The coaxial cables that connect the device under test to the network analyzer represented a potentially significant but readily-controlled source of error. Owing to the linearity of the system, connecting

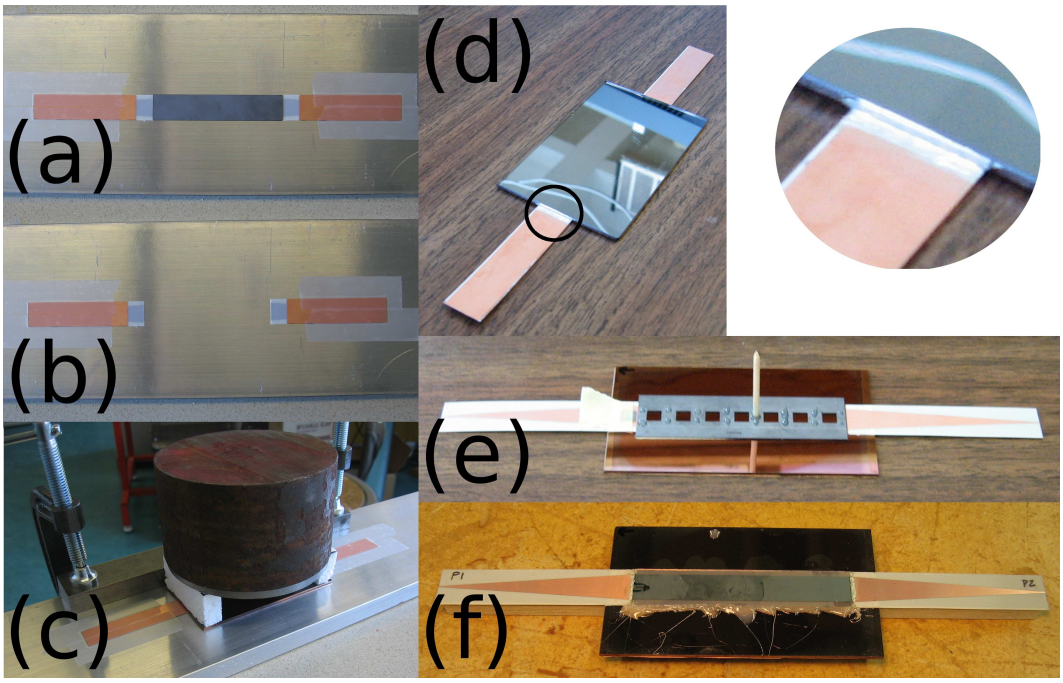

Figure 3.36: Assembly of the linear silicon/BL006 photonic bandgap device. The two Rogers RO4003c substrates were placed on a flat aluminum plate, positioned to be flush with a steel bar and precisely cut silicon spacer (a), and taped to the aluminum plate. The silicon spacer was removed (b), and the ground-plane structure was bonded to the Rogers substrates using an epoxy (c). Silver epoxy was used to electrically connect the grounds of the Rogers substrates to the glass ground-plane structure (d). A square placement tool (Fig. 3.35) was used to guide the placement of silicon squares and prevent inadvertent contact with the remainder of the alignment layer (e). The quartz superstrate was then placed over the silicon squares, epoxied, and electrically connected to the taper structures with silver epoxy. One side of the open structure was sealed with viscous epoxy, and the scattering parameters were measured. The structure was then filled with BL006 (f).

cables may be modeled as two-port networks described by 2×2 scattering matrices (Fig. 3.37). By measuring the scattering parameters of known loads and through sections, these matrices may be inferred and their effect subtracted from the measurements of the device under test.

A SOLT (Short-Open-Load-Thru) calibration kit (Wiltron Network Analyzer SMA/3.5 mm Calibration Kit, Model 3650) was used in the evaluation of the prototype photonic bandgap structure (§3.7). The calibration kit comprises three

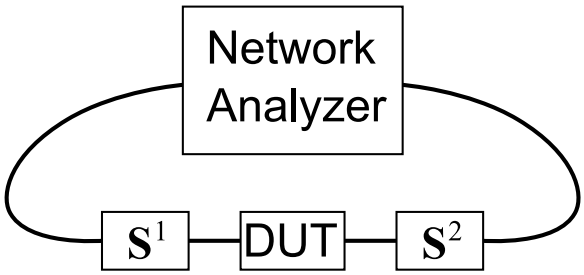

Figure 3.37: Coaxial connections modeled as two-port networks. A calibration finds the scattering matrix associated with each connection and applies a correction to the measured scattering parameters for the device under test (DUT).

coaxial-based terminations and a thru section, allowing compensation for the errors introduced by the lines. Note that this calibration does not compensate for reflections arising from the connection of the SMA end launcher to the microstrip line.

A 50-Ω microstrip thru-reflect-line (TRL) kit was designed and fabricated from Rogers RO4003c substrate using the photolithographic and etching processes described earlier (Fig. 3.38). The kit was used to calibrate the test fixture for measure-

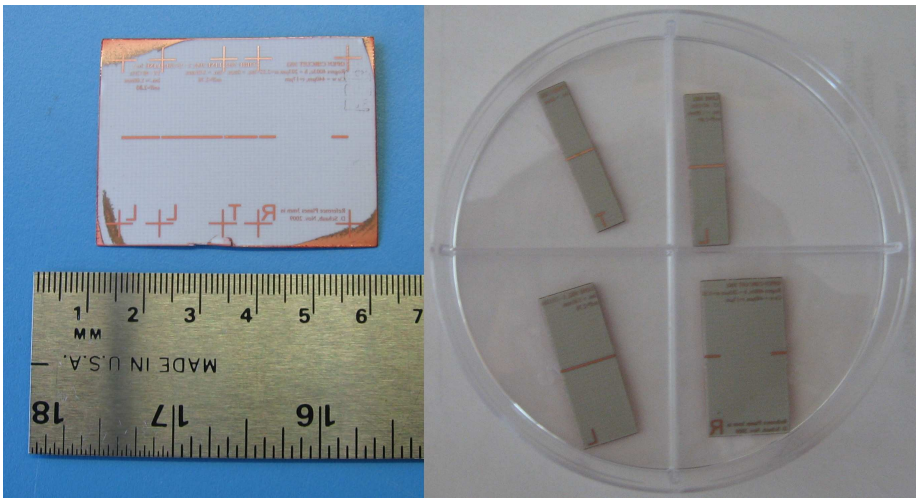

Figure 3.38: Fabricated 50-Ω thru-reflect-line microstrip calibration kit (Rogers RO4003c substrate). Dimensions were precisely controlled by using photolithographic techniques to pattern the signal layers and a wafer saw to cut individual sections to size.

ments involving the patch resonator and liquid crystal photonic bandgap structure. In addition to correcting errors that originated from the connections and cables, this calibration also removed the effect of the coaxial-microstrip transitions. The fabricated kit covered the frequency range of 3–40 GHz and comprised four sections: a thru line (zero electrical length), a reflection (open), and a two lines.

Chapter 4

Results

4.1 Spectral Transmission-Line Modeling Method

Numerical experiments were performed for several unit cells consisting of different geometries and materials in order to evaluate the accuracy and runtime characteristics of the algorithm. The simulated band diagrams and runtimes were compared with ones produced by the Rayleigh multipole, plane wave expansion, and time-marching TLM methods. With the exception of the Ansoft HFSS simulation, the data presented in this section were produced by single-threaded programs that were executed on a 2.4 GHz Intel Quad Core Duo processor with 4 GB of memory.

4.1.1 Confirmation of Accuracy

The first simulation involved computing the dispersion diagram for a benchmark test case consisting of a square lattice of sapphire disks ($\epsilon_r = 8.9$ [32]), which possess a radius of 20% of the lattice spacing (Fig. 4.1). The discretization of the unit cell

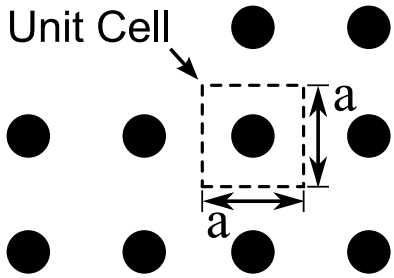

Figure 4.1: Overview of a two-dimensional photonic crystal possessing a square lattice. The white region represents the background dielectric (vacuum), while the dark disks correspond to sapphire ($\epsilon_r = 8.9$ [32]). The unit cell is contained within the dashed lines.

(Fig. 4.2) consists of a Cartesian mesh of 120×120 nodes. The resulting dimension of $\mathbf{S^I}$ (3.11) and $\mathbf{S^{II}}$ (3.15) is $72,000$. The fineness of the mesh ensures accuracy at higher frequency and significantly exceeds the mesh density of 10 nodes per wavelength. Such a fine discretization also minimized the "staircase" effect, which is the geometrical inaccuracy introduced by Cartesian approximations of curved boundaries.

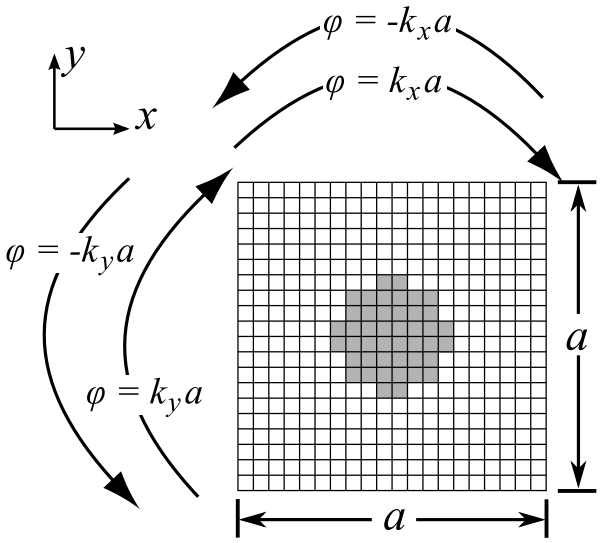

Figure 4.2: Unit cell discretized as a mesh of 20×20 nodes (coarsened from 120×120 to illustrate the discretization process). The arrows show the phase change sustained by pulses traversing the periodic boundaries.

The dispersion diagram was produced with the algorithm of §3.2.3 at 15 equidistantly-spaced points along each of the segments of the path Γ–X–M–Γ. The simulation carried out 100, 000 power method iterations and employed a Krylov subspace of dimension 250 for each point that was simulated in reciprocal space. The values of $\Omega a/c$ were 0.85, 2.55, 4.25, and 5.95. The values of these parameters strike a balance between runtime and accuracy and were found empirically by conducting several simulations. The simulated frequencies are plotted against a dispersion diagram produced by the Rayleigh multipole method in Fig. 4.3, and excellent agreement is observed.

During the simulation, the electric field configurations corresponding to the first three eigenmodes were recorded at the point $\mathbf{k} = (0, \pi/2a)$, which lies midway between Γ and X. The normalized eigenmodes are plotted as isovalue contours in Fig. 4.4 and are compared with those produced by Ansoft HFSS 11.1 (Ansoft Corporation, Pittsburgh, PA). The latter simulation was carried out on a mesh of 11,144 tetrahedra, arranged as a parallelepiped whose dimensions were 20 mm in the x-direction, 20 mm in the y-direction, and 0.5 mm in the z-direction. The

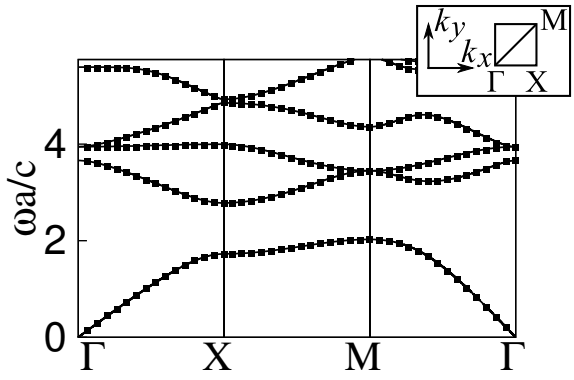

Figure 4.3: Band diagram computed with the spectral transmission-line modeling method and the Rayleigh multipole method. The individual data are the results of the spectral transmission-line modeling method, while the solid line was produced by the Rayleigh multipole method [203].

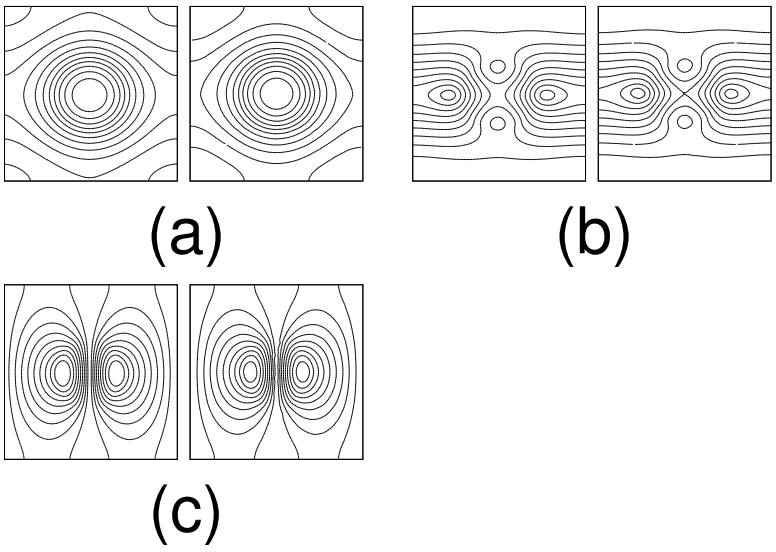

Figure 4.4: Calculated eigenmodes at $\mathbf{k} = (0, \pi/2d)$ in the irreducible Brillouin zone showing the normalized electric field magnitude. The frequencies of the modes are 2.5 GHz (a), 7.5 GHz (b), and 9.1 GHz (c). Each pair of figures comprises the simulation results produced by the spectral transmission-line modeling method (left) and Ansoft HFSS (right) and is plotted with 11 (a), 9 (b), and 9 (c) isovalue contours.

boundaries in the x- and y-directions were master-slave possessing phase delays of 0 and $\pi/2$, respectively, while those in the z-direction were PEC. The small separation of the plates ensured that only TM modes were computed. The electric field plots were calculated at $z = 0.25$ mm.

4.1.2 Evaluation of Numerical Performance

Further numerical experiments were performed in order to compare the algorithm's performance with that of established methods. Evaluations are based on the convergence of the first two bands at X in the irreducible Brillouin zone as a function of runtime and memory requirements. The first of these comparisons was carried out with the plane wave expansion method for a unit cell containing a thin cross of lithium niobate (Fig. 4.5). The runtime and memory use were varied by adjusting the number of unknowns, which corresponds to the number of plane waves used in

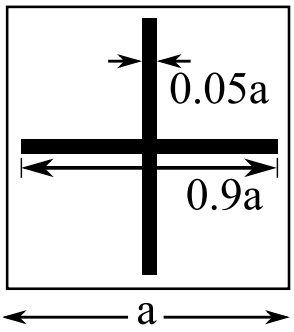

Figure 4.5: Unit cell containing a cross of the lithium niobate ($\epsilon_r = 84$ [204]). Note that the structure possesses mirror symmetry about both axes and is rotationally symmetric with rotations of $\pi/2$.

the plane wave expansion method and the number of nodes used in the spectral transmission-line modeling method. The spectral TLM simulations were carried out with $10m$ power method iterations (m is the number of nodes), and in each case the dimension of the Krylov subspace was 300.

The results of these simulations are shown graphically in Fig. 4.6. In each case, convergence was monotonic with respect to the number of unknowns and hence also monotonic with respect to runtime and memory usage. The memory figures used are estimates, as the actual amount of memory utilized depends on the implementation of the eigenvalue solver. A lower bound was used for the plane wave expansion method, while an upper bound was used for the transmission-line modeling method in order to conduct a conservative comparison. The lower bound corresponds to the amount of memory required to store the coefficient matrix, which, owing to the mirror symmetries of the unit cell, is real and symmetric. As a double precision floating point number requires 8 B of storage, $4n^2$ B are required to represent this matrix, where n is the number of plane waves used. The upper bound was taken to be the entirety of memory allocated for the calculations.

A second comparison was carried out with the plane wave method using the unit cell shown in Fig. 4.7. This cell contains a silicon square that possesses periodically

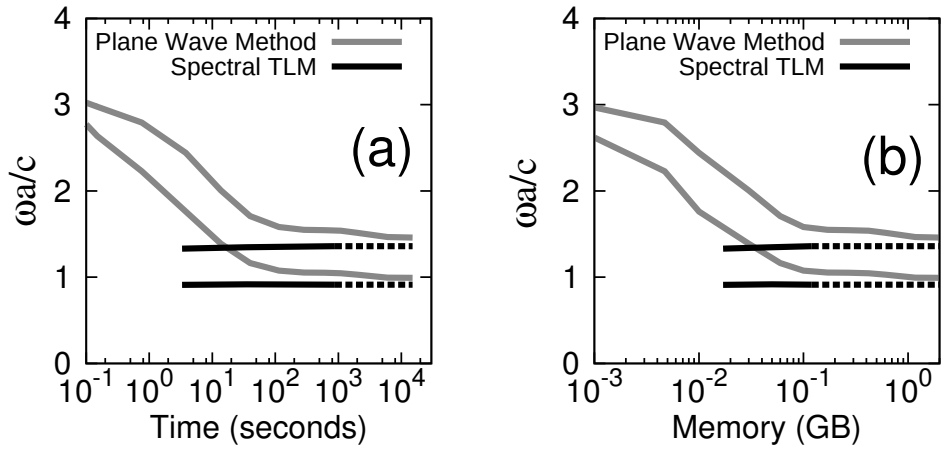

Figure 4.6: Calculated bandgap at X in the irreducible Brillouin zone as a function of runtime (a) and memory use (b) for the unit cell containing a cross of lithium niobate. Between 121 and 22,801 terms were used in the plane wave expansion, and between 625 and 10,000 nodes were used in spectral transmission-line simulation. The memory figures used in the plots are estimates. A lower bound based on the minimum memory required to store the coefficient matrix was used for the plane wave method. An upper bound found from the actual memory allocation was used with the spectral transmission-line modeling method. The horizontal dashed lines are provided for comparing the most accurate values of each method.

spaced square voids that lower the effective permittivity at low frequencies. While the contrast in permittivity is only moderate, the spatial variation is rapid, and consequently the Fourier series of the inverse permittivity function converges slowly.

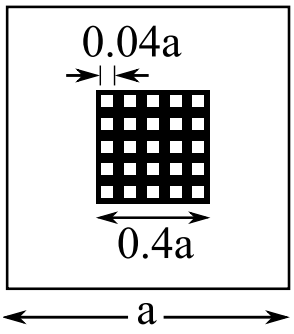

Figure 4.7: Unit cell containing a silicon square ($\epsilon_r = 12$ [202]) possessing 25 square holes. Note that the structure possesses mirror symmetry about both axes and is rotationally symmetric with rotations of $\pi/2$.

The convergence of each method as a function of runtime and memory is shown in Fig. 4.8 for point X in the irreducible Brillouin zone. The difference between the most accurate values of each method was 3% for the dielectric band and 2% for the air band.

Further simulations were conducted in order to compare the runtime characteristics of the spectral transmission-line modeling method to the those of the time-marching method. The test cases considered were the unit cells of the sapphire disk and lithium niobate cross, which were used in the previous examples. The problems were discretized on a 50×50 mesh, which was used by both the spectral and time-marching methods. The spectral method was executed for a range of runtimes by exponentially varying the number of power method iterations from 1 to $200,000$ for

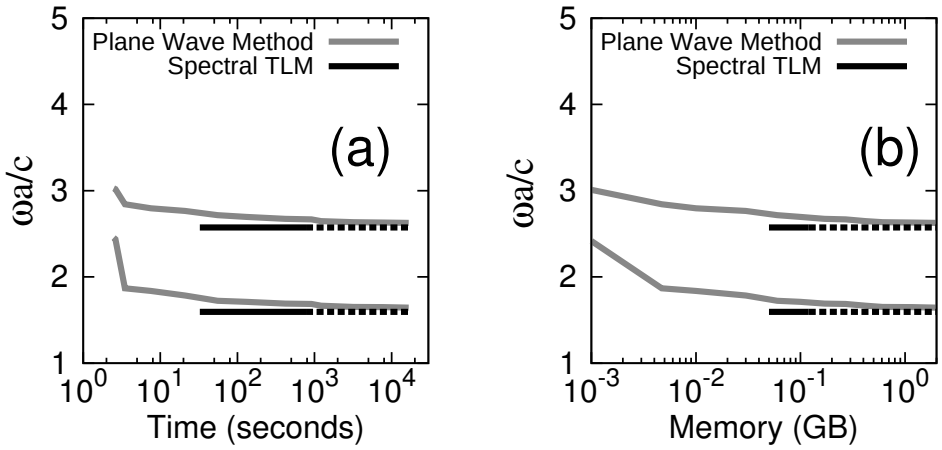

Figure 4.8: Calculated bandgap at X in the irreducible Brillouin zone as a function of runtime (a) and memory use (b) for the unit cell comprising a silicon square possessing square holes. Between 121 and $22,801$ terms were used in the plane wave expansion while between 2500 and $10,000$ nodes were used in spectral transmission line simulation. The memory figures used in the plots are estimates. A lower bound based on the minimum memory required to store the coefficient matrix was used for the plane wave method. An upper bound found from the actual memory allocation was used with the spectral transmission-line modeling method. The horizontal dashed lines are provided for comparing the most accurate values of each method.

a total of 300 simulations. The dimension of the Krylov subspace was maintained at a constant value of 300. Variation in the runtime of the time-marching method was effected by exponentially increasing the number of timesteps from 1 to 200,000, also yielding 300 simulations. The initial voltages of the latter simulations were produced with a Gaussian pulse injected at a randomly chosen point in the mesh, and the voltages were recorded at 128 randomly selected nodes for each timestep. Upon completion of time-stepping, the eigenmode frequencies were found using the procedure described in §2.2.2 and §3.1. The computed bandgaps as a function of runtime at X in the irreducible Brillouin zone are shown in Fig. 4.9.

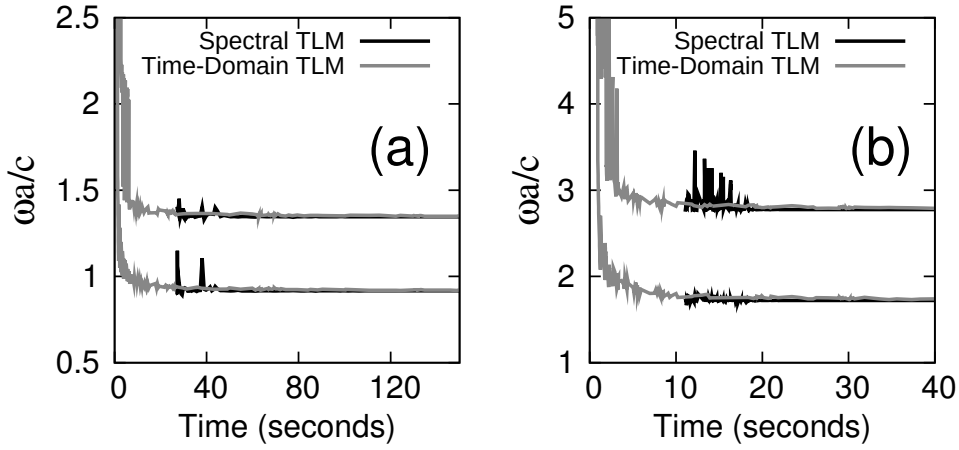

Figure 4.9: Calculated bandgap at X in the irreducible Brillouin zone as a function of runtime for the lithium niobate cross (a) and the sapphire rod (b). Note that the results of the spectral method are only plotted for times past approximately 25 s and 10 s in (a) and (b), respectively.

4.2 Circular Patch Resonator

4.2.1 Measured S-Parameters of the Unfilled Resonator

Evaluation of the circular patch resonator spanned two stages. Initial tests comprised the measurement of scattering parameters prior to the addition of BL006 in order to confirm its predicted operation for a known dielectric (air). The measured and simulated scattering parameters are compared in Fig. 4.10, which shows that the values of S_{21} are in good agreement for each of the resonances. The resonant frequencies and quality factors were extracted from the measured S_{21} using (3.46) and (3.47) and are given in Table 4.1. The agreement between the simulated and measured resonant frequencies and quality factors were found to be very good, with discrepancies no larger than 0.5% and 4.5%, respectively.

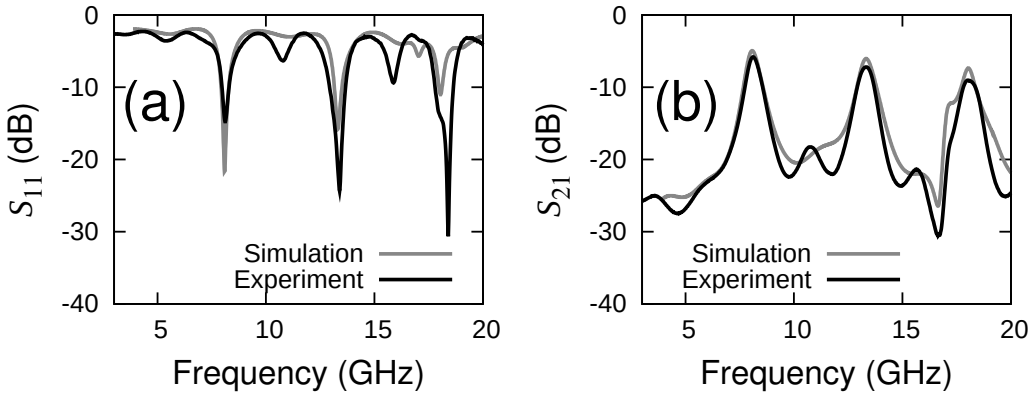

Figure 4.10: Comparison of the measured and simulated scattering parameter magnitudes of the unfilled circular patch resonator. The simulated and measured values have frequency resolutions of 10 MHz and 16.875 MHz, respectively. Note the good agreement of S_{21} near the first two resonances.

Mode Number	Simulated Resonant Frequency (GHz)	Measured Resonant Frequency (GHz)	Simulated Q	Measured Q
1	8.094	8.135	12.31	11.79
2	13.34	13.30	16.42	16.94

Table 4.1: Simulated and measured resonant frequencies and quality factors of the unfilled circular patch resonator (§3.6). These values were found using (3.46) and (3.47) for each of the resonances of the simulated and measured S_{21} series. Agreement between the resonant frequencies and quality factors is within 0.5% and 4.5%, respectively.

4.2.2 Measured S-Parameters of the Resonator Filled with BL006

Further tests were carried out upon filling the resonator with BL006. Measurements were performed on two occasions: five minutes after the structure was filled and again twenty days later to assess the stability of the electromagnetic characteristics of the device. On both occasions, scattering parameters were measured for 1-kHz bias voltages of 0 Vpp and 20 Vpp. These conditions correspond to director orientations that are nearly perpendicular and parallel, respectively, to the high-frequency electric field. Comparisons of the various S_{21} are shown in Fig. 4.11, while the extracted resonant frequencies are given in Table 4.2. Good agreement is observed for both bias voltages, suggesting that the properties of the resonator are stable with time.

Additional measurements were performed on the second occasion by varying the bias voltage between 0 Vpp and 20 Vpp in increments of 2.5 Vpp (Fig. 4.12). The resonant frequencies in each of the data series were extracted and plotted as a function of bias voltage in Fig. 4.13. An abrupt change is observed in each resonance as the bias voltage is increased past 5 Vpp, which may be considered the threshold voltage for switching. For higher voltages, Fig. 4.12 and 4.13 show that the resonator's electromagnetic characteristics depend continuously on the bias

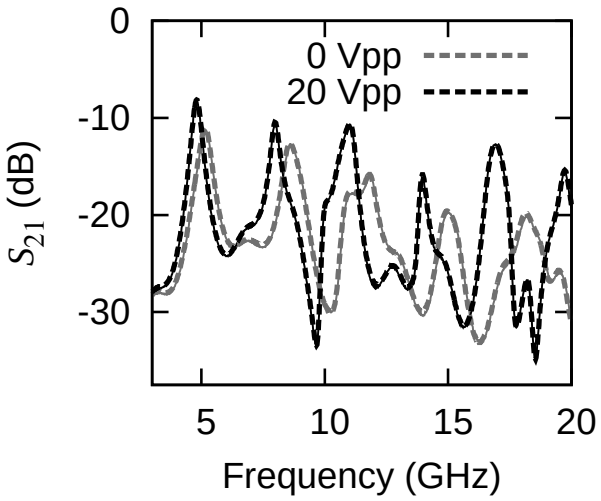

Figure 4.11: Measured S_{21} magnitude of the circular patch resonator filled with BL006 for no bias voltage (0 Vpp) and the maximum bias voltage (20 Vpp). The solid and dashed lines correspond to the original set of measurements and a second set of measurements taken twenty days later, respectively.

field, allowing the resonator to be continuously tuned.

4.2.3 Extracted Dielectric Constants and Loss Tangents

The measured scattering parameters were used in conjunction with the procedure described in §3.6.1 to find the dielectric constants and loss tangents for the frequencies of the first two resonances. The Ansoft HFSS model employed in the simulation

		First Measurement				Second Measurement			
		Perpendicular		Parallel		Perpendicular		Parallel	
Mode	Source	f (GHz)	Q	f (GHz)	Q	f (GHz)	Q	f (GHz)	Q
1	S_{12}	5.132	10.11	4.806	12.92	5.142	10.04	4.804	12.98
	S_{21}	5.130	10.11	4.807	12.94	5.141	10.02	4.804	13.01
2	S_{12}	8.639	13.10	7.992	21.76	8.663	13.08	7.978	21.73
	S_{21}	8.636	13.13	7.993	21.77	8.663	13.05	7.989	21.75

Table 4.2: Measured resonant frequencies and quality factors of the circular patch resonator filled with BL006 for the director orientations that are parallel and perpendicular to the electric field. The second measurement was taken twenty days after the first. The small discrepancies between values suggest that the electromagnetic characteristics of the resonator remain stable over timescales on the order of weeks.

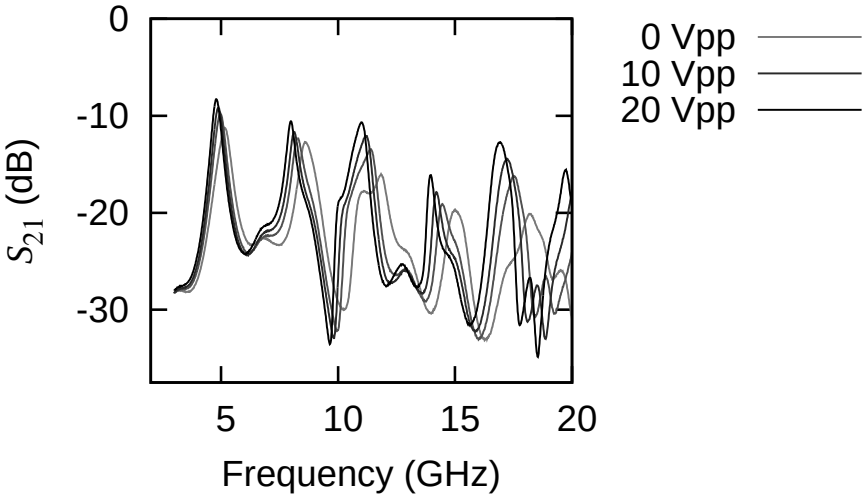

Figure 4.12: Dependence on bias voltage of the measured S_{21} magnitude of the circular patch resonator filled with BL006, shown for bias voltages of 0 Vpp, 7.5 Vpp, 10 Vpp, and 20 Vpp. The line darkness conveys voltage, where the darkest and lightest shades correspond to 20 Vpp and 0 Vpp, respectively.

of the unfilled structure (Fig. 3.11) was reused in the iterative process by adjusting the dielectric constant and loss tangent of the substrate material. Due to the enormous computational demands that resulted from the numerous iterations and fully

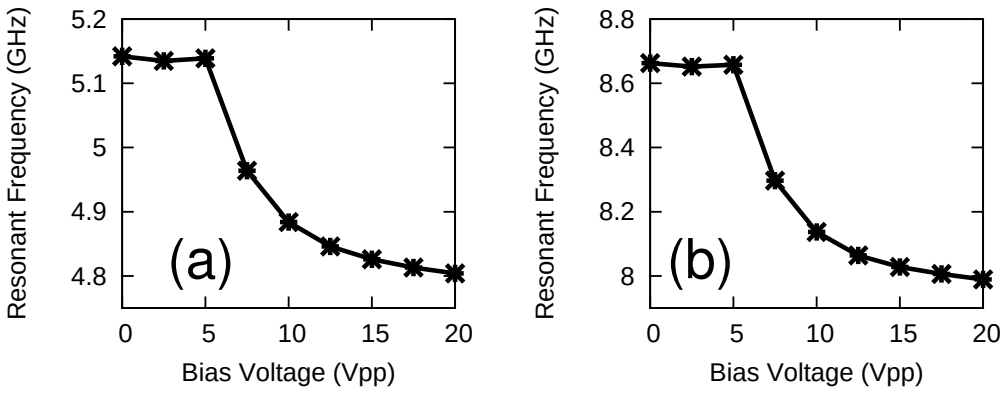

Figure 4.13: First (a) and second (b) resonant frequencies of the circular patch resonator filled with BL006 as a function of bias voltage. These values were calculated from the measured S_{21} magnitudes by using (3.46) and (3.47). Note the distinct threshold where switching occurs (near 5 Vpp). Also note what appears to be asymptotic convergence of the resonant frequencies to respective high-voltage limits.

discretized copper layers, only narrow frequency bands were calculated around each of the resonant peaks and -3 dB points. The computed dielectric constants and loss tangents are presented in Table 4.3, and a comparison of these results to several values found in the literature is given in Fig. 4.14 and Table 4.4. Agreement of the dielectric constants with those reported in [172] is noted as being particularly good. Finally, analysis of loss is presented in Fig. 4.15, which shows dielectric heating to be the primary loss mechanism of the filled resonator. Consequently, the extraction of loss tangents from the measured quality factors is well posed and therefore accurate.

4.3 Prototype Photonic Bandgap Device

The measured S_{11} and S_{21} magnitudes are compared with simulated values in Fig. 4.16. Good agreement is observed over the frequencies of the first band and bandgap. However, the second passband exhibits a relative attenuation of approximately 10 dB. Also, small changes in the scattering parameters on the order of one or two decibels were observed in response to adjusting the tension of the bolts.

	Parallel Orientation			Perpendicular Orientation		
Mode No.	f (GHz)	ϵ_r	$\tan\delta$	f (GHz)	ϵ_r	$\tan\delta$
1	4.804	3.12	0.015	5.141	2.69	0.036
2	7.989	3.11	0.007	8.663	2.62	0.035

Table 4.3: Extracted dielectric constants and loss tangents of BL006 for the director orientations that are parallel and perpendicular to the high-frequency electric field.

Parallel Orientation			Perpendicular Orientation		
f (GHz)	$\tan\delta$ [177]	$\tan\delta$	f (GHz)	$\tan\delta$ [177]	$\tan\delta$
4.804	0.021	0.015	5.141	0.073	0.036
7.989	0.012	0.007	8.663	0.055	0.035

Table 4.4: Comparison of the BL006 loss tangents found in [177] with those calculated in the present work. Reasonably good agreement is observed.

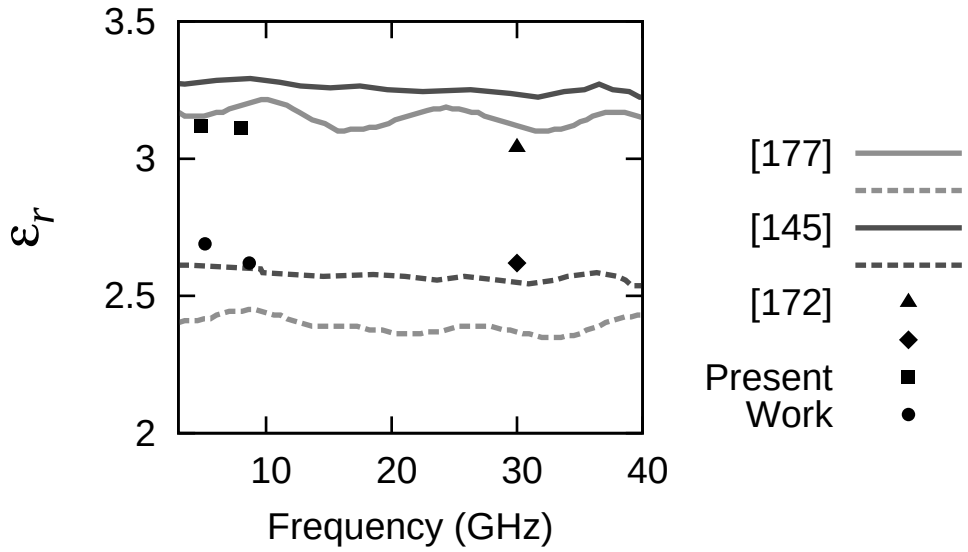

Figure 4.14: Comparison of the BL006 dielectric constants found in the literature to those calculated in the present work. Note that the values of [145,177] were derived using the same experimental technique. While the general agreement between the various methods is fair, the values derived in the present work fall within the observed variance and agree well with those of [172]. The continuous lines were generated in the present work with data from [145, 177].

4.4 Liquid Crystal Photonic Bandgap Device

4.4.1 Measured S-Parameters of the Unfilled Photonic Bandgap Device

Evaluation of the liquid crystal photonic bandgap device followed that of the circular patch resonator. The scattering parameters measured prior to the addition of BL006 are shown against simulated values in Fig. 4.17. Agreement was found to be good, although some deviation is noted around 8 GHz where the experimental data exhibit ripples that are absent from the simulation. At frequencies above 8 GHz, the measured S_{21} appears to be shifted from the simulation by approximately -5 dB. However, the prominent features and bandgap edges and attenuation are in excellent accord.

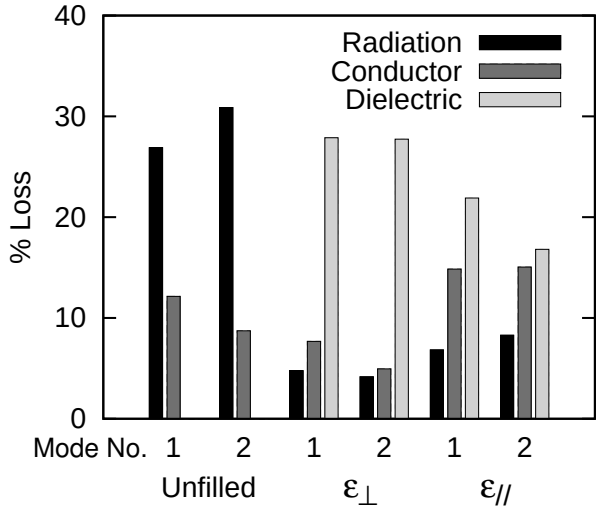

Figure 4.15: Simulated radiation, dielectric, and conductor losses of the circular patch resonator as percentages of total loss at the center frequency of each mode. In each case, the remaining loss (on the order of 50%) is due to the coupling lines. The losses shown are those that affect the resonator's quality factor.

4.4.2 Measured S-Parameters of the Photonic Bandgap Device Filled with BL006

Further measurements were taken after filling the bandgap device with BL006. Comparisons of the simulated and measured S_{11} and S_{21} for bias voltages of 0 Vpp

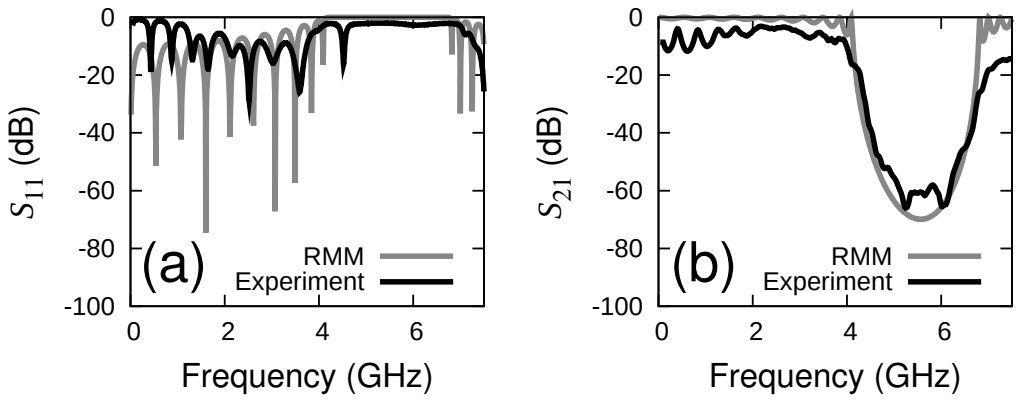

Figure 4.16: Comparison of the simulated and measured scattering parameter magnitudes of the prototype photonic bandgap device.

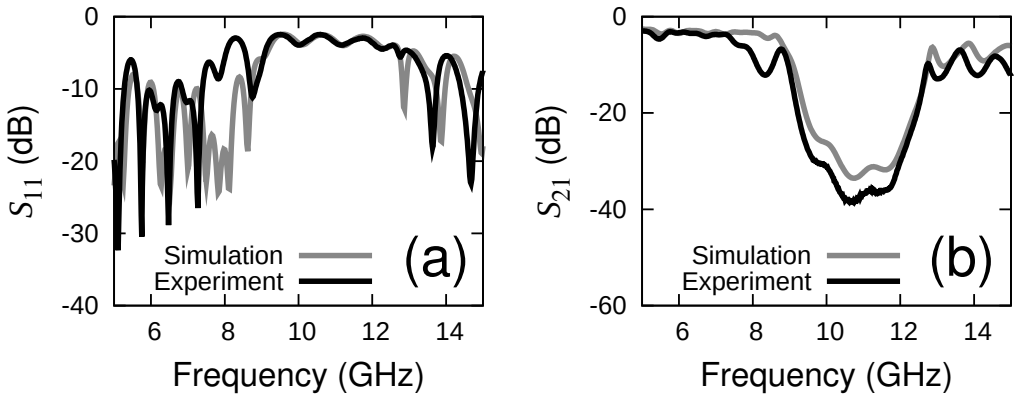

Figure 4.17: Comparison of the simulated and measured S_{11} (a) and S_{21} (b) magnitudes of the unfilled liquid crystal photonic bandgap device. The simulation is that of Fig. 3.29 (produced with Ansoft HFSS 12). Additional simulations where the dielectric constant of the Rogers substrate was changed showed that the ripples at frequencies above the bandgap are due to resonances in the Rogers substrate. The small attenuation in the measured S_{21} at higher frequencies and disagreement around 8 GHz are of unknown origin but likely involve the these resonances, whose greater prominence in the measured results may be due to imperfections in construction.

and 20 Vpp are shown in Fig. 4.18 and 4.19. Excellent agreement is observed in both cases, with only small discrepancies near the ripples in the bandgap. The full range

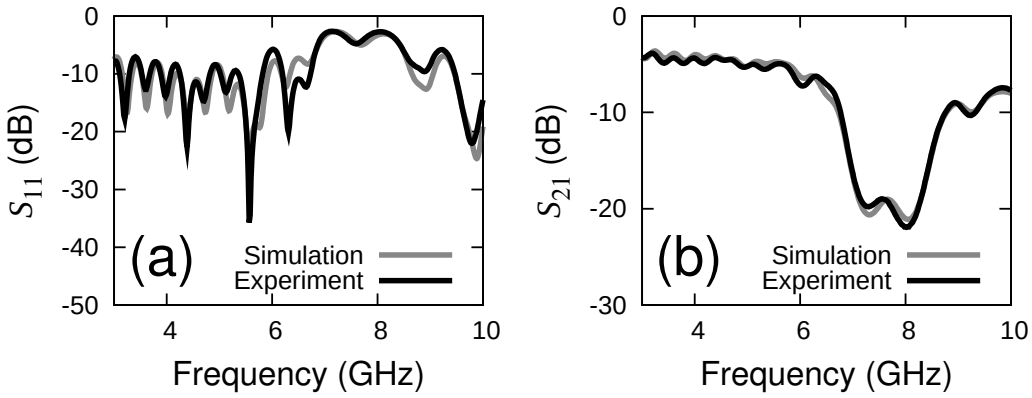

Figure 4.18: Comparison of the simulated and measured S_{11} (a) and S_{21} (b) magnitudes of the liquid crystal photonic bandgap device in the absence of an alignment field, where the simulation data are that of Fig. 3.30. Note the excellent agreement over the entire frequency band, which may be attributed to carrying out the simulations with the experimentally-derived material properties of BL006.

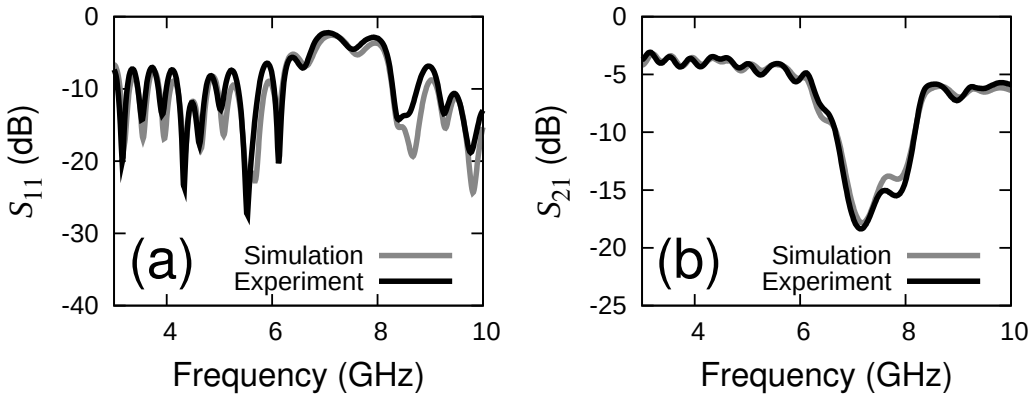

Figure 4.19: Comparison of the simulated and measured S_{11} (a) and S_{21} (b) manitudes of the liquid crystal photonic bandgap device in the presence of an alignment field, where the simulation data are that of Fig. 3.31. Once again, note the excellent agreement over the entire frequency band.

of experimentally-realized bandgap tuning is illustrated in Fig. 4.20, which shows that application of the maximum bias voltage is accompanied by a small shift and considerable contraction of the first bandgap. The frequencies between 8.5 GHz and 9 GHz can thus be switched "on" or "off" with an extinction ratio of approximately 20 dB. Additional measurements over a range of bias voltages between 0 Vpp and

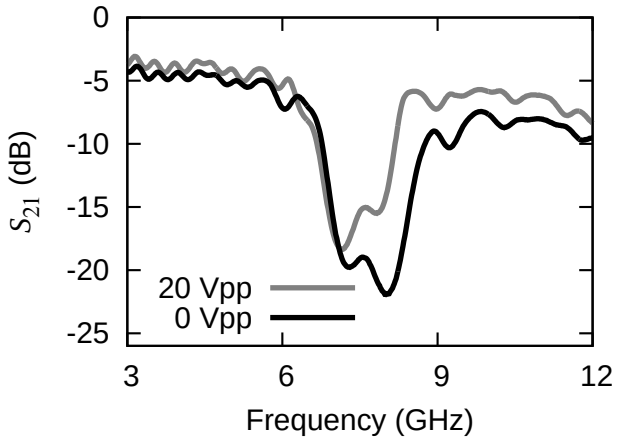

Figure 4.20: Extreme positions of the measured bandgap shown juxtaposed in terms of S_{21} magnitude. Application of a 20 Vpp bias voltage results in a contraction of the bandgap of approximately 500 MHz. This response is also accompanied by a small shift of the bandgap.

20 Vpp showed, once again, that the structure's electromagnetic characteristics are continuously tunable with the applied bias voltage (Fig. 4.21). The fabricated liquid crystal photonic bandgap device was thus found to possess a "tunable" bandgap.

4.4.3 *S*-Parameter Comparisons using an Alternate Characterization of BL006

Additional simulations of the bandgap structure were conducted using a characterization of BL006 found in [177]. A comparison of these simulations to experimental results is shown in Fig. 4.22, which is used alongside Fig. 4.18 and 4.19 as a metric in the evaluation the resonator-based permittivity measurements.

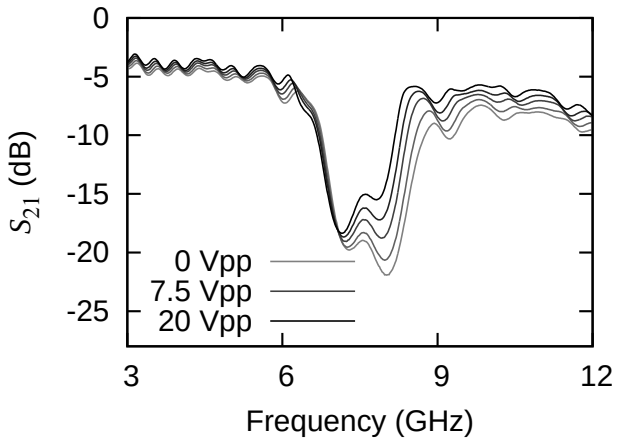

Figure 4.21: Continuous tuning of the bandgap of the liquid crystal photonic bandgap device, shown in terms of the S_{21} magnitude for bias voltages of 0 Vpp, 5 Vpp, 7.5 Vpp, 10 Vpp, and 20 Vpp. The line darkness conveys the voltage, where the darkest and lightest shades correspond to 20 Vpp and 0 Vpp, respectively.

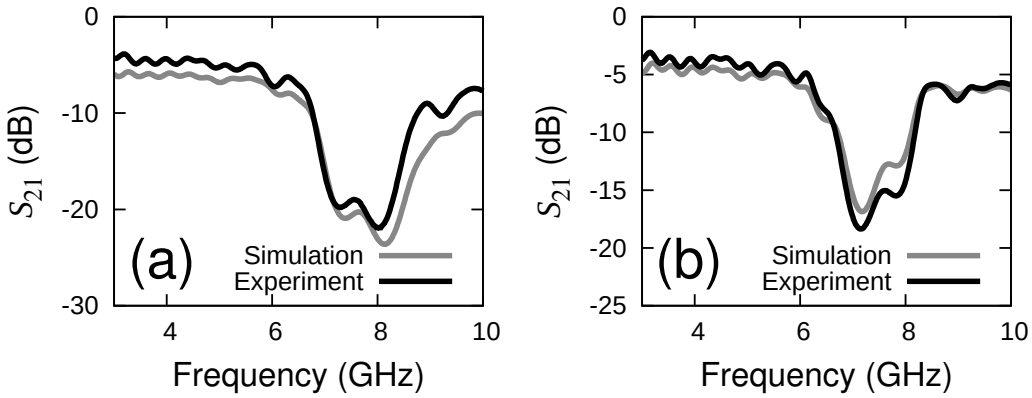

Figure 4.22: Comparison of the simulated and measured S_{21} magnitude in the absence (a) and presence (b) of an alignment field where the simulation was based on an alternate characterization of BL006 reported in [177] (the frequency-dependent dielectric constant is shown in Fig. 4.14). Note the lesser agreement when compared with that of Fig. 4.18 and 4.19.

Chapter 5

Discussion

5.1 Spectral Transmission-Line Modeling Method

The numerical experiments of §4.1.1 for a typical unit cell show that the method produces accurate results. Excellent agreement is observed between the band structures produced by the spectral transmission-line and Rayleigh multipole methods (Fig. 4.3). Similarly, the field plots produced by the method and Ansoft HFSS are in very good agreement (Fig. 4.4). These results validate the algorithm and, moreover, the general approach of treating the TLM discretization as a spectral problem.

The remainder of the results (§4.1.2) establish the method's speed and memory use against that of the plane wave and the time-domain transmission-line modeling methods. The two unit cells used in these evaluations (Fig. 4.5 and 4.7) are characterized by rapidly varying spatial features, and in the first case, high contrast in permittivity as well. These properties were expected to result in slow convergence

of the plane wave method owing to the slow convergence of the Fourier series in the plane wave expansion. Comparisons of the runtimes of the spectral transmission-line modeling method and the plane wave method for point X in the irreducible Brillouin zone confirm this and show that in both cases the convergence of the spectral transmission line is at least two orders of magnitude faster and requires at least an order of magnitude less memory (Fig. 4.6 and 4.8).

In the case of the lithium niobate cross, some discrepancy exists between the most accurate results of each method, likely due to incomplete convergence of the plane wave method. This assessment is supported by examining the convergence leading up to the most accurate calculations. Increasing the number of nodes fourfold from $2,500$ to the final number of $10,000$ changed the values computed by the spectral transmission-line modeling method by less than 1%. In contrast, doubling the number of plane waves from $12,321$ to the final number of $22,801$ yielded a difference of approximately 5%. Unfortunately, the memory requirements arising from additional plane waves were prohibitive and prevented more accurate simulations using the plane wave method.

The unit cells comprising the sapphire rod and lithium niobate cross were further employed to produce a comparison of the runtimes between the spectral and time-marching transmission-line modeling methods (Fig. 4.9). While the initial convergence of the time-marching method is slightly faster, the spectral method converged more quickly to higher accuracy, particularly for the example involving the cross of lithium niobate; after 70 seconds, the spectral method converged to within 0.1% of the final computed value while the time-marching method converged to within 1%. These examples illustrate that the methods require comparable computational resources. However, the spectral method produces the spatial configuration of the eigenmodes without additional computation.

5.2 Circular Patch Resonator

Discussion of the circular patch resonator may be divided into an assessment of its accuracy and a demonstration of its utility. The accuracy of this method ultimately lies with the strict coherence of experimental measurements to simulated results. This was confirmed by comparing the simulated and measured S_{21} of the unfilled structure (Fig. 4.10). A more quantitative analysis involved a comparison of the resonant frequencies and quality factors, which revealed a difference of no greater than 0.5% and 4.5%, respectively, for the first two modes (4.1). Higher-order modes were similarly compared, but the calculated quality factors were found in less accord. It is hypothesized that the closer spacing of modes at higher frequencies may compromise the accuracy of using (3.46) and (3.47) to determine resonant frequencies and quality factors. As the frequency is approximately proportional to the inverse square root of the dielectric constant, the error in the frequencies of the first two modes corresponds to an approximate error of 1% in the dielectric constant, when the former is used to infer the latter. Both the error and frequency range covered by the first two resonances were deemed satisfactory.

Confidence in the inferred permittivity also rests with the stability of the resonator's properties over time. The second measurement (taken twenty days after the first) reveals a small increase in the resonant frequencies for the perpendicular orientation, which may be due to the fact that the first measurement was taken five minutes after filling the structure with BL006. This length of time may have been exceeded by the timescales of the transient phenomena associated with the filling process, such as director distortions that produce visible disclination lines (§2.3.2). For this reason, the data of the second measurement were used in calculating the material properties.

Two further issues may have affected the computed permittivity values. First, a non-zero pretilt angle (§2.3.3) may have resulted in an overestimation of the perpendicular dielectric constant, as the electric field in this case is not perfectly orthogonal to the director. Generally, pretilt depends on the alignment layer, rubbing process, and liquid crystal [63] and is conventionally measured with instruments that were unavailable. An attempt was made to measure the isotropic permittivity of the liquid crystal, which, in conjunction with high-bias voltage measurements, would have allowed an inferential determination of the perpendicular permittivity as in [177]. However, this attempt failed when one of the electrical connections succumbed to the stress induced by the heating.

The second issue concerns Fig. 4.13, which reveals that the convergence to the high-voltage limit is incomplete (although not by very much). Higher bias voltages may have resulted in still lower resonant frequencies and thus higher calculated dielectric constants. However, this avenue of investigation was excluded by the DC block and bias tee, whose breakdown voltages could not be exceeded. While these limitations may have slightly narrowed the difference between the computed dielectric constants of the parallel and perpendicular orientations, they have not lessened the predictive value of the resonator measurements, as common alignment layers, rubbing parameters, liquid crystal layer thicknesses, and alignment fields were used in each experiment. This reasonably ensured that the resonator and bandgap structures shared a common director configuration (and therefore effective dielectric constant) for a given bias voltage.

The utility of the resonator-derived permittivity is demonstrated by the excellent agreement between the measured and simulated scattering parameters of the liquid crystal photonic bandgap structure (Fig. 4.18 and 4.19). This assessment is further supported by a comparison of the experimental results of the bandgap

structure to a simulation that was based on an alternate characterization of BL006 reported in literature (Fig. 4.22). The considerably poorer agreement strongly validates the rationale for the resonator and justifies the deliberate selection of process parameters that were common to both devices.

5.3 Liquid Crystal Photonic Bandgap Device

The excellent agreement of the measured and simulated scattering parameters (Fig. 4.18 and 4.19), and the demonstration of continuous tuning (Fig. 4.21) convey the successful realization of a dynamically-tunable microwave photonic bandgap device. A few issues require explanation. The first concerns the prominent ripples that appear in the the bandgaps shown in Fig. 4.18 and 4.19 and the first and second passbands shown in Fig. 4.17. During the course of HFSS simulations, several simulated field plots were reviewed for different frequencies. The voltage standing wave ratios in both microstrip taper sections were found to reach pronounced maxima at the ripple peaks, suggesting that the origin of these ripples lie with resonances in the microstrip tapers. This conclusion was strengthened upon observing a frequency shift in the ripples in response to modifying the simulated permittivity of the Rogers substrate. The same field plots implicate the presence of approximately Neumann boundary conditions at both ends of each structure. This result is consistent with the geometrical and physical properties of the device, as the connections to the 50-Ω lines and those to the waveguide section (both unfilled and filled with BL006) are abrupt transitions to higher impedances. While the triangular taper enjoys a simple geometry, the linear change of trace width along the length of the taper leads to a nonlinear change in the impedance, which is greatest near each of the ports. The resonances and attendant ripples could possibly be reduced or

eliminated by replacing each triangular taper with an exponential or Klopfenstein taper, for which the change of impedance is more uniformly distributed over the length of the taper.

The second issue concerns the differences between the simulated and measured results. The case where the structure is filled with BL006 but not subject to an alignment field is considered first (Fig. 4.18). Further simulations, which were performed by increasing the dielectric constant of the Rogers substrate from 3.55 to 3.7, showed that the discrepancies are a result of a small shift in the aforementioned resonances of the taper structures. This shift, which is approximately 100 MHz for the ripple in the bandgap, may have resulted from a deviation of substrate permittivity from manufacturer-specified values, a deviation of taper lengths from design values, or a difference in boundary conditions. Careful measurement of the taper structures excluded length as a cause. However, dimensional inaccuracies associated with the manually placed components (estimated to less than 500 μm) may have resulted in boundary conditions different from those of the simulation. Similarly, the substrate permittivity could not be eliminated as a cause in view the difference between the measured values reported in [205] and those given by the manufacturer.

In the case where the filled structure was subject to the maximal bias field (Fig. 4.19), the discrepancies appear to be the sum of two components: the aforementioned shift in the resonance of the taper structures and partial switching of the liquid crystal in the volume between the silicon squares and the upper conductor. This hypothesis was formed by conducting additional simulations in which the liquid crystal in these regions was assigned permittivities between those of the parallel and perpendicular orientations (the simulation of Fig. 4.19 assumed that no switching occurred in these regions). These simulations showed that an inter-

mediate permittivity eliminated much of the residual disagreement. However, a rigorous a priori hypothesis cannot be formed as the effect of the silicon surfaces on the liquid crystal has not been quantified.

The discrepancies in the simulated and measured results are greatest for the unfilled structure (Fig. 4.17). It is hypothesized that the ripple near 8 GHz in the experimental data results from resonance of the taper structures. The reason for its absence from the simulated data is unclear but may be due to small errors in fabrication that resulted in different boundary conditions at the junctions between the waveguide and tapers. The ripples in the second passband appear more pronounced in the measured data, suggesting stronger resonance in the tapers whose associated loss may also have contributed to the noticeable attenuation of S_{21} above 8 GHz. This hypothesis is supported by considering the greatly diminished ripples in the passbands for the filled device, where the impedance discontinuities at junctions between the waveguide and tapers are significantly less due to the small difference between the dielectric constants of BL006 and the Rogers RO4003c substrate.

Chapter 6

Conclusion & Future Work

6.1 Conclusion

This thesis described research of photonic bandgap materials that spanned two topics. The first contribution concerned the development of a eigenvalue-based transmission-line modeling method for the calculation of dispersion diagrams and Bloch modes. This work entailed the spectral characterization of the transmission-line modeling method discretization and the development and evaluation of an efficient sparse-matrix eigenvalue algorithm that exploited the latent structure of the scattering matrices. The second contribution concerned development of a liquid crystal-based tunable photonic bandgap device whose bandgap could be continuously tuned in response to an applied bias voltage. This work included the design, construction, and experimental evaluation of several devices, including a prototype linear microstrip photonic bandgap structure, a circular patch resonator that was used for permittivity measurement, and the liquid crystal photonic bandgap structure itself.

The band structures produced by the spectral transmission-line modeling meth-

od agreed very well with those produced by the plane wave, Rayleigh multipole, and the time-marching transmission-line modeling methods for each of the three unit cells considered. Electric field plots produced by the spectral method and Ansoft HFSS are in similar accord. This confirms the method's accuracy and, more generally, validates the conceptualization of the transmission-line modeling method discretization as a spectral problem. Further numerical simulations showed the spectral transmission-line modeling method to be considerably faster and significantly less memory intensive than the plane wave method for unit cells whose Fourier series converge slowly. Numerical comparisons to its time-marching counterpart revealed similar speed and memory use. From these findings, the spectral method is recommended in lieu of the plane wave method for unit cells characterized by high aspect ratios, high contrast in the dielectric constant, or rapidly varying spatial detail. Its use is also advised in place of the time-marching method, as Bloch modes are found automatically without additional computation.

The measured scattering parameters of the unfilled circular patch resonator agreed very well with full-wave simulations produced by Ansoft HFSS. The measured and simulated resonant frequencies and quality factors of the first two modes agree to within 0.5% and 4.5%, respectively, which strongly suggests that the inferred dielectric constants are correct to within approximately 1%. The extracted permittivity was found to agree very well with values reported by [172] and moderately with those reported by [145, 177] (note that agreement between the results of [145] and [177] is only fair). The electromagnetic characteristics of the resonator filled with BL006 were unchanged after three weeks, suggesting that such a device remains stable for at least such time durations.

The fabricated liquid crystal photonic bandgap device exhibited significant tuning in the range of 6–9 GHz, which consisted of a small shift and considerable

stretching of the first bandgap. The bias voltage could be used to continuously tune the bandgap between two extreme positions. The measured scattering parameters of the liquid crystal photonic bandgap device agree very well with simulations produced by Ansoft HFSS using the resonance-derived permittivities of BL006. The substantially poorer agreement between the measured data and HFSS simulations produced with the BL006 characterization of [177] affirms the utility and validity of the circular patch resonator.

More generally, this work provides further evidence of the value of nematic liquid crystals as tunable microwave dielectrics and suggests that future work may stand to benefit from adopting the approach presented here, wherein the permittivity measurement employs geometries and process parameters that are common to those of the final application.

6.2 Future Work

Several avenues of future work are possible. With respect to resonance-based permittivity measurements, characterizations of several other liquid crystals with the resonator of §3.6 would contribute to the limited body of knowledge on the microwave properties these materials, which are expected to find greater use in microwave engineering in the future. It would also be interesting to determine the isotropic permittivity of BL006, which could then be used in conjunction with the other measured values to infer pretilt angles. Performing such an experiment would require a resonator that is able to withstand the associated thermal shock or a method of heating that is less likely to result in destructive temperature gradients (such as heating in an oven). Results would need to be confirmed with a conventional method of measuring pretilt.

Research involving the liquid crystal photonic bandgap device may be continued on several fronts. The bandgap frequency may be increased by scaling the structure's dimensions with the lattice constant and modifying the tapers accordingly. However, it seems doubtful that the manual assembly process described in this thesis affords sufficient control over dimensional tolerances for any significant foray into higher frequency work. Instead, one-dimensional or two-dimensional periodicity might be realized as a patterned signal conductor in a covered coplanar waveguide-type structure (where an additional ground plane is placed over the original signal/ground metalization). Such a design would leverage the precision of the photolithographic process to enforce nearly all dimensions and limit manual assembly to placement of the ground plane.

While the structure presented in this thesis may be employed in its present form as a tunable filter, other uses are also possible. For example, tuning of the second band may be exploited in negative group velocity applications. Such development would require a detailed investigation of the band structure as a function of lattice geometry and materials in order to identify parameters that yield a pronounced change in the slope of the second band in response to tuning. The tuning of the second band of the structure developed in this thesis (Fig. 3.28) consists primarily of a shift, which does not yield a change in group velocity. Also, measurements performed on experimentally-realized devices would need to be de-embedded to remove the effect of tapers or other feed-line structures.

Finally, tuning of the band structure might find use in the modulation of negative refraction inherent to many photonic bandgap structures. For example, with the correct choice of geometry and materials, it may be possible to develop a lens based on a tunable photonic crystal slab whose focal point can be shifted in response to tuning of the band structure. Further work is needed to determine how

and to what extent dynamically tunable photonic bandgap materials could be used in such applications.

Appendix A

Spectral Properties of the Pseudoperiodic Vector Wave Equation

The spectral properties of the vector wave equation are derived in order to justify the numerical algorithms used to compute band structures. In particular, the following analysis derives the spectral characteristics of the differential equation

$$\underline{\epsilon}(\mathbf{r})^{-1}\nabla\times\underline{\mu}\,(\mathbf{r})^{-1}\,\nabla\times\mathbf{E}\,(\mathbf{r})+\omega^2\mathbf{E}\,(\mathbf{r})=0 \tag{A.0.1}$$

where ω^2, $\mathbf{E}(\mathbf{r})$, $\underline{\mu}(\mathbf{r})$, and $\underline{\epsilon}(\mathbf{r})$ are the angular frequency squared (eigenvalue), electric field, magnetic permeability tensor, and electric permittivity tensor, respectively. Note that $\nabla\times$ is the curl operator with respect to position ($\mathbf{r}$). As the

material tensors describe a photonic crystal, they must obey

$$\begin{aligned} \underline{\epsilon}\,(\mathbf{r}) &= \underline{\epsilon}\,(\mathbf{r} + n_1\mathbf{a}_1 + n_2\mathbf{a}_2 + n_3\mathbf{a}_3) \\ \underline{\mu}\,(\mathbf{r}) &= \underline{\mu}\,(\mathbf{r} + n_1\mathbf{a}_1 + n_2\mathbf{a}_2 + n_3\mathbf{a}_3) \qquad \forall n_1, n_2, n_3 \in \mathbb{Z} \end{aligned} \tag{A.0.2}$$

where $\{\mathbf{a}_1, \mathbf{a}_2, \mathbf{a}_3\}$ is the set of linearly independent lattice vectors that define the unit cell. Under these conditions, Bloch's theorem [31] restricts $\mathbf{E}(\mathbf{r})$ to a space whose functions may be written as a phase ϕ multiplied by a function that is strictly periodic with the lattice. This phase is related to the wavevector $\mathbf{k}$ by

$$\phi = e^{i\mathbf{k}\cdot\mathbf{r}} \tag{A.0.3}$$

Characterization of (A.0.1) is carried out by restating the problem for a fixed value of $\mathbf{k}$ and then showing that the inverse of $\underline{\epsilon}(\mathbf{r})^{-1}\nabla\times\underline{\mu}(\mathbf{r})^{-1}\nabla\times$ is an operator that is compact and self-adjoint in a space that is precisely defined. These properties are sufficient to show that (A.0.1) possesses only discrete eigenvalues, which form a monotonically increasing set of positive numbers. The analysis is based on the weak formulation so that boundary conditions between disparate materials are automatically satisfied. Note that the symbols □ and ■ denote the end of a lemma and proposition, respectively.

A.1 Definition of Functional Spaces

Several functional spaces are used throughout this section. In each case, the domain of the functions Ω comprises the surface area (surface volume) of the scaled and twisted unit torus and is characterized by its direct lattice vectors $\{\mathbf{a}_1, \mathbf{a}_2, \mathbf{a}_3\}$. The

reciprocal lattice vectors

$$G \equiv \{\mathbf{G} \in \mathbb{R}^3 : (\exists l, n, m \in \mathbb{Z})\,(\mathbf{G} = l\mathbf{g}_1 + m\mathbf{g}_2 + n\mathbf{g}_3)\} \tag{A.1.1}$$

satisfy the relation $\mathbf{g}_p \cdot \mathbf{a}_q = 2\pi\delta_{p,q}$ and may be used to expand an arbitrary square integrable function in terms of its Fourier series

$$f(\mathbf{r}) = \sum_{\mathbf{G}\in G} f_{\mathbf{G}} e^{i\mathbf{G}\cdot\mathbf{r}} \tag{A.1.2}$$

Note that the special case of the cubic lattice gives $\Omega = \mathbb{T}^3$. The following notation is used to simplify expressions

$$\begin{aligned} x_{\sup} &= \sup\left\{\left\|\underline{\mathbf{x}}(\mathbf{r})\,\mathbf{u}\right\|_{[L^2(\Omega)]^3} : \forall \mathbf{u} \in \left[L^2(\Omega)\right]^3 \text{where } \|\mathbf{u}\| \leq 1\right\} \\ x_{\inf} &= \inf\left\{\left\|\underline{\mathbf{x}}(\mathbf{r})\,\mathbf{u}\right\|_{[L^2(\Omega)]^3} : \forall \mathbf{u} \in \left[L^2(\Omega)\right]^3 \text{where } \|\mathbf{u}\| \geq 1\right\} \end{aligned} \tag{A.1.3}$$

where $\underline{\mathbf{x}}(\mathbf{r})$ may be $\underline{\epsilon}(\mathbf{r})$, $\underline{\epsilon}(\mathbf{r})^{-1}$, $\underline{\mu}(\mathbf{r})$, or $\underline{\mu}(\mathbf{r})^{-1}$. Each of the following functional spaces is complete in the norm induced by the given inner product (and thus a Hilbert space):

1. *Space of weighted scalar square integrable functions:* $L^2_w(\Omega)$

This space is equipped with the inner product

$$(u, v)_{L^2_w(\Omega)} = \int_\Omega w(\mathbf{r})\, u(\mathbf{r})\, \overline{v(\mathbf{r})} d\mathbf{r} \tag{A.1.4}$$

where $\int_\Omega$ is the Lebesgue integral and $w(\mathbf{r})$ is a bounded positive and piecewise continuous real function that satisfies $C^{-1} < w(\mathbf{r}) < C$ for some $C > 0$ and for all

$\mathbf{r} \in \Omega$. The integral of (A.1.4) evaluates to a complex number, is linear in the first slot, Hermitian upon exchange of v with u, and positive-definite. Hence it satisfies the properties of an inner product and induces the norm

$$\|u\|^2_{L^2_w(\Omega)} = (u,u)_{L^2_w(\Omega)} \tag{A.1.5}$$

When $w(\mathbf{r}) = 1$ the subscript w is dropped. This space is complete in the norm of (A.1.5), which may be seen by considering that $\|\cdot\|_{L^2_w(\Omega)}$ is equivalent to $\|\cdot\|_{L^2(\Omega)}$, that is

$$C^{-1}\|u\|_{L^2_w(\Omega)} \leq \|u\|_{L^2(\Omega)} \leq C\|u\|_{L^2_w(\Omega)} \tag{A.1.6}$$

which shows that a Cauchy sequence in $L^2_w(\Omega)$ is also a Cauchy sequence in $L^2(\Omega)$. Completeness of $L^2_w(\Omega)$ rests with the fact that $L^2(\Omega)$ is complete and that all members of $L^2(\Omega)$, including the limits of all Cauchy sequences, are also members of $L^2_w(\Omega)$

2. Space of weighted vector square integrable functions: $[L^2_w(\Omega)]^3$

This space is based on

$$\left[L^2(\Omega)\right]^3 = L^2(\Omega) \times L^2(\Omega) \times L^2(\Omega) \tag{A.1.7}$$

and is equipped with the inner product

$$(\mathbf{u},\mathbf{w})_{[L^2_w(\Omega)]^3} = \int_\Omega (\underline{\mathbf{w}}(\mathbf{r})\,\mathbf{u}(\mathbf{r})) \cdot \overline{\mathbf{v}(\mathbf{r})} d\mathbf{r} \tag{A.1.8}$$

where $\underline{\mathbf{w}}(\mathbf{r})$ is a bounded second-rank Hermitian positive-definite tensor that satisfies $C^{-1} < (\underline{\mathbf{w}}(\mathbf{r})\mathbf{x}) \cdot \overline{\mathbf{x}}/|\mathbf{x}|^2 < C$ for some $C > 0$ and for all $\mathbf{r} \in \Omega,\ \mathbf{x} \in \mathbb{C}^3 \setminus \mathbf{0}$. The elements of this tensor are assumed to be piecewise continuous. The integral of (A.1.8) possesses the properties of an inner product and induces the norm

$$\|\mathbf{u}\|^2_{[L^2_w(\Omega)]^3} = (\mathbf{u}, \mathbf{u})_{[L^2_w(\Omega)]^3} \tag{A.1.9}$$

This space is also complete in the norm of (A.1.9).

3. *Space of scalar square integrable functions whose divergence lies in $[L^2(\Omega)]^3$: $H^1(\Omega)$*

This is a Sobolev space defined as

$$H^1(\Omega) = \left\{ u \in L^2(\Omega) : D^\alpha u \in L^2(\Omega) \ \ \forall \alpha \in \mathbb{N}_0^3 : |\alpha| \leq 1 \right\} \tag{A.1.10}$$

where $|\alpha| = \|\alpha\|_1$ and D is a weak derivative defined as

$$\int_\Omega \left(D^\alpha f(\mathbf{r})\right) \phi(\mathbf{r})\, d\mathbf{r} = (-1)^{|\alpha|} \int_\Omega f(\mathbf{r}) \frac{\partial^{|\alpha|} \phi(\mathbf{r})}{\partial x^{\alpha_x} \partial y^{\alpha_y} \partial z^{\alpha_z}} d\mathbf{r} \tag{A.1.11}$$

where $\phi \in C^\infty(\Omega)$. This space is equipped with the inner product

$$(u, v)_{H^1(\Omega)} = \sum_{|\alpha| \leq 1} (D^\alpha u, D^\alpha v)_{L^2(\Omega)} \tag{A.1.12}$$

which induces the norm

$$\|u\|^2_{H^1(\Omega)} = (u, u)_{H^1(\Omega)} \tag{A.1.13}$$

This space is complete (cf. [43]). Note that the given inner product and norm are arbitrary, as they are not used explicitly.

4. *Space of vector square integrable functions whose curl lies in* $[L^2(\Omega)]^3$*:* $H(\text{curl}, \Omega)$

This is a Sobolev space defined as

$$H\left(\text{curl}, \Omega\right) = \left\{\mathbf{u} \in \left[L^2\left(\Omega\right)\right]^3 : \nabla \times \mathbf{u} \in \left[L^2\left(\Omega\right)\right]^3\right\} \tag{A.1.14}$$

where the weak curl is defined as

$$\int_\Omega \nabla \times \mathbf{u} \cdot \phi d\mathbf{r} = \int_\Omega \mathbf{u} \cdot \nabla \times \phi d\mathbf{r} \quad \forall \phi \in \left[C^\infty\left(\Omega\right)\right]^3 \tag{A.1.15}$$

This space is equipped with the inner product

$$\left(\mathbf{u}, \mathbf{v}\right)_{H(\text{curl},\Omega)} = \left(\mathbf{u}, \mathbf{v}\right)_{\left[L^2_{\underline{\epsilon}(\mathbf{r})}(\Omega)\right]^3} + \left(\nabla_\mathbf{k} \times \mathbf{u}, \nabla_\mathbf{k} \times \mathbf{v}\right)_{[L^2(\Omega)]^3} \tag{A.1.16}$$

where $\nabla_\mathbf{k} = \nabla + i\mathbf{k}$ and $\underline{\epsilon}(\mathbf{r})$ is the material permittivity tensor. Note that this definition, based on a shift of $i\mathbf{k}$, departs slightly from convention [45]. This inner product induces the norm

$$\left\|\mathbf{u}\right\|^2_{H(\text{curl},\Omega)} = \left(\mathbf{u}, \mathbf{u}\right)_{H(\text{curl},\Omega)} \tag{A.1.17}$$

The space of (A.1.14)–(A.1.17) is consistent with the axioms of an inner product space and moreover is complete, which is shown in the following proposition.

Proposition 1: *The space of (A.1.14)–(A.1.17) is complete.*

Proof. The following lemmas are required to complete this proof.

Lemma 1.1: *Given an inner product space* X, $(\mathbf{u}_n, \mathbf{v}) \rightarrow (\mathbf{u}, \mathbf{v})$ $\forall \mathbf{v} \in X$ *where* $\mathbf{u} \in X$ *is the limit of the convergent sequence* $\{\mathbf{u}_n \in X\}$.

A proof of this lemma is given in [43]. $\square$

Lemma 1.2: *Given a normed space, if the sequence* $\{\mathbf{u}_n + \mathbf{v}_n\}$ *converges to the limit* $\mathbf{c}$, *and furthermore if the sequence* $\{\mathbf{v}_n\}$ *converges to the limit* $\mathbf{v}$, *then the sequence* $\{\mathbf{u}_n\}$ *converges to the limit* $\mathbf{c} - \mathbf{v}$.

The relations

$$\begin{aligned} &\forall \epsilon > 0 \ \exists N : \|\mathbf{u}_n + \mathbf{v}_n - \mathbf{c}\| < \epsilon \text{ when } n > N \\ &\epsilon > 0 \ \exists N : \|\mathbf{v}_n - \mathbf{v}\| < \epsilon \text{ when } n > N \end{aligned} \tag{A.1.18}$$

may be used to show that

$$\forall \epsilon > 0 \ \exists N : \|\mathbf{u}_n + \mathbf{v}_n - \mathbf{c}\| + \|\mathbf{v}_n - \mathbf{v}\| < \epsilon \text{ when } n > N \tag{A.1.19}$$

By the triangle inequality

$$\|\mathbf{u}_n + \mathbf{v}_n - \mathbf{c} - \mathbf{v}_n + \mathbf{v}\| < \|\mathbf{u}_n + \mathbf{v}_n - \mathbf{c}\| + \|\mathbf{v}_n - \mathbf{v}\| \tag{A.1.20}$$

which gives

$$\forall \epsilon > 0 \ \exists N : \|\mathbf{u}_n + \mathbf{v} - \mathbf{c}\| < \epsilon \text{ when } n > N \tag{A.1.21}$$

showing that $\{\mathbf{u}_n\}$ converges to $\mathbf{c}-\mathbf{v}$. $\square$

Proof of completeness may be carried out in the manner of [43] by considering the Cauchy sequence $\{\mathbf{u}\}$ and its convergence

$$\lim_{m,l\to\infty}\left(\|\mathbf{u}_m-\mathbf{u}_l\|^2_{\left[L^2_{\underline{\epsilon}(\mathbf{r})}(\Omega)\right]^3}+\|\nabla_{\mathbf{k}}\times\mathbf{u}_m-\nabla_{\mathbf{k}}\times\mathbf{u}_l\|^2_{[L^2(\Omega)]^3}\right)=0 \tag{A.1.22}$$

As each term is positive

$$\lim_{m,l\to\infty}\|\mathbf{u}_m-\mathbf{u}_l\|^2_{\left[L^2_{\underline{\epsilon}(\mathbf{r})}(\Omega)\right]^3}=0 \tag{A.1.23a}$$

$$\lim_{m,l\to\infty}\|\nabla_{\mathbf{k}}\times\mathbf{u}_m-\nabla_{\mathbf{k}}\times\mathbf{u}_l\|^2_{[L^2(\Omega)]^3}=0 \tag{A.1.23b}$$

By virtue of (A.1.6)–(A.1.9)

$$\lim_{m,l\to\infty}\|\mathbf{u}_m-\mathbf{u}_l\|^2_{\left[L^2_{\underline{\epsilon}(\mathbf{r})}(\Omega)\right]^3}=0\iff\lim_{m,l\to\infty}\|\mathbf{u}_m-\mathbf{u}_l\|^2_{[L^2(\Omega)]^3}=0 \tag{A.1.24}$$

Because these spaces are complete, $\mathbf{u}_l$ of (A.1.23a) converges to $\mathbf{c}_1\in[L^2_{\underline{\epsilon}(\mathbf{r})}(\Omega)]^3$ (and also $\mathbf{c}_1\in[L^2(\Omega)]^3$) and $\nabla_{\mathbf{k}}\times\mathbf{u}_l$ of (A.1.23b) to $\mathbf{c}_2\in[L^2(\Omega)]^3$. Expanding $\nabla_{\mathbf{k}}$ gives

$$0=\lim_{l\to\infty}\|\nabla_{\mathbf{k}}\times\mathbf{u}_l-\mathbf{c}_2\|_{[L^2(\Omega)]^3}=\lim_{l\to\infty}\|\nabla\times\mathbf{u}_l+i\mathbf{k}\times\mathbf{u}_l-\mathbf{c}_2\|_{[L^2(\Omega)]^3} \tag{A.1.25}$$

Noting that $i\mathbf{k}\times$ is a bounded operator, the sequence $\{i\mathbf{k}\times\mathbf{u}_l\in[L^2(\Omega)]^3\}$ converges to $\mathbf{c}_3\in[L^2(\Omega)]^3$ and hence, using lemma 1.2, $\{\nabla\times\mathbf{u}_l\}$ converges to $\mathbf{c}_2-\mathbf{c}_3\in[L^2(\Omega)]^3$. Using Lemma 1.1 twice yields

$$
\begin{aligned}
(\mathbf{c}_2 - \mathbf{c}_3, \phi)_{[L^2(\Omega)]^3} &= \left(\lim_{l\to\infty} \nabla \times \mathbf{u}_l, \phi\right)_{[L^2(\Omega)]^3} = \lim_{l\to\infty} (\nabla \times \mathbf{u}_l, \phi)_{[L^2(\Omega)]^3} \\
&= \lim_{l\to\infty} (\mathbf{u}_l, \nabla \times \phi)_{[L^2(\Omega)]^3} = (\mathbf{c}_1, \nabla \times \phi)_{[L^2(\Omega)]^3}
\end{aligned}
\tag{A.1.26}
$$

which shows that $\mathbf{c}_2 - \mathbf{c}_3 \in [L^2(\Omega)]^3$ is the weak curl of $\mathbf{c}_1$. Consequently, $\mathbf{c}_1 \in H(\text{curl}, \Omega)$. Using the triangle inequality with

$$
\begin{aligned}
&\lim_{l\to\infty} \|\nabla \times \mathbf{u}_l - \nabla \times \mathbf{c}_1\|_{[L^2(\Omega)]^3} = 0 \\
&\lim_{l\to\infty} \|i\mathbf{k} \times \mathbf{u}_l - i\mathbf{k} \times \mathbf{c}_1\|_{[L^2(\Omega)]^3} = 0
\end{aligned}
\tag{A.1.27}
$$

produces

$$
\lim_{l\to\infty} \|\nabla_{\mathbf{k}} \times \mathbf{u}_l - \nabla_{\mathbf{k}} \times \mathbf{c}_1\|_{[L^2(\Omega)]^3} = 0 \tag{A.1.28}
$$

Finally, using (A.1.28) along with

$$
\lim_{l\to\infty} \|\mathbf{u}_l - \mathbf{c}_1\|_{\left[L^2_{\underline{\varepsilon}(\mathbf{r})}(\Omega)\right]^3} = 0 \tag{A.1.29}
$$

gives

$$
\lim_{l\to\infty} \|\mathbf{u}_l - \mathbf{c}_1\|_{H(\text{curl},\Omega)} = 0 \tag{A.1.30}
$$

which shows that $\mathbf{c}_1 \in H(\text{curl}, \Omega)$ is indeed the limit of the arbitrary Cauchy sequence $\{\mathbf{u}_l\}$. ■

5. *Subspace of $H(\text{curl}, \Omega)$ whose members may be written as $\nabla_{\mathbf{k}}\phi$, $\phi \in H^1(\Omega)$: $\nabla_{\mathbf{k}} S$*

This space inherits the inner product and norm of (A.1.14)–(A.1.17) and is shown by the proof of the following proposition to be closed (complete).

Proposition 2: *The space* $\nabla_{\mathbf{k}} S$ *is a closed subspace of* $H(\mathrm{curl}, \Omega)$.

Proof. Three lemmas are required to complete this proof. In each case $\mathbf{k}$ and $\underline{\epsilon}(\mathbf{r})$ are fixed and $\mathbf{k} \notin G$.

Lemma 2.1: *(Poincaré-Type Inequality): For all* $\phi \in H^1(\Omega)$ *there exists* $C_1 > 0$ *such that* $\|\nabla_{\mathbf{k}}\phi\|_{[L^2_{\underline{\epsilon}(\mathbf{r})}(\Omega)]^3} \geq C_1 \|\phi\|_{L^2(\Omega)}$.

This may readily be shown by noting that

$$\left\| \sqrt{\underline{\epsilon}\,(\mathbf{r})} \nabla_{\mathbf{k}} \phi \right\|_{[L^2(\Omega)]^3} \geq \sqrt{\epsilon_{\inf}}\, \|\nabla_{\mathbf{k}}\phi\|_{[L^2(\Omega)]^3} \tag{A.1.31}$$

and expanding ϕ as a Fourier series

$$\nabla_{\mathbf{k}} \sum_{\mathbf{G}\in G} \phi_{\mathbf{G}} e^{i\mathbf{G}\cdot\mathbf{r}} = \sum_{\mathbf{G}\in G} i\,(\mathbf{k}+\mathbf{G})\,\phi_{\mathbf{G}} e^{i\mathbf{G}\cdot\mathbf{r}} \tag{A.1.32}$$

where the $\phi_{\mathbf{G}}$ are the Fourier series coefficients, giving

$$\sqrt{\epsilon_{\inf}} \|\nabla_{\mathbf{k}}\phi\|_{[L^2(\Omega)]^3} \geq C_1 \|\phi\|_{L^2(\Omega)} \tag{A.1.33}$$

where C_1 is a constant independent of ϕ given by $C_1 = (\sqrt{\epsilon_{\inf}} \min |\mathbf{k}+\mathbf{G}| : \mathbf{G} \in G\}) > 0$. Thus,

$$\|\nabla_{\mathbf{k}}\phi\|_{\left[L^2_{\underline{\epsilon}(\mathbf{r})}(\Omega)\right]^3} \geq C_1 \|\phi\|_{L^2(\Omega)} \quad \square \tag{A.1.34}$$

Lemma 2.2: *For all* $\phi \in H^1(\Omega)$ *and* $\alpha \in \mathbb{N}_0^3$ *satisfying* $|\alpha| = 1$ *there exists* $C_2 > 0$ *such that* $\|\nabla_{\mathbf{k}}\phi\|_{[L^2_{\underline{\epsilon}(\mathbf{r})}(\Omega)]^3} \geq C_2 \|D^\alpha \phi\|_{L^2(\Omega)}$.

Once again, expanding ϕ as a Fourier series gives

$$\begin{aligned} \left\| \sqrt{\underline{\epsilon}\,(\mathbf{r})} \nabla_{\mathbf{k}} \phi \right\|_{[L^2(\Omega)]^3} &\geq \sqrt{\epsilon_{\inf}} \left\| \sum_{\mathbf{G} \in G} i\,(\mathbf{k}+\mathbf{G})\,\phi_{\mathbf{G}} e^{i\mathbf{G}\cdot\mathbf{r}} \right\|_{[L^2(\Omega)]^3} \\ &\geq C_2 \left\| \sum_{\mathbf{G} \in G} i\mathbf{G}\phi_{\mathbf{G}} e^{i\mathbf{G}\cdot\mathbf{r}} \right\|_{[L^2(\Omega)]^3} = C_2 \left\| \nabla \phi \right\|_{[L^2(\Omega)]^3} \end{aligned} \tag{A.1.35}$$

where C_2 is a constant independent of ϕ given by

$$C_2 = \sqrt{\epsilon_{\inf}} \min \left\{ |\mathbf{k}|, \min \left\{ \frac{|\mathbf{k}+\mathbf{G}'|}{|\mathbf{G}'|} : \mathbf{G}' \in G \backslash \mathbf{0} \right\} \right\} > 0 \tag{A.1.36}$$

Finally, note that

$$\|\nabla \phi\|_{[L^2(\Omega)]^3} \geq \|D^\alpha \phi\|_{L^2(\Omega)} \tag{A.1.37}$$

which strengthens the inequality and gives

$$\|\nabla_{\mathbf{k}} \phi\|_{\left[L^2_{\underline{\epsilon}(\mathbf{r})}(\Omega)\right]^3} \geq C_2 \|D^\alpha \phi\|_{L^2(\Omega)} \quad \square \tag{A.1.38}$$

Lemma 2.3: *For all* $\phi \in H^1(\Omega)$ *there exists* $C_3 > 0$ *such that* $\|\phi\|_{H^1(\Omega)} \geq C_3 \|\nabla_{\mathbf{k}} \phi\|_{H(\mathrm{curl},\Omega)}$.

Expanding the norm appearing in the right-hand side gives

$$\|\nabla_{\mathbf{k}} \phi\|^2_{H(\mathrm{curl},\Omega)} = \|\nabla_{\mathbf{k}} \times \nabla_{\mathbf{k}} \phi\|^2_{[L^2(\Omega)]^3} + \left\| \sqrt{\underline{\epsilon}\,(\mathbf{r})} \nabla_{\mathbf{k}} \phi \right\|^2_{[L^2(\Omega)]^3} \tag{A.1.39}$$

Note that the order of differentiation with respect to the spatial index may be

exchanged so that $\nabla_{\mathbf{k}} \times \nabla_{\mathbf{k}}(\cdot) = \mathbf{0}$, giving

$$\|\nabla_{\mathbf{k}}\phi\|^2_{H(\mathrm{curl},\Omega)} = \left\|\sqrt{\underline{\epsilon}\,(\mathbf{r})}\nabla_{\mathbf{k}}\phi\right\|^2_{[L^2(\Omega)]^3} \tag{A.1.40}$$

The right-hand side may be estimated with an application of the triangle inequality

$$\left\|\sqrt{\underline{\epsilon}\,(\mathbf{r})}\,(\nabla + i\mathbf{k})\,\phi\right\|_{[L^2(\Omega)]^3} \leq \sqrt{\epsilon_{\mathrm{sup}}}\left(\|\nabla\phi\|_{[L^2(\Omega)]^3} + \|\mathbf{k}\phi\|_{[L^2(\Omega)]^3}\right) \leq C_3^{-1}\,\|\phi\|_{H^1(\Omega)} \tag{A.1.41}$$

where $C_3^{-1} = \sqrt{\epsilon_{\mathrm{sup}}}(1 + |\mathbf{k}|) > 0$ (and importantly, $C_3 > 0$), giving the main result

$$\|\phi\|_{H^1(\Omega)} \geq C_3\,\|\nabla_{\mathbf{k}}\phi\|_{H(\mathrm{curl},\Omega)} \qquad \square \tag{A.1.42}$$

Completeness of $\nabla_{\mathbf{k}}S$ may be shown by demonstrating that every Cauchy sequence converges to a limit in the space. The approach used here is derived from [43]. Convergence of a given Cauchy sequence $\{\mathbf{u}_n\}$ in $\nabla_{\mathbf{k}}S$ is expressed as convergence in the space's norm

$$\lim_{k,l\to\infty}\left(\|\,(\mathbf{u}_k - \mathbf{u}_l)\,\|^2_{H_2(\mathrm{curl},\Omega)}\right) = 0 \tag{A.1.43}$$

which may be expanded as

$$\lim_{k,l\to\infty}\left(\|\,(\mathbf{u}_k - \mathbf{u}_l)\,\|^2_{\left[L^2_{\underline{\epsilon}(\mathbf{r})}(\Omega)\right]^3} + \|\nabla_{\mathbf{k}}\times\mathbf{u}_k - \nabla_{\mathbf{k}}\times\mathbf{u}_l\|^2_{[L^2(\Omega)]^3}\right) = 0 \tag{A.1.44}$$

As both terms are positive, each must converge to zero giving

$$\lim_{k,l\to\infty}\|\,(\mathbf{u}_k - \mathbf{u}_l)\,\|^2_{\left[L^2_{\underline{\epsilon}(\mathbf{r})}(\Omega)\right]^3} = 0 \tag{A.1.45}$$

Writing $\mathbf{u}_n$ as $\nabla_{\mathbf{k}}\phi_n$ and exploiting lemmas 2.1 and 2.2 gives

$$\lim_{k,l\to\infty} \|\phi_k - \phi_l\|^2_{L^2(\Omega)} + \lim_{k,l\to\infty} \sum_{|\alpha|=1} \|D^\alpha\phi_k - D^\alpha\phi_l\|^2_{L^2(\Omega)} = 0 \tag{A.1.46}$$

The limits may be collected giving

$$\lim_{k,l\to\infty} \|\phi_k - \phi_l\|^2_{H^1(\Omega)} = 0 \tag{A.1.47}$$

showing that $\{\phi_n\}$ is Cauchy in $H^1(\Omega)$, which by virtue of being complete contains the limit of this sequence ϕ_{lim} and consequently, $\nabla_{\mathbf{k}}\phi_{\text{lim}} \in \nabla_{\mathbf{k}}S$. Finally, using lemma 2.3 and the explicit definition of convergence gives

$$\begin{aligned} &\forall\epsilon > 0 \ \exists N : \|\phi_n - \phi_{\text{lim}}\|_{H^1(\Omega)} < \epsilon \text{ when } n > N \\ \implies \quad &\forall\epsilon > 0 \ \exists N : \|\nabla_{\mathbf{k}}\phi_n - \nabla_{\mathbf{k}}\phi_{\text{lim}}\|_{H(\text{curl},\Omega)} < \epsilon C_3^{-1} \text{ when } n > N \end{aligned} \tag{A.1.48}$$

which further implies that

$$\forall\epsilon > 0 \ \exists N : \|\nabla_{\mathbf{k}}\phi_n - \nabla_{\mathbf{k}}\phi_{\text{lim}}\|_{H(\text{curl},\Omega)} < \epsilon \text{ when } n > N \tag{A.1.49}$$

and shows that $\nabla_{\mathbf{k}}\phi_{\text{lim}}$ is the limit of the sequence $\{\nabla_{\mathbf{k}}\phi_n\}$. ■

A.2 Spectrum of the Variational Problem

The variational problem may be found using the approach given in [45] by multiplying by a sufficiently smooth testing function $\overline{\mathbf{F}}$ and integrating the result over

the domain Ω

$$\int_{\Omega} \left(\nabla \times \underline{\mu}\left(\mathbf{r}\right)^{-1} \nabla \times \mathbf{E} \right) \cdot \overline{\mathbf{F}} d\mathbf{r} - \omega^2 \int_{\Omega} \left(\underline{\epsilon}\left(\mathbf{r}\right) \mathbf{E} \right) \cdot \overline{\mathbf{F}} d\mathbf{r} = 0 \tag{A.2.1}$$

Using the generic vector identities

$$\begin{aligned} \nabla \cdot (\mathbf{a} \times \mathbf{b}) &= (\nabla \times \mathbf{a}) \cdot \mathbf{b} - \mathbf{a} \cdot (\nabla \times \mathbf{b}) \\ \mathbf{a} \cdot (\mathbf{b} \times \mathbf{c}) &= (\mathbf{a} \times \mathbf{b}) \cdot \mathbf{c} \end{aligned} \tag{A.2.2}$$

with the divergence theorem gives

$$\begin{aligned} \int_{\Omega} \left(\underline{\mu}\left(\mathbf{r}\right)^{-1} \nabla \times \mathbf{E} \right) \cdot \left(\nabla \times \overline{\mathbf{F}} \right) d\mathbf{r} + \int_{\partial\Omega} \hat{\mathbf{n}} \times \left(\underline{\mu}\left(\mathbf{r}\right)^{-1} \nabla \times \mathbf{E} \right) \cdot \overline{\mathbf{F}} \\ -\omega^2 \int_{\Omega} \left(\underline{\epsilon}\left(\mathbf{r}\right) \mathbf{E} \right) \cdot \overline{\mathbf{F}} d\mathbf{r} = 0 \end{aligned} \tag{A.2.3}$$

where $\hat{\mathbf{n}}$ is the unit normal vector on $\partial\Omega$. The following analysis assumes that $\underline{\epsilon}(\mathbf{r})$ and $\underline{\mu}(\mathbf{r})$ are second-rank Hermitian positive-definite tensors that are bounded from above and below, where the latter property ensures that $\underline{\mu}(\mathbf{r})^{-1}$ exists. Note that these restrictions are consistent with the electromagnetic properties of most conventional lossless materials.

Further work requires the domain of the problem to be specified. The band structure of a photonic crystal can examined by considering only the unit cell. This follows from Bloch's theorem, which states that the time-harmonic field in an infinite crystal must satisfy

$$\mathbf{E}\left(\mathbf{r} - \mathbf{d}\right) = e^{i\mathbf{k}\cdot\mathbf{d}} \mathbf{E}\left(\mathbf{r}\right) \tag{A.2.4}$$

from which it may be deduced that the field must be the product of a strictly

periodic function and a phase

$$\mathbf{E}(\mathbf{r}) = e^{i\mathbf{k}\cdot\mathbf{r}}\mathbf{E}_p(\mathbf{r}) \tag{A.2.5}$$

Although this expression may be substituted into (2.17a), this approach leads to working in the space of quasi-periodic functions. Analysis may be simplified by studying an equivalent problem in the space of strictly periodic functions, as done in [206]. The curl operator has the following effect on a Bloch function

$$\nabla \times \left[e^{i\mathbf{k}\cdot\mathbf{r}}\mathbf{E}_{\mathrm{p}}(\mathbf{r})\right] = e^{i\mathbf{k}\cdot\mathbf{r}}\left[i\mathbf{k}\times\mathbf{E}_{\mathrm{p}}(\mathbf{r}) + \nabla\times\mathbf{E}_{\mathrm{p}}(\mathbf{r})\right] \tag{A.2.6}$$

Therefore, the eigenvalue problem may be reformulated as

$$\begin{aligned}\int_{\Omega}\left(\underline{\mu}(\mathbf{r})^{-1}\nabla_{\mathbf{k}}\times\mathbf{E}_{\mathrm{p}}\right)\cdot\left(\overline{\nabla_{\mathbf{k}}\times\mathbf{F}_{\mathrm{p}}}\right)d\mathbf{r} \\ + \int_{\partial\Omega}\left[\hat{\mathbf{n}}\times\left(\underline{\mu}(\mathbf{r})^{-1}\nabla_{\mathbf{k}}\times\mathbf{E}_{\mathrm{p}}\right)\right]\cdot\overline{\mathbf{F}}_{\mathrm{p}} + \omega^2\int_{\Omega}\left(\underline{\epsilon}(\mathbf{r})\,\mathbf{E}_{\mathrm{p}}\right)\cdot\overline{\mathbf{F}}_{\mathrm{p}}d\mathbf{r} = 0\end{aligned} \tag{A.2.7}$$

where $\nabla_{\mathbf{k}} = \nabla + i\mathbf{k}$ and $\partial\Omega$ is the boundary of Ω, which is now defined as the subset of $\mathbb{R}^3$ occupied by the unit cell

$$\mathbb{R}^3_{\mathrm{UC}} = \left\{\mathbf{r}\in\mathbb{R}^3 : \mathbf{g}_i\cdot\mathbf{r} \le 2\pi \ \forall i\in\{1,2,3\}\right\} \tag{A.2.8}$$

where $\mathbf{g}_i$ are the reciprocal lattice vectors. Similarly, the irreducible Brillouin zone (unit cell of the reciprocal lattice) may be defined as

$$\mathbb{R}^3_{\mathrm{IBZ}} = \left\{\mathbf{k}\in\mathbb{R}^3\backslash G : \mathbf{a}_i\cdot\mathbf{k} \le 2\pi \ \forall i\in\{1,2,3\}\right\} \tag{A.2.9}$$

where $\mathbf{a}_i$ are the direct lattice vectors. Note that the condition $\mathbf{k}\notin G$ ensures that

$\mathbf{k}+\mathbf{G} \neq \mathbf{0}\ \forall \mathbf{G} \in G$. As $\mathbf{E}_\mathrm{p}$ and $\mathbf{F}_\mathrm{p}$ are periodic, the boundary term vanishes, leaving

$$\int_\Omega \left(\underline{\mu}\left(\mathbf{r}\right)^{-1} \nabla_\mathbf{k} \times \mathbf{E}_\mathrm{p}\right) \cdot \left(\overline{\nabla_\mathbf{k} \times \mathbf{F}_\mathrm{p}}\right) d\mathbf{r} - \omega^2 \int_\Omega \left(\underline{\epsilon}\left(\mathbf{r}\right) \mathbf{E}_\mathrm{p}\right) \cdot \overline{\mathbf{F}}_\mathrm{p} d\mathbf{r} = 0 \tag{A.2.10}$$

The correct space for $\mathbf{E}_\mathrm{p}$ and $\mathbf{F}_\mathrm{p}$ is now identified as $H(\mathrm{curl}, \Omega)$. Without additional treatment, the null space of the $\nabla_\mathbf{k}\times$ operator presents difficulty in the ensuing analysis. This issue may be resolved by using the Helmholtz decomposition, following the approach used in [45], which rests on decomposing $H(\mathrm{curl}, \Omega)$ as a direct sum of two closed subspaces

$$H\left(\mathrm{curl}, \Omega\right) = H_2\left(\mathrm{curl}, \Omega\right) \oplus \nabla_\mathbf{k} S \tag{A.2.11}$$

where $H_2(\mathrm{curl}, \Omega) = \nabla_\mathbf{k} S^\perp$. This decomposition stipulates that

$$\left(\mathbf{u}, \mathbf{v}\right)_{H(\mathrm{curl},\Omega)} = 0 \quad \forall \mathbf{u} \in H_2\left(\mathrm{curl}, \Omega\right),\ \ \mathbf{v} \in \nabla_\mathbf{k} S \tag{A.2.12}$$

a trivial consequence of which is that

$$\left(\mathbf{u}, \mathbf{v}\right)_{\left[L^2_{\underline{\epsilon}(\mathbf{r})}(\Omega)\right]^3} = 0 \quad \forall \mathbf{u} \in H_2\left(\mathrm{curl}, \Omega\right),\ \ \mathbf{v} \in \nabla_\mathbf{k} S \tag{A.2.13}$$

Equation A.2.10 may now be written as

$$\begin{aligned}&\int_\Omega \left(\underline{\mu}\left(\mathbf{r}\right)^{-1} \nabla_\mathbf{k} \times \left(\mathbf{E}_1 + \mathbf{E}_2\right)\right) \cdot \left(\overline{\nabla_\mathbf{k} \times \left(\mathbf{F}_1 + \mathbf{F}_2\right)}\right) d\mathbf{r} \\ &-\omega^2 \int_\Omega \left(\underline{\epsilon}\left(\mathbf{r}\right)\left(\mathbf{E}_1 + \mathbf{E}_2\right)\right) \cdot \left(\overline{\mathbf{F}_1 + \mathbf{F}_2}\right) d\mathbf{r} = 0 \quad \forall \mathbf{F}_1 \in H_2\left(\mathrm{curl}, \Omega\right) \quad \forall \mathbf{F}_2 \in \nabla_\mathbf{k} S\end{aligned} \tag{A.2.14}$$

where $\mathbf{E}_1 \in H_2(\mathrm{curl}, \Omega)$ and $\mathbf{E}_2 \in \nabla_\mathbf{k} S$. Using (A.2.11), the identity $\nabla_\mathbf{k} \times \nabla_\mathbf{k} \phi = 0$,

and (A.2.13) gives two equations

$$\begin{aligned}&\int_{\Omega}\left(\underline{\mu}\left(\mathbf{r}\right)^{-1}\nabla_{\mathbf{k}}\times\mathbf{E}_{1}\right)\cdot\left(\overline{\nabla_{\mathbf{k}}\times\mathbf{F}_{1}}\right)d\mathbf{r}\\&-\omega^{2}\int_{\Omega}\left(\left(\underline{\epsilon}\left(\mathbf{r}\right)\mathbf{E}_{1}\right)\cdot\overline{\mathbf{F}}_{1}+\left(\underline{\epsilon}\left(\mathbf{r}\right)\mathbf{E}_{2}\right)\cdot\overline{\mathbf{F}}_{2}\right)d\mathbf{r}=0\quad\forall\mathbf{F}_{1}\in H_{2}\left(\mathrm{curl},\Omega\right)\end{aligned}\tag{A.2.15}$$

and

$$\omega^{2}\int_{\Omega}\left(\underline{\epsilon}\left(\mathbf{r}\right)\mathbf{E}_{2}\right)\cdot\overline{\mathbf{F}}_{2}d\mathbf{r}=0\quad\forall\mathbf{F}_{2}\in\nabla_{\mathbf{k}}S\tag{A.2.16}$$

As the second equation implies that $\mathbf{E}_2 = 0$, (A.2.14) is reduced to finding a solution in $H_2(\mathrm{curl}, \Omega)$. The remaining analysis concerns finding the inverse differential operator contained within (A.0.1) and begins by defining a sesquilinear form as

$$\tilde{a}\left(\mathbf{u},\mathbf{v}\right)=\int_{\Omega}\left(\underline{\mu}\left(\mathbf{r}\right)^{-1}\nabla_{\mathbf{k}}\times\mathbf{u}\right)\cdot\left(\overline{\nabla_{\mathbf{k}}\times\mathbf{v}}\right)d\mathbf{r}\quad\forall\mathbf{u},\mathbf{v}\in H_{2}\left(\mathrm{curl},\Omega\right)\tag{A.2.17}$$

This sesquilinear form is bounded and coercive. The latter of property may be expressed as

$$\tilde{a}\left(\mathbf{u},\mathbf{u}\right)\geq K\|\mathbf{u}\|_{H(\mathrm{curl},\Omega)}^{2}\quad\forall\mathbf{u},\mathbf{v}\in H_{2}\left(\mathrm{curl},\Omega\right)\tag{A.2.18}$$

for some $K > 0$. These properties are proved in the following proposition

Proposition 3: *The sesquilinear form of (A.2.17) bounded and coercive.*

Proof. The following lemma is required for this proof.

Lemma 3.1: *For all* $\psi \in H^1(\Omega)$ *there exists* $D > 0$ *such that* $\|\psi\|_{H^1(\Omega)}^2 \leq D\|\nabla_{\mathbf{k}}\psi\|_{[L^2(\Omega)]^3}^2$

This may readily be shown by expanding ψ as a Fourier series

$$\left\| \sum_{\mathbf{G}\in G} \psi_{\mathbf{G}} e^{i\mathbf{G}\cdot\mathbf{r}} \right\|^2_{H^1(\Omega)} = \sum_{\mathbf{G}\in G} \left(1+|\mathbf{G}|^2\right) |\psi_{\mathbf{G}}|^2 \tag{A.2.19}$$

where the $\psi_{\mathbf{G}}$ are the Fourier series coefficients. Thus,

$$\|\psi\|^2_{H^1(\Omega)} \leq D \|\nabla_{\mathbf{k}}\psi\|^2_{[L^2(\Omega)]^3} \tag{A.2.20}$$

where D is a constant independent of ψ given by $D = \max\{(1+|\mathbf{G}|^2)/|\mathbf{k}+\mathbf{G}|^2 : \mathbf{G}\in G\} > 0$. $\square$

Boundedness is readily shown with the Cauchy–Schwartz inequality

$$\begin{aligned}
|\tilde{a}(\mathbf{u},\mathbf{v})| &\leq \mu_{\text{sup}}^{-1} \left| \int_\Omega (\nabla_{\mathbf{k}}\times\mathbf{u}) \cdot \left(\overline{\nabla_{\mathbf{k}}\times\mathbf{v}}\right) d\mathbf{r} \right| \\
&\leq \mu_{\text{sup}}^{-1} \left| (\nabla_{\mathbf{k}}\times\mathbf{u}, \nabla_{\mathbf{k}}\times\mathbf{v})_{[L^2(\Omega)]^3} \right| \\
&\leq \mu_{\text{sup}}^{-1} \|\nabla_{\mathbf{k}}\times\mathbf{u}\|_{[L^2(\Omega)]^3} \|\nabla_{\mathbf{k}}\times\mathbf{v}\|_{[L^2(\Omega)]^3} \\
&\leq \mu_{\text{sup}}^{-1} \|\mathbf{u}\|_{H(\text{curl},\Omega)} \|\mathbf{v}\|_{H(\text{curl},\Omega)} \qquad \forall \mathbf{u},\mathbf{v} \in H_2(\text{curl},\Omega)
\end{aligned} \tag{A.2.21}$$

Showing that (A.2.17) is coercive is somewhat more involved. Two projection operators of $\mathbb{C}^3$ may be defined as

$$\begin{aligned}
P_{\times,\mathbf{G}}\mathbf{t} &= -\frac{1}{|\mathbf{G}+\mathbf{k}|^2} (\mathbf{G}+\mathbf{k})\times(\mathbf{G}+\mathbf{k})\times\mathbf{t} \\
P_{\cdot,\mathbf{G}}\mathbf{t} &= \frac{1}{|\mathbf{G}+\mathbf{k}|^2} (\mathbf{G}+\mathbf{k})(\mathbf{G}+\mathbf{k})\cdot\mathbf{t}
\end{aligned} \tag{A.2.22}$$

where $P_{\times,\mathbf{G}}P_{\cdot,\mathbf{G}} = P_{\cdot,\mathbf{G}}P_{\times,\mathbf{G}} = \underline{\mathbf{0}}$, $P_{\times,\mathbf{G}} + P_{\cdot,\mathbf{G}} = \underline{\mathbf{I}}$, and $\mathbf{t}\in\mathbb{C}^3$. The sesquilinear

form may be estimated by using a bound for the inverse permeability and expanding the integral as a Fourier series

$$\tilde{a}\left(\mathbf{u},\mathbf{u}\right) \quad \geq \quad \mu_{\text{inf}}^{-1}\left(\nabla_{\mathbf{k}}\times\mathbf{u},\nabla_{\mathbf{k}}\times\mathbf{u}\right)_{[L^2(\Omega)]^3} \tag{A.2.23}$$

which may be written as

$$\tilde{a}\left(\mathbf{u},\mathbf{u}\right) \geq \mu_{\text{inf}}^{-1}\sum_{\mathbf{G}\in G}\left|\left(\mathbf{G}+\mathbf{k}\right)\times\mathbf{u}_{\mathbf{G}}\right|^2 \tag{A.2.24}$$

Employing the generic identity

$$\left|\mathbf{a}\times\mathbf{u}\right| = \frac{1}{\left|\mathbf{a}\right|}\left|\mathbf{a}\times\mathbf{a}\times\mathbf{u}\right| \quad \text{when} \quad \mathbf{a}\neq\mathbf{0} \tag{A.2.25}$$

gives

$$\tilde{a}\left(\mathbf{u},\mathbf{u}\right) \geq \mu_{\text{inf}}^{-1}\sum_{\mathbf{G}\in G}\frac{1}{\left|\mathbf{G}+\mathbf{k}\right|^2}\left|\left(\mathbf{G}+\mathbf{k}\right)\times\left(\mathbf{G}+\mathbf{k}\right)\times\mathbf{u}_{\mathbf{G}}\right|^2 \tag{A.2.26}$$

Using (A.2.22) this may be written as

$$\tilde{a}\left(\mathbf{u},\mathbf{u}\right) \geq \mu_{\text{inf}}^{-1}\sum_{\mathbf{G}\in G}\left|\mathbf{G}+\mathbf{k}\right|^2\left|P_{\times,\mathbf{G}}\mathbf{u}_{\mathbf{G}}\right|^2 \tag{A.2.27}$$

A scalar function $\psi\in H^1(\Omega)$ may be defined as

$$iP_{\cdot,\mathbf{G}}\left(\mathbf{G}+\mathbf{k}\right)\psi_{\mathbf{G}} = -P_{\cdot,\mathbf{G}}\mathbf{u}_{\mathbf{G}} \tag{A.2.28}$$

This definition is consistent with the inclusion of ψ in $H^1(\Omega)$, which may be seen

by considering

$$\begin{aligned} iP_{\cdot,\mathbf{G}}\left(\mathbf{G}+\mathbf{k}\right)\psi_{\mathbf{G}} = i\left(\mathbf{G}+\mathbf{k}\right)\psi_{\mathbf{G}} &= -P_{\cdot,\mathbf{G}}\mathbf{u}_{\mathbf{G}} \\ &= -\frac{\left(\mathbf{G}+\mathbf{k}\right)\left(\mathbf{G}+\mathbf{k}\right)}{\left|\mathbf{G}+\mathbf{k}\right|^2}\cdot\mathbf{u}_{\mathbf{G}} \end{aligned} \tag{A.2.29}$$

which, using lemma 3.1, yields

$$\begin{aligned} \left\|\psi\right\|^2_{H^1(\Omega)} \leq D\left\|\nabla_{\mathbf{k}}\psi\right\|^2_{[L^2(\Omega)]^3} &= D\sum_{\mathbf{G}\in G}\left|\left(\mathbf{G}+\mathbf{k}\right)\psi_{\mathbf{G}}\right|^2 \\ &= D\sum_{\mathbf{G}\in G}\frac{\left|\left(\mathbf{G}+\mathbf{k}\right)\left(\mathbf{G}+\mathbf{k}\right)\cdot\mathbf{u}_{\mathbf{G}}\right|^2}{\left|\mathbf{G}+\mathbf{k}\right|^4} \\ &\leq D\sum_{\mathbf{G}\in G}\frac{\left|\mathbf{G}+\mathbf{k}\right|^4\left|\mathbf{u}_{\mathbf{G}}\right|^2}{\left|\mathbf{G}+\mathbf{k}\right|^4} = D\left\|\mathbf{u}\right\|^2_{[L^2(\Omega)]^3} \end{aligned} \tag{A.2.30}$$

Noting that $P_{\cdot,\mathbf{G}}(\mathbf{u}_{\mathbf{G}}+i(\mathbf{G}+\mathbf{k})\psi)=\mathbf{0}$ and $P_{\times,\mathbf{G}}(\mathbf{G}+\mathbf{k})\psi=\mathbf{0}$, (A.2.27) may be written as

$$\begin{aligned} \tilde{a}\left(\mathbf{u},\mathbf{u}\right) &\geq \mu_{\text{inf}}^{-1}\sum_{\mathbf{G}\in G}\left|\mathbf{G}+\mathbf{k}\right|^2\left|\left(P_{\times,\mathbf{G}}+P_{\cdot,\mathbf{G}}\right)\left(\mathbf{u}_{\mathbf{G}}+i\left(\mathbf{G}+\mathbf{k}\right)\psi_{\mathbf{G}}\right)\right|^2 \\ &= \mu_{\text{inf}}^{-1}\sum_{\mathbf{G}\in G}\left|\mathbf{G}+\mathbf{k}\right|^2\left|\mathbf{u}_{\mathbf{G}}+i\left(\mathbf{G}+\mathbf{k}\right)\psi_{\mathbf{G}}\right|^2 \\ &\geq E\left\|\mathbf{u}+\nabla_{\mathbf{k}}\psi\right\|^2_{[L^2(\Omega)]^3} \end{aligned} \tag{A.2.31}$$

where $E = \min\{\mu_{\text{inf}}^{-1}|\mathbf{G}+\mathbf{k}|^2 : \mathbf{G} \in G\} > 0$. Finally, consider that

$$\begin{aligned}
\tilde{a}(\mathbf{u},\mathbf{u}) &\geq E\mu_{\text{inf}}^{-1} \left\| \sqrt{\underline{\epsilon}(\mathbf{r})}\,(\mathbf{u}+\nabla_{\mathbf{k}}\psi) \right\|^2_{[L^2(\Omega)]^3} \\
&= E\mu_{\text{inf}}^{-1} \left\| \mathbf{u}+\nabla_{\mathbf{k}}\psi \right\|^2_{\left[L^2_{\underline{\epsilon}(\mathbf{r})}(\Omega)\right]^3} \\
&= F \left\| \mathbf{u} \right\|^2_{\left[L^2_{\underline{\epsilon}(\mathbf{r})}(\Omega)\right]^3} + F \left\| (\mathbf{G}+\mathbf{k})\,\psi \right\|^2_{\left[L^2_{\underline{\epsilon}(\mathbf{r})}(\Omega)\right]^3} \\
&\geq F \left\| \mathbf{u} \right\|^2_{\left[L^2_{\underline{\epsilon}(\mathbf{r})}(\Omega)\right]^3}
\end{aligned} \tag{A.2.32}$$

where (A.2.13) has been used and $F = E\epsilon_{\text{inf}}^{-1} > 0$. Using (A.2.32), (A.2.23), and letting $K = \frac{1}{2}\min\{\mu_{\text{inf}}^{-1}, F\} > 0$ gives

$$\tilde{a}(\mathbf{u},\mathbf{u}) \geq K\|\mathbf{u}\|^2_{H(\text{curl},\Omega)} \tag{A.2.33}$$

which shows that the sesquilinear form is coercive. ■

Thus, by the Lax–Milgram theorem [43] for every $\mathbf{u} \in [L^2_{\underline{\epsilon}(\mathbf{r})}(\Omega)]^3$ there exists a $\mathbf{w} \in H_2(\text{curl},\Omega)$ such that

$$\tilde{a}(\mathbf{w},\mathbf{v}) = \int_\Omega (\underline{\epsilon}(\mathbf{r})\,\mathbf{u}) \cdot \overline{\mathbf{v}} d\mathbf{r} \quad \forall \mathbf{v} \in H_2(\text{curl},\Omega) \tag{A.2.34}$$

As $\underline{\epsilon}(\mathbf{r})$ is bounded the right-hand side is a bounded linear functional. The operator $A : [L^2_{\underline{\epsilon}(\mathbf{r})}(\Omega)]^3 \to H_2(\text{curl},\Omega)$ may be defined as $\mathbf{w} = A\mathbf{u}$

$$\tilde{a}(A\mathbf{u},\mathbf{v}) = \int_\Omega (\underline{\epsilon}(\mathbf{r})\,\mathbf{u}) \cdot \overline{\mathbf{v}} d\mathbf{r} \quad \forall \mathbf{u} \in \left[L^2_{\underline{\epsilon}(\mathbf{r})}(\Omega)\right]^3, \forall \mathbf{v} \in H_2(\text{curl},\Omega) \tag{A.2.35}$$

This may be repeated for $\mathbf{v}$, yielding

$$\tilde{a}\left(\mathbf{u}, B\mathbf{v}\right) = \int_{\Omega} \left(\underline{\epsilon}\left(\mathbf{r}\right)\mathbf{u}\right) \cdot \overline{\mathbf{v}} d\mathbf{r} \quad \forall \mathbf{u} \in H_2\left(\mathrm{curl}, \Omega\right), \forall \mathbf{v} \in \left[L^2_{\underline{\epsilon}(\mathbf{r})}\left(\Omega\right)\right]^3 \tag{A.2.36}$$

From the definition of the sesquilinear form (A.2.17), it may be readily shown that $A = B$ if $\underline{\mu}\left(\mathbf{r}\right)^{-1}$ and $\underline{\epsilon}(\mathbf{r})$ are Hermitian and positive-definite. Moreover, using (A.2.33) and the Cauchy–Schwarz inequality, the following series of inequalities

$$\begin{aligned} K \left\|A\mathbf{u}\right\|_{H(\mathrm{curl},\Omega))} \left\|A\mathbf{u}\right\|_{\left[L^2_{\underline{\epsilon}(\mathbf{r})}(\Omega)\right]^3} &\leq K \left\|A\mathbf{u}\right\|^2_{H(\mathrm{curl},\Omega)} \\ &\leq \left|\tilde{a}\left(A\mathbf{u}, A\mathbf{u}\right)\right| = \left| \int_{\Omega} \left(\underline{\epsilon}\left(\mathbf{r}\right)\mathbf{u}\right) \cdot \left(\overline{A\mathbf{u}}\right) d\mathbf{r} \right| \\ &\leq \left\|A\mathbf{u}\right\|_{\left[L^2_{\underline{\epsilon}(\mathbf{r})}(\Omega)\right]^3} \left\|\mathbf{u}\right\|_{\left[L^2_{\underline{\epsilon}(\mathbf{r})}(\Omega)\right]^3} \end{aligned} \tag{A.2.37}$$

$\forall \mathbf{u} \in [L^2_{\underline{\epsilon}(\mathbf{r})}(\Omega)]^3$ may be used to show that

$$\left\|A\mathbf{u}\right\|_{H(\mathrm{curl},\Omega)} \leq K^{-1} \left\|\mathbf{u}\right\|_{\left[L^2_{\underline{\epsilon}(\mathbf{r})}(\Omega)\right]^3} \quad \forall \mathbf{u} \in \left[L^2_{\underline{\epsilon}(\mathbf{r})}\left(\Omega\right)\right]^3 \tag{A.2.38}$$

demonstrating that the operator A is bounded (note that $K^{-1} > 0$). The eigenvalue equation may now be written as

$$\underline{\epsilon}\left(\mathbf{r}\right)\mathbf{u} = \omega^2 \underline{\epsilon}\left(\mathbf{r}\right) I A\mathbf{u} \tag{A.2.39}$$

where I is the injection $I : H_2(\mathrm{curl}, \Omega) \rightarrow [L^2_{\underline{\epsilon}(\mathbf{r})}(\Omega)]^3$ (henceforth implicitly contained within A). Noting that $\underline{\epsilon}(\mathbf{r})$ is invertible, (A.2.39) may be written as

$$\mathbf{u} = \omega^2 A\mathbf{u} \tag{A.2.40}$$

where A is the inverse to the differential operator of (A.0.1). The operator A is compact in the space $[L^2_{\underline{\epsilon}(\mathbf{r})}(\Omega)]^3$. Proof of the following proposition is required to show this.

Proposition 4: *The injection* $H_2(\mathrm{curl}, \Omega) \rightarrow [L^2_{\underline{\epsilon}(\mathbf{r})}(\Omega)]^3$ *is compact.*

Proof. This is a modification of a proof of Rellich's Theorem found in [207]. Given a bounded set B in $H_2(\mathrm{curl}, \Omega)$, it is necessary to show that for each sequence in $\mathbf{v}_k \subset B$ there is a subsequence $\mathbf{u}_k$ that converges in $[L^2_{\underline{\epsilon}(\mathbf{r})}(\Omega)]^3$. As B is a ball in $H_2(\mathrm{curl}, \Omega)$, each sequence contains a subsequence in $H_2(\mathrm{curl}, \Omega)$, that converges weakly to an element $\mathbf{u}$. It is possible to redefine this sequence by letting $\mathbf{u}_n \rightarrow \mathbf{u}_n - \mathbf{u}$, so that the subsequence $\mathbf{u}_n$ converges weakly to $\mathbf{0}$. Using (A.2.13), the $[L^2_{\underline{\epsilon}(\mathbf{r})}(\Omega)]^3$ norm of the n^{th} member of the sequence may be expressed as

$$\begin{aligned} \|\mathbf{u}_n\|^2_{\left[L^2_{\underline{\epsilon}(\mathbf{r})}(\Omega)\right]^3} &\leq \|\mathbf{u}_n\|^2_{\left[L^2_{\underline{\epsilon}(\mathbf{r})}(\Omega)\right]^3} + \|\nabla_{\mathbf{k}}\psi_n\|^2_{\left[L^2_{\underline{\epsilon}(\mathbf{r})}(\Omega)\right]^3} = \|\mathbf{u}_n + \nabla_{\mathbf{k}}\psi_n\|^2_{\left[L^2_{\underline{\epsilon}(\mathbf{r})}(\Omega)\right]^3} \\ &\leq \epsilon_{\text{sup}} \|\mathbf{u}_n + \nabla_{\mathbf{k}}\psi_n\|^2_{[L^2(\Omega)]^3} \end{aligned} \tag{A.2.41}$$

where ψ_n is determined in accordance with (A.2.28). This expression may be split into two terms

$$J_{1,n} = \sum_{\substack{\mathbf{G}\in G \\ |\mathbf{G}+\mathbf{k}|\leq R}} |\mathbf{u}_{\mathbf{G},n} + i\,(\mathbf{G}+\mathbf{k})\,\psi_{\mathbf{G},n}|^2 \tag{A.2.42a}$$

$$J_{2,n} = \sum_{\substack{\mathbf{G}\in G \\ |\mathbf{G}+\mathbf{k}|> R}} |\mathbf{u}_{\mathbf{G},n} + i\,(\mathbf{G}+\mathbf{k})\,\psi_{\mathbf{G},n}|^2 \tag{A.2.42b}$$

such that

$$\|\mathbf{u}_n\|^2_{\left[L^2_{\underline{\epsilon}(\mathbf{r})}(\Omega)\right]^3} \leq \epsilon_{\text{sup}}\,(J_{1,n} + J_{2,n}) \tag{A.2.43}$$

The second term may be estimated as follows

$$R^2 J_{2,n} \leq \sum_{\substack{\mathbf{G}\in G \\ |\mathbf{G}+\mathbf{k}|>R}} |\mathbf{G}+\mathbf{k}|^2 \left|\mathbf{u}_{\mathbf{G},n} + i\left(\mathbf{G}+\mathbf{k}\right)\psi_{\mathbf{G},n}\right|^2 \tag{A.2.44}$$

The $|\mathbf{G}+\mathbf{k}| > R$ condition may be relaxed because each term of the resultant sum is non-negative. Furthermore, (A.2.12), (A.2.21), and the second equation of (A.2.31) may be reused in the present discussion by setting $\underline{\mu}(\mathbf{r})^{-1} = \underline{\mathbf{I}}$ to give

$$\begin{aligned}
J_{2,n} \quad &\leq \quad \frac{1}{R^2}\sum_{\mathbf{G}\in G} |\mathbf{G}+\mathbf{k}|^2 \left|\mathbf{u}_{\mathbf{G},n} + i\left(\mathbf{G}+\mathbf{k}\right)\psi_{\mathbf{G},n}\right|^2 \\
&\leq_{(A.2.31)} \quad \frac{1}{R^2}\tilde{a}\left(\mathbf{u}_n + \nabla_{\mathbf{k}}\psi_n, \mathbf{u}_n + \nabla_{\mathbf{k}}\psi_n\right) \\
&\leq_{(A.2.21)} \quad \frac{1}{R^2}\left\|\mathbf{u}_n + \nabla_{\mathbf{k}}\psi_n\right\|^2_{H(\mathrm{curl},\Omega)} \\
&=_{(A.2.12)} \quad \frac{1}{R^2}\left(\left\|\mathbf{u}_n\right\|^2_{H(\mathrm{curl},\Omega)} + \left\|\nabla_{\mathbf{k}}\psi_n\right\|^2_{H(\mathrm{curl},\Omega)}\right) \\
&= \quad \frac{1}{R^2}\left(\left\|\mathbf{u}_n\right\|^2_{H(\mathrm{curl},\Omega)} + \left\|\nabla_{\mathbf{k}}\psi_n\right\|^2_{\left[L^2_{\underline{\epsilon}(\mathbf{r})}(\Omega)\right]^3}\right) \\
&\leq \quad \frac{1}{R^2}\left(\left\|\mathbf{u}_n\right\|^2_{H(\mathrm{curl},\Omega)} + \epsilon_{\mathrm{sup}}\left\|\nabla_{\mathbf{k}}\psi_n\right\|^2_{[L^2(\Omega)]^3}\right)
\end{aligned} \tag{A.2.45}$$

Finally, using (A.2.30) this becomes

$$\begin{aligned}
J_{2,n} \quad &\leq \quad \frac{1}{R^2}\left(\left\|\mathbf{u}_n\right\|^2_{H(\mathrm{curl},\Omega)} + \epsilon^{-1}_{\mathrm{sup}}\epsilon_{\mathrm{sup}}\left\|\mathbf{u}_n\right\|^2_{\left[L^2_{\underline{\epsilon}(\mathbf{r})}(\Omega)\right]^3}\right) \\
&\leq \quad \frac{1}{R^2}\left(1 + \epsilon^{-1}_{\mathrm{sup}}\epsilon_{\mathrm{sup}}\right)\left\|\mathbf{u}_n\right\|^2_{H(\mathrm{curl},\Omega)}
\end{aligned} \tag{A.2.46}$$

As $\mathbf{u}_n$ belongs to a bounded set in $H_2(\mathrm{curl},\Omega)$, its norm is bounded from above by a constant greater than zero that is independent of n. Thus, for any $\delta > 0$ there exists an R such that

$$J_{2,n} \leq \delta/2 \tag{A.2.47}$$

Note that foregoing procedure is required for estimating $J_{2,n}$ as weak convergence does not imply convergence in the norm (strong convergence).

The term $J_{1,n}$ is estimated more readily. Given that $\mathbf{u}_n \rightharpoonup \mathbf{0}$ as $n \to \infty$ in $H_2(\mathrm{curl}, \Omega)$, the following holds

$$\lim_{n\to\infty} \quad l\left(\mathbf{u}_n\right) = 0 \quad \forall l\left(\cdot\right) \in H_2'\left(\mathrm{curl}, \Omega\right) \tag{A.2.48}$$

where $l(\cdot)$ is an arbitrary bounded linear functional and $H_2'(\mathrm{curl}, \Omega)$ is the continuous dual of $H_2(\mathrm{curl}, \Omega)$. A collection of bounded linear functionals may be defined as

$$l_{\mathbf{G}'}\left(\cdot\right) = \int_\Omega e^{-i\mathbf{G}'\cdot\mathbf{r}}\left(\cdot\right) d\mathbf{r} \tag{A.2.49}$$

and hence

$$\lim_{n\to\infty} \quad l_{\mathbf{G}'}\left(\mathbf{u}_{\mathbf{G},n} e^{i\mathbf{G}\cdot\mathbf{r}}\right) = 0 \quad \forall \mathbf{G}' \in G \tag{A.2.50}$$

which, using (A.2.28), gives

$$\lim_{n\to\infty} \quad l_{\mathbf{G}'}\left(i\left(\mathbf{G}+\mathbf{k}\right)\psi_{\mathbf{G},n} e^{i\mathbf{G}\cdot\mathbf{r}}\right) = 0 \quad \forall \mathbf{G}' \in G \tag{A.2.51}$$

and finally,

$$\lim_{n\to\infty} \quad \left|\mathbf{u}_{\mathbf{G},n} + i\left(\mathbf{G}+\mathbf{k}\right)\psi_{\mathbf{G},n}\right| = 0 \quad \forall \mathbf{G} \in G : \left|\mathbf{G}+\mathbf{k}\right| \leq R \tag{A.2.52}$$

Thus for any $\delta > 0$ there is a value of n such that

$$J_{1,n} \leq \delta/2 \tag{A.2.53}$$

Finally, for any $\delta > 0$ there exists values of n and R (independent of n) such that

$$\|\mathbf{u}_n\|^2_{\left[L^2_{\underline{\epsilon}(\mathbf{r})}(\Omega)\right]^3} \leq \epsilon_{\sup}\delta \tag{A.2.54}$$

which proves that $\mathbf{u}_n$ is strongly convergent in $[L^2_{\underline{\epsilon}(\mathbf{r})}(\Omega)]^3$ and therefore the injection $H_2(\mathrm{curl}, \Omega) \to [L^2_{\underline{\epsilon}(\mathbf{r})}(\Omega)]^3$ is compact. ■

The final result is shown by the following proposition.

Proposition 5: *The eigenvalue problem of (A.2.1) possesses eigenvalues (ω^2) that form a discrete set of positive numbers that commence at a minimum value greater than zero and increase monotonically. The associated eigenmodes are mutually orthogonal with respect to the energy inner product of $[L^2_{\underline{\epsilon}(\mathbf{r})}(\Omega)]^3$.*

Proof. The operator A in $[L^2_{\underline{\epsilon}(\mathbf{r})}(\Omega)]^3$ is compact as it is a composition of a bounded operator and a compact injection [42]. For all $\mathbf{v} \in [L^2_{\underline{\epsilon}(\mathbf{r})}(\Omega)]^3$ a bounded linear functional may be defined as

$$l(\mathbf{u}) = (A\mathbf{u}, \mathbf{v})_{\left[L^2_{\underline{\epsilon}(\mathbf{r})}(\Omega)\right]^3} \tag{A.2.55}$$

$\forall \mathbf{u} \in [L^2_{\underline{\epsilon}(\mathbf{r})}(\Omega)]^3$. By the Riesz representation theorem [43], there exists a unique $\mathbf{z}$ that satisfies

$$(\mathbf{u}, \mathbf{z})_{\left[L^2_{\underline{\epsilon}(\mathbf{r})}(\Omega)\right]^3} = (A\mathbf{u}, \mathbf{v})_{\left[L^2_{\underline{\epsilon}(\mathbf{r})}(\Omega)\right]^3} \tag{A.2.56}$$

The adjoint operator $A^* : [L^2_{\underline{\epsilon}(\mathbf{r})}(\Omega)]^3 \to [L^2_{\underline{\epsilon}(\mathbf{r})}(\Omega)]^3$ may now be defined as $A^*\mathbf{v} = \mathbf{z}$, and hence

$$(\mathbf{u}, A^*\mathbf{v})_{\left[L^2_{\underline{\epsilon}(\mathbf{r})}(\Omega)\right]^3} = (A\mathbf{u}, \mathbf{v})_{\left[L^2_{\underline{\epsilon}(\mathbf{r})}(\Omega)\right]^3} \quad \forall \mathbf{u}, \mathbf{v} \in \left[L^2_{\underline{\epsilon}(\mathbf{r})}(\Omega)\right]^3 \tag{A.2.57}$$

By substituting $\mathbf{v}$ with $A\mathbf{v}$ and $\mathbf{u}$ with $A\mathbf{u}$ in (A.2.35) and (A.2.36) respectively and subsequently equating the the right-hand sides, the following relation may be found

$$(\mathbf{u}, A\mathbf{v})_{\left[L^2_{\underline{\epsilon}(\mathbf{r})}(\Omega)\right]^3} = (A\mathbf{u}, \mathbf{v})_{\left[L^2_{\underline{\epsilon}(\mathbf{r})}(\Omega)\right]^3} \quad \forall \mathbf{u}, \mathbf{v} \in \left[L^2_{\underline{\epsilon}(\mathbf{r})}(\Omega)\right]^3 \tag{A.2.58}$$

This leads to the conclusion that $A^* = A$; that is, the operator A is self-adjoint.

The spectrum of a compact self-adjoint operator is very special. In particular, the continuous and residual spectra are empty and the point spectrum consists of discrete values that can only accumulate at zero and must be of finite multiplicity [42]. This allows A to be expressed as

$$A(\cdot) = \sum_{\omega^{-2} \in \sigma(A)} \omega^{-2} \mathbf{u}_\omega (\cdot, \mathbf{u}_\omega)_{\left[L^2_{\underline{\epsilon}(\mathbf{r})}(\Omega)\right]^3} \tag{A.2.59}$$

where $\sigma(A)$ is the spectrum of A and

$$(\mathbf{u}_{\omega 1}, \mathbf{u}_{\omega 2})_{\left[L^2_{\underline{\epsilon}(\mathbf{r})}(\Omega)\right]^3} = \delta_{1,2} \tag{A.2.60}$$

Returning to the original eigenvalue problem of (A.2.1) and recalling that A is the inverse of the differential operator, the following holds

$$\underline{\epsilon}(\mathbf{r})^{-1} \nabla \times \underline{\mu}(\mathbf{r})^{-1} \nabla \times (\cdot) = A^{-1}(\cdot) = \sum_{\omega^{-2} \in \sigma(A)} \omega^2 \mathbf{u}_\omega (\cdot, \mathbf{u}_\omega)_{\left[L^2_{\underline{\epsilon}(\mathbf{r})}(\Omega)\right]^3} \tag{A.2.61}$$

from which it may be concluded that the eigenvalues (ω^2) form a discrete set of positive numbers that commence at a minimum value greater than zero and increase monotonically. Moreover, the associated eigenmodes are mutually orthogonal with respect to the energy inner product of $[L^2_{\underline{\epsilon}(\mathbf{r})}(\Omega)]^3$. ■

Appendix B

Rayleigh Multipole Method

The mathematical discussion of the Rayleigh multipole method (RMM) found in this section summarizes the work of [57,58]. Significant groundwork was performed much earlier by Twersky [208,209], who made substantial contributions to the theory of diffraction gratings comprising dielectric rods. Without loss of generality, the following derivations are based on the TM polarization ($\mathbf{E} = E_z\hat{\mathbf{e}}_\mathbf{z}$). With minimal adjustment to the boundary conditions, this procedure can also accommodate the TE polarization.

The Rayleigh multipole method is formulated from diffraction grating analysis (Fig. B.1), which consists of determining the transmitted and reflected orders due

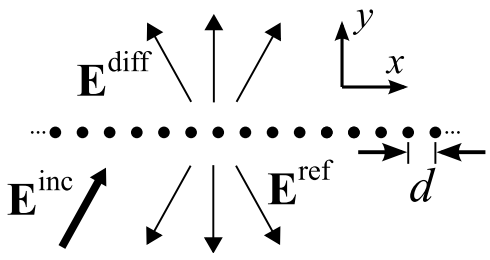

Figure B.1: Diffraction grating showing the incident ($\mathbf{E}^{\text{inc}}$), diffracted ($\mathbf{E}^{\text{diff}}$), and reflected ($\mathbf{E}^{\text{ref}}$) fields. Note that $\mathbf{E}^{\text{inc}} = e^{i(k_x x + k_y y)}\hat{\mathbf{e}}_z$

to an incident plane wave with the wavenumber $\mathbf{k} = (k_x, k_y)$. The problem is periodic along the extent of the grating, as both the incident field and geometry have translational invariance expressed as

$$\begin{aligned} E_z^{\text{inc}}(\mathbf{r} + d\hat{\mathbf{x}}) &= e^{ik_x d} E_z^{\text{inc}}(\mathbf{r}) \\ \epsilon(\mathbf{r} + d\hat{\mathbf{x}}) &= \epsilon(\mathbf{r}) \end{aligned} \tag{B.0.1}$$

where $\mathbf{r} = (x, y) \in \mathbb{R}^2$. Hence the field above $(+y)$ and below $(-y)$ the grating can be expressed as the product of a function that is periodic with the grating and a phase, which may be expanded as

$$E_z(\mathbf{r}) = \sum_{n=-\infty}^{\infty} C_n e^{ik_x x} f_n(y) + E_z^{\text{inc}}(\mathbf{r}) \tag{B.0.2}$$

where

$$k_x^n = k_x + \frac{2\pi n}{d} \tag{B.0.3}$$

As the terms of the Fourier series are orthogonal to each other and the medium above and below the grating is homogeneous, each term of the series must be a solution to the the homogeneous Helmholtz equation

$$\left(\nabla^2 + k^2\right) E_z(\mathbf{r}) = 0 \tag{B.0.4}$$

Consequently, the $f_n(y)$ terms appearing in (B.0.2) are identified as $e^{+ik_y^n y}$ above the grating and $e^{-ik_y^n y}$ below the grating, where the sign of the exponent ensures that field is outgoing and

$$k_y^n = \sqrt{k^2 - (k_x^n)^2} \tag{B.0.5}$$

where the square root is defined in terms of its principal value. Orders for which k_y^n is real are propagating, while the remainder are evanescent.

The task of computing the scattered field thus amounts to calculating the C_n coefficients. The foregoing discussion is general, without reference to a particular geometry or material composition. The Rayleigh multipole method requires that $\epsilon(\mathbf{r})$ conform to a collection of non-intersecting circular geometries in the unit cell. For simplicity, the unit cell is assumed to comprise only a single circular discontinuity. Under this condition, the field outside the circular discontinuities may be expanded as

$$E_z(\mathbf{r}) = \sum_{m=-\infty}^{\infty} \sum_{n=-\infty}^{\infty} B_n H_n^{(1)}\left(k\left|\mathbf{r} - md\hat{\mathbf{x}}\right|\right) e^{i[k_x md + \arg(\mathbf{r} - md\hat{\mathbf{x}})]} + E_z^{inc}(\mathbf{r}), \quad \mathbf{r} \notin D_C \tag{B.0.6}$$

where $H_n^{(1)}$ is the Hankel function of the first kind, and D_C is the subset of $\mathbb{R}^2$ occupied by the circular discontinuities. This expression treats the scattered field as a sum of outgoing cylindrical harmonics originating from each circular discontinuity. A second expansion for the field exists in the annular region around the central disk $(m = 0)$ up to its nearest neighbor

$$E_z(\mathbf{r}) = \sum_{n=-\infty}^{\infty} \left(A_n J_n(kr) + B_n H_n^{(1)}(kr)\right) e^{in\arg(\mathbf{r})} \tag{B.0.7}$$

where r is the Euclidean norm of $\mathbf{r}$. The boundary conditions on the interface between the circular discontinuity and the surrounding region require that the field and its first derivative be continuous along the boundary's normal direction (the latter condition is derived from continuity requirements of the magnetic field). This

gives the relation

$$A_n = \left(\frac{\mu_0 k H'^{(1)}_n (ka) J_n (\upsilon ka) - \mu_0 \upsilon k H^{(1)}_n (ka) J'_n (\upsilon ka)}{\mu_0 \upsilon k J_n (ka) J'_n (\upsilon ka) - \mu_0 k J'_n (ka) J_n (\upsilon ka)} \right) B_n = M_n B_n \quad \text{(B.0.8)}$$

where $\upsilon = \sqrt{\epsilon_r}$ and a are the the refractive index and radius of the circular discontinuity, respectively, and $'$ denotes differentiation with respect to r. Note that the materials considered here are non-magnetic. Substituting (B.0.8) into (B.0.7) and equating with (B.0.6) gives

$$\begin{aligned} &\sum_{n=-\infty}^{\infty} M_n B_n J_n (kr) e^{in\arg(\mathbf{r})} \\ &\qquad = \sum_{\substack{s=-\infty \\ s\neq 0}}^{\infty} \sum_{m=-\infty}^{\infty} B_m H^{(1)}_m \left(k \left|\mathbf{r} - sd\hat{\mathbf{x}}\right|\right) e^{i[k_x sd + m\arg(\mathbf{r} - sd\hat{\mathbf{x}})]} + E^{inc}_z (\mathbf{r}) \end{aligned} \quad \text{(B.0.9)}$$

Using Graf's addition theorem [210], this may be rewritten as

$$\begin{aligned} &\sum_{n=-\infty}^{\infty} M_n B_n J_n (kr) e^{in\arg(\mathbf{r})} \\ &= \sum_{\substack{s=-\infty \\ s\neq 0}}^{\infty} \sum_{n=-\infty}^{\infty} \sum_{q=-\infty}^{\infty} B_{q-n} H^{(1)}_{q-n} (ksd) J_n (kr) e^{i[k_x sd + (n-q)\arg(sd\hat{\mathbf{x}}) + n\arg(\mathbf{r})]} + E^{inc}_z (\mathbf{r}) \end{aligned} \quad \text{(B.0.10)}$$

As the terms on each side are orthogonal expansions with respect to $e^{in\arg(\mathbf{r})}$, (B.0.10) becomes

$$M_n B_n = \sum_{m=-\infty}^{\infty} B_m S_m + E^{inc}_n \quad \text{(B.0.11)}$$

where

$$E^{inc}_n = \left(\frac{k_y + ik_x}{|\mathbf{k}|} \right)^n \quad \text{(B.0.12)}$$

may be found by expanding the incident plane wave as an infinite sum of Bessel

functions of the first kind [210] and

$$S_m = \sum_{s=1}^{\infty} H_m^{(1)}(skd)\left[(-1)^{-m} e^{-isdk_x} + e^{isdk_x}\right] \tag{B.0.13}$$

Known as the lattice sum, this equation states the central disk's incoming field as the sum of scattered fields from the other disks in the grating. This sum is actually conditionally convergent but can be made absolutely convergent by letting $k \to k + i\epsilon$ ($\epsilon > 0$). Equation (B.0.13) may be recast into a more quickly converging series by means of a Poisson summation and integral expansion of the Hankel functions for $m = 0$ [211] and $m \neq 0$ [212]. Alternatively, this expression may be evaluated by numerically integrating a transformed function [213]. Both methods were implemented and found to agree well with each other, although the former was found to be considerably faster and was therefore used in calculations. Solving for the B_n coefficients allows the field to be expressed in terms of cylindrical harmonics. The field can also be represented as a sum of transmitted and reflected plane waves. These can be recovered using Green's first theorem [58]

$$\begin{aligned} &\int_{U\setminus C} \left(V(\mathbf{r}')\,\nabla^2_{\mathbf{r}'} G(\mathbf{r};\mathbf{r}') - G(\mathbf{r};\mathbf{r}')\,\nabla^2_{\mathbf{r}'} V(\mathbf{r}')\right) dA_{\mathbf{r}'} = \\ &\oint_{\partial U \cup \partial C} \left(V(\mathbf{r}')\frac{\partial}{\partial n'} G(\mathbf{r};\mathbf{r}') - G(\mathbf{r};\mathbf{r}')\frac{\partial}{\partial n'} V(\mathbf{r}')\right) ds_{\mathbf{r}'} \end{aligned} \tag{B.0.14}$$

where $G(\mathbf{r};\mathbf{r}')$ is the two-dimensional quasi-periodic Green's function for the Helmholtz equation defined as [58]

$$G(\mathbf{r};\mathbf{r}') = -\frac{i}{4}\sum_{n=-\infty}^{\infty} H_0^{(1)}\left(k\left|\mathbf{r}-\mathbf{r}'-nd\hat{\mathbf{x}}\right|\right) e^{ik_x nd} = \frac{1}{2id}\sum_{n=-\infty}^{\infty} \frac{1}{k_y^n} e^{i\left(k_x^n x + k_y^n |y|\right)} \tag{B.0.15}$$

and the contours and areas of integration are those shown in Fig. B.2. Exploiting

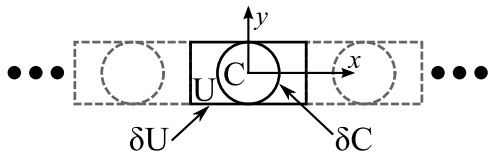

Figure B.2: Unit cell showing the contours and areas of integration appearing in (B.0.14)

the identity [210]

$$J_{v+1}(z) H_v(z) - J_v(z) H_{v+1}(z) = \frac{2i}{\pi z} \tag{B.0.16}$$

allows (B.0.2) to be rewritten in terms of the transmitted and reflected orders

$$\begin{aligned} E_z(\mathbf{r}) &= \sum_{n=-\infty}^{\infty} \frac{2e^{i\left(k_x^n x + k_y^n y\right)}}{k_y^n d} T_n, & y > 0 \\ E_z(\mathbf{r}) &= \sum_{n=-\infty}^{\infty} \frac{2e^{i\left(k_x^n x - k_y^n y\right)}}{k_y^n d} R_n, & y < 0 \end{aligned} \tag{B.0.17}$$

where

$$\begin{aligned} T_n &= \sum_{m-\infty}^{\infty} \left(\frac{k_y^n - i k_x^n}{|\mathbf{k}|} \right)^m B_m, & y > 0 \\ R_n &= \sum_{m-\infty}^{\infty} \left(\frac{-k_y^n - i k_x^n}{|\mathbf{k}|} \right)^m B_m, & y < 0 \end{aligned} \tag{B.0.18}$$

Equations (B.0.17) and (B.0.18) are stated exactly. The scattered field can be approximated by computing the first few terms of B_m around $m = 0$ and computing the first few diffracted and reflected orders around $n = 0$. The accuracy of this approximation rests on the number of terms included in the expansions and the frequencies of interest. Lower frequencies yield a more quickly converging B_m and fewer propagating orders, and hence fewer terms are required to obtain a given accuracy. Note that in addition to propagating orders, a sufficient number of evanescent orders must be retained when other objects are in close proximity

to the grating. In the case of stacked diffraction gratings, these evanescent orders strongly influence the propagating modes associated with the overall structure.

Multiple gratings of the same kind can be arranged as a stack (Fig. 2.7). The homogeneous regions of space are unbounded in the x-direction and are characterized by constant $\epsilon(\mathbf{r})$. These regions comprise the space between the individual gratings and the space above and below the grating stack. In these regions, the field can once again be expressed as the sum of plane waves when the structure is subject to illumination by a single plane wave. This result follows from the fact that such a composite structure still satisfies (B.0.1). Furthermore, the field in these regions can be expressed as the sum of components traveling (decaying) in the $+y$ and $-y$ directions denoted by $E_{z+}(\mathbf{r})$ and $E_{z-}(\mathbf{r})$, respectively

$$\begin{aligned} E_{z+}(\mathbf{r}) &= \left[\ \ldots, \quad e^{ik_x^{-1}x+ik_y^{-1}y}, \quad e^{ik_x^{0}x+ik_y^{0}y}, \quad e^{ik_x^{+1}x,+ik_y^{+1}y}, \quad \ldots \right]^{\mathrm{T}} \cdot \mathbf{v}_+ \\ E_{z-}(\mathbf{r}) &= \left[\ \ldots, \quad e^{ik_x^{-1}x-ik_y^{-1}y}, \quad e^{ik_x^{0}x-ik_y^{0}y}, \quad e^{ik_x^{+1}x,-ik_y^{+1}y}, \quad \ldots \right]^{\mathrm{T}} \cdot \mathbf{v}_- \end{aligned} \tag{B.0.19}$$

where $\mathbf{v}_+$ and $\mathbf{v}_-$ are column vectors of coefficients of the individual plane waves propagating (or decaying) in the $+y$ and $-y$ directions, respectively. The transmission and reflection matrices associated with a single grating are defined as

$$\begin{aligned} \mathbf{v}_+^{\text{trans(above)}} &= \mathbf{T}_{\text{up}}(\omega, k_x)\, \mathbf{v}_+^{\text{below}} \\ \mathbf{v}_-^{\text{trans(below)}} &= \mathbf{T}_{\text{down}}(\omega, k_x)\, \mathbf{v}_-^{\text{above}} \\ \mathbf{v}_-^{\text{refl(below)}} &= \mathbf{R}_{\text{up}}(\omega, k_x)\, \mathbf{v}_+^{\text{below}} \\ \mathbf{v}_+^{\text{refl(above)}} &= \mathbf{R}_{\text{down}}(\omega, k_x)\, \mathbf{v}_-^{\text{above}} \end{aligned} \tag{B.0.20}$$

where the superscripts indicate the region of space (Fig. B.3) and the subscripts in-

dicate the direction of propagation with respect to the y-axis. The quantities $\mathbf{v}_+^{\text{below}}$ and $\mathbf{v}_-^{\text{above}}$ are the components of the incident field, while $\mathbf{v}_+^{\text{refl(above)}}$, $\mathbf{v}_-^{\text{trans(below)}}$, $\mathbf{v}_-^{\text{refl(below)}}$, $\mathbf{v}_+^{\text{refl(above)}}$ are the components of the scattered field. Note that the elements of these matrices depend on incident plane wave parameters ω and k_x. These matrices map the coefficients of the incident fields on each side of the diffraction grating to the transmitted and reflected fields. Thus, the field in the homogeneous regions above and below each grating may be expressed as

$$\begin{aligned} \mathbf{v}_+^{\text{above}} &= \mathbf{T}_{\text{up}}(\omega, k_x)\,\mathbf{v}_+^{\text{below}} + \mathbf{R}_{\text{down}}(\omega, k_x)\,\mathbf{v}_-^{\text{above}} \\ \mathbf{v}_-^{\text{below}} &= \mathbf{T}_{\text{down}}(\omega, k_x)\,\mathbf{v}_-^{\text{above}} + \mathbf{R}_{\text{up}}(\omega, k_x)\,\mathbf{v}_+^{\text{below}} \end{aligned} \tag{B.0.21}$$

As gratings in the present discussion possess mirror symmetry about the axis defining translational invariance (x-axis), $\mathbf{T}_{\text{up}}(\omega, k_x) = \mathbf{T}_{\text{down}}(\omega, k_x)$ and $\mathbf{R}_{\text{up}}(\omega, k_x) = \mathbf{R}_{\text{down}}(\omega, k_x)$, and hence the subscripts can be removed.

As some or all of each grating's scattered field is also the incoming field to other grating(s), the total field associated with a multilayer structure can be expressed as the solution to a linear system of equations using the $\mathbf{T}(\omega, k_x)$ and $\mathbf{R}(\omega, k_x)$ matrices. Moreover, the variables representing the fields between gratings can be eliminated to produce the transmission and reflection matrices associated with the

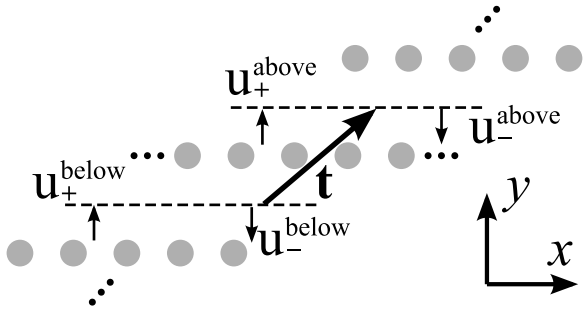

Figure B.3: Diffraction grating stack showing the translation vector $\mathbf{t}$.

entire grating stack. For example, the transmission and reflection matrices for a two-layer stack are found to be

$$\begin{aligned}\mathbf{T'}_2(\omega, k_x) &= \mathbf{T'}(\omega, k_x)\left(\mathbf{I} - \mathbf{R'}(\omega, k_x)^2\right)^{-1}\mathbf{T'}(\omega, k_x)\\ \mathbf{R'}_2(\omega, k_x) &= \mathbf{R'}(\omega, k_x) + \mathbf{T'}(\omega, k_x)\left(\mathbf{I} - \mathbf{R'}(\omega, k_x)^2\right)^{-1}\mathbf{T'}(\omega, k_x)\end{aligned} \tag{B.0.22}$$

The $'$ denotes a shift in the reference plane effected by

$$\begin{aligned}\mathbf{T'} &= \mathbf{DTD}\\ \mathbf{R'} &= \mathbf{D^{-1}RD}\end{aligned} \tag{B.0.23}$$

where $\mathbf{D}$ is the diagonal matrix that advances phase and is defined as

$$\mathbf{D}_{j,k} = \delta_{j,k}e^{i(k_y t_y/2 + k_x t_x/2)} \tag{B.0.24}$$

where t_x and t_y are the x and y components, respectively, of the translation vector (Fig. B.3). Provided that the spacing between gratings is invariant throughout the structure, (B.0.22) can be solved recursively by using the matrices associated with a two-layer structure to generate the matrices for a four layer structure and so forth. If the computational cost of the single layer matrices is treated as a constant, this approach bears a computational complexity of $\mathcal{O}(\log(n))$, where n is the number of grating layers.

The transmission and reflection matrices can also be used to calculate the dispersion diagrams for structures of infinite extent. The translation operator (with

arguments suppressed)

$$\mathcal{T} = \begin{bmatrix} \mathbf{T}' - \mathbf{R}'\mathbf{T}'^{-1}\mathbf{R}' & \mathbf{R}'\mathbf{T}'^{-1} \\ \mathbf{T}'^{-1}\mathbf{R}' & \mathbf{T}'^{-1} \end{bmatrix} \tag{B.0.25}$$

maps the field from below the grating to field above (Fig. B.3). The action of the operator on the field quantities appearing in Fig. B.3 may be expressed as

$$\mathcal{T} \begin{bmatrix} \mathbf{u}_+^{\text{below}} \\ \mathbf{u}_-^{\text{below}} \end{bmatrix} = \begin{bmatrix} \mathbf{u}_+^{\text{above}} \\ \mathbf{u}_-^{\text{above}} \end{bmatrix} \tag{B.0.26}$$

The eigenvectors of this operator represent the modes supported by the infinite structure, while the eigenvalues, which may be expressed as $e^{i(k_x t_x + k_y t_y)}$, are the difference in phase (and possibly magnitude) between any two field values separated by the translation vector (Fig. B.3). Eigenvalues of unit modulus correspond to propagating modes located at (k_x, k_y) in the irreducible Brillouin zone. Band diagrams may be computed by solving the spectral problem of (B.0.25) for distinct values of ω and k_x in a manner that depends on the lattice and choice of path in reciprocal space. As with the plane wave method, this produces a dense matrix. However, the evanescent orders decay rapidly as the order increases, so the constituent transmission and reflection matrices can be accurately approximated by retaining only a modest number of terms.

The standard dispersion diagram for a square lattice may be found in three steps. The first section (Γ–X) may be computed by setting k_x to zero and solving the eigenvalue problem for distinct values of ω separated by regularly spaced intervals. The value of k_y is recovered from those eigenvalues whose moduli are close to unity, and a mark is plotted on the band diagram at the coordinate (k_y, ω). The

procedure for finding the second part (X–M) is identical to that of the first with the exception of setting $k_x = \pi/d$ throughout. The third section (M–Γ) must be dealt with somewhat differently in order to ensure that the calculated modes satisfy $k_x = k_y$. Exploiting the fact that the stack of diffraction gratings can also be defined diagonally (Fig. 2.7) allows the problem to be formulated in a coordinate system that is rotated by $\pi/4$. The values k'_x and k'_y are related to their counterparts in the original coordinate system by

$$\begin{aligned} k'_x &= k_x - k_y \\ k'_y &= k_x + k_y \end{aligned} \tag{B.0.27}$$

The problem is evaluated in the same manner as Γ–X, albeit by setting the length of the translation vector to $d/\sqrt{2}$, the disk spacing to $\sqrt{2}d$, and k'_x to zero, which ensures that $k_x = k_y$.

Appendix C

Process Parameters & Mechanical Drawings

C.1 Nanofabrication Process Parameters

C.1.1 Sputtering Processes

Sputtering was carried out with a Semicore/MRC 8667 sputtering system. Upon loading the machine with samples, the chamber was evacuated with a roughing pump to a residual pressure of 50 mT and subsequently to 6 μT with a cryopump. Sputtering was performed in an argon atmosphere of 6 mT, corresponding to an argon flow rate of approximately 40–45 sccm. The plasma was formed with a DC power source and targets were cleaned prior to deposition by sputtering onto an unused glass slide for 30 seconds. The sputtering parameters for each material used are given in Table C.1.

Material	Power (W)	Target Diameter (mm)	Rate (nm/min)	Final Thickness (nm)
Ti	300	152.4	46	35
Cu	200	152.4	147	1175
ITO	200	139.7	77	58

Table C.1: Sputtering process parameters.

C.1.2 Plasma Etching Process

The parameters used in plasma etching polyvinyl alcohol layers (to determine their thickness by measuring the resultant step profile) are given in Table C.2. Etching was carried out with a Trion RIE/ICP plasma etcher for a duration of 3 seconds. Doubling this time did not appear to result in significant further etching or a visible reduction of the underlying ITO layer. The parameters given here are based on the work of [214].

Parameter	Value
Pressure (mT)	35
CH_4 Flow Rate (sccm)	10
Ar Flow Rate (sccm)	28
Inductive Coupled Plasma Power (W)	150
Reactive Ion Etching Power (W)	150

Table C.2: Plasma etching process parameters.

C.1.3 Removal of Organic Residue

Samples were cleaned with a piranha solution prior to the deposition of sputtered material. The solution comprised a 4:1 ratio of 95%–98% hydrosulfuric acid (Fischerbrand 351296–4) and 30% hydrogen peroxide (Fischer H324–4). It was prepared by slowly adding the hydrogen peroxide to the sulfuric acid, as this process is very exothermic. Samples were immersed for 5 minutes, rinsed with distilled water, and then dried with nitrogen.

C.1.4 Wet Etching Processes

The copper of the Rogers RO4003c substrate was etched with a solution containing 40% ferric chloride and 1% hydrochloric acid (415 Copper Etchant, MG Chemicals). Etching times increased as the solution became depleted but did not exceed approximately 20 minutes. Sputtered copper was etched in about 10 minutes with a 15%–20% solution of ammonium persulfate (APS Copper Etch 100, Transene Company). Titanium layers were etched in approximately 5 minutes using a 10% buffered oxide etch solution, whose active component is buffered hydrofluoric acid.

C.1.5 Photolithographic Process

Photolithography was carried out with a positive photoresist (FujiFilm HPR 504, Catalog No. 820006), which was spin coated onto samples at a rotational speed of 3000 RPM for a duration of 30 seconds. Samples were then soft baked at 115 °C for 60 seconds and exposed to ultraviolet light using an ABM contact mask aligner under a positive mask for 5.0 seconds. Samples were subsequently immersed in developer (MF-354, Rohm Haas Microposit) for 20 seconds and then rinsed with distilled water. The patterned photoresist was inspected under an optical microscope. In cases where defects were observed, the patterned photoresist was removed with acetone and the foregoing process was repeated. Samples that were satisfactorily patterned were then hard baked for 30 minutes at a temperature of 120 °C. Photoresist layers used to protect samples during processing with the wafer saw were formed by spin coating the same photoresist at a rotational speed of 500 RPM and hard baking without patterning.

C.2 Mechanical Drawings

C.2.1 Microstrip Photonic Bandgap Device Prototype

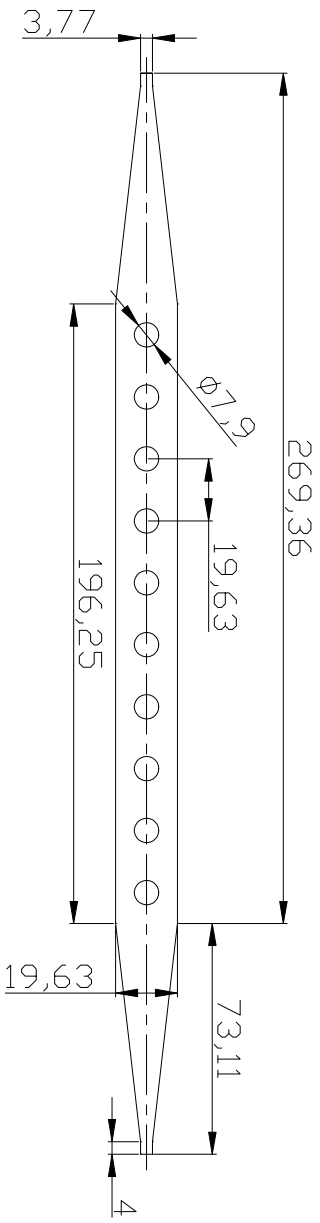

Figure C.1: Drawing of the signal (metal) layer of the microstrip photonic bandgap device prototype. The placement of the sapphire overlaid.

C.2.2 Thru-Reflect-Line Calibration Kit Mask

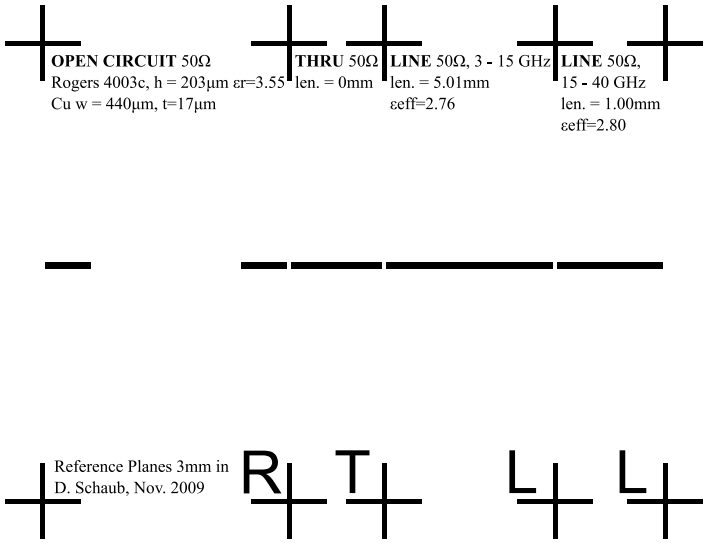

Figure C.2: Thru-reflect-line calibration kit mask shown scaled 2:1.

C.2.3 Circular Patch Resonator Mask

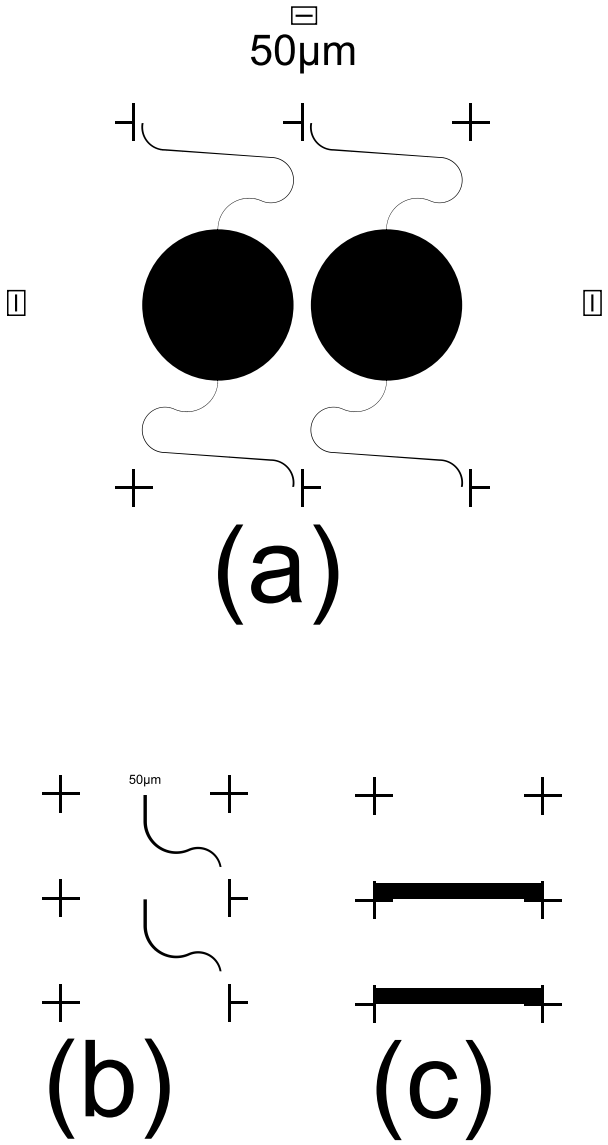

Figure C.3: Circular patch resonator masks for (a) quartz superstrate, (b) Rogers RO4003c signal conductor, and (c) Rogers RO4003c ground conductor. Drawing is scaled 1:1.

C.2.4 Liquid Crystal Photonic Bandgap Mask

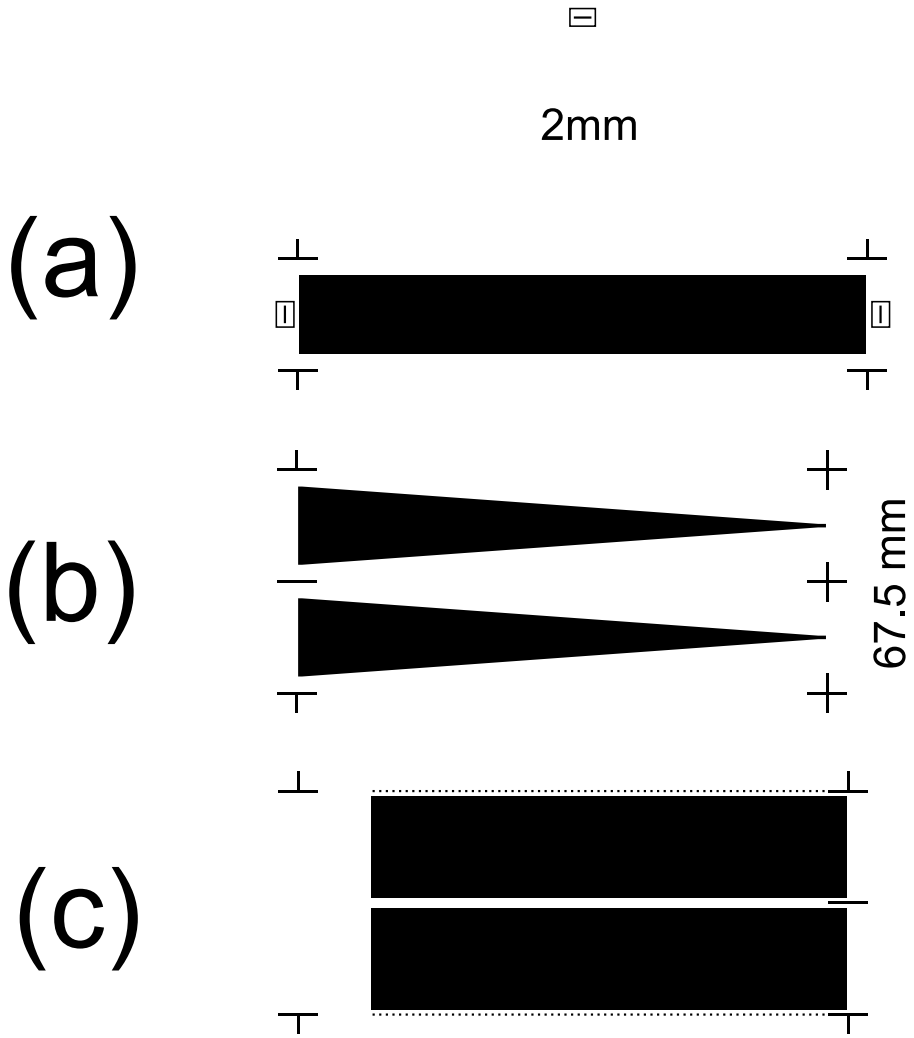

Figure C.4: Liquid crystal photonic bandgap masks for (a) quartz superstrate, (b) Rogers RO4003c signal conductor, and (c) Rogers RO4003c ground conductor. Drawing is scaled 1:1.

C.2.5 Buffing Machine

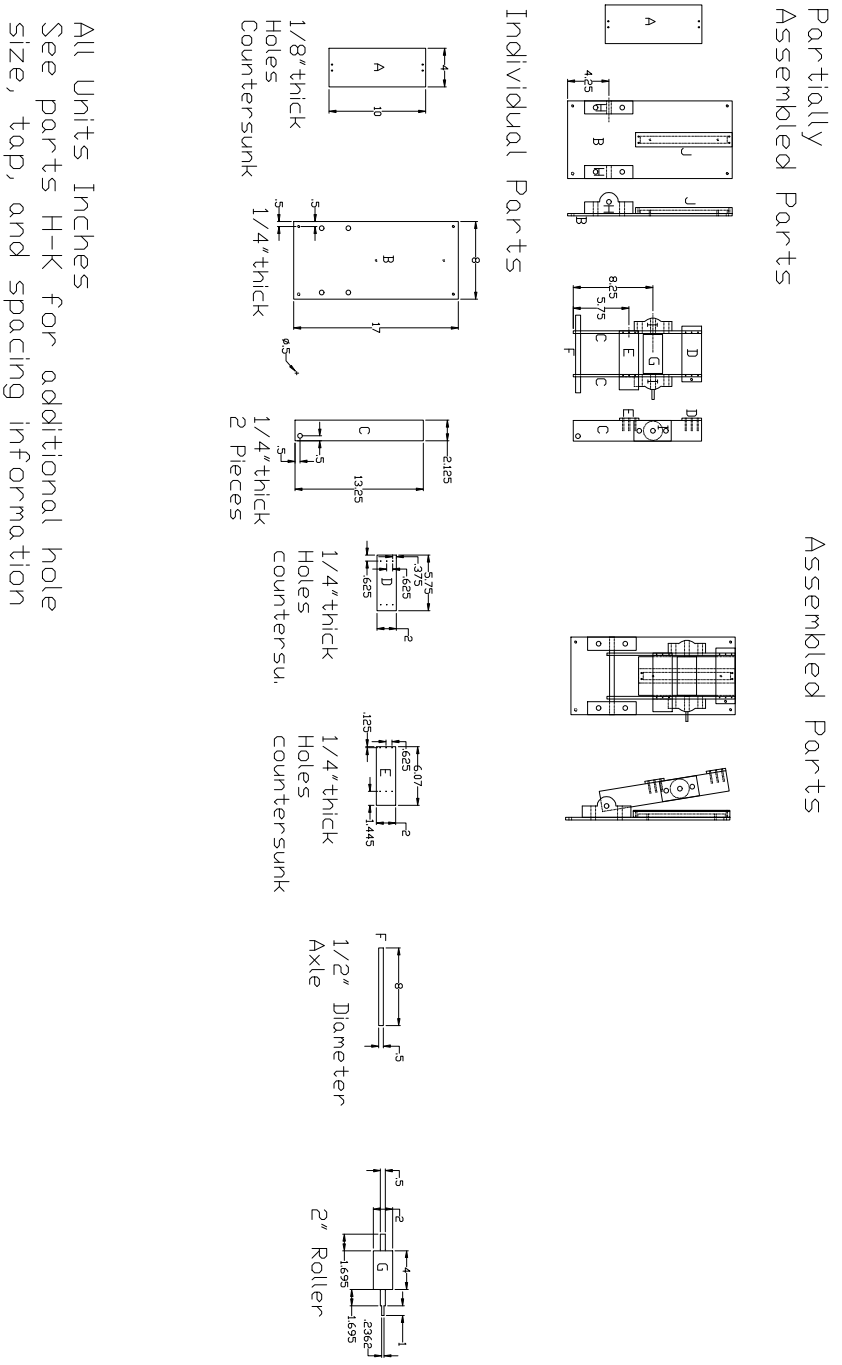

Figure C.5: Drawing of buffing machine, comprising the stage (A), platform (B), drum assembly (C)–(F), roller (G), pillow block drum assembly bearings (H), drum bearings (I), linear stage bearing (J), and stage motor bearing (K).

References

[1] L. Brillouin, *Wave Propagation in Periodic Structures*, 2nd ed. New York: McGraw-Hill, 1946, ch. 7.

[2] J.-M. Lourtioz, H. Benisty, V. Berger, J.-M. Grard, D. Maystre, and A. Tchelnokov, *Photonic Crystals: Towards Nanoscale Photonic Devices*. Berlin, Germany: Springer-Verlag, 2005, ch. 1, 5, 6.

[3] C. A. Balanis, *Antenna Theory*, 3rd ed. Hoboken, New Jersey: Wiley-Interscience, 2005, ch. 6, 14.

[4] J. W. Strutt, "On the maintenance of vibrations by forces of double frequency, and on the propagation of waves through a medium endowed with a periodic structure," *Philosophical Magazine*, vol. 24, no. 147, pp. 145–159, August 1887.

[5] G. W. Hill, "On the part of the motion of the lunar perigee which is a function of the mean motion of the sun and moon," *Acta Mathematica*, vol. 8, no. 1, pp. 1–36, December 1886.

[6] G. Floquet, "Sur les équations différentielles linéaires à coefficients périodiques," *Annales Scientifiques de l'École Normale Supérieure*, vol. 2, pp. 47–88, August 1883.

[7] F. Bloch, "Über die Quantenmechanik der Elektronen in Kristallgittern," *Zeitschrift für Physik*, vol. 52, no. 7, pp. 555–600, July 1929.

[8] J. Pierce and L. Field, "Traveling-wave tubes," *Proceedings of the IRE*, vol. 35, no. 2, pp. 108–111, February 1947.

[9] L. Chu and J. Jackson, "Field theory of traveling-wave tubes," *Proceedings of the IRE*, vol. 36, no. 7, pp. 853–863, July 1948.

[10] J. Pierce, "Theory of the beam-type traveling-wave tube," *Proceedings of the IRE*, vol. 35, no. 2, pp. 111–123, February 1947.

[11] R. Stegen and R. Reed, "Arrays of closely-spaced nonresonant slots," *Transactions of the IRE Professional Group on Antennas and Propogation*, vol. 2, no. 3, pp. 109–113, July 1954.

[12] A. Thomas and F. Zucker, "Radiation from modulated surface wave structures - I," *IRE International Convention Record*, vol. 5, pp. 153–160, March 1957.

[13] R. Pease, "Radiation from modulated surface wave structures - II," *IRE International Convention Record*, vol. 5, pp. 161–165, March 1957.

[14] R. Elliott, "Serrated waveguide–part I: Theory," *IRE Transactions on Antennas and Propagation*, vol. 5, no. 3, pp. 270–275, July 1957.

[15] K. Kelly and R. Elliott, "Serrated waveguide–part II: Experiment," *IRE Transactions on Antennas and Propagation*, vol. 5, no. 3, pp. 276–283, July 1957.

[16] T. Leonard and L. Young, "Frequency selective surfaces," *Antennas and Propagation Society International Symposium, 1977*, vol. 15, pp. 560–563, June 1977.

[17] C.-H. Tsao and R. Mittra, "Spectral-domain analysis of frequency selective surfaces comprised of periodic arrays of cross dipoles and Jerusalem crosses," *IEEE Transactions on Antennas and Propagation*, vol. 32, no. 5, pp. 478–486, May 1984.

[18] R. Mittra, R. Hall, and C.-H. Tsao, "Spectral-domain analysis of circular patch frequency selective surfaces," *IEEE Transactions on Antennas and Propagation*, vol. 32, no. 5, pp. 533–536, May 1984.

[19] R. Abhari and G. Eleftheriades, "Metallo-dielectric electromagnetic bandgap structures for suppression and isolation of the parallel-plate noise in high-speed circuits," *IEEE Transactions on Microwave Theory and Techniques*, vol. 51, no. 6, pp. 1629–1639, June 2003.

[20] T.-L. Wu, Y.-H. Lin, T.-K. Wang, C.-C. Wang, and S.-T. Chen, "Electromagnetic bandgap power/ground planes for wideband suppression of ground bounce noise and radiated emission in high-speed circuits," *IEEE Transactions on Microwave Theory and Techniques*, vol. 53, no. 9, pp. 2935–2942, September 2005.

[21] F. Glandorf and I. Wolff, "A spectral-domain analysis of periodically nonuniform microstrip lines," *IEEE Transactions on Microwave Theory and Techniques*, vol. 35, no. 3, pp. 336–343, March 1987.

[22] D. Nesic and A. Nesic, "1-D microstrip PBG band-pass filter without etching in the ground plane and with sinusoidal variation of the characteristic impedance," *5th International Conference on Telecommunications in Modern Satellite, Cable and Broadcasting Service (TELSIKS)*, vol. 1, pp. 181–183, September 2001.

[23] P. Baccarelli, C. Di Nallo, S. Paulotto, and D. Jackson, "A full-wave numerical approach for modal analysis of 1-D periodic microstrip structures," *IEEE Transactions on Microwave Theory and Techniques*, vol. 54, no. 4, pp. 1350–1362, June 2006.

[24] Y. Qian, V. Radisic, and T. Itoh, "Simulation and experiment of photonic band-gap structures for microstrip circuits," *Proceedings of the 1997 Asia-Pacific Microwave Conference*, vol. 2, pp. 585–588, December 1997.

[25] Y. Qian and T. Itoh, "Planar periodic structures for microwave and millimeter wave circuit applications," *1999 IEEE MTT-S International Microwave Symposium Digest*, vol. 4, pp. 1533–1536, June 1999.

[26] V. Radisic, Y. Qian, R. Coccioli, and T. Itoh, "Novel 2-D photonic bandgap structure for microstrip lines," *IEEE Microwave and Guided Wave Letters*, vol. 8, no. 2, pp. 69–71, February 1998.

[27] F. Falcone, T. Lopetegi, and M. Sorolla, "1-D and 2-D photonic bandgap microstrip structures," *Microwave and Optical Technology Letters*, vol. 22, no. 6, pp. 411–412, September 1999.

[28] D. Ahn, J.-S. Park, C.-S. Kim, J. Kim, Y. Qian, and T. Itoh, "A design of the low-pass filter using the novel microstrip defected ground structure," *IEEE Transactions on Microwave Theory and Techniques*, vol. 49, no. 1, pp. 86–93, January 2001.

[29] C.-S. Kim, J.-S. Park, D. Ahn, and J.-B. Lim, "A novel 1-D periodic defected ground structure for planar circuits," *IEEE Microwave and Guided Wave Letters*, vol. 10, no. 4, pp. 131–133, April 2000.

[30] E. Yablonovitch, "Inhibited spontaneous emission in solid-state physics and electronics," *Physical Review Letters*, vol. 58, no. 20, pp. 2059–2062, May 1987.

[31] K. Inoue and K. Ohtaka, *Photonic Crystals: Physics, Fabrication and Applications*. Berlin, Germany: Springer-Verlag, 2004, ch. 1, 2, 3.

[32] J. D. Joannopoulos, R. D. Meade, and J. N. Winn, *Photonic Crystals*, 2nd ed. Princeton, New Jersey: Princeton University Press, 2008, ch. 1–5, 10.

[33] K. Sakoda, *Optical Properties of Photonic Crystals*. Berlin, Germany: Springer-Verlag, 2001, ch. 1, 2.

[34] R. Ziolkowski and N. Engheta, "Metamaterial special issue introduction," *IEEE Transactions on Antennas and Propagation*, vol. 51, no. 10, pp. 2546–2549, October 2003.

[35] K. Busch and S. John, "Liquid-crystal photonic-band-gap materials: The tunable electromagnetic vacuum," *Physical Review Letters*, vol. 83, no. 5, pp. 967–970, August 1999.

[36] K. Yoshino, K. Nakayama, Y. Kawagishi, S. Tatsuhara, M. Ozaki, and A. A. Zakhidov, "Properties of liquid crystals in photonic crystal, synthetic opal," *Molecular Crystals and Liquid Crystals Science and Technology. Section A. Molecular Crystals and Liquid Crystals*, vol. 329, pp. 433–440, August 1999.

[37] K. Yoshino, Y. Shimoda, Y. Kawagishi, K. Nakayama, and M. Ozaki, "Temperature tuning of the stop band in transmission spectra of liquid-crystal infiltrated synthetic opal as tunable photonic crystal," *Applied Physics Letters*, vol. 75, no. 7, pp. 932–934, August 1999.

[38] P. Oswald and P. Pieranksi, *Nematic and Cholesteric Liquid Crystals*. Boca Raton, Florida: Taylor & Francis, 2005, ch. A.I–A.III, B.I–B.IV.

[39] L. M. Blinov, *Electro-optical and Magneto-optical Properties of Liquid Crystals*. New York: John Wiley & Sons, 1983, ch. 1, 2.

[40] L. Vicari, Ed., *Optical Applications of Liquid Crystals*. Temple Back, Bristol, United Kingdom: Institute of Physics Publishing, 2003, ch. 1.

[41] V. Chigrinov, *Liquid Crystal Devices*. Boston: Artech House, 1999, ch. 1, 2.

[42] G. W. Hanson and A. B. Yakovlev, *Operator Theory for Electromagnetics*. New York: Springer-Verlag, 2002, ch. 1, 3, 4, app. A.

[43] B. D. Reddy, *Introductory Functional Analysis*. New York: Springer-Verlag, 1998, ch. 4, 5, 7.

[44] R. Petit, Ed., *Electromagnetic Theory of Gratings*. Berlin, Germany: Springer-Verlag, 1980, ch. 1, app. A.

[45] P. Šolín, *Partial Differential Equations and the Finite Element Method*. Hoboken, New Jersey: John Wiley and Sons, 2006, ch. 7.

[46] H. Ammari, Ed., *Modeling and Computations in Electromagnetics: A Volume Dedicated to Jean-Claude Nédélec*. Berlin, Germany: Springer-Verlag, 2008, ch. 7.

[47] P. B. Johns and R. L. Beurle, "Numerical solution of 2-dimensional scattering problems using a transmission-line matrix," *Proceedings of the Institution of Electrical Engineers*, vol. 118, no. 9, pp. 1203–1208, September 1971.

[48] G. Kron, "Equivalent Circuit of the Field Equations of Maxwell-I," *Proceedings of the IRE*, vol. 32, no. 5, pp. 289–299, May 1944.

[49] L. E. Kinsler, A. R. Frey, A. B. Coppens, and J. V. Sanders, *Fundamentals of Acoustics*, 3rd ed. New York: John Wiley & Sons, 1982, ch. 10.

[50] P. Schavemaker and L. van der Sluis, *Electrical Power System Essentials*. The Atrium, Southern Gate, Chichester, West Sussex, England: John Wiley & Sons, 2008, ch. 3.

[51] D. M. Pozar, *Microwave Engineering*, 3rd ed. Hoboken, New Jersey: John Wiley and Sons, 2005, ch. 2, 3, 4, app. F.

[52] C. Christopoulos, *The Transmission-Line Modeling Method: TLM*. Piscataway, New Jersey: John Wiley & Sons, 1995, ch. 5, p. 232.

[53] M. Weiner, *Electromagnetic Analysis Using Transmission Line Variables*. Singapore: World Scientific Publishing Co. Pte. Ltd., 2001.

[54] A. Taflove and S. Hagness, *Computational Electrodynamics: The Finite Difference Time Domain Method*, 2nd ed. Norwood, Massachusetts: Artech House, 2000.

[55] G. Romo and T. Smy, "Dispersion relation calculation of photonic crystals using the transmission line matrix method," *International Journal of Numerical Modelling: Electronic Networks, Devices and Fields*, vol. 17, no. 5, pp. 451–459, September 2004.

[56] G. Romo and T. Smy, "Modeling of photonic crystals using a real-valued transmission line matrix method," *Journal of Applied Physics*, vol. 94, no. 4, pp. 2177–2182, August 2003.

[57] L. C. Botten, R. C. McPhedran, N. A. Nicorovici, A. A. Asatryan, C. M. de Sterke, P. A. Robinson, K. Busch, G. H. Smith, and T. N. Langtry, "Rayleigh Multipole Methods for Photonic Crystal Calculations," *Progress in Electromagnetic Research*, vol. 41, pp. 21–60, 2003.

[58] L. C. Botten, N.-A. P. Nicorovici, A. A. Asatryan, R. C. McPhedran, C. M. de Sterke, and P. A. Robinson, "Formulation for electromagnetic scattering and propagation through grating stacks of metallic and dielectric cylinders for photonic crystal calculations. Part I. Method," *Journal of the Optical Society of America A*, vol. 17, no. 12, pp. 2165–2176, December 2000.

[59] B. Stevensson, A. V. Komolkin, D. Sandström, and A. Maliniak, "Structure and molecular ordering extracted from residual dipolar couplings: A molecular dynamics simulation study," *The Journal of Chemical Physics*, vol. 114, no. 5, pp. 2332–2339, February 2001.

[60] I.-C. Khoo, *Liquid Crystals: Physical Properties and Nonlinear Optical Phenomena*. New York: John Wiley & Sons, 1995, ch. 2.

[61] S. Chandrasekhar, *Liquid Crystals*. Cambridge, United Kingdom: Cambridge University Press, 1977, ch. 2.

[62] E. B. Priestley, P. J. Wojtowicz, and P. Sheng, *Introduction to Liquid Crystals*. New York: Plenum Press, 1975, ch. 6.

[63] K. Takatoh, M. Hasegawa, M. Koden, N. Itoh, R. Hasegawa, and M. Sakamoto, *Alignment Technologies and Applications of Liquid Crystal Devices*. New York: Taylor & Francis, 2005, ch. 2, 5.

[64] M. F. Toney, T. P. Russell, J. A. Logan, H. Kikuchi, J. M. Sands, and S. K. Kumar, "Near-surface alignment of polymers in rubbed films," *Nature*, vol. 374, no. 6524, pp. 709–711, April 1995.

[65] S. Jun and Y.-S. Cho, "Deformation-induced bandgap tuning of 2D silicon-based photonic crystals," *Optics Express*, vol. 11, no. 21, pp. 2769–2774, October 2003.

[66] S. Kim and V. Gopalan, "Strain-tunable photonic band gap crystals," *Applied Physics Letters*, vol. 78, no. 20, pp. 3015–3017, May 2001.

[67] M. J. Madou, *Fundamentals of Microfabrication: The Science of Miniaturization*, 2nd ed. Boca Raton, Florida: CRC Press, 2002, ch. 4.

[68] C. W. Wong, P. T. Rakich, S. G. Johnson, M. Qi, H. I. Smith, E. P. Ippen, L. C. Kimerling, Y. Jeon, G. Barbastathis, and S.-G. Kim, "Strain-tunable silicon photonic band gap microcavities in optical waveguides," *Applied Physics Letters*, vol. 84, no. 8, pp. 1242–1244, February 2004.

[69] C. W. Wong, Y. B. Jeong, G. Barbastathis, and S.-G. Kim, "Strain-tuning of periodic optical devices: tunable gratings and photonic crystals," *12th International Conference on TRANSDUCERS, Solid-State Sensors, Actuators and Microsystems*, vol. 1, pp. 202–205, June 2003.

[70] Y. J. Rao, "Recent progress in applications of in-fibre Bragg grating sensors," *Optics and Lasers in Engineering*, vol. 31, no. 4, pp. 297–324, April 1999.

[71] Z. Ghattan, T. Hasek, R. Wilk, M. Shahabadi, and M. Koch, "Sub-terahertz on-off switch based on a two-dimensional photonic crystal infiltrated by liquid crystals," *Optics Communications*, vol. 281, no. 18, pp. 4623–4625, September 2008.

[72] V. A. Tolmachev, "Tuning of the photonic band gaps and the reflection spectra of a one-dimensional photonic crystal based on silicon and a liquid crystal," *Optics and Spectroscopy*, vol. 99, no. 5, pp. 765–769, November 2005.

[73] A. E. Miroshnichenko, E. Brasselet, and Y. S. Kivshar, "Light-induced orientational effects in periodic photonic structures with pure and dye-doped nematic liquid crystal defects," *Physical Review A*, vol. 78, no. 5, p. 053823, November 2008.

[74] S. A. Myslivets, V. A. Gunyakov, V. P. Gerasimov, V. Y. Zyryanov, S. Y. Vetrov, V. F. Shabanov, V. G. Arkhipkin, and G. N. Kamaev, "Control over the transmission spectrum of a one-dimensional photonic crystal with a liquid-crystal layer," *Doklady Physics*, vol. 52, no. 3, pp. 134–138, March 2007.

[75] E. Astrova, T. Perova, Y. Zharova, S. Grudinkin, V. Tolmachev, and V. Melnikov, "Electro-tunable one-dimensional photonic crystal structures based on grooved silicon infiltrated with liquid crystal," *Journal of Luminescence*, vol. 121, no. 2, pp. 298–300, December 2006.

[76] V. A. Tolmachev, S. A. Grudinkin, J. A. Zharova, V. A. Melnikov, E. V. Astrova, and T. S. Perova, "Electro-tuning of the photonic band gap in SOI-based structures infiltrated with liquid crystal," in *Silicon Photonics and Photonic Integrated Circuits*, G. C. Righini, S. K. Honkanen, L. Pavesi, and L. Vivien, Eds., vol. 6996, no. 1. SPIE, April 2008, p. 69961Z.

[77] T. S. Perova, V. A. Tolmachev, E. V. Astrova, Y. A. Zharova, and S. M. O'Neill, "Tunable one-dimensional photonic crystal structures based on grooved Si infiltrated with liquid crystal E7," *Physica Status Solidi (c)*, vol. 4, no. 6, pp. 1961–1965, May 2007.

[78] V. Y. Zyryanov, V. A. Gunyakov, S. A. Myslivets, V. G. Arkhipkin, and V. F. Shabanov, "Electrooptical switching in a one-dimensional photonic crystal," *Molecular Crystals and Liquid Crystals*, vol. 488, pp. 118–126, January 2008.

[79] R. Ozaki, H. Moritake, K. Yoshino, and M. Ozaki, "Analysis of defect mode switching response in one-dimensional photonic crystal with a nematic liquid crystal defect layer," *Journal of Applied Physics*, vol. 101, no. 3, p. 033503, February 2007.

[80] I. D. Villar, I. Matias, F. Arregui, and R. Claus, "Analysis of one-dimensional photonic band gap structures with a liquid crystal defect towards development of fiber-optic tunable wavelength filters," *Optics Express*, vol. 11, no. 5, pp. 430–436, March 2003.

[81] S. Weiss, H. Ouyang, J. Zhang, and P. Fauchet, "Electrical and thermal modulation of silicon photonic bandgap microcavities containing liquid crystals," *Optics Express*, vol. 13, no. 4, pp. 1090–1097, February 2005.

[82] E. Brasselet, A. E. Miroshnichenko, D. F. Chen, W. Krolikowski, and Y. S. Kivshar, "Polarizational nonlinear optical response of photonic structures with a liquid crystal defect," *Optics Letters*, vol. 34, no. 4, pp. 488–490, February 2009.

[83] R. Ozaki, H. Miyoshi, M. Ozaki, and K. Yoshino, "Tunable defect mode in one-dimensional photonic crystal with liquid crystal defect layer," *Molecular Crystals and Liquid Crystals*, vol. 433, pp. 247–257, June 2005.

[84] C.-Y. Liu, "Creation of tunable absolute bandgaps in a two-dimensional anisotropic photonic crystal modulated by a nematic liquid crystal," *Physics Letters A*, vol. 372, no. 31, pp. 5198–5202, July 2008.

[85] C.-Y. Liu, N.-W. Zhang, H.-W. Wang, and L.-W. Chen, "Efficient tunable negative refraction photonic crystal achieved by an elliptic rod lattice with a nematic liquid crystal," *Physica B: Condensed Matter*, vol. 404, no. 21, pp. 4060–4070, November 2009.

[86] C.-Y. Liu and L.-W. Chen, "Tunable band gap in a photonic crystal modulated by a nematic liquid crystal," *Physical Review B*, vol. 72, no. 4, p. 045133, July 2005.

[87] P. Halevi, J. H. Arroyo-Nunez, and J. A. Reyes-Cervantes, "Two-dimensional photonic crystal infiltrated by liquid crystal: response to applied electric field," in *Photonic Crystal Materials and Devices*, A. Adibi, A. Scherer, and S. Y. Lin, Eds., vol. 5000, no. 1. SPIE, July 2003, pp. 224–236.

[88] J. A. Reyes-Avendaño and P. Halevi, "Electrical tuning of refraction in a two-dimensional photonic crystal infilled with a liquid crystal," *Revista Mexicana De Física*, vol. 54, no. 6, pp. 407–410, December 2008.

[89] J. Arriaga, L. Dobrzynski, and B. Djafari-Rouhani, "Electrotunable band gaps of one- and two-dimensional photonic crystal structures based on silicon and liquid crystals," *Journal of Applied Physics*, vol. 104, no. 6, p. 063108, September 2008.

[90] A. Rixon, M. Cryan, J. Pereda, and C. Railton, "Modelling of 2D photonic crystals with liquid crystal infilling," in *2006 International Conference on Transparent Optical Networks*, vol. 4, June 2006, pp. 249–252.

[91] D. Xu and G. Xiong, "Transmission spectra investigation on tunable bandgap of liquid crystal infiltrated photonic crystal," *Journal of Materials Science*, vol. 39, no. 2, pp. 679–681, January 2004.

[92] H. Takeda and K. Yoshino, "TE-TM mode coupling in two-dimensional photonic crystals composed of liquid-crystal rods," *Physical Review E*, vol. 70, no. 2, p. 026601, August 2004.

[93] E. Kosmidou, E. Kriezis, and T. Tsiboukis, "Analysis of tunable photonic crystal devices comprising liquid crystal materials as defects," *IEEE Journal of Quantum Electronics*, vol. 41, no. 5, pp. 657–665, May 2005.

[94] E. P. Kosmidou, E. E. Kriezis, and T. D. Tsiboukis, "FDTD analysis of photonic crystal defect layers filled with liquid crystals," *Optical and Quantum Electronics*, vol. 37, no. 1, pp. 149–160, January 2005.

[95] L. Moretti, V. Mocella, L. Sirleto, G. Bonasso, and I. Rendina, "Tunable two dimensional photonic crystal based on liquid crystals," in *Photonic Materials, Devices, and Applications*, G. Badenes, D. Abbott, and A. Serpenguzel, Eds., vol. 5840, no. 1. SPIE, May 2005, pp. 667–673.

[96] P. Dardano, L. Sirleto, V. Mocella, I. Rendina, and L. Moretti, "Tunable T-Shaped waveguide in two dimensional photonic crystals based on liquid crystals," *Molecular Crystals and Liquid Crystals*, vol. 453, pp. 165–175, September 2006.

[97] T. Yasuda, Y. Tsuji, and M. Koshiba, "Tunable light propagation in photonic crystal coupler filled with liquid crystal," *IEEE Photonics Technology Letters*, vol. 17, no. 1, pp. 55–57, January 2005.

[98] G. Alagappan, X. W. Sun, P. Shum, and M. B. Yu, "Tunable superprism and polarization splitting in a liquid crystal infiltrated two-dimensional photonic crystal made of silicon oxynitride," *Optics Letters*, vol. 31, no. 8, pp. 1109–1111, April 2006.

[99] S. W. Leonard, J. P. Mondia, H. M. van Driel, O. Toader, S. John, K. Busch, A. Birner, U. Gösele, and V. Lehmann, "Tunable two-dimensional photonic crystals using liquid crystal infiltration," *Physical Review B*, vol. 61, no. 4, pp. R2389–R2392, January 2000.

[100] J. Martz, R. Ferrini, F. Nüesch, L. Zuppiroli, B. Wild, L. A. Dunbar, R. Houdré, M. Mulot, and S. Anand, "Liquid crystal infiltration of InP-based planar photonic crystals," *Journal of Applied Physics*, vol. 99, no. 10, p. 103105, May 2006.

[101] M. A. Dündar, H. H. J. E. Kicken, A. Y. Silov, R. Nötzel, F. Karouta, H. W. M. Salemink, and R. W. van der Heijden, "Birefringence-induced mode-dependent tuning of liquid crystal infiltrated InGaAsP photonic crystal nanocavities," *Applied Physics Letters*, vol. 95, no. 18, p. 181111, November 2009.

[102] M. A. Dündar, H. H. J. E. Kicken, A. Y. Silov, R. Ntzel, F. Karouta, and R. W. van der Heijden, "Liquid crystal tuning of InGaAsP photonic crystal membrane type nanocavities," in *Proceedings of the Fourteenth Annual Symposium of the IEEE Photonics Benelux Chapter*, S. Beri, P. Tassin, G. Craggs, X. Leijtens, and J. Danckaert, Eds. Brussels: VUBPress Brussels University Press, November 2009, pp. 101–104.

[103] I. Barbu, H. Kicken, P. Nouwens, R. van der Heijden, F. Karouta, R. Ntzel, and H. Salemink, "Liquid crystal-infiltrated nanocavity and waveguide in deeply etched InP-based photonic crystals," in *14th European Conference on Integrated Optics*, June 2008, pp. 197–200.

[104] C.-Y. Liu and L.-W. Chens, "Tunable channel drop filter in a two-dimensional photonic crystal modulated by a nematic liquid crystal," *Journal of Nanomaterials*, vol. 2006, p. 52946, 2006.

[105] H. H. J. E. Kicken, I. Barbu, S. P. Kersten, M. A. Dündar, R. W. van der Heijden, F. Karouta, R. Nötzel, E. van der Drift, and H. W. M. Salemink, "Tuning of narrow-bandwidth photonic crystal devices etched in InGaAsP planar waveguides by liquid crystal infiltration," in *Photonic and Phononic Crystal Materials and Devices IX*, A. Adibi, S.-Y. Lin, and A. Scherer, Eds., vol. 7223, no. 1. SPIE, February 2009, p. 72230C.

[106] C.-Y. Liu, Y.-T. Peng, J.-Z. Wang, and L.-W. Chen, "Creation of tunable bandgaps in a three-dimensional anisotropic photonic crystal modulated by a nematic liquid crystal," *Physica B: Condensed Matter*, vol. 388, no. 1-2, pp. 124–129, January 2007.

[107] C.-Y. Liu and L.-W. Chen, "Tunable full bandgap in a three-dimensional photonic crystal modulated by a nematic liquid crystal," *Physica E: Low-dimensional Systems and Nanostructures*, vol. 35, no. 1, pp. 173–177, October 2006.

[108] A. D'Orazio, "Infiltrated liquid crystal photonic bandgap devices for switching and tunable filtering," *Fiber and Integrated Optics*, vol. 22, no. 3, pp. 161–172, May 2003.

[109] D. M. Walba, D. A. Zummach, M. D. Wand, W. N. Thurmes, K. M. Moray, and K. E. Arnett, "Synthesis of ferroelectric liquid crystal oligomer glasses for second-order nonlinear optics," in *Liquid Crystal Materials, Devices, and Applications II*, U. Efron and M. D. Wand, Eds., vol. 1911, no. 1. SPIE, 1993, pp. 21–28.

[110] S. Kishio, M. Ozaki, K. Yoshino, T. Sakurai, N. Mikami, and R. Higuchi, "Characteristics of optical switching and memory effects utilizing deformation of helicoidal structure of ferroelectric liquid crystals with large spontaneous polarization," *Japanese Journal of Applied Physics*, vol. 26, pp. 513–516, January 1987.

[111] Q.-B. Meng, C.-H. Fu, S. Hayami, Z.-Z. Gu, O. Sato, and A. Fujishima, "Effects of external electric field upon the photonic band structure in synthetic opal infiltrated with liquid crystal," *Journal of Applied Physics*, vol. 89, no. 10, pp. 5794–5796, May 2001.

[112] D. Kang, J. E. Maclennan, N. A. Clark, A. A. Zakhidov, and R. H. Baughman, "Electro-optic behavior of liquid-crystal-filled silica opal photonic crystals: Effect of liquid-crystal alignment," *Physical Review Letters*, vol. 86, no. 18, pp. 4052–4055, April 2001.

[113] G. Mertens, T. Röder, R. Schweins, K. Huber, and H.-S. Kitzerow, "Shift of the photonic band gap in two photonic crystal/liquid crystal composites," *Applied Physics Letters*, vol. 80, no. 11, pp. 1885–1887, March 2002.

[114] S. Kubo, Z.-Z. Gu, K. Takahashi, A. Fujishima, H. Segawa, and O. Sato, "Tunable photonic band gap crystals based on a liquid crystal-infiltrated inverse opal structure," *Journal of the American Chemical Society*, vol. 126, no. 26, pp. 8314–8319, June 2004.

[115] H. Matthias, T. Röder, R. B. Wehrspohn, H.-S. Kitzerow, S. Matthias, and S. J. Picken, "Spatially periodic liquid crystal director field appearing in a photonic crystal template," *Applied Physics Letters*, vol. 87, no. 24, p. 241105, December 2005.

[116] A. D. Remenyuk, E. V. Astrova, R. F. Vitman, T. S. Perova, and V. A. Tolmachev, "Alignment of liquid crystal E7 in composite photonic crystals based on single crystal silicon," in *Opto-Ireland 2005: Optoelectronics, Photonic Devices, and Optical Networks*, J. G. McInerney, G. Farrell, D. M.

Denieffe, L. P. Barry, H. S. Gamble, P. J. Hughes, and A. Moore, Eds., vol. 5825, no. 1. SPIE, June 2005, pp. 400–407.

[117] A. D. Remenyuk, E. V. Astrova, R. F. Vitman, T. S. Perova, V. A. Tolmachev, and J. K. Vij, "Investigation into the orientation of the liquid-crystal mixture E7 in composite photonic crystals based on single-crystal silicon," *Physics of the Solid State*, vol. 48, no. 2, pp. 384–391, February 2006.

[118] H. Matthias, S. L. Schweizer, R. B. Wehrspohn, and H.-S. Kitzerow, "Liquid crystal director fields in micropores of photonic crystals," *Journal of Optics A: Pure and Applied Optics*, vol. 9, no. 9, pp. S389–S395, September 2007.

[119] P. Halevi, J. A. Reyes-Avendaño, and J. A. Reyes-Cervantes, "Electrically tuned phase transition and band structure in a liquid-crystal-infilled photonic crystal," *Physical Review E*, vol. 73, no. 4, p. 040701, April 2006.

[120] F. Du, Y.-Q. Lu, and S.-T. Wu, "Electrically tunable liquid-crystal photonic crystal fiber," *Applied Physics Letters*, vol. 85, no. 12, pp. 2181–2183, September 2004.

[121] L. Scolari, T. Alkeskjold, J. Riishede, A. Bjarklev, D. Hermann, A. Anawati, M. Nielsen, and P. Bassi, "Continuously tunable devices based on electrical control of dual-frequency liquid crystal filled photonic bandgap fibers," *Optics Express*, vol. 13, no. 19, pp. 7483–7496, September 2005.

[122] M. Haakestad, T. Alkeskjold, M. Nielsen, L. Scolari, J. Riishede, H. Engan, and A. Bjarklev, "Electrically tunable photonic bandgap guidance in a liquid-crystal-filled photonic crystal fiber," *IEEE Photonics Technology Letters*, vol. 17, no. 4, pp. 819–821, April 2005.

[123] C.-Y. Liu and L.-W. Chen, "Tunable photonic-crystal waveguide Mach Zehnder interferometer achieved by nematic liquid-crystal phase modulation," *Optics Express*, vol. 12, no. 12, pp. 2616–2624, June 2004.

[124] X. Chen, X. Dong, J. J. Hu, P. Shum, Y. Wang, Y. Qiu, G. Lin, and H. Hong, "Tunable Mach-Zehnder interferometer in a two-dimensional photonic crystal with liquid crystal infiltration," in *Photonic Crystals and Photonic Crystal Fibers for Sensing Applications III*, H. H. Du and H. Fudouzi, Eds., vol. 6767, no. 1. SPIE, October 2007, p. 676709.

[125] B. Maune, M. Lončar, J. Witzens, M. Hochberg, T. Baehr-Jones, Y. Qiu, D. Psaltis, and A. Scherer, "Liquid crystal electric tuning of a photonic crystal laser," in *Tuning the Optical Response of Photonic Bandgap Structures*, P. M. Fauchet and P. V. Braun, Eds., vol. 5511, no. 1. SPIE, October 2004, pp. 26–37.

[126] B. Maune, M. Lončar, J. Witzens, M. Hochberg, T. Baehr-Jones, D. Psaltis, A. Scherer, and Y. Qiu, "Liquid-crystal electric tuning of a photonic crystal laser," *Applied Physics Letters*, vol. 85, no. 3, pp. 360–362, July 2004.

[127] R. Ozaki, Y. Matsuhisa, M. Ozaki, and K. Yoshino, "Low driving voltage tunable laser based on one-dimensional photonic crystal containing liquid crystal defect layer," *Molecular Crystals and Liquid Crystals*, vol. 441, pp. 87–95, November 2005.

[128] Y. Matsuhisa, A. Fujii, M. Ozaki, W. Haase, and K. Yoshino, "Wavelength-variable laser in a hybrid photonic crystal containing ferroelectric liquid crystal," *Molecular Crystals and Liquid Crystals*, vol. 477, pp. 245–254, January 2007.

[129] J. Cos, J. Ferre-Borrull, J. Pallares, and L. Marsal, "Tunable Fabry-Pérot filter based on one-dimensional photonic crystals with liquid crystal components," *Optics Communications*, vol. 282, no. 6, pp. 1220–1225, March 2009.

[130] A. E. Miroshnichenko, E. Brasselet, and Y. S. Kivshar, "All-optical switching and multistability in photonic structures with liquid crystal defects," *Applied Physics Letters*, vol. 92, no. 25, p. 253306, June 2008.

[131] R. W. Lee, "The magnetic field dependence of the microwave dielectric constant of a liquid crystal at 3 kmc," Master's thesis, Michigan State University. Dept. of Physics, Michigan, 1954.

[132] E. F. Carr and R. D. Spence, "Influence of a magnetic field on the microwave dielectric constant of a liquid crystal," *The Journal of Chemical Physics*, vol. 22, no. 9, pp. 1481–1485, September 1954.

[133] E. F. Carr, "Microwave dielectric measurements in liquid crystals," *The Journal of Chemical Physics*, vol. 26, no. 2, pp. 420–422, February 1957.

[134] E. F. Carr, "Influence of electric and magnetic fields on the microwave dielectric constant of a liquid crystal with a positive dielectric anisotropy," *The Journal of Chemical Physics*, vol. 42, no. 2, pp. 738–742, January 1965.

[135] H. Moritake, K. Toda, T. Kamei, Y. Utsumi, and W. Haase, "Microwave phase shifter with ferroelectric liquid crystal having large tilt angle," *Molecular Crystals and Liquid Crystals*, vol. 434, pp. 199–207, June 2005.

[136] S. Muller, P. Scheele, C. Weil, M. Wittek, C. Hock, and R. Jakoby, "Tunable passive phase shifter for microwave applications using highly anisotropic liquid crystals," in *2004 IEEE MTT-S International Microwave Symposium Digest*, vol. 2, June 2004, pp. 1153–1156.

[137] T. Kuki, H. Fujikake, T. Nomoto, and Y. Utsumi, "Design of a microwave variable delay line using liquid crystal, and a study of its insertion loss," *Electronics and Communications in Japan (Part II: Electronics)*, vol. 85, no. 2, pp. 36–42, February 2002.

[138] T. Kuki, H. Fujikake, H. Kamoda, and T. Nomoto, "Microwave variable delay line using a membrane impregnated with liquid crystal," in *2002 IEEE MTT-S International Microwave Symposium Digest*, vol. 1, June 2002, pp. 363–366.

[139] T. Kuki, H. Fujikake, and T. Nomoto, "Microwave variable delay line using dual-frequency switching-mode liquid crystal," *IEEE Transactions on Microwave Theory and Techniques*, vol. 50, no. 11, pp. 2604–2609, November 2002.

[140] F. Goelden, A. Lapanik, S. Mueller, A. Gaebler, W. Haase, and R. Jakoby, "Investigations on the behavior of ferroelectric liquid crystals at microwave frequencies," in *European Microwave Conference, 2007*, October 2007, pp. 106–109.

[141] F. Sahbani, N. Tentillier, A. Gharsallah, A. Gharbi, and C. Legrand, "New tunable coplanar microwave phase shifter with nematic crystal liquid," in *3rd International Design and Test Workshop, 2008. IDT 2008*, December 2008, pp. 78–81.

[142] F. Goelden, A. Gaebler, M. Goebel, A. Manabe, S. Mueller, and R. Jakoby, "Tunable liquid crystal phase shifter for microwave frequencies," *Electronics Letters*, vol. 45, no. 13, pp. 686–687, June 2009.

[143] N. Martin, P. Laurent, G. Prigent, P. Gelin, and F. Huret, "Improvement of an inverted microstrip line-based microwave tunable phase-shifter using liquid crystal," in *33rd European Microwave Conference*, vol. 3, October 2003, pp. 1417–1420.

[144] N. Martin, P. Laurent, G. Prigent, P. Gelin, and F. Huret, "Technological evolution and performances improvements of a tunable phase-shifter using liquid crystal," *Microwave and Optical Technology Letters*, vol. 43, no. 4, pp. 338–341, November 2004.

[145] Y. Utsumi, N. T. Bach, T. Kamei, R. Ozaki, and H. Moritake, "Comparison of microwave measurements and theoretical calculations of dielectric birefringence for a liquid crystal loaded CPW-FE phase shifter," *Molecular Crystals and Liquid Crystals*, vol. 510, pp. 197–213, September 2009.

[146] N. Martin, N. Tentillier, P. Laurent, B. Splingart, F. Huret, P. Gelin, and C. Legrand, "Electrically microwave tunable components using liquid crystals," in *32nd European Microwave Conference, 2002*, September 2002, pp. 1–4.

[147] B. A. Belyaev, A. A. Leksikov, A. M. Serzhantov, and V. F. Shabanov, "Controllable liquid-crystal microwave phase shifter," *Technical Physics Letters*, vol. 34, no. 6, pp. 463–466, June 2008.

[148] H. Fujikake, T. Kuki, T. Nomoto, Y. Tsuchiya, and Y. Utsumi, "Thick polymer-stabilized liquid crystal films for microwave phase control," *Journal of Applied Physics*, vol. 89, no. 10, pp. 5295–5298, May 2001.

[149] H. Fujikake, T. Kuki, H. Kamoda, F. Sato, and T. Nomoto, "Voltage-variable microwave delay line using ferroelectric liquid crystal with aligned submicron polymer fibers," *Applied Physics Letters*, vol. 83, no. 9, pp. 1815–1817, September 2003.

[150] J. Yeh, C. Chang, C.-C. Cheng, J.-Y. Huang, and S. Hsu, "Microwave characteristics of liquid-crystal tunable capacitors," *IEEE Electron Device Letters*, vol. 26, no. 7, pp. 451–453, July 2005.

[151] F. Yang and J. R. Sambles, "Microwave liquid crystal wavelength selector," *Applied Physics Letters*, vol. 79, no. 22, pp. 3717–3719, November 2001.

[152] F. Yang and J. R. Sambles, "A liquid crystal microwave wavelength selector," *Liquid Crystals Today*, vol. 11, pp. 1–2, December 2002.

[153] F. Yang and J. R. Sambles, "Microwave liquid-crystal variable phase grating," *Applied Physics Letters*, vol. 85, no. 11, pp. 2041–2043, September 2004.

[154] A. Mirfatah and J. Laurin, "Tunable hairpin resonator based on liquid crystal," in *13th International Symposium on Antenna Technology and Applied Electromagnetics and the Canadian Radio Science Meeting, 2009. ANTEM/URSI 2009*, February 2009, pp. 1–4.

[155] Y. Utsumi, T. Kamei, and R. Naito, "Measurements of effective dielectric permittivity of microstrip-line-type liquid crystal devices using inductive coupled ring resonator," *Electronics Letters*, vol. 39, no. 11, pp. 849–850, May 2003.

[156] B. Sanadgol, S. Holzwarth, and J. Kassner, "30 GHz liquid crystal phased array," in *Antennas Propagation Conference, 2009. LAPC 2009. Loughborough*, November 2009, pp. 589–592.

[157] A. Moessinger, S. Dieter, W. Menzel, S. Mueller, and R. Jakoby, "Realization and characterization of a 77 GHz reconfigurable liquid crystal reflectarray," in *13th International Symposium on Antenna Technology and Applied Electromagnetics and the Canadian Radio Science Meeting, 2009. ANTEM/URSI 2009*, February 2009, pp. 1–4.

[158] A. Moessinger, R. Marin, J. Freese, S. Mueller, A. Manabe, and R. Jakoby, "Investigations on 77 GHz tunable reflectarray unit cells with liquid crystal," in *First European Conference on Antennas and Propagation, 2006. EuCAP 2006*, November 2006, pp. 1–4.

[159] R. Marin, A. Mossinger, J. Freese, A. Manabe, and R. Jakoby, "Realization of 35 GHz steerable reflectarray using highly anisotropic liquid crystal," in *IEEE Antennas and Propagation Society International Symposium 2006*, July 2006, pp. 4307–4310.

[160] W. Hu, M. Ismail, R. Cahill, J. Encinar, V. Fusco, H. Gamble, R. Dickie, D. Linton, N. Grant, and S. Rea, "Electronically reconfigurable monopulse reflectarray antenna with liquid crystal substrate," in *The Second European Conference on Antennas and Propagation, 2007. EuCAP 2007*, November 2007, pp. 1–6.

[161] A. Moessinger, R. Marin, S. Mueller, J. Freese, and R. Jakoby, "Electronically reconfigurable reflectarrays with nematic liquid crystals," *Electronics Letters*, vol. 42, no. 16, pp. 899–900, August 2006.

[162] B. A. Belyaev, N. A. Drokin, V. F. Shabanov, and V. N. Shepov, "A study of the microwave dielectric permittivity of liquid crystals in electric and magnetic fields," *Technical Physics*, vol. 43, no. 1, pp. 105–109, January 1998.

[163] H. Xu, O. Trushkevych, N. Collings, and W. A. Crossland, "Measurement of dielectric anisotropy of some liquid crystals for microwave applications," *Molecular Crystals and Liquid Crystals*, vol. 502, pp. 235–244, May 2009.

[164] C. Druon and J. M. Wacrenier, "A measuring cell for the dielectric study of liquid crystals having high transition temperatures (up to 200 degrees c) in the frequency range 1 Hz–1 GHz," *Journal of Physics E: Scientific Instruments*, vol. 16, no. 2, p. 151, February 1983.

[165] Y. Utsumi and T. Kamei, "Dielectric permittivity measurements of liquid crystal in the microwave and millimeter wave ranges," *Molecular Crystals and Liquid Crystals*, vol. 409, pp. 355–370, January 2004.

[166] Y. Utsumi, T. Kamei, and R. Naito, "Dielectric properties of microstrip-line adaptive liquid crystal devices," *Electronics and Communications in Japan (Part II: Electronics)*, vol. 87, no. 10, pp. 13–24, October 2004.

[167] F. Yang and J. R. Sambles, "Determination of the microwave permittivities of nematic liquid crystals using a single-metallic slit technique," *Applied Physics Letters*, vol. 81, no. 11, pp. 2047–2049, September 2002.

[168] F. Yang and J. R. Sambles, "Determination of the permittivity of nematic liquid crystals in the microwave region," *Liquid Crystals*, vol. 30, no. 5, pp. 599–602, May 2003.

[169] J. Parka, J. Krupka, R. Dabrowski, and J. Wosik, "Measurements of anisotropic complex permittivity of liquid crystals at microwave frequencies," *Journal of the European Ceramic Society*, vol. 27, no. 8-9, pp. 2903–2905, 2007.

[170] F. Goelden, A. Lapanik, A. Gaebler, S. Mueller, W. Haase, and R. Jakoby, "Systematic investigation of nematic liquid crystal mixtures at 30 GHz," in *2007 Digest of the IEEE/LEOS Summer Topical Meetings*, July 2007, pp. 202–203.

[171] A. Penirschke, S. Muller, P. Scheele, C. Weil, M. Wittek, C. Hock, and R. Jakoby, "Cavity perturbation method for characterization of liquid crystals up to 35 GHz," in *34th European Microwave Conference, 2004*, vol. 2, October 2004, pp. 545–548.

[172] S. Mueller, A. Moessinger, R. Marin, F. Goelden, A. Lapanik, W. Haase, and R. Jakoby, "Liquid crystals - microwave characterization and tunable devices," *Frequenz*, vol. 61, no. 9-10, pp. 217–223, 2007.

[173] B. Splingart, N. Tentillier, F. Huret, and C. Legrand, "Liquid crystals applications to R.F. and microwave tunable components," *Molecular Crystals and Liquid Crystals Science and Technology. Section A. Molecular Crystals and Liquid Crystals*, vol. 368, pp. 183–190, August 2001.

[174] S. Bulja, D. Mirshekar-Syahkal, M. Yazdanpanahi, R. James, S. Day, and F. Fernandez, "Planar transmission line method for measurement of dielectric constants of liquid crystals in 60 GHz band," in *Asia Pacific Microwave Conference, 2009. APMC 2009*, December 2009, pp. 341–344.

[175] R. James, F. Fernandez, S. Day, S. Bulja, and D. Mirshekar-Syahkal, "Accurate modeling for wideband characterization of nematic liquid crystals for microwave applications," *IEEE Transactions on Microwave Theory and Techniques*, vol. 57, no. 12, pp. 3293–3297, December 2009.

[176] S. Mueller, A. Penirschke, C. Damm, P. Scheele, M. Wittek, C. Weil, and R. Jakoby, "Broad-band microwave characterization of liquid crystals using a temperature-controlled coaxial transmission line," *IEEE Transactions on Microwave Theory and Techniques*, vol. 53, no. 6, pp. 1937–1945, June 2005.

[177] T. Kamei, Y. Utsumi, H. Moritake, K. Toda, and H. Suzuki, "Measurements of the dielectric properties of nematic liquid crystals at 10 kHz to 40 GHz and application to a variable delay line," *Electronics and Communications in Japan (Part II: Electronics)*, vol. 86, no. 8, pp. 49–60, August 2003.

[178] B. W. Kernighan and D. M. Ritchie, *C Programming Language*, 2nd ed. Englewood Cliffs, New Jersey: Prentice Hall, 1988.

[179] M. Frigo and S. G. Johnson, "The FFTW web page," *http://www.fftw.org/*, 2008.

[180] E. Anderson, Z. Bai, C. Bischof, S. Blackford, J. Demmel, J. Dongarra, J. Du Croz, A. Greenbaum, S. Hammarling, A. McKenney, and D. Sorensen, *LAPACK Users' Guide*, 3rd ed. Philadelphia, Pennsylvania: Society for Industrial and Applied Mathematics, 1999.

[181] D. Lukashevich, A. Cangellaris, and P. Russer, "Reduced Order Modeling in TLM," in *The 19th Annual Review of Progress in Applied Computational Electromagnetics*, March 2003, pp. 371–376.

[182] D. Lukashevich, A. Cangellaris, and P. Russer, "Transmission line matrix method reduced order modeling," *2003 IEEE MTT-S International Microwave Symposium Digest*, vol. 2, pp. 1125–1128 vol.2, June 2003.

[183] D. Lukashevich and P. Russer, "Oblique-oblique projection in TLM-MOR for high-Q structures," *2005 European Microwave Conference*, vol. 2, 4 pp., October 2005.

[184] J. L. Goldberg, *Matrix Theory with Applications*. New York: McGraw-Hill, 1991, ch. 3, 6.

[185] F. Chatelin and M. Ahus, *Eigenvalues of Matrices*. Chichester, New York: John Wiley & Sons, 1993, ch. 6.

[186] Y. Saad, *Iterative Methods for Sparse Linear Systems*, 2nd ed. Philadelphia, Pennsylvania: Society for Industrial and Applied Mathematics, 2003, ch. 3, 4, 6, 7, 8.

[187] G. H. Golub and C. F. V. Loan, *Matrix Computations*, 2nd ed. Baltimore, Maryland: Johns Hopkins University Press, 1989, ch. 5.

[188] J. Nielsen and W. Hoefer, "A complete dispersion analysis of the condensed node TLM mesh," *IEEE Transactions on Magnetics*, vol. 27, no. 5, pp. 3982–3983, September 1991.

[189] M. Krumpholz and P. Russer, "On the dispersion in TLM and FDTD," *IEEE Transactions on Microwave Theory and Techniques*, vol. 42, no. 7, pp. 1275–1279, July 1994.

[190] H. M. Wu, J. H. Tang, Q. Luo, Z. M. Sun, Y. M. Zhu, Z. H. Lu, and Y. Wei, "Liquid-crystal alignment of rubbed polyimide films: A microscopic investigation," *Applied Physics B: Lasers and Optics*, vol. 62, no. 6, pp. 613–618, June 1996.

[191] J. Stohr, M. G. Samant, A. Cossy-Favre, J. Diaz, Y. Momoi, S. Odahara, and T. Nagata, "Microscopic origin of liquid crystal alignment on rubbed polymer surfaces," *Macromolecules*, vol. 31, no. 6, pp. 1942–1946, March 1998.

[192] S.-H. Paek, C. J. Durning, K.-W. Lee, and A. Lien, "A mechanistic picture of the effects of rubbing on polyimide surfaces and liquid crystal pretilt angles," *Journal of Applied Physics*, vol. 83, no. 3, pp. 1270–1280, February 1998.

[193] R. Arafune, K. Sakamoto, S. Ushioda, S. Tanioka, and S. Murata, "Importance of rubbing-induced inclination of polyimide backbone structures for determination of the pretilt angle of liquid crystals," *Phys. Rev. E*, vol. 58, no. 5, pp. 5914–5918, November 1998.

[194] K. Shirota, M. Yaginuma, T. Sakai, K. Ishikawa, H. Takezoe, and A. Fukuda, "Orientational relationship among polyimide alignment layer, liquid crystal monolayer, and bulk pretilt angle," *Applied Physics Letters*, vol. 69, no. 2, pp. 164–166, 1996.

[195] J. Lu, S. V. Deshpande, E. Gulari, J. Kanicki, and W. L. Warren, "Ultraviolet light induced changes in polyimide liquid-crystal alignment films," *Journal of Applied Physics*, vol. 80, no. 9, pp. 5028–5034, November 1996.

[196] G. P. Sinha, B. Wen, and C. Rosenblatt, "Large, continuously controllable nematic pretilt from vertical orientation," *Applied Physics Letters*, vol. 79, no. 16, pp. 2543–2545, October 2001.

[197] T. Sakai, K. Ishikawa, H. Takezoe, N. Matsuie, Y. Yamamoto, H. Ishii, Y. Ouchi, H. Oji, and K. Seki, "Surface orientation of main and side chains of polyimide alignment layer studied by near-edge x-ray absorption fine structure spectroscopy," *The Journal of Physical Chemistry B*, vol. 105, no. 38, pp. 9191–9195, September 2001.

[198] D. Guha and J. Siddiqui, "Resonant frequency of circular microstrip antenna covered with dielectric superstrate," *IEEE Transactions on Antennas and Propagation*, vol. 51, no. 7, pp. 1649–1652, July 2003.

[199] P. L. D. Abrie, *Design of RF and Microwave Amplifiers and Oscillators*, 2nd ed. Norwood, Massachusetts: Artech House, 2009, ch. 4.

[200] T. Bah, *Inkscape: Guide to a Vector Drawing Program*, 2nd ed. Upper Saddle River, New Jersey: Prentice Hall, 2009.

[201] S. M. Wentworth, *Fundementals of Electromagnetics with Engineering Applications*. Hoboken, New Jersey: John Wiley and Sons, 2005, app. E.

[202] K. Seeger, "Microwave dielectric constants of silicon, gallium arsenide, and quartz," *Journal of Applied Physics*, vol. 63, no. 11, pp. 5439–5443, June 1988.

[203] D. E. Schaub and D. R. Oliver, "Rapid Simulation of Linear PBG Microstrip Structures Using the Rayleigh Multipole Method," *IEEE Transactions on Microwave Theory and Techniques*, vol. 56, no. 1, pp. 49–55, January 2008.

[204] R. S. Weis and T. K. Gaylord, "Lithium niobate: Summary of physical properties and crystal structure," *Applied Physics A: Materials Science & Processing*, vol. 37, no. 4, pp. 191–203, August 1985.

[205] P. I. Dankov, B. N. Hadjistamov, I. P. Arestova, and V. P. Levcheva, "Measurement of dielectric anisotropy of microwave substrates by two-resonator method with different pairs of resonators," *PIERS Online*, vol. 5, no. 6, pp. 501–505, 2009.

[206] D. C. Dobson, J. Gopalakrishnan, and J. E. Pasciak, "An efficient method for band structure calculations in 3D photonic crystals," *Journal of Computational Physics*, vol. 161, no. 2, pp. 668–679, 2000.

[207] J.-L. L. Robert Dautray, *Mathematical Analysis and Numerical Methods for Science and Technology*. Berlin, Germany: Springer-Verlag, 1988, vol. 2, ch. 4.

[208] V. Twersky, "On scattering of waves by the infinite grating of circular cylinders," *IRE Transactions on Antennas and Propagation*, vol. 10, no. 6, pp. 737–765, November 1962.

[209] V. Twersky, "On the scatttering of waves by an infinite grating," *IRE Transactions on Antennas and Propagation*, vol. 4, no. 3, pp. 330–345, July 1956.

[210] M. Abramowitz and I. Stegun, *Handbook of Mathematical Functions*. New York: Dover, 1972, ch. 9.

[211] F. Oberhettinger, *Fourier Expansions*. New York: Academic Press, 1973, ch. 3.

[212] V. Twersky, "Elementary function representations of Schlömilch series," *Archive for Rational Mechanics and Analysis*, vol. 8, no. 1, pp. 323–332, January 1961.

[213] K. Yasumoto and K. Yoshitomi, "Efficient calculation of lattice sums for free-space periodic Green's function," *IEEE Transactions on Antennas and Propagation*, vol. 47, no. 6, pp. 1050–1055, June 1999.

[214] V. Gruev, K. Wu, J. Van der Spiegel, and N. Engheta, "Fabrication of a thin film micro polarization array," in *Proceedings of the 2006 IEEE International Symposium on Circuits and Systems. ISCAS 2006.*, September 2006, pp. 209–212.